

University of Southampton Research Repository ePrints Soton

Copyright © and Moral Rights for this thesis are retained by the author and/or other copyright owners. A copy can be downloaded for personal non-commercial research or study, without prior permission or charge. This thesis cannot be reproduced or quoted extensively from without first obtaining permission in writing from the copyright holder/s. The content must not be changed in any way or sold commercially in any format or medium without the formal permission of the copyright holders.

When referring to this work, full bibliographic details including the author, title, awarding institution and date of the thesis must be given e.g.

AUTHOR (year of submission) "Full thesis title", University of Southampton, name of the University School or Department, PhD Thesis, pagination

UNIVERSITY OF SOUTHAMPTON

FACULTY OF ENGINEERING AND THE ENVIRONMENT

Engineering Sciences

Application of Light Harvesting Materials to Silicon Photovoltaics

by

Mohd Adib Ibrahim

Thesis for the degree of Doctor of Philosophy

January 2014

UNIVERSITY OF SOUTHAMPTON

ABSTRACT

FACULTY OF ENGINEERING AND THE ENVIRONMENT

Thesis for the degree of Doctor of Philosophy

APPLICATION OF LIGHT HARVESTING MATERIALS TO SILICON PHOTOVOLTAICS

Mohd Adib Ibrahim

High material cost and poor optical absorption of silicon provides the principal motivation for researchers looking for alternative solutions to improve photo-excitation of silicon and leading to more efficient and cheaper solar cells. The present thesis investigates a novel technique of light harvesting (LH) using molecular layers attached to the surface, combined with improved surface passivation. Several surface modifications are produced using wet chemical routes, including hydrogen termination following the covalent attachment of alkyl monolayers. The deposition of Langmuir-Blodgett (LB) films on the passivated silicon surface is used to create LH structures to generate electron hole pairs in the semiconductor.

The interface properties of the passivated layers were characterised by the Spectroscopic Ellipsometry, Fourier Transform Infra-red Spectroscopy, Contact Angle and X-ray Photoelectron Spectroscopy. The passivation surfaces are characterised via surface photovoltage (SPV) measured by the Kelvin Probe (KP) method. An alternative of energy conversion model in photosynthesis and expression of the theory of surface current are derived that follows the Shockley solar cell equation.

We find that the alkyl passivated Si-decene samples possess a lower small surface potential than the native oxide samples (21 - 28 mV), a lower surface charge (approximately $2.6 \times 10^{+10}$ C/cm²) and a lower surface recombination velocity (SRV) (1020 cm/s). We make a preliminary determination as to the LH properties of silicon-decene samples which contain a DiO dye in the LB film. A different mechanism of charge trapping was observed in the silicon-decene-LB

sample. We show conclusively that the charge generated at the interface charge occurs only by illumination within the absorption band of the DiO dye at the wavelengths of 450 and 500 nm, and calculated this charge to be about $3.5 \times 10^{+10}$ C/cm². The mechanism of charge trapping and detrapping is described as a slow process with two identical lifetimes where the slower component differs for the decene and hexane samples. It is significant that this charge trapping via excitation of a molecular layer occurs only when the molecules are close to the surface.

Table of Contents

| | |
|---|--------------|
| ABSTRACT | i |
| Table of Contents | iii |
| List of Tables | ix |
| List of Figures | xi |
| List of Accompanying Materials | xix |
| DECLARATION OF AUTHORSHIP | xxi |
| Acknowledgements | xxiii |
| List of Symbols | xxv |
| Abbreviations | xxxi |
| Chapter 1 Research Review | 1 |
| 1.1 Introduction | 1 |
| 1.2 Motivation | 1 |
| 1.3 Approaches to the Solution | 2 |
| 1.4 Aim and Objectives | 3 |
| 1.5 Main Contributions | 4 |
| 1.6 Outline of the Thesis | 5 |
| Chapter 2 Photovoltaic Solar Cell Operation | 7 |
| 2.1 Introduction | 7 |
| 2.2 Optical Absorption in Silicon and Charge Carrier Generation | 7 |
| 2.3 Fundamentals of <i>p-n</i> Junctions | 9 |
| 2.3.1 Semiconductor Statistics | 9 |
| 2.3.2 In Thermal Equilibrium | 11 |
| 2.3.3 Under Applied Bias | 15 |
| 2.3.4 Surface Space Charge Region | 17 |
| 2.3.5 Relation of the Depletion Layer and Space Charge Density | 18 |
| 2.4 Operation of Solar Cell | 19 |
| 2.4.1 Solar Cell Structures | 20 |
| 2.4.2 Current-Voltage Junction under Illumination | 21 |
| 2.4.3 The Electrical Performance of Solar Cell | 22 |
| 2.5 Carrier Recombination Processes in Solar Cell | 25 |
| 2.5.1 Carrier Transport and Recombination | 26 |

| | | |
|------------------|--|-----------|
| 2.5.2 | Radiative Recombination | 27 |
| 2.5.3 | Band-to-band Auger Recombination | 27 |
| 2.5.4 | Recombination through Defect Levels | 28 |
| 2.5.5 | Minority Carrier Lifetime | 30 |
| 2.6 | Chapter Summary | 32 |
| Chapter 3 | Surface Semiconductor Characteristics | 33 |
| 3.1 | Surface States | 33 |
| 3.2 | Surface Recombination..... | 38 |
| 3.3 | Bulk and Surface Recombination Lifetime | 41 |
| 3.4 | Band Bending near the Surface | 44 |
| 3.5 | Chapter Summary | 45 |
| Chapter 4 | Energy Conversion in Photosynthesis: A Model for Solar Cell Application | 47 |
| 4.1 | Introduction..... | 47 |
| 4.2 | Light Harvesting and Kinetics of Electron Transport | 47 |
| 4.3 | The Model of Energy Conversion | 49 |
| 4.4 | Results and Discussion..... | 57 |
| 4.5 | Chapter Summary | 60 |
| Chapter 5 | Characterization of Surface Recombination by the Kelvin Probe | 61 |
| 5.1 | Introduction..... | 61 |
| 5.2 | Kelvin Probe Applied to Semiconductor Surface Study | 61 |
| 5.2.1 | Metal-Semiconductor System..... | 62 |
| 5.2.2 | Work Function and Contact Potential Difference | 64 |
| 5.3 | Literature Review of Band Bending Measurements by the Kelvin Probe | 65 |
| 5.4 | Methods of Kelvin Probe Measurements – Surface Photovoltage..... | 67 |
| 5.4.1 | Intensity Dependence of Surface Photovoltage Saturation..... | 68 |
| 5.4.2 | Intensity Dependence of Surface Photovoltage Constant..... | 68 |
| 5.5 | Measuring SPV and Surface Recombination by the Kelvin Probe..... | 71 |
| 5.5.1 | Photo-generated Current..... | 74 |
| 5.5.2 | Surface Current Derivation | 76 |
| 5.6 | Chapter Summary | 79 |

| | | |
|------------------|---|------------|
| Chapter 6 | Surface Passivation of Alkyl Monolayers on Silicon | 81 |
| 6.1 | Introduction..... | 81 |
| 6.2 | Preparation and Treatment for Surface Passivation..... | 82 |
| 6.2.1 | Silicon Oxide Terminated Surfaces | 83 |
| 6.2.2 | Hydrogen Terminated Surfaces | 85 |
| 6.2.3 | Organic Monolayer Passivation..... | 87 |
| 6.3 | Methodology..... | 91 |
| 6.3.1 | Experimental Procedure of Hydrogen Terminated Surface | 92 |
| 6.3.2 | Experimental Procedure of 1-Decene on the Silicon Surface... | 93 |
| 6.3.3 | Characterization Procedure | 94 |
| 6.4 | Result and Discussion..... | 98 |
| 6.4.1 | Characterization of 1-Decene Monolayer Samples | 98 |
| 6.4.2 | The Stability Study of 1-Decene Monolayer Passivation..... | 104 |
| 6.5 | Chapter Summary | 107 |
| Chapter 7 | Deposition of Langmuir-Blodgett Films on Silicon | 109 |
| 7.1 | Introduction..... | 109 |
| 7.2 | Background Study of LB Films | 109 |
| 7.2.1 | Mechanisms of LB Films Formation | 110 |
| 7.2.2 | Methods and Parameter Control of LB Films Formation | 114 |
| 7.2.3 | Literature Review on the LB Films..... | 116 |
| 7.3 | Methodology..... | 117 |
| 7.3.1 | Experimental Procedure | 117 |
| 7.3.2 | Substrate and LB Films Preparation | 119 |
| 7.3.3 | Samples Identification..... | 120 |
| 7.4 | Chapter Summary | 122 |
| Chapter 8 | Electrical Characterisation of Silicon Surfaces..... | 123 |
| 8.1 | Introduction..... | 123 |
| 8.2 | Methodology..... | 123 |
| 8.2.1 | Kelvin Probe Method..... | 124 |
| 8.2.2 | Photo-conductance Decay Method..... | 125 |
| 8.3 | Result and Discussion..... | 126 |
| 8.3.1 | Estimation of Diffusion Length..... | 126 |
| 8.3.2 | Measurement of Barrier Height | 129 |
| 8.3.3 | Estimation of Surface Current | 134 |

| | | |
|---------------------------|---|------------|
| 8.3.4 | Estimation of Surface Recombination Velocity | 136 |
| 8.4 | Chapter Summary | 146 |
| Chapter 9 | Charge Trapping Passivated Silicon Surface via Illumination of Dye Monolayers..... | 149 |
| 9.1 | Introduction..... | 149 |
| 9.2 | Understanding of Fast and Slow Charge Trapping | 150 |
| 9.2.1 | Literature Review on the Charge Trapping | 150 |
| 9.2.2 | Calculating Lifetime Decay for Charge Trapping | 151 |
| 9.3 | Results and Discussion..... | 152 |
| 9.3.1 | Absorption Spectrum Measurements | 152 |
| 9.3.2 | Charge Trapping by Illumination of Dye Monolayers..... | 153 |
| 9.3.3 | Effect of Light Absorption through Dye Monolayers..... | 167 |
| 9.4 | Chapter Summary | 169 |
| Chapter 10 | Conclusion and Future Work..... | 171 |
| 10.1 | Introduction..... | 171 |
| 10.2 | Conclusions and Key Contributions | 171 |
| 10.3 | Future Work | 177 |
| Appendices | | 179 |
| Appendix 1 | Characterization Procedure of Kelvin Probe Measurements | 181 |
| A. | Introduction..... | 181 |
| B. | Light Source of Bentham Spectrometer..... | 181 |
| C. | Solar Cells Calibration | 182 |
| D. | Light Intensity Distribution Test | 182 |
| E. | Photon Flux Determination..... | 184 |
| F. | Measurement Procedure..... | 186 |
| Appendix 2 | Publications..... | 191 |
| Glossary | | 195 |
| List of References | | 197 |

List of Tables

| | | |
|------------------|--|-----|
| Table 4.1 | A summary of reaction and process involved in the proposed system of the simplified model of photosynthesis. | 53 |
| Table 6.1 | A summary of Percentage Component of XP spectra. | 101 |
| Table 6.2 | The relative atomic concentration (%) of the elements present in the samples by XPS..... | 103 |
| Table 6.3 | Water contact angles of the samples..... | 107 |
| Table 7.1 | Samples structure, description and identification with LB films..... | 121 |
| Table 8.1 | Summary results of V_{spv} , Q_{sc} , J_{os} and SRV values for Si samples with SPM treatment..... | 139 |
| Table 8.2 | Summary results of V_{spv} , Q_{sc} , J_{os} and SRV values for Si samples with several passivated surfaces..... | 140 |
| Table 8.3 | A summary of the different passivated sample on the Si surface with the effective recombination lifetime and implied SRV as measured by the PCD and KP method..... | 141 |
| Table 8.4 | A summary of several sample of Si treated with SPM etched and native oxide with the effective recombination lifetime and implied SRV as measured by the PCD and KP method..... | 142 |
| Table 9.1 | A summary of 2-lifetimes fit of charge trapping and detrapping on the different samples..... | 168 |

List of Figures

| | | |
|-------------------|--|----|
| Figure 1.1 | Schematic diagram of the novel photovoltaic structure. Light absorbs by the dye molecular layer and transfer the energy by non radiative resonance transfer process. The energy transfer occurs by a dipole-dipole resonance interaction between the energy donor and acceptor [4]. The energy is then collected by electrons from the base and by holes from the emitter (thick arrow). Charge separation takes place at the junction (dashed arrow) [3]. 3 | 3 |
| Figure 1.2 | A summary of main contribution and research framework 4 | 4 |
| Figure 2.1 | The optical absorption of silicon – absorption coefficient and the absorption depth [8]. 8 | 8 |
| Figure 2.2 | Diagram of uniformly doped $p-n$ junction; a) charge density; b) electric field; c) potential [1] and d) band diagram of $p-n$ junction in thermal equilibrium where the electric field, qV_{bi} is the difference of V_p and V_n [2]. 13 | 13 |
| Figure 2.3 | Band diagram of $p-n$ junction in the dark [11]. 16 | 16 |
| Figure 2.4 | A typical structure of a conventional silicon solar cell. The minority carriers (electrons) move from the base and holes from the emitter (thick arrow) across the junction. Charge separation takes place at the junction by the electric field (dashed line). 21 | 21 |
| Figure 2.5 | The effect of light on the $I-V$ characteristic of a solar cell compared to a diode [16]. 23 | 23 |
| Figure 2.6 | Measured $I-V$ characteristic of a solar cell, also showing the maximum power point. 24 | 24 |
| Figure 2.7 | $P-V$ characteristic of a solar cell with the maximum power point. 25 | 25 |
| Figure 2.8 | Schematic diagram of electron and hole trapping (a) Electron trapping and detrapping; (b) electron-hole | |

recombination; and (c) hole trapping and detrapping [11]. A (---) dashed line represent energy transition of traps state..... 30

Figure 3.1 Silicon atom structures of cleaved Si (111): a) incomplete silicon atoms on the surface known as traps (blue colour); b) native oxide - oxidation occurs with oxygen bonds at Si/SiO₂ interface (red colour). 35

Figure 3.2 Schematic diagram of a surface dipole layer [13]. Symbol 'd' is the length of the dipole and 'ϑ' represent an ordered dipole layer oriented at an angle θ with respect to the surface..... 36

Figure 3.3 The four fundamental transitions of a surface state energy level, E_s (a) transitions of electron and holes in a semiconductor (the arrows indicate the electron transition) [18]; and (b) mixed electron / hole transition rate of surface state–band transitions [13]. 40

Figure 3.4 The mechanism of carrier flows (lifetime) associated with surface recombination where τ_{os} is the effective lifetime related to surface recombination; τ_{diff} is lifetime related to diffusion to the surface and τ_b is bulk lifetime. 43

Figure 3.5 Generation rate, G vs. distance, x from the silicon surface..... 43

Figure 3.6 Band diagrams of surface showing three different mechanisms: accumulation, depletion and inversion at the surface of *n-type* semiconductors [12]..... 45

Figure 4.1 Typical energy diagram over charge separation of ET in the bacterial photosynthesis. In addition to the ET steps in Eq. 4.1, the electron can decay to the 'ground state P'. Free energy refers to the vacuum level [4]. 48

Figure 4.2 A schematic diagram of a simple proton pumps circuit to the show the elementary physico-chemical processes. It is assumed that all ETs are 1 electron or 1 H⁺ events. (modified from Crofts [56]). 51

| | | |
|-------------------|--|----|
| Figure 4.3 | A schematic depiction of chemical energy flows in the primary processes of bacterial photosynthesis, forming the basis of the proposed system of the simplified model of photosynthesis..... | 52 |
| Figure 4.4 | A schematic diagram of excitation of P in Checkpoint 1B of the simplified model..... | 56 |
| Figure 4.5 | Graph of photosynthetic energy conversion that have a similarity with the I - V characteristic (a) Rate of photosynthetic energy conversion K vs. Electrochemical potential $\Delta\mu$ and (b) Power P vs. Electrochemical potential $\Delta\mu$ | 59 |
| Figure 5.1 | A schematic band diagram of metal-semiconductor (n -type) shows the barrier height, δV_s and splitting of quasi-Fermi levels E_{Fn} and E_{Fp} in the depletion region. | 63 |
| Figure 5.2 | The dependence of SPV constant for diffusion length determination by plotting collection efficiency, $(1/\eta_L)$ against absorption depth $(1/\alpha)$ (points: data, lines: theory)..... | 71 |
| Figure 5.3 | The band diagram of semiconductor (n -type) with surface states under illumination. Φ is the photon flux, V_{spv} is the surface photovoltage, W is the depletion width; E_{Fn} and E_{Fp} are the quasi-Fermi levels for electrons and holes, respectively..... | 73 |
| Figure 5.4 | Typical graph of $(\exp qV/kT - 1)$ vs. photon flux, Φ - a linear slope represents C_L in Eq. 5.37 that used to estimate the SRV..... | 79 |
| Figure 6.1 | Schematic of alkene monolayer passivation process..... | 83 |
| Figure 6.2 | Schematic of the hydrogen terminated Si (100) and Si (111) surface [85]. | 86 |
| Figure 6.3 | Structural molecular of a silicon cluster with decene chain. The tilt angle is 35.5° from the surface normal and d_{chain} is the chain length projected on the surface normal [111]..... | 91 |

| | | |
|--------------------|---|-----|
| Figure 6.4 | Measuring of water contact angle, Θ on the solid surface e.g. silicon substrate..... | 97 |
| Figure 6.5 | FTIR spectra of 1-decene (double distilled) monolayer directly attached to Si surface (a) hydrosilylation at 160 °C, $\tau = 12 \mu\text{s}$; (b) hydrosilylation with Lewis acid catalyst at 90 °C, $\tau = 10 \mu\text{s}$; and (c) hydrosilylation with Lewis acid catalyst at 110 °C, $\tau = 11 \mu\text{s}$ | 99 |
| Figure 6.6 | XP survey spectrum of Si (111)-C ₁₀ H ₂₁ in the presence of C ₂ H ₅ AlCl ₂ prepared by mild thermal hydrosilylation reaction of 1-decene. | 100 |
| Figure 6.7 | High-resolution XP spectra of surfaces (C 1s region) in the presence of C ₂ H ₅ AlCl ₂ prepared by mild thermal hydrosilylation reaction of 1-decene..... | 101 |
| Figure 6.8 | High-resolution XP spectra of surfaces (Si 2p region) prepared by the thermal reaction of 1-decene. | 102 |
| Figure 6.9 | Spectra of the imaginary part of the pseudo dielectric function ϵ_2 measured by ellipsometry measurement on sample Si after organic passivation of <i>n-type</i> surfaces. The spectra of the same samples are shown after 24 hours and 144 hours exposure to air. | 105 |
| Figure 6.10 | The estimation of surface micro roughness growth as a function of time, before and after alkene monolayer passivation from ellipsometry measurement. The apparent roughness over time for Si (111) <i>n-type</i> is shown after 24 hours and 144 hours exposure to air. | 105 |
| Figure 6.11 | Images of water contact angles of the samples a) Native oxide; and 1-decene monolayers b) 24 hours; c) 192 hours and d) 624 hours..... | 106 |
| Figure 7.1 | The surfactant orientation at an air-water interface. | 111 |
| Figure 7.2 | Deposition of a floating monolayer onto a solid substrate. | 112 |
| Figure 7.3 | Different type of LB deposition a) <i>Y-type</i> ; b) <i>X-type</i> and <i>Z-type</i> [130]. | 112 |

| | | |
|-------------------|--|-----|
| Figure 7.4 | Schematic diagram of a Langmuir film balance with a Wilhelmy plate electro-balance and barrier function for measuring the surface pressure. | 113 |
| Figure 7.5 | Schematic cross section of the structure of a dye monolayer deposited on silicon surface - a) formation of hydrophobic group by HMDS or 1-decene; b) two layers of cadmium stearate were initially deposited followed by; c) a monolayer of DiO with stearic acid..... | 119 |
| Figure 7.6 | Schematic illustration of the stepped LB film structure on the sample: a) Hydrophobic group; b) Stearic acid; and c) DiO..... | 120 |
| Figure 8.1 | The theoretical value according to Eq. 5.22 for diffusion length determination by plotting the collection efficiency, $(1/\eta_c)$ against absorption depth $(1/\alpha)$ | 127 |
| Figure 8.2 | The experimental data for sample silicon native oxide by plotting photon flux, Φ against α^{-1} . The average diffusion length is estimated based several values of SPV - a) 38.5 mV; b) 44.7 mV; c) 52.5 mV; d) 58.6 mV and e) 83.4 mV. | 128 |
| Figure 8.3 | The barrier height measurement on silicon samples by plotting Photon Flux vs. SPV. A different SPV values for (i) Si etched with SPM solution at various days after exposed to air; (ii) Si native oxide (Measured at wavelength of 900 nm). | 130 |
| Figure 8.4 | The barrier height measurement on samples Si-decene and Si etched with SPM solution by plotting Photon Flux vs. SPV. Different SPV values are observed on 1 st and 3 rd days for both samples (Measured at wavelength of 900 nm)..... | 131 |
| Figure 8.5 | The barrier height measurement on samples Si-dec-LB and Si etched with SPM solution by plotting Photon Flux vs. SPV. Different SPV values are observed on 1 st and 3 rd days for both samples (Measured at wavelength of 900 nm)..... | 132 |

| | | |
|--------------------|---|-----|
| Figure 8.6 | The barrier height measurement on samples Si-hex-LB and Si etched with SPM solution by plotting Photon Flux vs. SPV. Different SPV values are observed on 1 st and 3 rd days for both samples (Measured at wavelength of 900 nm)..... | 133 |
| Figure 8.7 | The graph of photon flux, Φ vs. V_{spv} for sample S8 Si etched SPM at different days. Points are experimental data and line is obtained from calculation..... | 135 |
| Figure 8.8 | The graph of photon flux, Φ vs. V_{spv} for several of passivated samples on Si and typical of etched SPM at day 1. Points are experimental data and line is obtained from calculation..... | 136 |
| Figure 8.9 | Estimation of SRV at the front surface for samples (i) Si etched with SPM solution at day 1, 3 and 14; (ii) Si native oxide at 900 nm ($U_p = 1000$ cm/s)..... | 138 |
| Figure 8.10 | A measurement comparison of SRV - summary of inverse SRV data of graph of 1000/S (KP) vs. 1000/S (Sinton)..... | 144 |
| Figure 9.1 | Absorption spectrum of several dyes including mixed of DiO:SA, SA, DiO and 1-decene in hexane using Avantes and UV-Vis Spectrometer..... | 153 |
| Figure 9.2 | SPV measurements on silicon <i>n-type</i> Si native oxide at 900 nm wavelength..... | 155 |
| Figure 9.3 | SPV measurements on 1-decene monolayers of silicon surface (after 48 and 504 hours exposed in air) at wavelength 900 nm..... | 156 |
| Figure 9.4 | Two lifetimes fitted to the experimental data for generation charge trapping and lifetime charge detrapping for sample Si-decene (48 hours) at wavelength 900 nm..... | 158 |
| Figure 9.5 | Two lifetimes fitted to the experimental data for generation charge trapping and lifetime charge detrapping for sample Si-decene (504 hours) at wavelength 900 nm..... | 159 |

| | | |
|--------------------|---|-----|
| Figure 9.6 | Changes of work function upon illumination of sample Si-dec-2L 1.5 DiO:SA for wavelength 450, 500 and 600 nm. Sign of ‘ <i>on</i> ’ and ‘ <i>off</i> ’ light indicated mechanism of charge trapping and detrapping, respectively..... | 160 |
| Figure 9.7 | Two lifetime fitted to the experimental data for generation charge trapping and lifetime charge detrapping for sample Si-dec-2L 1.5 DiO:SA at wavelength 450 nm. | 162 |
| Figure 9.8 | Two lifetime fitted to the experimental data for generation charge trapping and lifetime charge detrapping for sample Si-dec-2L 1.5 DiO:SA at wavelength 500 nm. | 162 |
| Figure 9.9 | Changes of work function upon illumination of sample Si-hex-2L 1.5 DiO:SA for wavelength 450, 500 and 600 nm. Sign of ‘ <i>on</i> ’ and ‘ <i>off</i> ’ light indicated mechanism of charge trapping and detrapping, respectively..... | 163 |
| Figure 9.10 | Two lifetimes fitted to the experimental data for generation charge trapping and lifetime charge detrapping for sample Si-hex-2L 1.5 DiO:SA at wavelength 450 nm. | 164 |
| Figure 9.11 | Two lifetimes fitted to the experimental data for generation charge trapping and lifetime charge detrapping for sample Si-hex-2L 1.5 DiO:SA at wavelength 500 nm. | 165 |
| Figure 9.12 | Changes of work function upon illumination of sample Si-hex-8L 1.5 DiO:SA for wavelength 450, 500 and 600 nm. Sign of ‘ <i>on</i> ’ and ‘ <i>off</i> ’ light indicated mechanism of charge trapping and detrapping, respectively..... | 166 |
| Figure 9.13 | Changes of work function upon illumination of sample Si-hex-2L SA for wavelength 450, 500 and 600 nm. Sign of ‘ <i>on</i> ’ and ‘ <i>off</i> ’ light indicated mechanism of charge trapping and detrapping, respectively..... | 167 |

| | | |
|--------------------|--|-----|
| Figure A1.1 | Schematic of characterization setup of KP measurement and light source angle for light intensity distribution test. | 183 |
| Figure A1.2 | Distribution of light intensity through calculated photon flux on a) y direction; and b) z direction. | 184 |
| Figure A1.3 | The gap ratio of intensity of light, $G(\lambda)$ is measured at different slit width from 1 mm to 10 mm. | 186 |
| Figure A1.4 | Sub-menu of 'Setup Probe and Data Acquisition' for KP Measurements. | 187 |
| Figure A1.5 | Sub-menu of 'Work Function Measurement' for KP Measurements. | 188 |
| Figure A1.6 | Interface of BenWin+ software of Bentham Spectrometer and KP software of KP Measurements. | 190 |

List of Accompanying Materials

| | |
|--------------------------|---|
| $CHCl_3$ | Chloroform |
| $C_{10}H_{20}$ | 1-decene |
| $C_{53}H_{85}ClN_2O_6$ | 3,3'-dioctadecyloxacarbocyanine perchlorate |
| C_6H_{14} | Hexane |
| $(CH_3)_3SiNHSi(CH_3)_3$ | Hexamethyldisilazane |
| HCl | Hydrochloric Acid |
| HF | Hydrogen Fluoride |
| H_2O | Water |
| H_2O_2 | Hydrogen Peroxide |
| H_2SO_4 | Sulphuric Acid |
| N_2 | Nitrogen |
| NH_4F | Ammonium Fluoride |
| NH_4OH | Ammonium Hydroxide |
| CH_3COCF_3 | 1,1,1-trifluoroacetone |
| $C_2H_5AlCl_2$ | Ethylaluminiumdichloride |
| $C_{18}H_{36}O_2$ | Stearic acid |
| $Si-Fz$ | Silicon <i>n-type</i> wafer (Float zone) |
| SiO_2 | Silicon Dioxide |

DECLARATION OF AUTHORSHIP

I, **Mohd Adib Ibrahim** declare that the thesis entitled **Application of Light Harvesting Materials to Silicon Photovoltaics** and the work presented in the thesis are both my own, and have been generated by me as the result of my own original research.

I confirm that:

- this work was done wholly or mainly while in candidature for a research degree at this University;
- where any part of this thesis has previously been submitted for a degree or any other qualification at this University or any other institution, this has been clearly stated;
- where I have consulted the published work of others, this is always clearly attributed;
- where I have quoted from the work of others, the source is always given. With the exception of such quotations, this thesis is entirely my own work;
- I have acknowledged all main sources of help;
- where the thesis is based on work done by myself jointly with others, I have made clear exactly what was done by others and what I have contributed myself;
- parts of this work have been published as listed in Appendix 2.

Signed: _____

Date: 18 January 2014

Acknowledgements

Foremost, *Alhamdulillah* and *Syukur* with the help of Allah the ultimate creator, for giving me a good health and opportunity to continue my life and managed to complete this thesis.

Most of all, I wish to thank my supervisor Professor Tom Markvart for being a most inspirational, compassionate and also his endless support throughout my PhD years. There simply are no words enough to express how deeply grateful I am to for his valuable guidance, active cooperation and assistance in my doctoral pursuit.

Secondly, I wish to express my special gratitude to Dr Lefteris Danos for his endless guidance, technical support and arrangements of the equipment usage in the Solar Energy Laboratory. Certainly, without him, it would be a hard time to make all the experiment stages a great success.

Immerse gratitude also goes to a number of experts that contributed their advice and supports during the present study. They are Dr Dmitry Bavykin, who provided endless advices in the study of photosynthesis and photovoltaic energy conversion and Dr Robert Greef, who provided endless technical supports and advices with the Ellipsometry equipment.

Special thanks are also offered to my PhD colleagues – Dr Nicholas Alderman, Dr Nazila Soleimani, Liping Fang and Thomas Parel for their insight and recommendations that contributed towards the completion of this study. I also wish to extend my thanks to Timothy Barendt (Summer Student from University of Oxford) for helping me in KP measurement and Photon Flux calibration for this study.

I convey my special acknowledgements to the National University of Malaysia (UKM), Ministry of Higher Education of Malaysia and Malaysia government for giving opportunity and financial support throughout of my PhD study.

I am deeply indebted to both my parents in law, Haji Zainal Ariffin Ahmad and Hajjah Saodah Abd Ghani for their unlimited sacrifices, doa and continuous supports throughout my studies.

To my beloved wife, Dr Zailin Zainal Ariffin for her continuous love, support, understanding and encouragement. Finally to my children, Muhammad Ariff and Nur Alya for their patience and love.

List of Symbols

| Symbol | | Unit |
|-----------|---|------|
| E | Energy | eV |
| E_c | Energy at conduction band | eV |
| E_F | Fermi level | eV |
| E_{Fn} | Quasi-Fermi level for electrons | eV |
| E_{Fp} | Quasi-Fermi level for holes | eV |
| E_g | Energy gap | eV |
| E_i | Intrinsic Fermi level | eV |
| E_{vac} | Vacuum energy level | eV |
| E_v | Energy at valence band | eV |
| E_t | Trap energy level | eV |
| E_{vs} | Energy at the top of the valence band of the surface | eV |
| E_{cs} | Energy at the top of the conduction band of the surface | eV |
| I_E | Ionization energy | eV |
| ξ | Electrostatic potential | V/cm |
| ξ_n | Electrostatic potential in the n-type semiconductor | V/cm |
| ξ_p | Electrostatic potential in the p-type semiconductor | V/cm |
| ξ_m | Maximum electrostatic potential | V/cm |
| f | Fermi-Dirac distribution function | - |
| V | Voltage | volt |
| V_b | Backing potential | volt |
| V_{bi} | Built-in potential | volt |
| V_f | Forward Bias | volt |
| V_j | Potential voltage dropped across the junction | volt |
| V_r | Reverse Bias | volt |
| V_{oc} | Open-circuit voltage | volt |
| V_n | Potential voltage in the n-type semiconductor | volt |
| V_p | Potential voltage in the p-type semiconductor | volt |

| Symbol | | Unit |
|--------------|--|-------------------|
| V_i | Semiconductor potential | volt |
| V_{so} | Equilibrium surface band bending | volt |
| φ_s | Surface potential | volt |
| V_{spv} | Surface photovoltage | mV |
| V_{cpd} | Contact potential difference | mV |
| ΔV_s | Changes in the surface band bending | mV |
| I | Current | A |
| I_D | Diode current | A |
| I_L | Photo-generated current | A |
| I_o | Saturation current | A |
| I_{sc} | Short circuit current | A |
| J | Current density | A/cm ² |
| J_L | Photo-generated current density | A/cm ² |
| J_n | Electron current density | A/cm ² |
| J_p | Hole current density | A/cm ² |
| J_o | Saturation current density | A/cm ² |
| J_{os} | Effective saturation current density | A/cm ² |
| J_s | Surface recombination current density | A/cm ² |
| k_B | Boltzmann constant | J/K |
| T | Absolute temperature | K |
| FF | Fill factor | - |
| h | Planck constant | J.s |
| c | Speed of light | ms ⁻¹ |
| q | Electron charge = 1.602×10^{19} C, absolute value | C |
| n | Concentration of free electron | cm ⁻³ |
| n_o | Concentration of electron in equilibrium | cm ⁻³ |
| n_i | Intrinsic carrier concentration | cm ⁻³ |
| n_n | Electron concentration in n-type semiconductor | cm ⁻³ |
| n_p | Electron concentration in p-type semiconductor | cm ⁻³ |
| n_s | Electrons concentration in the surface | cm ⁻³ |
| Δn | Excess carriers of electron | cm ⁻³ |

| Symbol | | Unit |
|--------------|--|-------------------------------|
| Δn_s | Excess carriers of electron at the surface | cm^{-3} |
| n_{st} | Electron occupation in the surface | cm^{-3} |
| n_{ts} | Filled surface states density | cm^{-3} |
| N | Surface charge atom density | cm^{-2} |
| N_{ss} | Surface state density | cm^{-2} |
| N_t | Defect states density in bulk | cm^{-3} |
| N_{ts} | Defect states density in the surface | cm^{-3} |
| N_A | Acceptor impurity concentration | cm^{-3} |
| N_C | Effective density of states in conduction band | cm^{-3} |
| p | Concentration of free hole | cm^{-3} |
| p_o | Concentration of hole in equilibrium | cm^{-3} |
| Δp | Excess carriers of holes | cm^{-3} |
| p_p | Hole concentration in p-type semiconductor | cm^{-3} |
| p_n | Hole concentration in n-type semiconductor | cm^{-3} |
| p_s | Holes concentration in the surface | cm^{-3} |
| p_{st} | Holes occupation in the surface | cm^{-3} |
| p_{ts} | Empty surface states density | cm^{-3} |
| N_D | Donor impurity concentration | cm^{-3} |
| N_V | Effective density of states in valence band | cm^{-3} |
| P | Power | Watt |
| P_{inc} | Incidence light power | Watt |
| λ | Wavelength | nm |
| Q | Charge density | C/cm^2 |
| Q_f | Fixed charge density | C/cm^2 |
| Q_{it} | Interface charge density | C/cm^2 |
| Q_{ss} | Net charge density in the surface states | C/cm^2 |
| Q_{sc} | Net charge density in the surface | C/cm^2 |
| G | Generation rate | $\text{cm}^{-3}\text{s}^{-1}$ |
| R | Recombination rate | $\text{cm}^{-3}\text{s}^{-1}$ |
| r_N | Net electron recombination rate | $\text{cm}^{-3}\text{s}^{-1}$ |

| Symbol | | Unit |
|--------------|--|-------------------------------|
| r_p | Net hole recombination rate | $\text{cm}^{-3}\text{s}^{-1}$ |
| S_s | Surface recombination velocity surface state | cm/s |
| S_p | Surface recombination velocity of hole | cm/s |
| S_{n0} | Surface recombination velocity parameter of electron | cm/s |
| S_{p0} | Surface recombination velocity parameter of hole | cm/s |
| S_{eff} | Effective surface recombination velocity | cm/s |
| S_{fs} | Surface recombination velocity at the front surface | cm/s |
| S_{rs} | Surface recombination velocity at the rear surface | cm/s |
| U_{eff} | Net recombination/generation rate | $\text{cm}^{-3}\text{s}^{-1}$ |
| U_s | Net recombination rate at the surface | $\text{cm}^{-3}\text{s}^{-1}$ |
| t | time | s |
| τ | Carrier lifetime | s |
| τ_{eff} | Effective carrier lifetime | s |
| τ_b | Bulk carrier lifetime | s |
| τ_s | Surface carrier lifetime | s |
| τ_n | Carrier lifetime for electron | s |
| τ_p | Carrier lifetime for hole | s |
| τ_{no} | Carrier lifetime for electron in equilibrium | s |
| τ_{po} | Carrier lifetime for hole in equilibrium | s |
| τ_{Aug} | Auger recombination lifetime | s |
| τ_{SRH} | Shockley-Hall-Read lifetime | s |
| τ_{esc} | Lifetime of electron release | s |
| τ_{cp} | Lifetime of hole capture | s |
| v | Carrier velocity | cm/s |
| v_n | Electron velocity | cm/s |
| v_p | Hole velocity | cm/s |
| v_{th} | Mean thermal carrier velocity | cm/s |
| m_{th}^* | Thermal velocity effective mass | cm/s |
| m_0 | Electron rest mass | - |
| L_n | Diffusion length of electrons | cm |
| L_p | Diffusion length of holes | cm |

| Symbol | | Unit |
|--------------|---|-------------------------------|
| D_n | Diffusion coefficient for electrons | cm^2/s |
| D_p | Diffusion coefficient for holes | cm^2/s |
| H | Thickness of the wafer | cm |
| W | Work function | mV |
| W_b | Work function of Schottky barrier heights | mV |
| W_s | Work function of semiconductor | mV |
| W_m | Work function of metal | mV |
| α | Optical absorption coefficient | cm^{-1} |
| D_n | Diffusion coefficient for electrons | cm^2/s |
| D_p | Diffusion coefficient for holes | cm^2/s |
| W_D | Depletion width | cm |
| W_{Dn} | Depletion width in the n-type semiconductor | cm |
| W_{Dp} | Depletion width in the p-type semiconductor | cm |
| x | Distance | cm |
| x_n | Distance of x in the n-type semiconductor | cm |
| x_p | Distance of x in the p-type semiconductor | cm |
| ρ | Resistivity | $\Omega \cdot \text{cm}$ |
| σ | Capture cross-section | cm^2 |
| σ_n | Capture cross-section of electrons | cm^2 |
| σ_p | Capture cross-section of holes | cm^2 |
| ϵ | Permittivity | F/cm |
| ϵ_o | Permittivity of vacuum | F/cm |
| ϵ_s | Permittivity of semiconductor | - |
| η_L | Collection efficiency | - |
| Φ | Photon Flux | $\text{cm}^{-2}\text{s}^{-1}$ |
| χ | Electron affinity | Volt |
| χ^* | Effective Electron affinity | Volt |
| μ | Drift mobility | cm^2/Vs |
| μ_n | Drift mobility of electron | cm^2/Vs |
| μ_p | Drift mobility of hole | cm^2/Vs |
| Θ | Angle | ° |

| Symbol | | Unit |
|-------------|---|--------------------------------|
| C | Auger recombination coefficient | cm^6/s |
| C_n | Auger recombination coefficient in n-type material | cm^6/s |
| C_p | Auger recombination coefficient in p-type material | cm^6/s |
| B_p | Material coefficient in p-type material | $\text{cm}^{-3}\text{s}^{-1}$ |
| B_n | Material coefficient in n-type material | $\text{cm}^{-3}\text{s}^{-1}$ |
| D_{it} | Density of interface states | $\text{cm}^{-2}\text{eV}^{-1}$ |
| K_s | Constant coefficient | - |
| g_t | Degeneracy factor of the surface state | - |
| r_n^{th} | Rate of conduction band electron captured in the surface state | $\text{cm}^{-3}\text{s}^{-1}$ |
| g_n^{th} | Rate of electron emission from the surface state into the conduction band | $\text{cm}^{-3}\text{s}^{-1}$ |
| r_p^{th} | Rate of hole captured from the surface state into the valence band | $\text{cm}^{-3}\text{s}^{-1}$ |
| g_n^{opt} | Rate of excite electrons from the surface state to the conduction band | $\text{cm}^{-3}\text{s}^{-1}$ |
| g_p^{opt} | Rate of hole transition from the surface state to the valence band | $\text{cm}^{-3}\text{s}^{-1}$ |
| $\rho(x)$ | Charge density in the space charge region | - |
| A | Area | cm^2 |
| d_{air} | Distance between the grounded sample and metal probe | nm |
| d_{chain} | Projection length of layer to the normal surface | nm |
| d_m | Thickness of micro roughness | nm |
| wt.% | Weight percentage | - |
| y_i | The composition | - |

Abbreviations

| | |
|------------------|---|
| <i>Al</i> | Aluminium |
| <i>AM</i> | Air mass |
| <i>ATP</i> | Adenosine Triphosphate |
| <i>ARC</i> | Anti-reflection Coating |
| <i>B</i> | Boron |
| <i>CPD</i> | Contact Potential Difference |
| <i>DI</i> | Deionised |
| <i>DiO</i> | 3,3'-dioctadecyloxacarbocyanine perchlorate |
| <i>Dec</i> | Decene |
| <i>DNA</i> | Deoxyribonucleic Acid |
| <i>FET</i> | Field-effect Transistor |
| <i>FTIR</i> | Fourier Transform Infrared Spectroscopy |
| <i>Fz</i> | Float zone silicon |
| <i>GaAs</i> | Gallium Arsenide |
| <i>Ge</i> | Germanium |
| <i>Hex, HMDS</i> | Hexamethyldisilazane |
| <i>HF</i> | Hydrogen Fluoride |
| <i>InP</i> | Indium Phosphide |
| <i>KP</i> | Kelvin Probe |
| <i>LB</i> | Langmuir Blodgett |
| <i>LEDs</i> | Light-emitting Diodes |
| <i>LH</i> | Light Harvesting |
| <i>MIS</i> | Metal-Insulator-Semiconductor |

| | |
|--------------|--|
| <i>MOS</i> | Metal-Oxide-Semiconductor |
| <i>p-n</i> | Junction formed by <i>p</i> - and <i>n</i> -type semiconductor |
| <i>PV</i> | Photovoltaic |
| <i>QSSPC</i> | Quasi-Steady-State Photo conductance |
| <i>RC</i> | Reaction Centre |
| <i>RCA</i> | Radio Corporation of America |
| <i>SA</i> | Stearic acid |
| <i>SAM</i> | Self-assembled molecule |
| <i>Sb</i> | Antimony |
| <i>SCR</i> | Space Charge Region / Depletion Region |
| <i>SHR</i> | Shockley-Hall-Read Statistics |
| <i>Si</i> | Silicon |
| <i>Si-C</i> | Silicon-Carbon |
| <i>Si-H</i> | Silicon-Hydrogen |
| <i>SPM</i> | Sulphuric acid-hydrogen peroxide mixture |
| <i>SPV</i> | Surface Photovoltage |
| <i>SR</i> | Spectral Response |
| <i>SRV</i> | Surface Recombination Velocity |
| <i>TOC</i> | Total Organic Content |
| <i>UV</i> | Ultra Violet |
| <i>UHV</i> | Ultrahigh Vacuum |
| <i>XPS</i> | X-ray Photoelectron Spectroscopy |
| <i>P</i> | Bacteriochlorophyll Dimer |
| <i>P*</i> | Excited Bacteriochlorophyll Dimer |
| <i>B</i> | Bacteriochlorophyll Molecule |
| <i>F</i> | Bacteriopheophytin Molecule |
| <i>Q</i> | Quinone |

Chapter 1 Research Review

1.1 Introduction

Solar energy has an important function in achieving sustainable and environmentally friendly resources to fulfil the energy requirements of humanity. Solar energy has been assimilated by biological organisms over millions of years; in particular, humans use it for numerous ends, including health, industry, religious belief and culture, architecture and construction purposes. The utilization of non-renewable fuel as a primary source of energy is necessary because fossil fuels have many adverse consequences and are not sustainable. Combustion products produce pollution, acid rain, and global warming. As an alternative solution to environmental pollution and future energy crises, much research is currently devoted to the development of photovoltaic (PV) solar cells that can work better because of the ever-present sun.

1.2 Motivation

PV technology is the most promising energy source in terms of clean and safe utilization of solar energy. In general, a PV system consists of solar cells and ancillary parts. Solar cells utilize energy from the sun by transforming solar radiation into electricity, with conversion efficiencies of commercial devices ranging between 15% and 20%. However, the high cost of solar cell materials and the low efficiency of PV cells are challenging, which limit the expansion of this technology. The breakdown of the cost of a solar cell is as follows: silicon wafer (65%), module assembly (25%), and cell fabrication (10%). The cost of the silicon wafer is divided into purification of silicon (35%), crystallization (35%), and sawing (30%).

A key disadvantage of silicon as a photovoltaic material is its low optical absorption by virtue of its indirect band gap. This means that long optical path is required, and thicker semiconductor wafers are needed to absorb the sunlight. This in turn implies that the photo-generated carriers must travel over

longer path lengths to produce the electricity. Thus, more material volume and a higher quality material are needed which leads to high material cost. Therefore, research is needed to discover ways of improving photo-excitation of silicon, leading to lower material usage and lower cost.

1.3 Approaches to the Solution

PV energy conversion has many similarities to photosynthetic systems. In a solar cell, the incident light energy creates electron-hole pairs in semiconductors, where the minority carriers are transported to the junction. The charges are then separated at the junction to produce electrical current and voltage. By contrast, photo-excited molecules in a photosynthetic system use the excitation energy transport from the light harvesting (LH) antenna to the RC. The electrons are then transferred between the molecular species across the membrane to generate a proton gradient. This gradient is necessary for adenosine triphosphate (ATP) synthesis in bacteria and for producing redox species that yield oxygen and sugar in higher plants.

The LH process is another interesting aspect of photosynthetic conversion mechanism due to its higher collection efficiency and because it transports energy rather than charge. This thesis explores the idea of specially designed dye molecules that are used to absorb light efficiently and couple the light absorption process for charge separation at the junction. The resulting novel PV structure converts photons into electricity in two natural stages: a molecular collector absorbs light with a high-optical absorption cross-section and then transfers energy to a semiconductor converter that separates the photo-generated charges at the junction to produce electricity. This novel PV structure can lead to efficient light absorption and energy conversion within a compact device, with low material requirements and low costs [3]. A novel PV structure has the potential to decrease the cost of PV manufacturing (Figure 1.1).

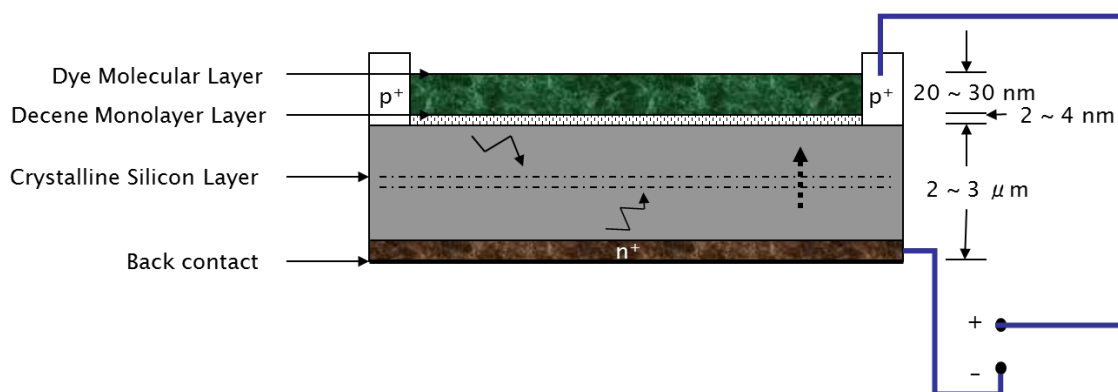


Figure 1.1 Schematic diagram of the novel photovoltaic structure. Light absorbs by the dye molecular layer and transfer the energy by non radiative resonance transfer process. The energy transfer occurs by a dipole-dipole resonance interaction between the energy donor and acceptor [4]. The energy is then collected by electrons from the base and by holes from the emitter (thick arrow). Charge separation takes place at the junction (dashed arrow) [3].

1.4 Aim and Objectives

The overall aim of this study is to develop a technique for charge injection into silicon by LH energy absorbed in organic dyes attached to the surface to overcome the poor optical absorption of silicon. This study also aims to develop novel surface passivation techniques and characterize the passivated layers by employing the Kelvin Probe (KP) method to assist in the efficient utilization of the proposed process. The research objectives are further presented in detail as follows:

1. To develop a method to attach organic dyes to silicon, enabling energy transfer between the chromosphere and silicon, as well as surface passivation.

2. To develop a mathematical model to estimate the surface recombination velocity for surface passivation and to investigate charge generation in the semiconductor based on the KP method.
3. To develop a simplified energy model of photosynthesis that parallels the operation of a solar cell.

1.5 Main Contributions

The main contribution of this study is on the attachment of LH materials (Figure 1.2).

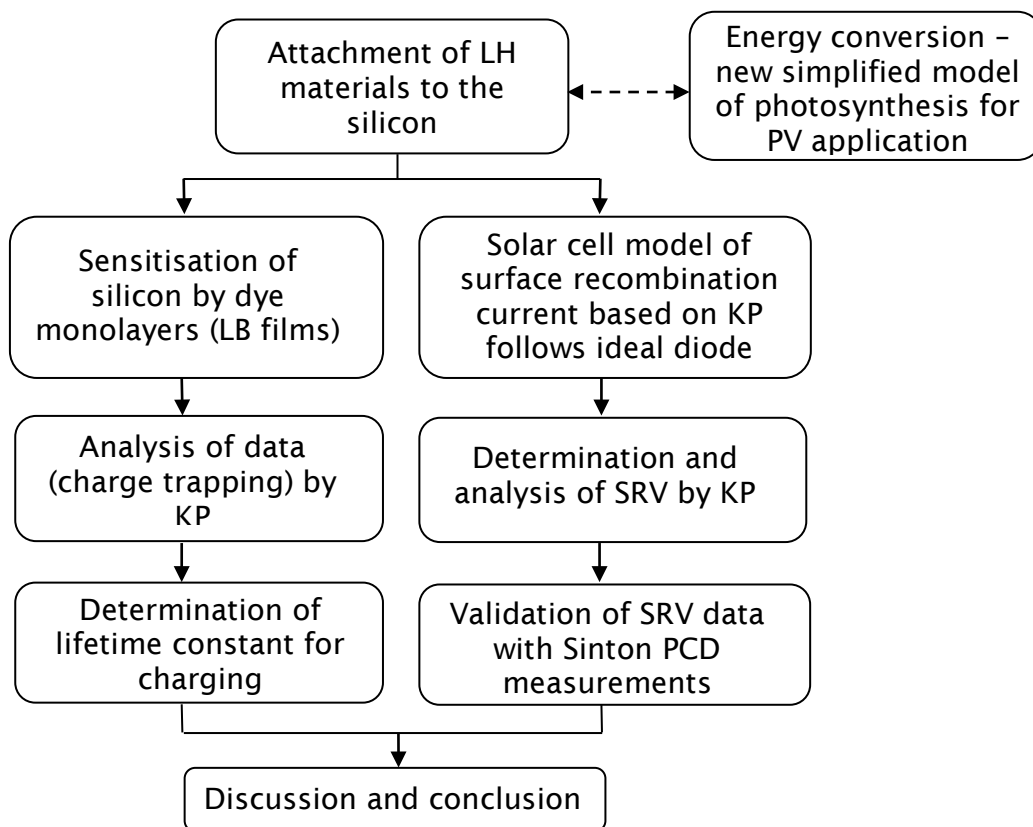


Figure 1.2 A summary of main contribution and research framework

An experiment was performed on the sensitization of silicon by dye monolayers. The formation of dye monolayers via a LB film on the silicon was analysed in relation to the charge-trapping mechanism through the KP method. A theoretical study carried out in this thesis shows that the surface recombination current, as measured by the KP method, follows the ideal diode equations. The surface recombination velocity (SRV) value was determined through a linear slope of the graph measured by KP. The SRV data were then validated with Sinton Photo-conductance Decay (PCD) measurements that show linkages between two different measurements. Aside from the main contributions, supporting analysis of a simplified model of photosynthetic energy conversion for PV application was also performed in this study.

1.6 Outline of the Thesis

This thesis is organized into 10 chapters with the following outline:

Chapter 1 provides the introduction, background, and motivation for this study.

Chapter 2 describes the physical fundamentals of silicon solar cells, including *p-n* junction equations, as well as their characteristics. A short review of recombination in solar cells is also provided.

Chapter 3 examines the characteristics of semiconductor surfaces and surface state properties. The role of surface charge, effect of charge on the surface, and band bending near the surface are also discussed.

Chapter 4 develops a simplified model of photosynthetic energy conversion and identifies the various components of chemical energy (or *chemical potential*) that can be described by the Shockley solar cell equation. This study focuses on the energy conversion process originating in the LH antenna and finally reaching the RC of photosynthesis. This process has similarities to PV energy.

Chapter 5 discusses KP as a tool for measuring the work function by means of SPV under illumination. KP is applied to determine the surface barrier height and diffusion length of the sample. A mathematical model is developed for SPV that follows an ideal diode.

Chapter 6 reviews the chemical routes that modify silicon surfaces, including hydrogen termination and organic monolayer passivation. An experimental procedure is described for the treatment of silicon surface and passivation by reacting with hydrogen and alkene groups. The obtained surfaces are characterized by X-ray photoelectron spectroscopy (XPS) and Fourier transform infrared spectroscopy (FTIR). Surface stability is characterized by ellipsometry and water contact angles.

Chapter 7 describes the experimental procedure used to deposit a dye monolayer via LB technique on the silicon substrate to form LH structures.

Chapter 8 examines the characterization of silicon surface passivation using the SPV measurements developed in Chapter 5 through the KP method. This characterization identifies the surface properties involving diffusion length, barrier height, and surface current. It then estimates the surface recombination velocity of the samples prepared by techniques described in Chapters 6 and 7.

Chapter 9 studies the trapping in silicon of charges photo-generated in the molecular structure on the surface of LB films. SPV, charge trapping, and decay upon illumination are monitored through KP. A preliminary experiment identifies several charge-trapping processes on the samples with different organic passivation layers, including Si-decene-LB and Si-hexane-LB. The results are compared with those in control samples containing native oxide.

The final chapter presents the conclusions drawn from this study and provides some recommendations for future research. KP characterization is described in detail in APPENDIX 1. A list of journal and conference papers is attached in APPENDIX 2.

Chapter 2 Photovoltaic Solar Cell Operation

2.1 Introduction

This chapter describes the operation of a solar cell and the general principles of photovoltaics. It also explains the electrical characteristics and the performance of silicon solar cells, and introduces a discussion on the p - n junction. This study shows how depletion region approximation can be applied on semiconductor surfaces. Depletion approximation is used as a basis for the formation of a new theoretical framework related to KP operation in Chapter 5 onward. A short review of recombination in solar cells that consists of all the mechanisms of the recombination processes is also given.

2.2 Optical Absorption in Silicon and Charge Carrier Generation

Semiconductor materials absorb incoming photons and promote electron movement toward the conduction band to generate an electron-hole pair. This process is called photogeneration. The important parameter in this process is the band gap energy E_g of the semiconductor. In an ideal case, no photons are absorbed for energy $h\nu < E_g$. In terms of wavelength, the photon energy is given by

$$E = h\nu = \frac{hc}{\lambda} \quad \text{Eq. 2.1}$$

where h is Planck constant, c is the speed of light, ν is the frequency, and λ is the wavelength of light.

Photons with energy $h\nu > E_g$ contribute the energy E_g to the photo-generated electron-hole pair after equilibrium; the excess energy (larger than the E_g) is lost in the process known as thermalisation [5, 6]. This excess energy is lost as heat and cannot be converted into useful power, which represents one of the fundamental loss mechanisms in a solar cell.

Absorption attenuates the light intensity inside the semiconductor. With depth x , the photon flux $\Phi(x)$ is given by [7]

$$\Phi(x) = \Phi(0)e^{-\alpha x} \quad \text{Eq. 2.2}$$

where $\Phi(0)$ is the number of photons on the surface $x = 0$ and α is the absorption coefficient. The absorption depth α^{-1} is the inverse of the absorption coefficient α . The light absorption properties of silicon can be characterized by a wavelength-dependent absorption coefficient (Figure 2.1).

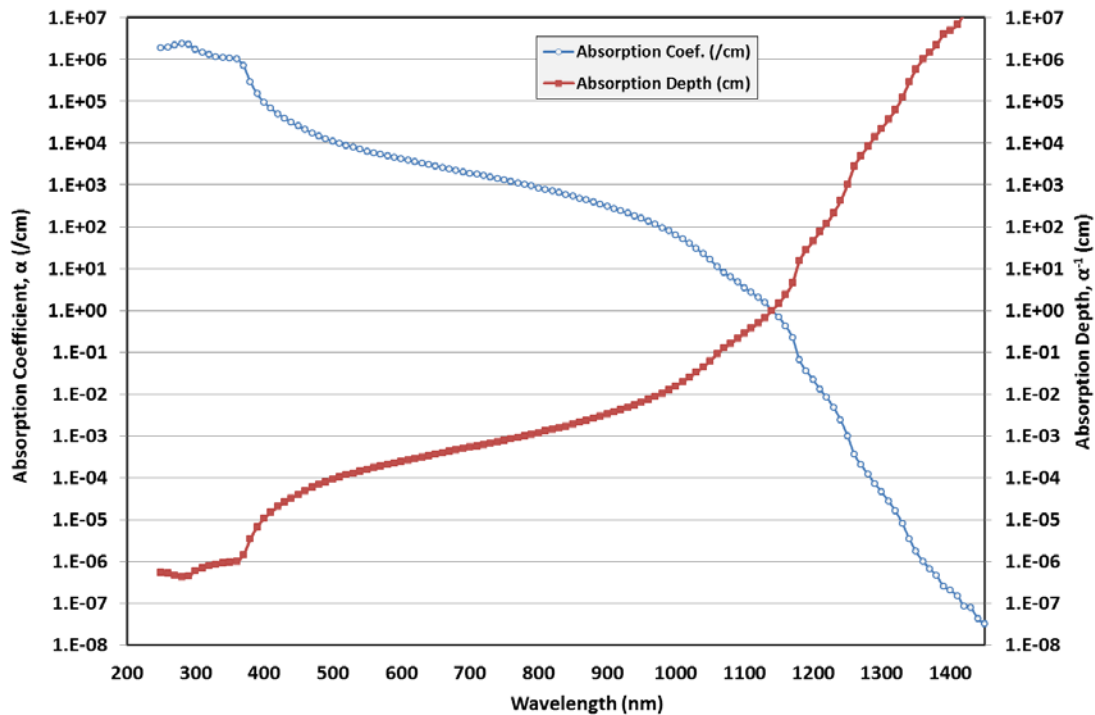


Figure 2.1 The optical absorption of silicon – absorption coefficient and the absorption depth [8].

Considering that the absorption coefficient depends on the wavelength, different wavelengths of light are absorbed at different depths in the semiconductor. At short wavelengths, high-frequency light (high-energy photons) has a large absorption coefficient and is strongly absorbed near the surface. The energy photons are sufficiently energetic to excite electrons

directly from the valence band to the conduction band. Long-wavelength light with a large absorption coefficient is absorbed much deeper in the silicon.

2.3 Fundamentals of p - n Junctions

The p - n junction is an effective interface between p -type and n -type layers of the same material. The most common material used in solar cells is crystalline silicon with indirect energy gap E_g of 1.12 eV [1]. Generally, the most essential part of solar cells is the p - n junction area, where photo-generated electron-hole pairs are separated by the internal electric field. In this section, the fundamentals of p - n junction in thermal equilibrium, in the dark, and in applied bias are explained further.

2.3.1 Semiconductor Statistics

Thermal excitation of electrons moving from the valence band to the conduction band occurs at a finite temperature, leaving an equal number of holes in the valence band. An intrinsic semiconductor is also known as an undoped semiconductor, which contains a number of excited electrons that is equal to the number of holes at any temperature above absolute zero. This process is balanced by the recombination of the electrons in the conduction band and holes in the valence band. At thermal equilibrium, the Boltzmann relation of n -type and p -type materials with equal Fermi levels is given by the following:

$$n = n_i \exp\left(\frac{E_F - E_i}{k_B T}\right) \quad \text{Eq. 2.3}$$

$$p = n_i \exp\left(\frac{E_i - E_F}{k_B T}\right) \quad \text{Eq. 2.4}$$

where n and p represent the electron and hole concentrations; n_i is the intrinsic carrier concentration; and E_i and E_F are the energy levels corresponding to the

intrinsic level and the Fermi level [1], respectively. The value of intrinsic carrier concentration n_i depends on the semiconductor material and the temperature (for silicon at 300 K, n_i is equal to $1.4 \times 10^{10} \text{ cm}^{-3}$) [9].

At thermal equilibrium, the pn product is equal to n_i^2 . A single Fermi level can thus be employed when no excess carriers or no net recombination exists. The Fermi level must be constant across the junction once equilibrium is established.

The pn product is no longer equal to n_i^2 when away from thermal equilibrium, where the densities of the minority carrier on both sides of the junction are changed. Thus, this study defines the quasi-Fermi levels for electrons and holes as follows:

$$n \equiv n_i \exp\left[\frac{E_{Fn} - E_i}{k_B T}\right] \quad \text{Eq. 2.5}$$

$$p \equiv n_i \exp\left[\frac{E_i - E_{Fp}}{k_B T}\right] \quad \text{Eq. 2.6}$$

where E_{Fn} and E_{Fp} are the quasi-Fermi levels for electrons and holes, respectively. From **Eq. 2.5** and **2.6**, the equation can be obtained as follows:

$$E_{Fn} \equiv E_i + k_B T \ln\left(\frac{n}{n_i}\right) \quad \text{Eq. 2.7}$$

$$E_{Fp} \equiv E_i - k_B T \ln\left(\frac{p}{n_i}\right) \quad \text{Eq. 2.8}$$

The pn product becomes

$$pn = n_i^2 \exp\left[\frac{E_{Fn} - E_{Fp}}{k_B T}\right] \quad \text{Eq. 2.9}$$

2.3.2 In Thermal Equilibrium

The combination of the two semiconductor layers creates a built-in potential and aligns the Fermi levels. Once the junction is formed, the electron flows from the n -side to the p -side, and the holes in the p -side move to the n -side to create a double-charged layer until it reaches equilibrium. A depletion region around this interface is depleted of free carriers; the depletion region is associated with the electric field acting as an electrical barrier to a further majority carrier diffusion [1, 10, 11]. The space charge and the potential curve of the p - n junction can be explained further in the form of a mathematical equation based on *depletion approximation*.

i. Depletion Approximation, Electric Field and Potential

The electric field and potential distributions across the depletion region are shown in Figure 2.2. The p -type material is on the left of the p - n junction, whereas the n -type material is on the right. The charge distribution shows the fixed dopant charge because of dopant ions; the negative charge is on the left of the junction and the positive charge is on the right. In practice, the charge gradually drops off into the neutral region over a very short distance because the total charge must be zero in thermal equilibrium.

$$N_A x_p = N_D x_n \quad \text{Eq. 2.10}$$

Based on Poisson equation,

$$-\frac{d^2 V_i}{dx^2} = \frac{\rho(x)}{\epsilon_s} = \frac{qN_A}{\epsilon_s} \quad -x_p \leq x \leq 0 \quad \text{Eq. 2.11}$$

$$\frac{d^2 V_i}{dx^2} = -\frac{\rho(x)}{\epsilon_s} = -\frac{qN_D}{\epsilon_s} \quad 0 \leq x \leq x_n \quad \text{Eq. 2.12}$$

The electric field strength, ζ is the function of electrostatic potential given by the integration in the above equation. Thus,

$$\xi(x) = -\frac{dV_i}{dx} = -\frac{qN_A x}{\epsilon_s} + C_1 \quad \text{Eq. 2.13}$$

where C_1 is the integration constant. When $x = -x_p$, and $C_1 = -qN_A x_p / \epsilon_s$, the constant of integration can be determined where $\xi(x) = 0$. Substituting this constant into **Eq. 2.13** results in the following:

$$\xi_p(x) = -\frac{qN_A(x+x_p)}{\epsilon_s} \quad -x_p \leq x \leq 0 \quad \text{Eq. 2.14}$$

Following the same procedure for *n-type* of the junction,

$$\xi_n(x) = \frac{qN_D(x-x_n)}{\epsilon_s} \quad 0 \leq x \leq x_n \quad \text{Eq. 2.15}$$

Integrating the electric field strength ξ leads to the potential as a function of distance. Thus,

$$V_p(x) = \frac{qN_A x^2}{2\epsilon_s} + \frac{qN_A(x x_p)}{\epsilon_s} + C_3 \quad \text{Eq. 2.16}$$

Following the same procedure for *n-type* of the junction,

$$\xi_n(x) = \frac{qN_D(x-x_n)}{\epsilon_s} \quad 0 \leq x \leq x_n \quad \text{Eq. 2.17}$$

Integrating the electric field strength ξ leads to the potential as a function of distance. Thus,

$$V_p(x) = \frac{qN_A x^2}{2\epsilon_s} + \frac{qN_A(x x_p)}{\epsilon_s} + C_3 \quad \text{Eq. 2.18}$$

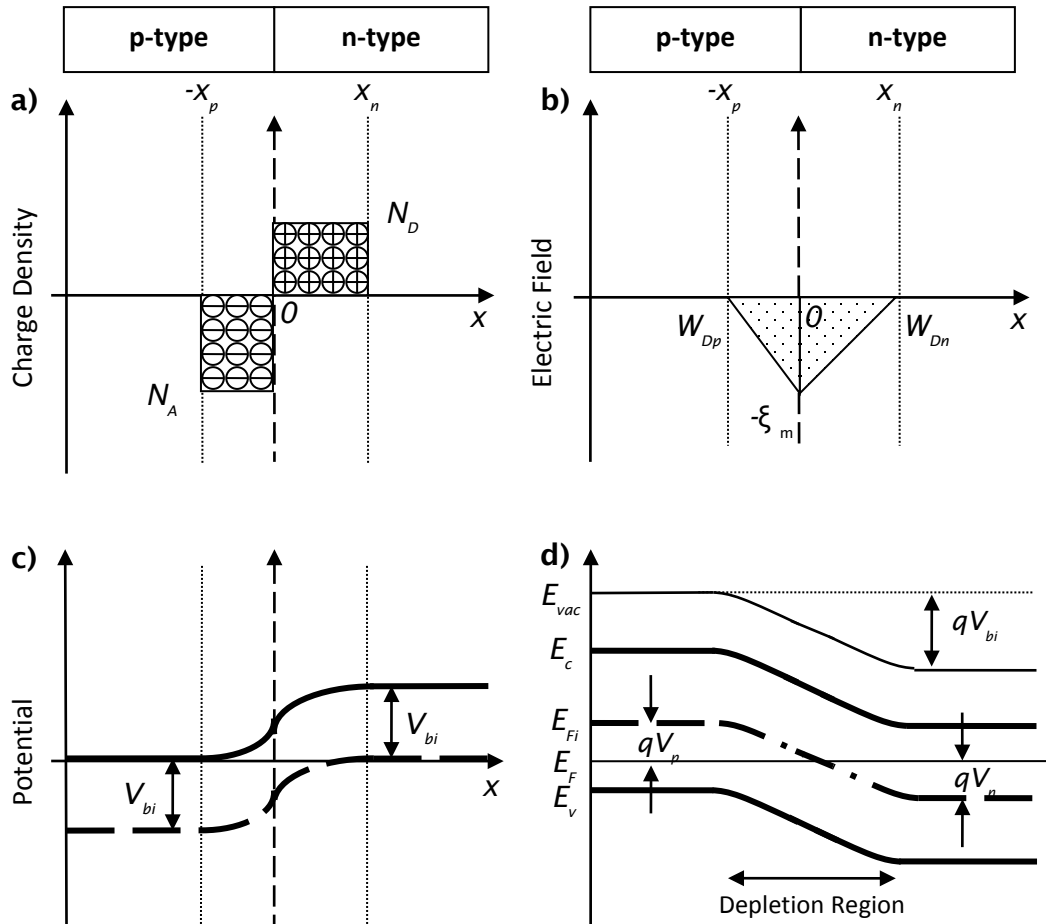


Figure 2.2 Diagram of uniformly doped *p-n* junction; a) charge density; b) electric field; c) potential [1] and d) band diagram of *p-n* junction in thermal equilibrium where the electric field, qV_{bi} is the difference of V_p and V_n [2].

A similar approach is applied for the *n-type* that results in the following:

$$V_n(x) = -\frac{qN_D x^2}{2\epsilon_s} + \frac{qN_D (xx_n)}{\epsilon_s} + C_4 \tag{Eq. 2.19}$$

At the boundary condition, $x = 0$. The integrations of Eqs. 2.18 and 2.19 become easier because of the constant $C_3 = C_4 = 0$. Thus,

$$V_p(x) = \frac{qN_A x^2}{2\epsilon_s} + \frac{qN_A(x x_p)}{\epsilon_s} \quad \text{Eq. 2.20}$$

$$V_n(x) = -\frac{qN_D x^2}{2\epsilon_s} + \frac{qN_D(x x_n)}{\epsilon_s} \quad \text{Eq. 2.21}$$

Given the value of the potential at $x = -x_p$, the Eq. 2.20 becomes the following:

$$V_p(-x_p) = -\frac{qN_A x_p^2}{2\epsilon_s} \quad \text{Eq. 2.22}$$

The potential at $x = x_n$ is as follows:

$$V_n(x_n) = \frac{qN_D x_n^2}{2\epsilon_s} \quad \text{Eq. 2.23}$$

The change in the potential across the junction is the built-in voltage, V_{bi} where the area under the triangle in the electric field distribution is also equal to V_{bi} . The total potential difference across the junction represents the built-in voltage. Thus,

$$V_{bi} = V_n(x_n) - V_p(-x_p) \quad \text{Eq. 2.24}$$

$$V_{bi} = \frac{q}{2\epsilon_s} (N_A x_p^2 + N_D x_n^2) \quad \text{Eq. 2.25}$$

The total charge for both sides must be equal (Eq. 2.10) to calculate the total depletion layer width W . Thus,

$$V_{bi} = \frac{q}{2\epsilon_s} N_A^2 x_p^2 \left(\frac{N_A + N_D}{N_A N_D} \right) = \frac{q}{2\epsilon_s} N_D^2 x_n^2 \left(\frac{N_A + N_D}{N_A N_D} \right) \quad \text{Eq. 2.26}$$

From Eq. 2.26, the depletion layer width for both sides of the junction is as follows:

$$W_{Dp} = x_p = \frac{1}{N_A} \sqrt{\frac{2\epsilon_s V_{bi}}{q} \frac{N_D N_A}{(N_A + N_D)}} \quad \text{Eq. 2.27}$$

$$W_{Dn} = x_n = \frac{1}{N_D} \sqrt{\frac{2\epsilon_s V_{bi}}{q} \frac{N_D N_A}{(N_A + N_D)}} \quad \text{Eq. 2.28}$$

$$W_D = W_{Dp} + W_{Dn} = \sqrt{\frac{2\epsilon_s V_{bi}}{q} \left(\frac{N_A + N_D}{N_A N_D} \right)} \quad \text{Eq. 2.29}$$

2.3.3 Under Applied Bias

The current density J is zero at equilibrium (i.e., in the dark and without applied bias). No minority carrier diffusion current exists in the neutral region and no net recombination is observed in the illustration of the band diagram (Figure 2.3).

The built-in voltage in equilibrium V_{bi} is determined by the difference in work functions of the n - and p -type materials V_n and V_p , respectively. The difference in work functions is equal to the difference in the shift of the Fermi levels from the intrinsic potential energy of the semiconductor because E_i is parallel to E_{vac} . Thus,

$$V_{bi} = \frac{1}{q} (V_n - V_p) \quad \text{Eq. 2.30}$$

The shift $E_i - E_F$ can be expressed in terms of the doping levels using Eqs. 2.3 and 2.4 for n - and p -type materials, respectively. Therefore, V_{bi} is defined as follows:

$$V_{bi} = \frac{k_B T}{q} \ln \left(\frac{pn}{n_i^2} \right) \quad \text{Eq. 2.31}$$

At low currents (Eq. 2.9), E_{Fn} and E_{Fp} remain relatively constant inside the depletion region, and the depletion width is much shorter than the diffusion length [2]. With this argument, the voltage in depletion region becomes

$$qV = E_{Fn} - E_{Fp} \quad \text{Eq. 2.32}$$

The qV equation can be re-arranged from Eq. 2.9 as follows:

$$qV = k_B T \ln\left(\frac{pn}{n_i^2}\right) \quad \text{Eq. 2.33}$$

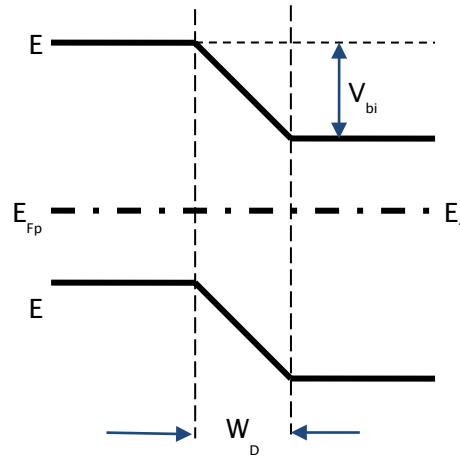


Figure 2.3 Band diagram of p - n junction in the dark [11].

If a voltage V is applied to the junction in the dark, the built-in potential barrier is decreased, and more majority carriers are able to diffuse across the junction. Therefore, a net current of electrons is observed from n - to p - and holes from p - to n -. The quasi-Fermi level in the depletion region split by the applied bias, remains flat across the depletion region, and only undergoes sharp changes at the interfaces. The quasi-Fermi levels return from the depletion region because

of a recombination of carriers. A net recombination which is included in the current occurs in that region.

In a $p-n$ junction under forward bias conditions, the applied electric field V_f decreases the internal built-in field V_{bi} . The potential barrier then becomes

$$V_{total} = V_{bi} - V_f \quad \text{Eq. 2.34}$$

Besides the decrease in potential difference across the junction, the width of the depletion layer is also decreased, followed by a decrease in the energy barrier heights for electrons and holes. Under these forward bias conditions, the current mainly flows from transport of electrons and holes across the junctions.

Under a reverse bias, the applied voltage V_r at the junction is increased. Thus, the diffusion current of the electrons and holes is lowered. The potential barrier height is as follows:

$$V_{total} = V_{bi} + V_r \quad \text{Eq. 2.35}$$

From **Eq. 2.9**, the pn product is no longer equal to ni^2 when the external bias is applied. Considering that the densities of the minority carrier on both sides of the junction are changed, the quasi-Fermi levels E_{Fn} and E_{Fp} are also modified. The quasi-Fermi levels describe non-equilibrium situations where the separation between the two quasi-Fermi levels gives rise to a recombination away from thermal equilibrium. This separation is related to the applied voltage.

2.3.4 Surface Space Charge Region

The interruption of symmetry by the presence of a surface introduces a charge in the surface states. This condition is compensated by a surface space charge region (SCR) and generally results in band bending to preserve the overall

charge neutrality. Only if no region of space charge exists will bands remain flat. The condition of charge neutrality is as follows [12]:

$$Q_{ss} + Q_{sc} = 0 \quad \text{Eq. 2.36}$$

where Q_{ss} and Q_{sc} are the net charge in surface states and the space charge per unit area in the SCR, respectively. Both Q_{ss} and Q_{sc} may change significantly upon illumination, where the absorbed photons induce the formation of free carriers; this scenario results from the creation of electron-hole pairs via band-to-band transitions or the release of captured carriers via trap-to-band transitions [13]. Applying a similar argument to this one-sided junction we obtain

$$Q_{ss} = -Q_{sc} = qN_D W_D \quad \text{Eq. 2.37}$$

where W is the space charge region width and N_D is the donor density.

2.3.5 Relation of the Depletion Layer and Space Charge Density

For better understand the band bending effect, there is an equation involved to relate the depletion region and space charge density. **Eq. 2.29** shows that the depletion layer's width depends on the doping density. Considering the *n-side* of a one-sided abrupt junction where the majority of the potential variation and depletion region are on the lightly doped side (i.e., for $N_A \gg N_D$), the equation is reduced to the following:

$$W_D = x_n = \sqrt{\frac{2\epsilon_s V_{bi}}{qN_D}} \quad \text{Eq. 2.38}$$

The potential across the depletion region is as follows:

$$V(x) = \frac{V_{bi}x}{W_D} \left(2 - \frac{x}{W_D} \right) \quad \text{Eq. 2.39}$$

A more accurate analysis [1] shows that the width of the depletion layer at thermal equilibrium for a one-sided abrupt junction should be decreased by “tails” because of thermal voltage. Thus, it transforms to the following:

$$W_D = \sqrt{\frac{2\epsilon_s}{qN_D} \left(V_{bi} - \frac{2kT}{q} \right)} \quad \text{Eq. 2.40}$$

Based on **Eq. 2.37**, the above equation can be multiplied with qN_D to measure the built-in voltage in the depletion region of the semiconductor. Thus,

$$Q_{sc} = qN_D \cdot W_D = \sqrt{\frac{2\epsilon_s}{qN_D} \left(V_{bi} - \frac{2kT}{q} \right)} \cdot qN_D \quad \text{Eq. 2.41}$$

When a voltage V is applied to the junction, the total electrostatic potential variation across the junction is given by $(V_{bi} - V)$. Thus,

$$Q_{sc} = \sqrt{2q\epsilon_s N_D \left(V_{bi} - V - \frac{kT}{q} \right)} \quad \text{Eq. 2.42}$$

This equation is valid only if no inversion layer exists in the semiconductor [14].

2.4 Operation of Solar Cell

Solar cell operation is based on the formation of a junction and depends on the PV effect to convert sunlight directly into electricity. In the conversion process, the incident energy of light creates mobile charged particles in the solar cell that are then separated from the structure of the device to produce electric current. A solar cell converts light into electricity by exploiting the PV effect

that exists at the semiconductor junctions. In general, the solar cell performs two processes: absorption of light and separation of electric charges. These charges (i.e., electrons and positively charged “holes”) are formed when light absorption excites electrons to higher energy levels in the semiconductor. The higher-energy electron then moves from the solar cell into the external circuit. The electron disperses its energy in the external circuit and returns to the solar cell.

2.4.1 Solar Cell Structures

Figure 2.4 shows a conventional planar of a solar cell structure where two neutral regions, emitter (*n-type*) and base (*p-type*), are separated by a *p-n* junction. The most common crystalline silicon solar cell consists of an absorber material of moderately doped *p-type* Si with an acceptor concentration of 10^{16} cm^{-3} and thickness of approximately $300 \mu\text{m}$. A thin layer of absorber with thickness of $< 1 \mu\text{m}$ is a highly doped *n-type* placed on the top layer of the cell. Metal contacts are used to extract the electrical current from the front and rear of the solar cell. The front contact structure that must allow light to pass through is in the form of widely spaced, thin metal strips (usually called *fingers*) that supply current to a larger bus bar. The anti-reflection coating cell is a thin layer of dielectric material that covers the solar cell to minimize light reflection from the top surface [10].

Solar cells are essentially semiconductor junctions under illumination. Light generates electron-hole pairs on both sides of the junction, namely, in the *n-type* emitter and in the *p-type* base. The generated minority carriers are electrons (from the base) and holes (from the emitter) that diffuse to the junction and are swept away by the electric field. Thus, they produce an electric current across the device. The *p-n* junction separates the carriers with an opposite charge and transforms the generated current between the bands into an electric current across the *p-n* junction.

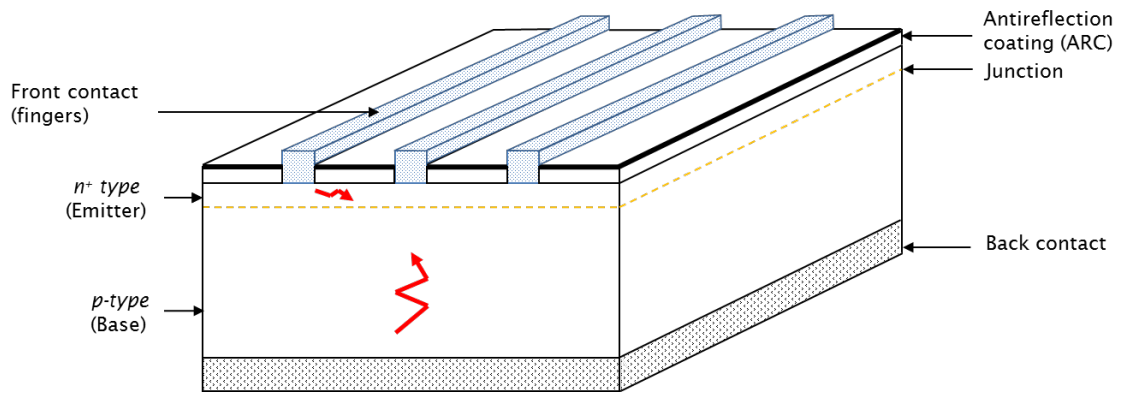


Figure 2.4 A typical structure of a conventional silicon solar cell. The minority carriers (electrons) move from the base and holes from the emitter (thick arrow) across the junction. Charge separation takes place at the junction by the electric field (dashed line).

2.4.2 Current-Voltage Junction under Illumination

If the junction is illuminated by photon $h\nu \geq E_g$, additional electron-hole pairs are generated in the semiconductors. The concentration of minority carriers at both sides of the semiconductor increases rapidly and causes a flow of the minority carriers across the depletion region. The electron flows from the *n*-side to the *p*-side, and the holes in the *p*-side that move to the *n*-side cause the photo-generated current density J_L .

Under an open circuit condition, the junction generates voltage V_{oc} by decreasing the built-in potential barrier across the junction to become $V_{bi} - V_{oc}$. The width of the depletion region also decreases and changes the concentration of electrons and holes under non-equilibrium conditions, as described by the quasi-Fermi levels. The quasi-Fermi level E_{Fn} is much higher in the *n*-type region than in the *p*-type region by the amount of qV_{oc} [15]. In a short circuit condition, both *n*-type and *p*-type regions are short circuited under illumination, where J_L flows through the external circuit. Given that the voltage is zero, the built-in potential barrier is unchanged. When the current flows inside the semiconductor, large differences of the quasi-Fermi levels are observed inside the depletion region.

2.4.3 The Electrical Performance of Solar Cell

PV energy conversion in solar cells is based on the principle of a p - n junction. In solar cell applications, the I - V characteristic can be obtained by drawing an equivalent circuit of the device (Figure 2.5). The output current I of the solar cell is equal to the difference between the light-generated current I_L and diode current I_D . When no illumination occurs, the current is allowed to pass under a forward bias because no generation of I_L occurs and is blocked under a reverse bias. The dark current of a solar cell is as follows:

$$I_{dark} = I_D \left[\exp\left(\frac{qV}{kT}\right) - 1 \right] \quad \text{Eq. 2.43}$$

This equation is known as the Shockley diode equation that neglects a current component due to recombination in the SCR. When a forward bias is applied, it injects minority carriers into the neutral regions of the diode. The minority carriers then diffuse toward the bulk, giving rise to a diode current. With illumination, the number of free carriers increases. The carriers created within one diffusion length to the junction without recombining are separated by the electric field and transported to the external circuit to form a photo-generated current I_L . This photocurrent is directly proportional to the intensity of light and depends on the incident spectrum and spectral response.

I_L is the light-generated current produced inside the solar cell in a short circuit. The external measured current is denoted as I_{sc} . The cell generates no power ($V = 0$) in a short circuit. All of the light-generated current passes through the diode (Figure 2.5). The overall current voltage at the operating point can be modelled as the sum of the dark and photocurrents, where the equation of I - V can be rearranged as follows:

$$I = I_L - I_{dark} \quad \text{Eq. 2.44}$$

$$I = I_L - I_D \left[\exp\left(\frac{qV}{kT}\right) - 1 \right] \quad \text{Eq. 2.45}$$

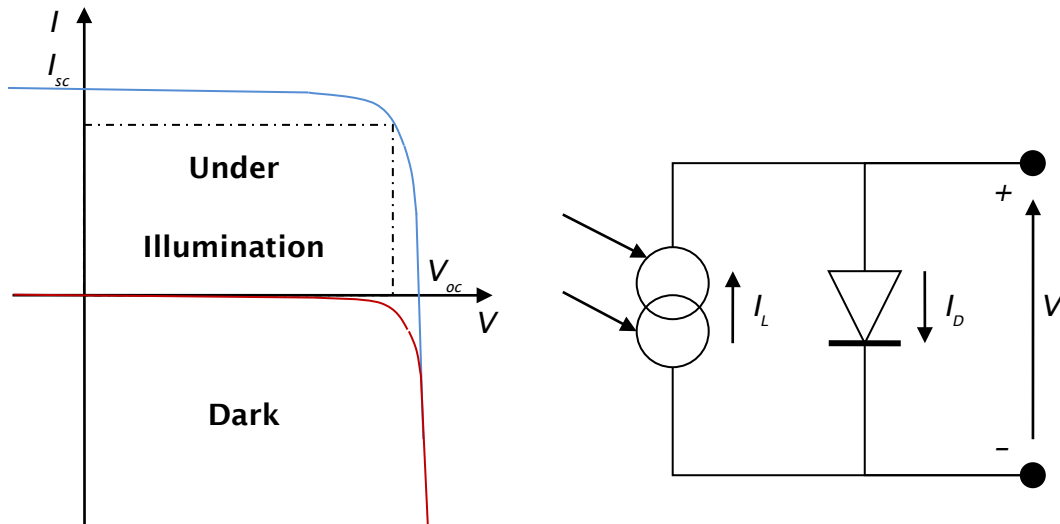


Figure 2.5 The effect of light on the I - V characteristic of a solar cell compared to a diode [16].

When a load is connected to the solar cell, the current decreases and a voltage develops as a charge builds up in the terminals. The resulting current can be viewed as a superposition of the following: a short circuit current caused by the absorption of photons and a *dark current* caused by the potential build up over the load that flows in the opposite direction. Under an open circuit (at $I = 0$), the cell generates a voltage (V_{oc}). Thus,

$$V_{oc} = \frac{kT}{q} \ln\left(\frac{I_L}{I_D} + 1\right) \quad \text{Eq. 2.46}$$

The cell delivers maximum power P_{max} when operating at an optimum point on the I - V products. This condition is shown graphically in Figures 2.6 and 2.7, where the position of the maximum power point represents the largest area of the rectangle shown.

The fill factor FF is defined as the ratio of the maximum power from the solar cell to the product of V_{oc} and I_{sc} by the following:

$$FF = \frac{I_{\max} \cdot V_{\max}}{V_{oc} \cdot I_{sc}} \quad \text{Eq. 2.47}$$

The energy conversion efficiency η of a solar cell is defined as the ratio of the maximum power delivered at the maximum power point to the incident light power. The maximum power can be calculated using the following equation:

$$P_{\max} = V_{\max} \cdot I_{\max} = FF \cdot V_{oc} \cdot I_{sc} \quad \text{Eq. 2.48}$$

$$\eta = P_{\max} / P_{inc} \quad \text{Eq. 2.49}$$

where V_{oc} , I_{sc} , FF , and P_{inc} are the open circuit voltage, short circuit current, fill factor, and incident light power, respectively.

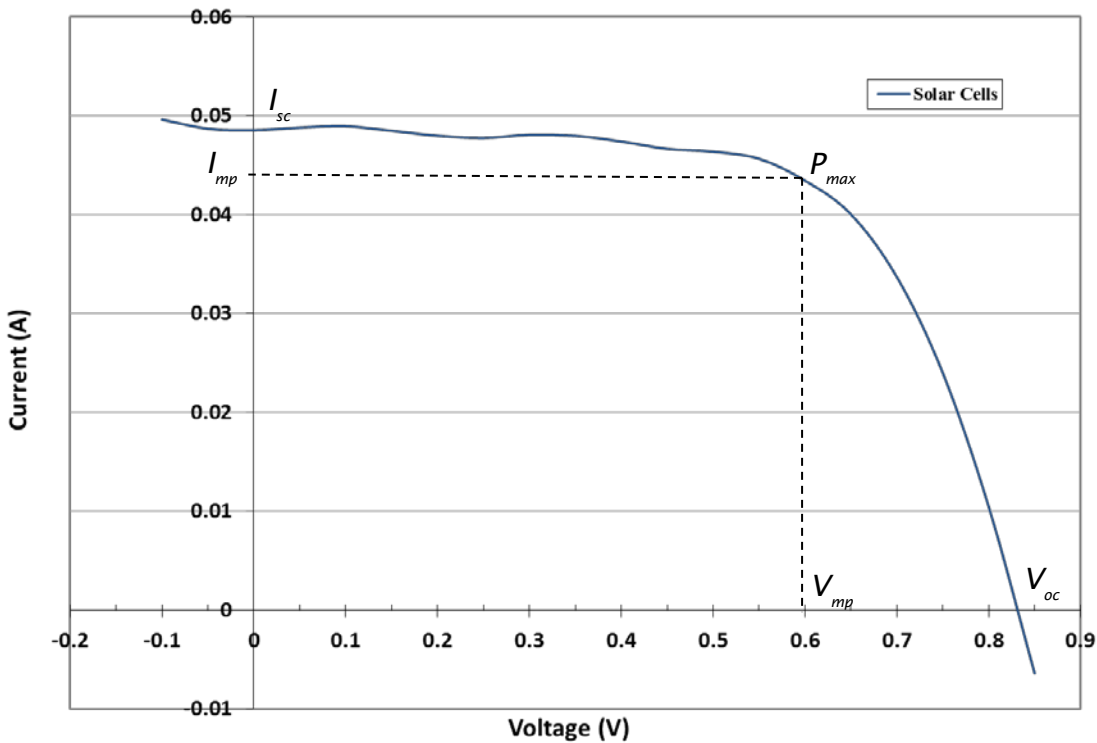


Figure 2.6 Measured I - V characteristic of a solar cell, also showing the maximum power point.

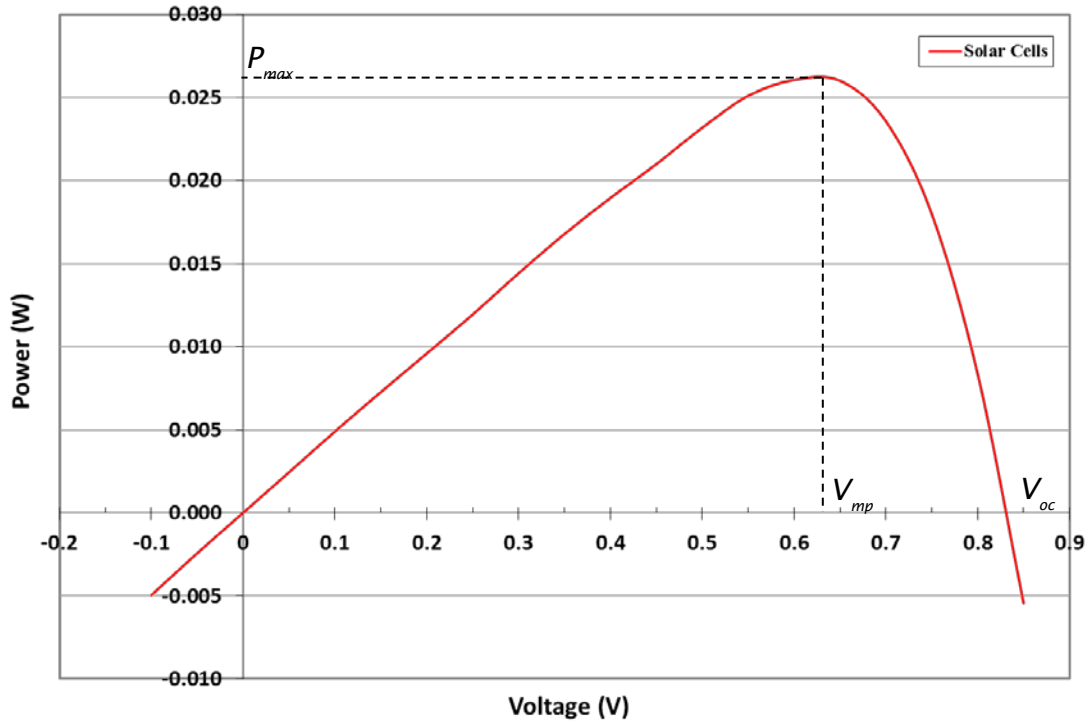


Figure 2.7 P - V characteristic of a solar cell with the maximum power point.

P_{inc} can be calculated by multiplying the incident power P_{in} and the surface area of the solar cell A_c in cm^2 . The standard conditions used in the characterization of solar cells are P_{in} of $100 \text{ mW}/\text{cm}^2$, with the illumination of air mass AM1.5 (Global) and measured at 25°C . In this study, the solar cell sample was calculated using the following electrical characteristics: FF is 0.65 ; P_{max} is 0.0261 W ; A_c is 7.49 cm^2 ; and η is 3.48% .

2.5 Carrier Recombination Processes in Solar Cell

Recombination mechanisms can be considered recovery processes when a semiconductor is disturbed from the equilibrium state after excess carriers have been introduced into a semiconductor. The parallel processes between generation and recombination are nature's order-restoring mechanisms, whereby the carrier excess or deficit inside a semiconductor is stabilized or

removed. Most recombination processes can be reversed to generate carriers. The generation processes are caused by thermal energy or light introduction via photon absorption to generate energy. The illumination of a semiconductor with photons of sufficient energy generates electron hole pairs. Three main recombination processes exist: (i) radiative recombination; (ii) band-to-band Auger recombination; and (iii) recombination via defect levels (surface or bulk).

2.5.1 Carrier Transport and Recombination

The carrier density gradient in the semiconductor causes carrier diffusion. The density gradient can be achieved by varying the doping concentration or by applying a thermal gradient in the semiconductor [17]. If no electric field exists, these carriers diffuse throughout the cell until the concentration is uniformly distributed. When an electric field is present, the movement of carriers is subjected to a force. The electrons move in the direction opposite that of the electric field, whereas the holes move in the same direction as the electric field.

Recombination is defined as a process through which electrons and holes are annihilated. Generation is the process through which electrons and holes are created. Recombination and generation affect current flow in semiconductors by manipulating the carrier concentration involved in the drift and diffusion process, and by changing the carrier concentration through time-dependent decay. The net recombination in a semiconductor is the sum of three recombination processes described below. Under *low injection*, the net recombination rate U is proportional to the excess carrier concentration Δn . The minority carrier lifetime τ can be defined as

$$\tau(\Delta n, n_o, p_o) = \frac{\Delta n}{U(\Delta n, n_o, p_o)} \quad \text{Eq. 2.50}$$

Low and *high injection* conditions indicate that the excess carrier concentration is much smaller or larger than the doping concentration, respectively. This

equation is mainly dependent on the injection density Δn and the doping concentration of the semiconductor through n_o and p_o .

2.5.2 Radiative Recombination

Radiative recombination is a process that is opposite the absorption of light. In this recombination, an electron in the conduction band “falls” and recombines with a hole in the valence band, whereby the excess energy is released in the form of a photon [18]. The emitted photon has energy similar to that of the band gap, and is usually only weakly absorbed and can exit the semiconductor. Radiative recombination may be the dominant recombination process in direct band gap semiconductors (e.g., GaAs) and in some devices (e.g., LEDs). The carrier lifetime and the rate of radiative recombination are as follows:

$$\tau_{radiative} = \frac{1}{B(n_o + p_o + \Delta n)} \quad \text{Eq. 2.51}$$

$$U_{radiative} = B(np - n_i^2) \quad \text{Eq. 2.52}$$

where B is a material constant with a value of $1.8 \times 10^{-15} \text{ cm}^3/\text{s}$ (silicon), $7.2 \times 10^{-10} \text{ cm}^3/\text{s}$ (GaAs), or $6.25 \times 10^{-10} \text{ cm}^3/\text{s}$ (InP); Δn is the excess carrier concentrations; n_o and p_o are the thermal equilibrium concentrations of electron and holes, respectively.

2.5.3 Band-to-band Auger Recombination

Band-to-band Auger recombination is a process through which one electron gives its extra energy to a second electron in the conduction band or valence band during recombination, subsequently moving it to a higher energy level. This recombination involves three carriers. The electron recombines with a hole, and then transmits its excess energy to a third charge carrier (either an electron in the conduction band or a hole in the valence band) instead of emitting a photon. This electron then returns to the conduction band edge.

Thus, the Auger lifetime τ_{Auger} is a function of the carrier concentration. The rate of Auger recombination is as follows:

$$\tau_{Auger} = \frac{1}{Cn^2} \quad \text{Eq. 2.53}$$

$$U_{Auger} = (C_p p + C_n n)(np - n_i^2) \quad \text{Eq. 2.54}$$

where C is the Auger recombination coefficient with a typical value of $1.66 \times 10^{-30} \text{ cm}^6/\text{s}$ [19]; C_p and C_n are the Auger recombination coefficients in p -type and n -type material, respectively; and n_i^2 is the intrinsic carrier concentration of the semiconductor. This equation shows that the Auger lifetime is inversely proportional to the doping concentration and decreases with increasing doping or injection level.

2.5.4 Recombination through Defect Levels

Recombination through defects is also called Shockley–Read–Hall (SRH) recombination. In SRH recombination, which was first introduced by Shockley and Read [20], and by Hall [21], the recombination rate via defects of concentration, N_t with a level at energy E_t within the band gap is described as follows:

$$U_{SRH} = \frac{np - n_i^2}{\tau_{po}(n + n_1) + \tau_{no}(p + p_1)} \quad \text{Eq. 2.55}$$

$$n_1 = n_i \exp\left(\frac{E_t - E_i}{k_B T}\right); \quad p_1 = p_i \exp\left(\frac{E_t - E_i}{k_B T}\right) \quad \text{Eq. 2.56}$$

where τ_{no} and τ_{po} are parameters proportional to the carrier lifetime for electrons and holes in equilibrium, respectively, and N_t is attributed to the particular defect state density in bulk [18]. Subscript “ t ” represents the “*trap*” that is known as “*defect*”. The capture lifetime constants of electrons τ_{no} and holes τ_{po} of bulk defects in silicon are as follows [18]:

$$\tau_{n0} = \frac{1}{\sigma_n v_{th} N_t}, \quad \tau_{p0} = \frac{1}{\sigma_p v_{th} N_t} \quad \text{Eq. 2.57}$$

where σ_n (σ_p) is the capture cross-section of electrons (holes), $v_{th} = \sqrt{8kT/\pi m_{th}^*}$ is the mean thermal carrier velocity, and m_{th}^* is the thermal velocity effective mass. At $T = 300$ K, m_{th}^* represents the value of the conduction band (valence band), namely, $m_{th}^* = 0.28m_0$ ($m_{th}^* = 0.41m_0$), where the electron rest mass m_0 is $m_0 = 0.91095 \times 10^{-30}$ [22]. Thus, the mean thermal carrier velocities for electrons and holes are 2.0×10^7 cm/s and 1.7×10^7 cm/s, respectively.

From **Eq. 2.50** and by employing $\Delta n = \Delta p$, the SRH lifetime τ_{SRH} that is dependent on the injection level can be calculated from **Eq. 2.55** as follows:

$$\tau_{SRH}(\Delta n) = \frac{\tau_{p0}(n_0 + n_1 \Delta n) + \tau_{n0}(n_0 + n_1 \Delta n)}{n_0 + p_0 + \Delta n} \quad \text{Eq. 2.58}$$

An energy state in the band gap may act as a recombination centre that captures both electrons and holes with almost equal probabilities [2]. An energy close to the conduction band edge or one whose cross-section for electron capture is much larger than that for hole capture indicates the presence of *electron traps*. Similarly, if the state is close to the valence band or has a higher cross-section for hole capture, it acts as a *hole trap*. Traps slow down the transport of carriers, but do not remove them completely. The mechanisms of electron and hole trapping are shown in Figure 2.8.

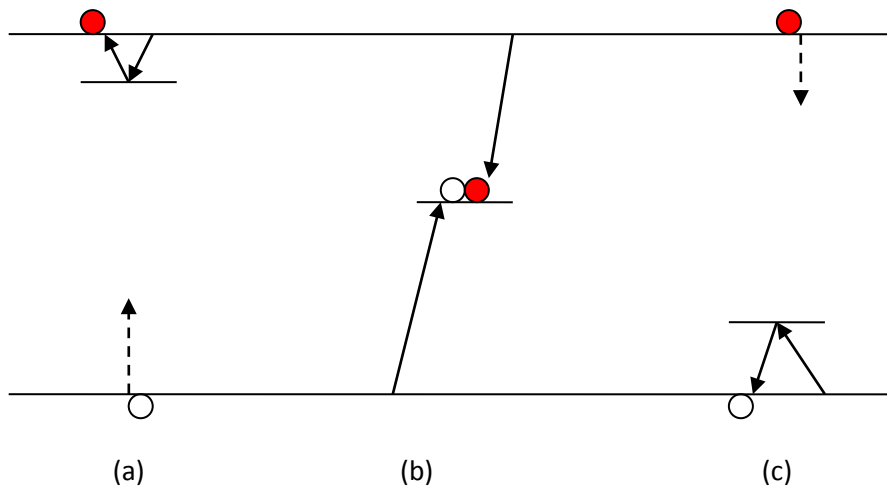


Figure 2.8 Schematic diagram of electron and hole trapping (a) Electron trapping and detrapping; (b) electron-hole recombination; and (c) hole trapping and detrapping [11]. A (---) dashed line represent energy transition of traps state.

2.5.5 Minority Carrier Lifetime

Carrier lifetime can be defined as the average time it takes for a minority carrier to recombine. Generally, the overall process is known as minority carrier recombination. Under *low injection*, the majority carrier concentration is assumed to be excitation independent. The excess carrier concentration Δn is much smaller than the doping concentration of the silicon wafer. In this case, the recombination effect can be discussed in terms of a minority carrier lifetime. From **Eq. 2.50**, the minority carrier lifetime can be written as follows:

$$\tau_n = \frac{1}{U}(n - n_o) \quad \text{Eq. 2.59}$$

This equation shows the recombination rate for *p-type* materials, where τ_n is the minority carrier (electron) lifetime that can also be written for the hole lifetime τ_p in *n-type* materials. Given that the total net recombination rate U in a

semiconductor is the sum of three different recombination processes, the lifetime can be calculated from the following:

$$\frac{1}{\tau_{bulk}} = \frac{1}{\tau_{radiative}} + \frac{1}{\tau_{Auger}} + \frac{1}{\tau_{SRH}} \quad \text{Eq. 2.60}$$

Different processes of recombination have different temperatures and doping dependencies, resulting in significant effects in the bulk lifetime. Radiative recombination is usually insignificant, and Auger recombination has a possible effect in highly doped silicon or under strong excitation. Bulk lifetime dependence is mainly affected by SRH lifetime and partially by Auger recombination. The most effective recombination centres are impurity levels or defect levels near the middle of the semiconductor band gap.

Diffusion length is the average length a carrier will diffuse before recombining; it may also be considered as the movement of the carrier between generation and recombination. For example, the diffusion length of holes as minority carriers is defined as

$$L_p = \sqrt{D_p \tau_p} \quad \text{Eq. 2.61}$$

where D_p , τ_p are the diffusion coefficient and minority carrier lifetime for holes, respectively.

The excess carriers decay exponentially with diffusion distance and time, and can be written as follows:

$$\delta p(x) = \delta p(0) \exp\left(-\frac{x}{L_p}\right) \quad \text{Eq. 2.62}$$

2.6 Chapter Summary

This chapter summarizes solar cell operation, including the formation of the p - n junction and the electrical performance of solar cells. The determination of SCR width and potential curve using *depletion approximation* is important to identify which factor contains the depletion region associated with the electric field. On the semiconductor surface, the charge in the surface state Q_{ss} affecting the overall charge neutrality is compensated by a surface charge in the SCR Q_{sc} and results in band-bending. The application of charge neutrality in different cases is significant, such as on the p - n junction and on the one-sided abrupt junction.

A review of carrier recombination consisting of all the mechanisms of the recombination processes in solar cells is also presented. A basis for the theoretical understanding of various recombination processes has been presented in this study. The bulk recombination mechanism in the silicon material includes radiative recombination, band-to-band Auger recombination, and recombination via defects. The excess energy emitted via photons can be characterized by the generation rate of electron-hole pairs exactly matching the recombination rate. Besides the recombination processes, a discussion on charge carrier trapping in the trap states is presented to identify the importance of this carrier in determining the carrier recombination lifetime.

Chapter 3 Surface Semiconductor Characteristics

3.1 Surface States

Surface states are electronic states caused by imperfect covalent bonds at the surface of a semiconductor. These states are capable of transferring charges between the species in the solution and charge carriers in the semiconductor. For silicon, the atoms of the surface layer have unsaturated bonds (the so-called dangling bonds) because of the lack of periodicity in the crystal lattice at the surface. These atoms are extremely unstable and react rapidly with oxygen and water in air. The silicon surfaces have a tendency to react with oxygen to form a thin oxide film called native oxide. Native oxide grows spontaneously on a clean silicon surface when exposed to air or a solution at ambient temperature. Native oxide can be removed chemically or terminated thermally with fluoride ion, hydrogen ion, and other species under ultraviolet (UV) conditions. However, native oxide can be re-formed depending on the initial condition of the surface and the cleanness of the air.

These surface states created by the dangling bonds act as recombination centres for electrons and holes. The dangling bonds are chemically and electrically active and tend to attract adsorbate molecules and atoms, so they can decrease or introduce states simultaneously [23]. Considering that the surfaces constantly try to minimize surface energy, surface states may be related to surface reconstruction [24] or relaxation [25]. This mechanism occurs through a change in the position and/or chemical bonding configuration of surface atoms. The decrease in surface recombination is known as surface passivation, which can be achieved by decreasing the number of dangling bonds by growing a layer on top of the semiconductor surface that links to most or all of the dangling bonds. Additional processing can be applied to improve the properties of surface state by passivation treatment or interface layer, thus preventing minority carriers from reaching the surface.

As defined by Kronik & Shapira [13], a surface is a boundary of media with different physical properties. A surface between a semiconductor and vacuum or gas is a *free surface*. The surface between a semiconductor and another solid is usually referred to as an *interface*. The termination of the periodic structure of a semiconductor at its free surface may form surface-localized electronic states within the semiconductor band gap and/or a double layer of charge (known as a *surface dipole*). The appearance of surface-localized states induces a charge transfer between the bulk and the surface to establish thermal equilibrium. The result of the charge transfer in a non-neutral region in the semiconductor bulk is usually referred to as the SCR discussed in **Section 2.3.4**. In the case of a semiconductor oxide surface, the presence of donors and/or acceptors because of unsaturated dangling bonds at the surface may result in a difference in electron and hole concentrations between the surface and the bulk. The surface dipole with an electric potential difference is associated in this process, and is called the *surface potential* of the layer. The potential difference at the surface is created by the electronic equilibrium between the surface and the bulk.

The silicon atom possesses four valence electrons and requires four bonds to saturate the valence shell. In the bulk structure of a crystal, each silicon atom requires four bordering atoms. Termination of the bulk structure on the surface causes broken bonds called unsaturated or dangling bonds. The traditional Si (111) surface would have one dangling bond on each surface atom, where each Si surface atom has a non-bonding orbital consisting of two electrons [26]. However, the dangling bonds of cleaved Si (111) are only occupied by a single electron and one unoccupied surface state per atom for the density of states in the band gap.

The number of surface states per area is principally given by the number of atoms per area on the surface. The silicon crystal atoms and dangling bonds on the surface are shown in Figure 3.1. When considered in the band diagram, the surface state density at the interface can also be considered as a per unit area per electron volt [14]. The Si native oxide thickness of 20 nm consists of a density of interface states $D_{it} > 10^{12} \text{ cm}^{-2}\text{eV}^{-1}$ [27, 28]. Surface modification or treatment on the dangling silicon bonds with hydrogen-terminated passivation

decreases the density of interface states, where $D_{it} < 1.5 \times 10^{10} \text{ cm}^{-2}\text{eV}^{-1}$ for Si (111) and $D_{it} < 5 \times 10^{10} \text{ cm}^{-2}\text{eV}^{-1}$ for Si (100) [27, 29].

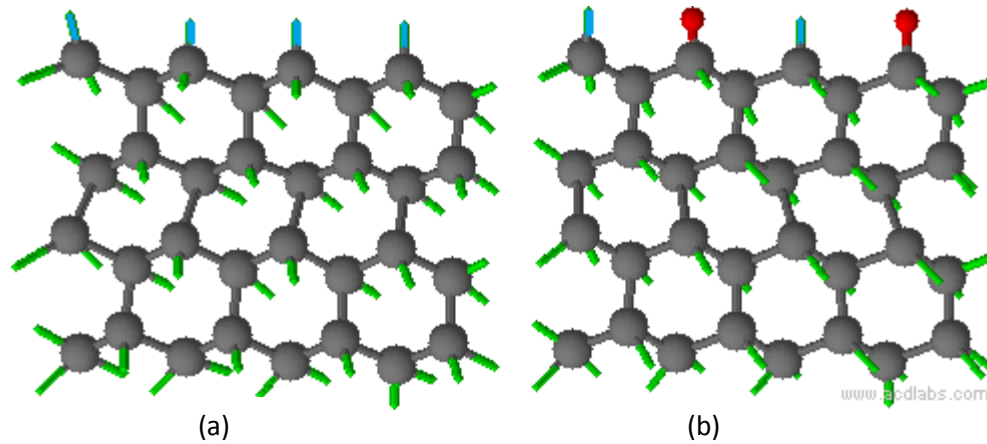


Figure 3.1 Silicon atom structures of cleaved Si (111): a) incomplete silicon atoms on the surface known as traps (blue colour); b) native oxide - oxidation occurs with oxygen bonds at Si/SiO₂ interface (red colour).

The ionization energy I_E for a semiconductor surface can be defined as the energy difference between the vacuum reference level E_{vac} and the top of the valence band at the surface E_{vs} . Thus,

$$I_E = E_{vac} - E_{vs} = E_{vac} - E_{cs} + E_g = W + E_g \quad \text{Eq. 3.1}$$

where E_{cs} is the conduction edge, W is the work function, and E_g is the energy band gap. This energy can be measured from the photoemission experiments.

The main factor in ionization energy variation is surface stoichiometry and structure. The addition of metals on the semiconductor surface (e.g., doped on the silicon) may result in dipole layers because of crystallographic anisotropy. The adsorbed species/atoms of the substrate create additional dipole layers that significantly modify the ionization energy of semiconductor surfaces. The

changes in the surface dipole and ionization energy are ascribed to the space charge layer affected by the external electric field or internal electric field.

The termination of the periodic structure of a semiconductor at its free surface may form a “tail” on the surface-localized electronic states and “spill out” into the vacuum. This condition means that the region outside the surface has a net negative charge, whereas the region inside the surface is left with a net positive charge. The separation of positive and negative charges over atomic distances is known as a microscopic dipole. This dipole creates an effective surface barrier that opposes further electron transfer (ET) from the conduction band into a vacuum. The mechanism of a dipole charge occurs when electrons reaching the surface are deflected by the negative charge outside of the material and are attracted by the positive charge inside the material. The relation between the dipole moment and the magnitude of the potential can be estimated at the surface, as shown in Figure 3.2.

The surface dipole induced by foreign atoms (adsorbates) on semiconductor surfaces act as acceptors and donors when they are near the conduction band minimum and the valence band maximum, respectively. Upon surface treatment, the defect formation and the charge transfer mechanism between the adsorbate atoms and the substrate surface can be estimated by the work function measurements.

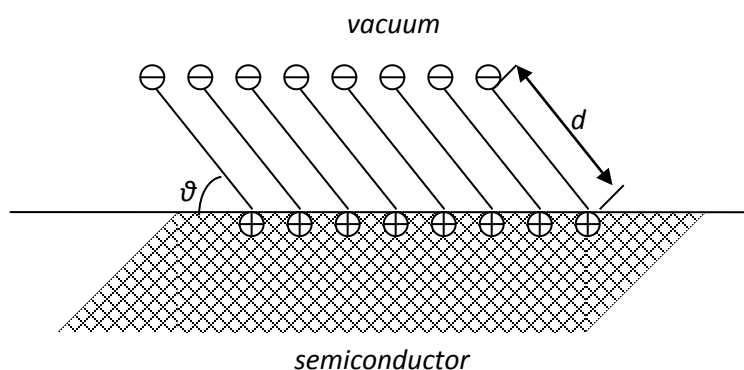


Figure 3.2 Schematic diagram of a surface dipole layer [13]. Symbol ‘ d ’ is the length of the dipole and ‘ θ ’ represent an ordered dipole layer oriented at an angle θ with respect to the surface.

The work function of semiconductors can be written in terms of ionization energy as follows:

$$W = I_E - qV_s - (E_F - E_{vs}) \quad \text{Eq. 3.2}$$

The changes in surface band bending ΔV_s are mainly ascribed to adatoms that may also change in the ionization energy. The change in adsorbate-induced work function can be written as follows:

$$\Delta W = \Delta I_E - qV_s \quad \text{Eq. 3.3}$$

Thus, when both work function and surface potential are measured as a function of SPV measurement, the adsorbate-induced variation of the ionization energy can be determined. The advantage of KP is that it can operate in the dark and monitor changes in the work function during adsorption of adatoms on the semiconductor surfaces.

The surface state has a significant effect on the optical and electronic properties of the semiconductor surface due to difference in the surface state density and energy distribution (i.e., polished and cleaned surfaces). Thus, various surface treatments can be performed through surface passivation to decrease the SRV. Given that the Si/SiO₂ interface layer on silicon becomes insulating and is considered electrically defective for electronic connection and charge transfer, monolayers based on silicon-carbon (Si-C) bonds may provide a solution for surface interface characteristics. Some surface treatment techniques performed by researchers include the following: nanowires [30]; thermally induced hydrosilylation such as alkenes [31, 32] and alkynes [33, 34]; photochemical hydrosilylation (UV) [35]; and porous silicon through Grignard reagents [36, 37].

The surfactant refers to a monolayer or a sub-monolayer of adsorbates on the surface that are usually organic and amphiphilic, such as hydrocarbon-based surfactants or LB films. Generally, their compounds contain polar groups that can either be ionic or non-ionic. For LB films, the amphiphilic molecules generally consist of a hydrophilic head and a hydrophobic tail (see details in

Section 7.2.1). The surfactant can also be defined as a substance that lowers surface tension, thereby increasing spreading and wetting properties. Considering that the surface states consist of dangling bonds, the chemical reaction of the surface treatment decreases the surface free energy and surface tension, assisting in the formation of a monolayer structure on the treated surface. The surface free energy can also be considered a macroscopic dipole (as explained in an earlier section). In terms of monolayer stability, the Si-C bond is the most promising given its characteristics of thermodynamic and kinetic stability. These findings are ascribed to the high bond strength and low bond polarity. The interface dipole formed by the adsorption of saturated hydrocarbon and inert gas atoms can be clarified through van der Waals interaction between surfactants and the surface without any movement of charge.

3.2 Surface Recombination

The non-saturated “dangling” bonds or partially bonded silicon atoms at the surface contributes a large density of recombination-active surface states within the band gap and may have a major effect on the performance of solar cells. The decrease in surface recombination by decreasing the number of dangling bonds (or passivation) can be achieved by growing a layer on top of the semiconductor surface that links to some of these dangling bonds. Additional processing can be applied to improve the properties of the surface state by passivation treatment or window layer, thus preventing minority carriers from reaching the surface.

The properties of surfaces and interfaces are subject to the electronic states that are localized near the surface or interface. The properties of electronic states include localized states, delocalized conduction, and valence band states. The semiconductor surface in three dimensions may be roughly divided into the surface region and the space charge region underneath it. The surface region may consist of the first few layers of atoms where oxide is present, and can be considered as part of the surface region. Underneath this region, an area of SCR with thickness of less than 0.1 nm to half of the width of the

crystal usually exists [38]. The parameters involved in the surface state consist of electron occupation n_{st} , hole occupation p_{st} , and the surface state energy E_t . The surface state density N_{ts} can be defined as a sum of n_{st} and p_{st} , and is related to standard Fermi Dirac statistics as follows [13]:

$$\frac{n_{st}}{N_{ts}} = \frac{1}{1 + g_t \exp[(E_t - E_F)/kT]} \quad \text{Eq. 3.4}$$

where g_t is the degeneracy factor of the surface state.

The charge transfer rates to and from the bulk bands can be determined by SRH statistics [12, 18]. This method has been discussed in **Section 2.5.4** for bulk defects, but will be presented in more detail and applied to surface states in this section.

The dynamic properties of surface states can be explained through the four possible electron and hole transitions at the surface state energy E_t , as illustrated in Figure 3.3 [13, 18]. Figure 3.3(a) shows the arrows that indicates the electron transitions for (1) electron capture by an empty defect level; (2) electron emission by a filled defect level; (3) hole capture by a filled defect level; and (4) hole emission by an empty defect level. Given the thermal excitation, the following conditions may be observed: (i) conduction band electrons may be captured in the surface state at the rate of r_n^{th} ; (ii) electron emission from the surface state into the conduction band at the rate of g_n^{th} ; (iii) a hole may be captured from the surface state into the valence band at the rate of g_p^{th} ; and (iv) hole emission by surface state at the rate of r_p^{th} . If the semiconductor is illuminated, absorbed photons may excite electrons from the surface state to the conduction band at the rate of g_n^{opt} . Similar analogous expressions may be written for surface state-valence bands for hole transitions at the rate of g_p^{opt} (Figure 3.3b). All rates are in per unit volume. SRV is an important parameter that affects the dark saturation current and the quantum efficiency of solar cells [39].

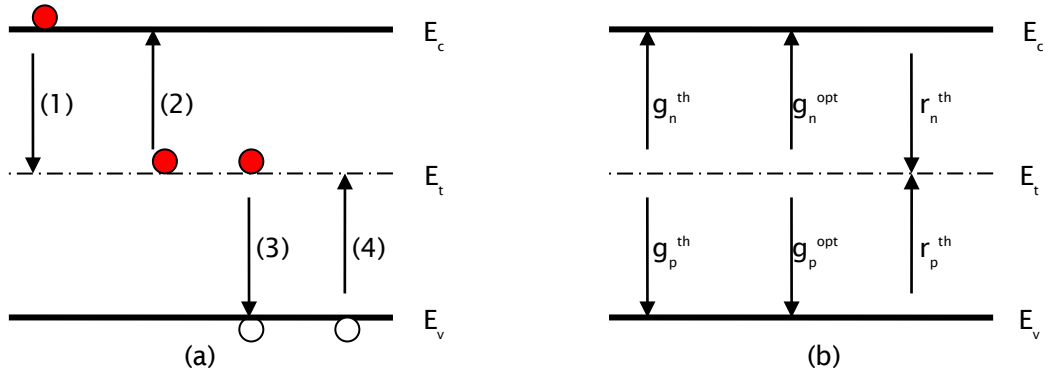


Figure 3.3 The four fundamental transitions of a surface state energy level, E_t (a) transitions of electron and holes in a semiconductor (the arrows indicate the electron transition) [18]; and (b) mixed electron / hole transition rate of surface state–band transitions [13].

An SRV, S , at the semiconductor surface can be defined as follows:

$$U_s \equiv S \Delta n_s \tag{Eq. 3.5}$$

where Δn_s is the excess minority carrier concentration on the surface [18].

Surface recombination can be determined from the extended SRH recombination, as shown in **Eq. 2.55**. The surface recombination rate U_s (rate per unit area) via a single-level surface state located at energy E_t can be determined by the following:

$$U_s = \frac{n_s p_s - n_i^2}{\frac{n_s + n_1}{S_{p0}} + \frac{p_s + p_1}{S_{n0}}} \tag{Eq. 3.6}$$

$$S_{n0} \equiv \sigma_n v_{th} N_{st} \quad \text{Eq. 3.7}$$

$$S_{p0} \equiv \sigma_p v_{th} N_{st} \quad \text{Eq. 3.8}$$

where S_{n0} and S_{p0} are the SRV parameters of electrons and holes; n_s and p_s are the electron and hole concentrations at the surface, respectively; σ_n and σ_p are the capture cross-sections for electrons and holes, respectively; v_{th} is the thermal velocity of the charge carriers (approximately 10^7 cm/s in Si at 300 K [17]); N_{st} is the number of surface states per unit area; and E_t is the energy level of the defect (trap).

From **Eqs. 3.5** and **3.6**, SRV principally depends on the elementary properties of the surface defects. As a result of the relationship between the surface properties and the SRV, the treatment of surface passivation is the most promising method to decrease the surface recombination rate on semiconductor surfaces.

3.3 Bulk and Surface Recombination Lifetime

The total recombination rate U_{eff} is the sum of the individual recombination rates U_n which are significantly affected by both bulk and surface of the semiconductor. Considering that the recombination rates are the inverse of reciprocal carrier lifetimes, the following equation is derived:

$$U_{eff} = \sum_n U_n \Rightarrow \frac{1}{\tau_{eff}} = \sum_n \frac{1}{\tau_n} \quad \text{Eq. 3.9}$$

The effective lifetime τ_{eff} can be written as follows:

$$\frac{1}{\tau_{eff}} = \frac{1}{\tau_b} + \frac{1}{\tau_s} \quad \text{Eq. 3.10}$$

where τ_b and τ_s are the bulk and surface lifetimes, respectively.

The bulk and surface contributions can be separated from the total recombination rate by investigating the individual processes and mechanisms of recombination. Using a simple kinetic argument, the surface lifetime τ_s can be divided into two sub-components of a lifetime. Thus,

$$\tau_s = \tau_{os} + \tau_{diff} \quad \text{Eq. 3.11}$$

where τ_{os} is the effective lifetime of the carriers to recombine on the surface and τ_{diff} is the hole diffusion lifetime that represents the time taken by the minority carriers to diffuse on the surface.

The mechanism of carrier flows (lifetime) associated with surface recombination is shown clearly in Figure 3.4. **Eq. 3.11** is valid in general and applicable to any optical absorption depth. τ_{os} is equated to $H/2S$ when the excess carrier density has sufficient time to distribute uniformly. The diffusion lifetime τ_{diff} is approximated by an expression valid for the complete range of S and is found by simply adding the expressions of limiting values for both cases of high and low S [40]. Thus,

$$\tau_{diff} = \frac{H^2}{D\pi^2} \quad \text{Eq. 3.12}$$

In this study, the illumination is initiated by white light using the AM1.5 spectrum. The generation rate $G(\lambda, x)$ is given as a function of the distance of x from the surface as follows:

$$G(\lambda, x) = \int_0^x \alpha(\lambda) \cdot \Phi(\lambda) [1 - R(\lambda)] e^{-\alpha(\lambda)x} \quad \text{Eq. 3.13}$$

As shown in Figure 3.5, carrier generation occurs within a distance of 5 μm to 10 μm from the surface. If the recombination lifetime τ_{os} is very short, uniform distribution cannot be established on time. The surface traps will also occur rapidly while being filled with minority carriers during a time much shorter than that shown in **Eq. 3.12**. This study assumes that the time taken is very short and will be neglected in the analysis of surface recombination data, which is in agreement with the observed results.

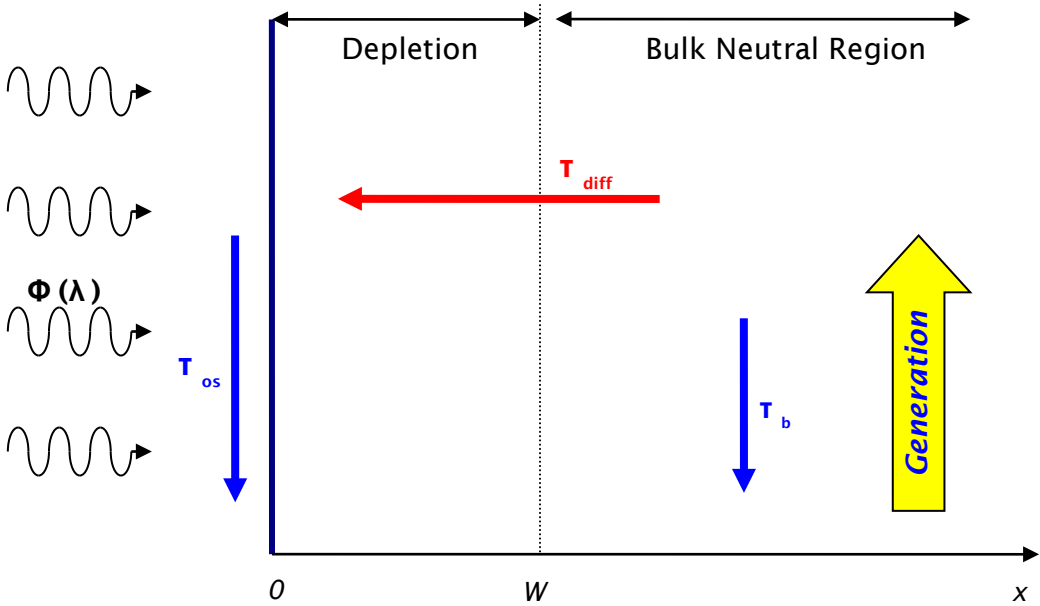


Figure 3.4 The mechanism of carrier flows (lifetime) associated with surface recombination where τ_{os} is the effective lifetime related to surface recombination; τ_{diff} is lifetime related to diffusion to the surface and τ_b is bulk lifetime.

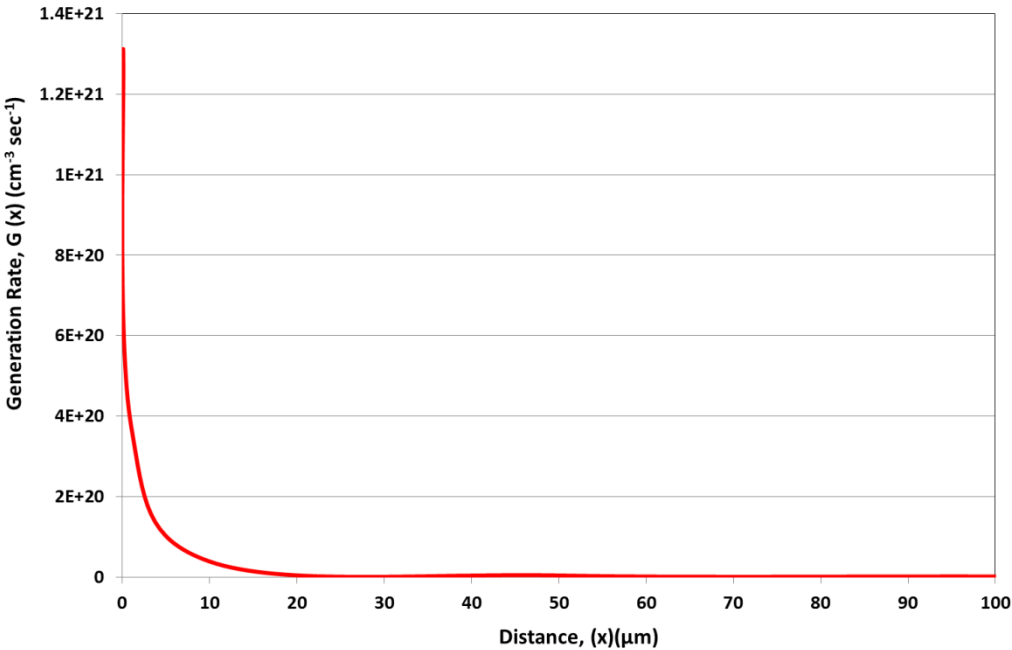


Figure 3.5 Generation rate, G vs. distance, x from the silicon surface.

3.4 Band Bending near the Surface

As discussed in **Section 2.3.3**, the presence of a charge on the silicon surface will cause the bands to bend, creating an electric field and an SCR. Thus, the bands are bent upward if $\sigma > 0$ and downward if $\sigma < 0$, where σ is the free charge density. When $\sigma = 0$, the condition of the flat bands is met, provided that no surface states are present. The flat band potential has the same function as the potential of zero charge for metals. In thermal equilibrium, surface band bending adjusts to maintain the condition of surface charge neutrality. As the charge is present on the surface states, it also results in the formation of an SCR underneath the surface. In turn, the band bending affects the surface concentration of electrons and holes and the surface recombination rate.

Upon illumination, the excess carriers are generated in the bulk, causing band-bending changes in the semiconductor. Band bending is possible in accumulation, depletion, or inversion conditions [41]. A downward band bending represents an accumulation of electron charges in the depletion region that makes the surface more conductive. A large amount of positive charge trapped in the semiconductor-oxide interface/surface region is illustrated in Figure 3.6(a). Given that the depletion region has negative signs because of the increased distance between the Fermi level and the conduction band bottom, the space charge layer is filled with mobile electrons that leave positively charged bulk donors uncompensated. At the depleted surface, the minority carrier is slightly higher than the majority carrier where the positive charge is accumulated in the depletion region. The most negative charge is trapped in the semiconductor-oxide interface/surface region. The negative charge on the surface is below the Fermi level E_F , which creates an upward bending of the bands (Figure 3.6b).

The cases of accumulated and depleted regions in capacitance measurements were used in the study of surface states and Si-SiO₂ interface [42]. Under inversion, a highly negative charge is trapped in the semiconductor-oxide interface/surface region, whereas a positive charge that accumulated because of the minority carriers in the depletion region is larger than the majority carriers. A larger upward band bending of the bands decreases the

concentration of the majority carriers (electrons) on the surface and increases the gap between the Fermi level and the conduction band (Figure 3.6c). The inversion region possibly occurs with high energy photons that are supplied by a large number of minority carriers to form a larger upward band bending [43]. For example, this inversion region of the SPV is formed with $h\nu > 3.2$ eV after heating the sample porous Si/crystalline Si layer [44].

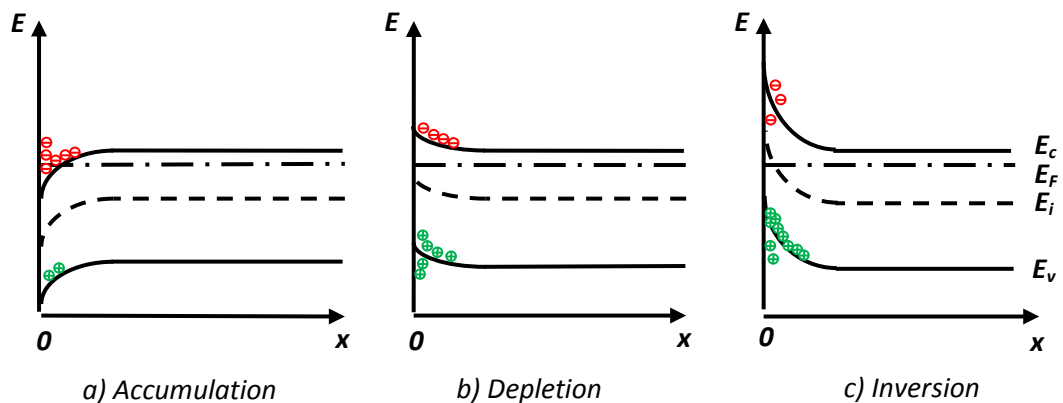


Figure 3.6 Band diagrams of surface showing three different mechanisms: accumulation, depletion and inversion at the surface of *n-type* semiconductors [12].

3.5 Chapter Summary

This chapter examines the characteristics of the semiconductor surface. It defines the surface state and explains the surface state properties. The SRV in flat band and band bending conditions mainly depends on the properties of the surface state, charge carrier concentration, capture cross-sections for electrons and holes, injection level on the surface, and doping level of semiconductors. The charge effect on the surface, especially fast trap and slow trap mechanisms, has an important function in the formation of the surface potential and the barrier height of the semiconductor surface. A mechanism of charge trapping related to the surface charge on the passivated Si surface will be demonstrated in Chapter 9.

Chapter 4 Energy Conversion in Photosynthesis: A Model for Solar Cell Application

4.1 Introduction

Today, the artificial systems for solar energy conversion are called solar cells. Solar cells convert solar energy directly into electricity by utilizing light energy to produce current and voltage in an external circuit. The principal aim of this thesis is to study LH as a means of improving solar cell operation. PV energy conversion has many similarities with photosynthetic systems. In this study, a detailed review of photosynthetic electron and energy transfer is necessary. In particular, LH, charge separation, and catalysis that have significant functions in electron transport in both systems are considered [45]. In the conversion process, the incident energy of light creates mobile charged particles in semiconductors that are then separated by the device structure and produce an electrical current. By contrast, photo-excited molecules in a photosynthetic system can be used to transfer electrons across a bacterial membrane between molecular species. The purple bacteria were chosen in this study to demonstrate the similar principle of natural photosynthesis, where the ET system in photosynthesis can be applied as a model for solar cells.

4.2 Light Harvesting and Kinetics of Electron Transport

The photosynthetic electron transport chain of the bacterial membrane is a cyclic pathway of ET. The product of light-driven cyclic electron transport is an electrochemical potential whose potential can be transformed into ATP that powers a large number of cellular processes. Photosynthetic organisms are equipped with an LH antenna system that harvests solar light and absorbs photons. Photosynthetic organisms contain about 50 to 1000 molecules of LH antenna, plus other light-gathering pigments for each photochemical RC [46]. Once the excitation energy reaches the RC, the primary photochemical redox reactions are initiated.

The elementary photosynthetic reaction in purple bacteria corresponds to the electron transportation across the photosynthetic membrane. Electron transport occurs in the RC of bacterial photosynthesis, receiving excitation energy of light absorbed by the LH centre. As shown in Figure 4.1, the molecule involved in the electron transport chain consists of a primary electron donor (a bacteriochlorophyll dimer, P), bacteriochlorophyll molecule B , bacteriopheophytin molecule J , and quinone Q . Two sets of cofactors involving B , F , and Q are arranged in two branches (labelled A and B) that span the membrane. The primary quinone Q_A and the secondary quinone Q_B , are linked by H-bond throughout a $His-Fe^{2+}-His$ complex.

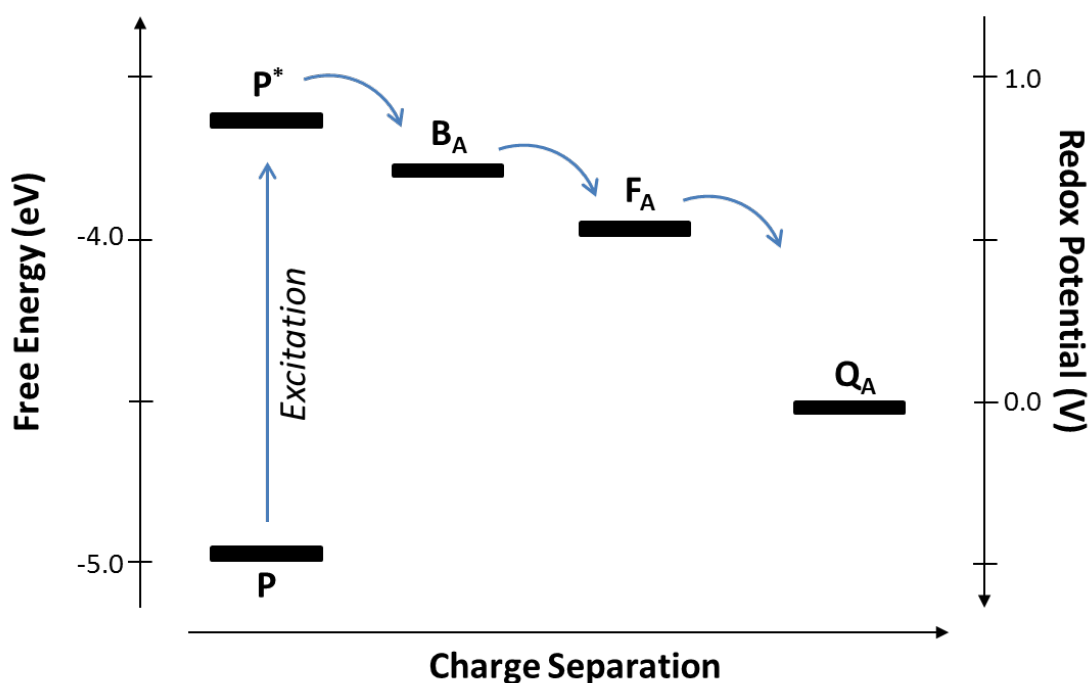
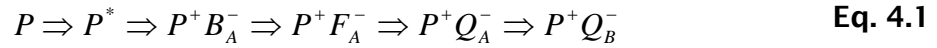


Figure 4.1 Typical energy diagram over charge separation of ET in the bacterial photosynthesis. In addition to the ET steps in Eq. 4.1, the electron can decay to the 'ground state P '. Free energy refers to the vacuum level [4].

Bacterial photosynthesis begins at the RC where the charge is separated across the membrane. Absorption of photon or energy transfer from LH complexes in

the membranes raises the photochemical pigment of the ground state P , with light emission $h\nu$, to its first excited singlet state P^* , where g is the rate constant for light absorption by P and $1/\tau$ is the rate constant for deactivation of P^* back to P . The excitation of P is followed by several intermediate steps that complete the ET to the primary electron acceptor Q_A , where the probability of the charge separation (Figure 4.1) completed is over 90% under physiological conditions [4]. The RC is a site of ET from the primary electron donor P to the quinone. Thus,



4.3 The Model of Energy Conversion

The complete process of energy generation and storage in photosynthesis can be divided into four phases as follows: (i) light absorption and energy delivery by antenna systems, (ii) primary ET in RCs, (iii) energy stabilization by secondary processes, and (iv) synthesis and export of stable products [47]. The main focus of this study is the creation of energy in secondary phases of primary electron in RCs, where free energy can be produced by the generation of the following energy sources: chemical potential [48, 49], electrochemical potential [50], electrostatic potential [51, 52], and the proton gradient, as described by chemiosmotic theory. Following Bolton [48], this study defines the chemical potential μ , which exists between the ground state P and the excited state P^* of the dye by $\mu = k_B T \ln(x_H/x_L)$, where x_H is the mole fraction of P^* in the presence of an external light source; x_L is the mole fraction of P^* at equilibrium in the dark; k_B is Boltzmann constant; and T is ambient temperature.

Archer and Bolton [49] consider the chemical potential in photochemical conversion process between the ground state R , and the excited state R^* , of molecule chromospheres. This chemical potential μ is equivalent to the Gibbs energy difference of ΔG_{RR^*} since $\mu = \Delta G_{RR^*} = \Delta G_{RR^*}^o + k_B T \ln(N_u/N_l)$, where N_u and N_l are the photo-stationary concentrations of R^* and R , respectively [53]. It is usual [54] to define the electrochemical potential as the sum of the electrical

and chemical potentials in the free energy changes by $\mu' = \mu + ze$, where z is the valence of the charge and e is the sign of the charge (± 1).

Electrostatic potential Ψ is the energy stored where the trans-membrane electrical potential generates an electric field from the uncompensated transfer of electrons or protons across the membrane [54]. Mitchell's [55] chemiosmotic theory assumes that electron and hydrogen transfers are arranged vectorially across bioenergetic membranes. This condition allows protons (hydrogen ions) to move across the membrane to establish an electrochemical gradient. The complete expression of the electrochemical potential of a charged solute is as follows:

$$\mu' = \mu^{\circ} + k_B T \ln \{c\} / \{c^{\circ}\} + ze.(E - E^{\circ}) \quad \text{Eq. 4.2}$$

where μ° and c° are the chemical potential and concentration (1 M) under standard conditions, respectively, and E° is the electrical potential in the standard state. In the application of the electrochemical potential to the proton gradient (H^+) translocation driven by a membrane with a protonic charge ($ze = 1$), the following equation is derived:

$$\Delta\mu'_{H^+} = \Delta\Psi - 2.3k_B T .\Delta pH \quad \text{Eq. 4.3}$$

where $\Delta\Psi = \Psi_{out} - \Psi_{in}$; $\Delta pH \equiv -\log \{H^+\} = pH_{out} - pH_{in}$ and $\Delta\mu'_{H^+} = (\mu_{H^+})_{out} - (\mu_{H^+})_{in}$.

This study discusses how the elementary redox reaction of ET from P to Q is coupled to the proton transfer. The primary photosynthesis conversion process describes an ET and a photochemical proton pump in the RC-quinone cycle. Translating the redox reaction into a spatial arrangement of electron and proton transport, proton pump models are created across the bacterial membrane by considering the effect of $\Delta\Psi$ and ΔpH (Figure 4.2).

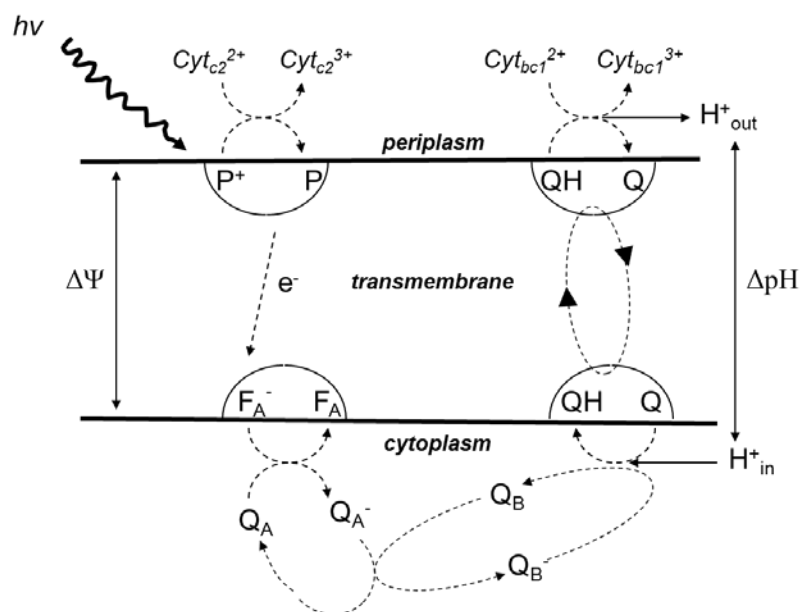


Figure 4.2 A schematic diagram of a simple proton pumps circuit to the show the elementary physico-chemical processes. It is assumed that all ETs are 1 electron or 1 H^+ events. (modified from Crofts [56]).

This diagram shows the relative orientation of the molecules of the electron transport chain, such as between two molecules (donor P and acceptor Cyt_{c_2}), sequential between donor Q_A^- and acceptor Q_B , plus proton H^+_{in} , to form semi Quinone QH in a photochemical reaction. The primary donor must be oxidized to P^+ to keep the RC neutral when an electron is in the latter state. The proton pump operates against a proton gradient in equilibrium with a driving force from the overall ETs from P^+ to QH_2 .

The reduction-quinone cycle and proton pump circuit diagram (Figure 4.2) inspired the outline of the simplified model of photosynthesis for solar cell application. Figure 4.3 shows a simplified schematic model of bacterial photosynthesis in two regions of the membrane (negative n and positive p) where electron and proton transport occurs across the membrane. This model can be divided into two sides with eight checkpoints. It considers the exciton transport from the LH antenna to RC and the redox reaction of the primary electron transport in RC from P to Q , as well as H^+ .

This model describes the redox reaction scheme of the primary electron transport from P to Q and the existence of H^+ concentration. Several redox reactions involved in the photosynthesis model are shown in Figure 4.3. These reactions are as follows: $1A$ is the photo-excitation of antenna molecules by light and $1B$ corresponds to the excitation of the primary pair P through LH exciton transfer. $R1$, $R2$, $R3$, and $R4$ represent redox reactions of molecular species that involve electron-proton transfer (Figure 4.1). $M5$ and $M6$ describe the diffusion of molecules across the membrane. These reactions contain three cyclic pathways: $C1$ represents the overall ET in the quinone reduction cycle; $C2$ is the diffusion of Q across the membrane; and $C3$ is the movement of H^+ concentration through the “load” from H_p^+ to H_n^+ . The generation of H^+ concentration is considered as the “load”. This process means that the stored potential energy is used to produce the high energy phosphate bond of ATP as follows [57]:

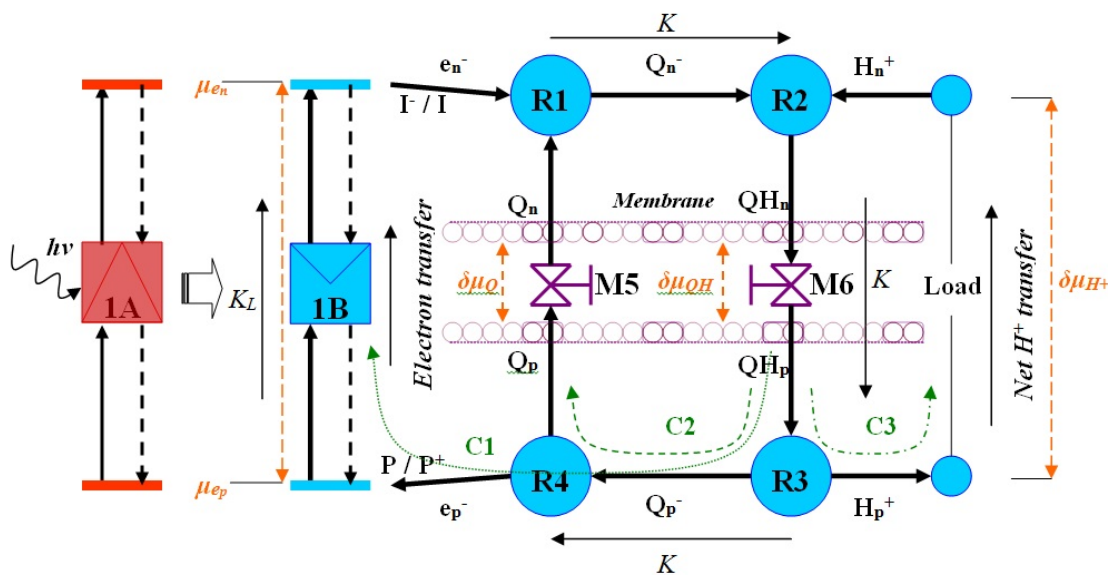
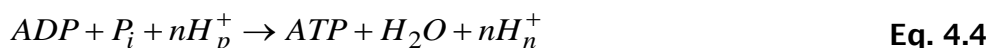


Figure 4.3 A schematic depiction of chemical energy flows in the primary processes of bacterial photosynthesis, forming the basis of the proposed system of the simplified model of photosynthesis.

This figure shows the difference in H^+ concentrations across the membrane in the periplasm. As a result, cyclic electron transport occurs, a trans-membrane proton gradient is generated, and ATP is synthesized. By assuming first-order rate constants for the energy storage process, the optimum free energy difference is determined between the ground of P and excited states of P^* [58]. The equilibrium on each side of the membrane takes place in the form of “sequential energy transfer”, where H_n^+ protonates into Q_n^- to form QH_n . The generation of H^+ concentration results from the energy stored in the “load” used for ATP synthesis. As an approximation, this study considers quinone as a proton carrier in this model. The model makes several assumptions about the operation conditions by ignoring the existence of a possible intermediate electron state at B and H . It assumes that the charge separation occurs from P^* directly to Q . This study also notes that the time derivatives of each concentration involved in the reaction are vanishing in the steady state. The reactions that comprise the model are illustrated in Table 4.1.

Table 4.1 A summary of reaction and process involved in the proposed system of the simplified model of photosynthesis.

| Checkpoint | Reaction | Process Involved |
|------------|--|---|
| 1A. | $A + hv \rightleftharpoons A^*$ | - Photo excitation |
| 1B. | $P + A^* \xrightleftharpoons[\frac{1}{\tau}]{g} P^* + A$ | - Light harvesting |
| R1. | $P^* + Q_n \xrightleftharpoons[k_1]{k_1} P^+ + Q_n^-$ | - Primary charge separation |
| R2. | $Q_n^- + H_n^+ \xrightleftharpoons[k_2]{k_2} QH_n$ | - Protonation H^+ to Q_n^- |
| R3. | $QH_p \xrightleftharpoons[k_3]{k_3} Q_p^- + H_p^+$ | - Dissociation of QH |
| R4. | $P^+ + Q_p^- \xrightleftharpoons[k_4]{k_4} P + Q_p$ | - Reduction of dimer P |
| M5. | $Q_p \xrightleftharpoons[k_5]{k_5} Q_n$ | - Diffusion of Q across the membrane |
| M6. | $QH_n \xrightleftharpoons[k_6]{k_6} QH_p$ | - Diffusion of QH across the membrane |

} Quasi - equilibrium
"sequential energy transfer"

In Table 4.1, reactions 1A and 1B are the energy conversion processes of a light absorber with two quantum states, where the absorption of a photon of light from LH antenna A occurs through exciton transfer and promotes an electron from the ground state P to an excited state P^* , in RC [59]. The rate of excitation is illumination g and the lifetime of the excited state with respect to transitions to ground state τ .

Consider redox reaction R1, where k_1 and k_1' are the forward and backward rate constants to introduce the chemical potential. The equilibrium constant is as follows:

$$K_{eq} = \frac{[P^*][Q_n]}{[P^+][Q_n^-]} = \frac{[P_o^*][Q_{n_o}]}{[P_o^+][Q_{n_o}^-]} \quad \text{Eq. 4.5}$$

where the bracketed quantities denote the concentrations of P^* , P^+ , Q_n^- , and Q_n ; and “ $_o$ ” denotes the concentration in the standard state. This equation can be rearranged as follows:

$$\frac{[P^*][Q_n]}{[P_o^*][Q_{n_o}]} = \frac{[P^+][Q_n^-]}{[P_o^+][Q_{n_o}^-]} \quad \text{Eq. 4.6}$$

Each concentration can be related to a chemical potential.

$$\frac{[P^*]}{[P_o^*]} = \exp\left(\frac{\mu_{[P^*]}}{k_B T}\right); \frac{[P^+]}{[P_o^+]} = \exp\left(\frac{\mu_{[P^+]}}{k_B T}\right); \frac{[Q_n]}{[Q_{n_o}]} = \exp\left(\frac{\mu_{[Q_n]}}{k_B T}\right); \frac{[Q_n^-]}{[Q_{n_o}^-]} = \exp\left(\frac{\mu_{[Q_n^-]}}{k_B T}\right);$$

Eq. 4.6 can be rewritten with chemical potentials as follows:

$$\mu_{[P^*]} + \mu_{[Q_n]} = \mu_{[P^+]} + \mu_{[Q_n^-]} \quad \text{Eq. 4.7}$$

A similar approach is applied to redox reaction R2, R3 and R4. Thus,

$$\mu_{[Q_n^-]} + \mu_{[H_n^+]} = \mu_{[QH_n]} \quad \text{Eq. 4.8}$$

$$\mu_{[QH_p]} = \mu_{[Q_p^-]} + \mu_{[H_p^+]} \quad \text{Eq. 4.9}$$

$$\mu_{[P^*]} + \mu_{[Q_p^-]} = \mu_{[P]} + \mu_{[Q_p]} \quad \text{Eq. 4.10}$$

Eqs. 4.8 and 4.9 can be arranged as follows:

$$\mu_{[H_p^+]} - \mu_{[H_n^+]} = \mu_{[QH_n]} - \mu_{[QH_p]} - (\mu_{[Q_n^-]} - \mu_{[Q_p^-]}) \quad \text{Eq. 4.11}$$

Thus,

$$\delta\mu_{[H^+]} = \delta\mu_{[QH]} - \delta\mu_{[Q^-]} \quad \text{Eq. 4.12}$$

Eqs. 4.7 and 4.10 can be arranged as follows:

$$\mu_{[Q_n^-]} - \mu_{[Q_p^-]} = \mu_{[Q_p]} - \mu_{[Q_n]} + \mu_{[P]} - \mu_{[P^*]} + \mu_{[P^*]} - \mu_{[P]} \quad \text{Eq. 4.13}$$

Utilizing a simple approach, the following equation is derived:

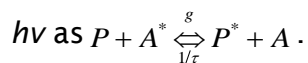
$$\delta\mu_{[Q^-]} = \delta\mu_{[Q]} - (\mu_{[P^*]} - \mu_{[P]}) \quad \text{Eq. 4.14}$$

Substituting Eq. 4.14 into Eq. 4.12 and rearranging these equations result in the following:

$$(\mu_{[P^*]} - \mu_{[P]}) = \delta\mu_{[H^+]} + \delta\mu_{[Q]} - \delta\mu_{[QH]} \quad \text{Eq. 4.15}$$

where $\Delta\mu = (\mu_{[P^*]} - \mu_{[P]})$ is the photo-generated chemical potential, which is a representation of the chemical potentials $\mu_{[P^*]}$ and $\mu_{[P]}$ that govern the occupancy of the excited species of P^* and P , respectively.

A diagram of the excitation of P in reaction 1B is shown in Figure 4.4. **Eq. 4.16** governs the time evolution determined by considering direct light absorption



$$\frac{dP^*}{dt} = g[P][A^*] - \frac{1}{\tau}[P^*][A] - K = 0 \quad \text{Eq. 4.16}$$

where τ is the lifetime of the excited state of P^* , g is the photo-excitation rate of P^* , A^* is the exciton of antenna LH, K is the rate of the photosynthetic energy conversion, and ΔE is the excitation energy of P .

As assumed in steady-state conditions, g is the rate of energy transfer from the photo-excited antenna to the RC. This rate was discussed in detail by Markvart [4, 60], who supposed that g is proportionate to the illumination intensity. Considering that the antenna system is a purely physical process and does not involve any chemistry [47], the existence of antenna A , can be ignored and **Eq. 4.16** can be simplified by introducing $[P_0^*]$ as the equilibrium occupation of P^* .

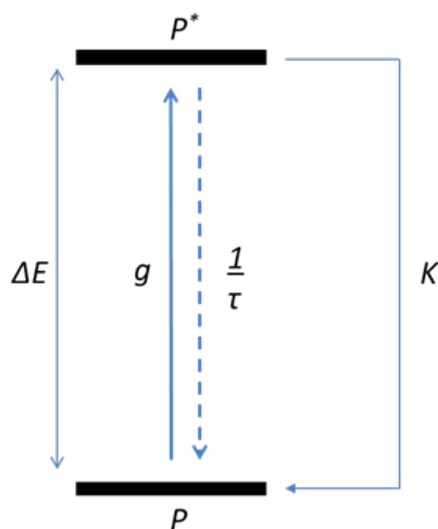


Figure 4.4 A schematic diagram of excitation of P in Checkpoint 1B of the simplified model.

Thus,

$$K = g[P] - \frac{[P_o^*]}{\tau} \cdot \frac{[P^*]}{[P_o^*]} \quad \text{Eq. 4.17}$$

Introducing the concentration of [P] and the standard state, the following equation is derived:

$$K = g[P] - \frac{[P_o^*]}{\tau} \cdot \frac{[P]}{[P_o]} \cdot \frac{[P^*]}{[P_o^*]} \cdot \frac{[P_o]}{[P]} \quad \text{Eq. 4.18}$$

Substituting of K_L and K_o values into **Eq. 4.18**:

$$K_L = g[P]; \quad K_o = \frac{[P_o^*]}{\tau} \frac{[P]}{[P_o]}; \quad \left(\frac{[P^*]}{[P_o^*]} \right) = \exp\left(\frac{\mu_{[P^*]}}{k_B T} \right); \quad \left(\frac{[P]}{[P_o]} \right) = \exp\left(\frac{\mu_{[P]}}{k_B T} \right);$$

The equation can be obtain in the following:

$$K = K_L - K_o \exp\left(\frac{\mu_{[P^*]} - \mu_{[P]}}{k_B T} \right) \quad \text{Eq. 4.19}$$

From **Eq. 4.15**, the final result of the equation model is as follows:

$$K = K_L - K_o \left[e^{\left(\frac{\delta\mu_{H^+}}{k_B T} \right)} e^{\left(\frac{\delta\mu_Q}{k_B T} \right)} e^{\left(\frac{\delta\mu_{QH}}{k_B T} \right)} - 1 \right] \quad \text{Eq. 4.20}$$

4.4 Results and Discussion

The principal result of the model is contained in **Eq. 4.20**. It has a similarity to the I - V characteristic of the solar cell (**Eq. 4.21**). In the solar cell's I - V characteristic, the output current I is equal to the difference between the light-generated current I_L and the dark diode current I_o . In the photosynthesis model, I is replaced by the equivalent symbol of K that is the rate of the photosynthetic energy conversion [4, 51]. **Eq. 4.20** shows a similar formula of

the Shockley equation that could be applied to measure the chemical potential in photosynthesis. As the energy model is developed, the electron transports can be described by an analogue of the Shockley equation. Thus,

$$I = I_L - I_o \left[\exp\left(\frac{qV}{kT}\right) - 1 \right] \quad \equiv \quad K = K_L - K_o \left(\exp\left(\frac{\Delta\mu}{k_B T}\right) - 1 \right) \quad \text{Eq. 4.21}$$

where the reaction rates K_L and K_o are the photosynthetic equivalents of the photo-generated and dark saturation current, respectively, and $\Delta\mu$ is the electrochemical potential that includes both the chemical (electron concentration) and electrostatic (qV) parts, unlike in the solar cell.

The simple model of the energy conversion process shows the detailed balance between the energy of the absorbed light and the free energy delivered to the excited state. The simple model for electron transport in photosynthesis created by Markvart [51, 59] was used as a basis for solar cell application. The absorption of photon raises the photochemical pigment of the ground state P with light emission $h\nu$ to its first excited singlet state P^* . The estimated value of the magnitude order of excitation rate g is 1 s^{-1} and the natural lifetime of chlorophyll is $1/\tau = 18 \text{ ns}$ [61]. The electrochemical potential $\Delta\mu$ can be calculated using an analogue of the Shockley equation (Eq. 4.20), where the $\Delta\mu$ value is calculated as 0.93 eV and K_L is 1.55 eV/s. The maximum power point (MPP) values are plotted in Figure 4.5 as P_{mpp} at 1.26 J/s, K_{mpp} at 1.50 eV/s, and $\Delta\mu_{mpp}$ at 0.84 eV, corresponding to the wavelength of bacteria at 800 nm.

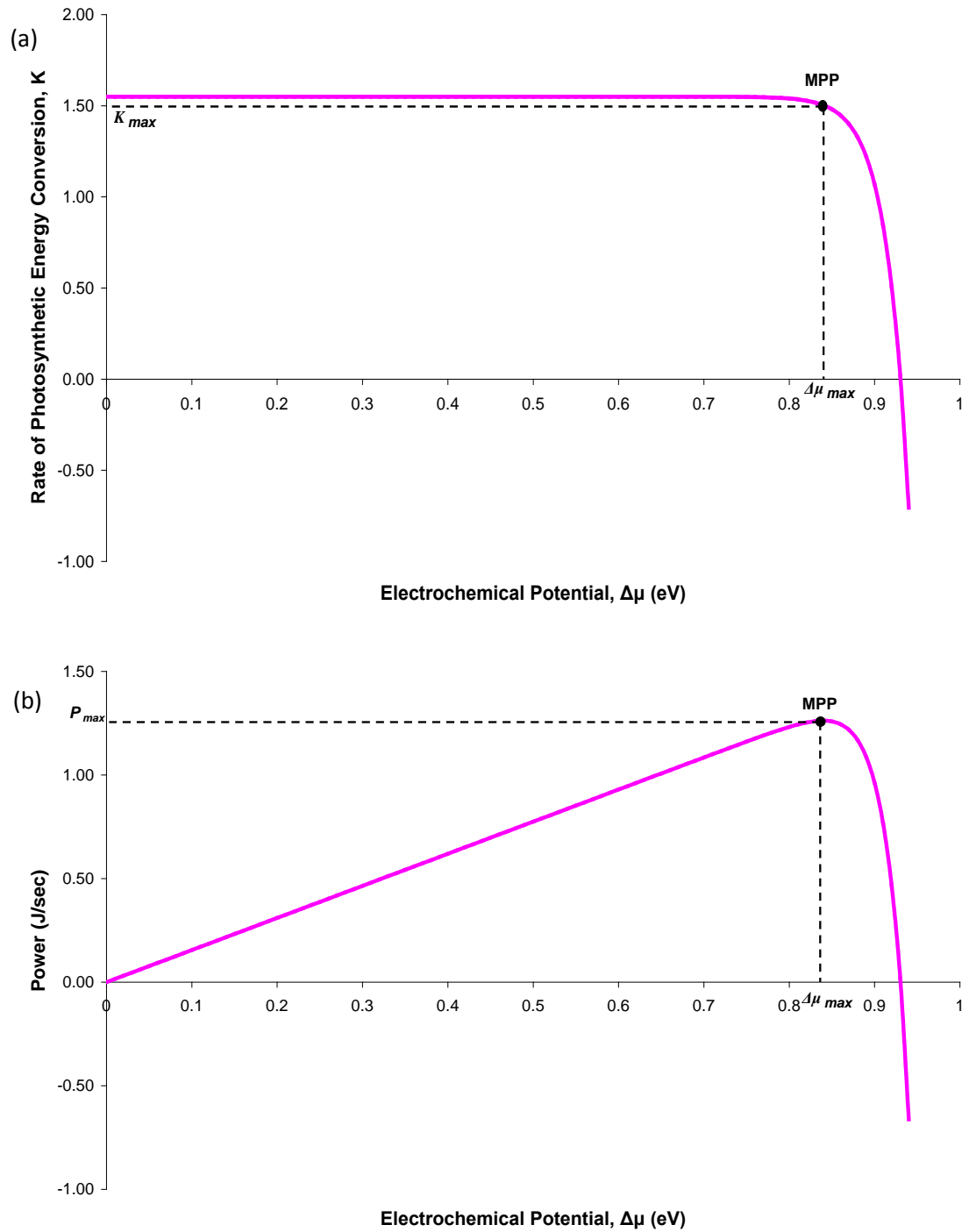


Figure 4.5 Graph of photosynthetic energy conversion that have a similarity with the I - V characteristic (a) Rate of photosynthetic energy conversion K vs. Electrochemical potential $\Delta\mu$ and (b) Power P vs. Electrochemical potential $\Delta\mu$.

4.5 Chapter Summary

A simplified model for the primary energy conversion step in photosynthesis has been successfully developed by identifying the most significant chemical potentials involved in the photosynthetic system. The selection of each value from the literature was justified with an appropriate explanation to connect to the simplified model of photosynthesis. The new Shockley solar cell equation was determined, where the electrochemical $\Delta\mu$ can be classified into three chemical potentials. These potentials are as follows: $\delta\mu_{QH}$ shows the diffusion of QH , from negative to positive region of membrane; $\delta\mu_{H^+}$ shows the proton pumping transfer from $H_p^+ \rightarrow H_n^+$, which represents the proton transfer movement from “in” \rightarrow “out” of membrane cells; and $\delta\mu_Q$ shows the diffusion of oxidized quinone Q , from the positive to the negative membrane. This study shows that the internal free energy in bacterial photosynthesis bears many similarities to the voltage of qV (Eq. 4.21) in the Shockley equation, which describes the operation of a solar cell.

Chapter 5 Characterization of Surface Recombination by the Kelvin Probe

5.1 Introduction

The surface of a semiconductor contains the largest number of non-saturated “dangling” bonds that become a centre of recombination. Generally, this surface consists of a large density of defects where a localized charge occupies the surface states by following Fermi–Dirac statistics. In thermal equilibrium, the net surface charges in the surface states are balanced by the space charges in the SCR. The induced SPV is uniformly illuminated by monochromatic light of energy higher than the band gap. Electron–hole pairs are generated in the bulk semiconductor and diffuse a minority carrier toward the SCR. Band bending occurs when a surface charge exists on the surface. This study focuses on SPV characterization via KP methods that have become significant tools to determine the minority carrier diffusion length of semiconductors. This study also considers the surface barrier changes related to the surface and bulk properties of the semiconductor material.

5.2 Kelvin Probe Applied to Semiconductor Surface Study

The KP method was established by Lord Kelvin in 1898 to investigate the charge transport by electrical conduction between two metallic surfaces [62]. When one metal plate is brought close to the other metal plate while it is connected electrically, it creates contact potential differences (CPD) between two metal plates because of electron transport. V_{CPD} is defined as the difference between the work functions of two conductors where the electrons flow from one conductor to the other until an equilibrium condition is reached. Zisman developed a vibrating capacitor based on Lord Kelvin’s principle in 1932 [63]. This invention allowed the CPD to be quantified through the vibration of one

metal plate relative to the other metal plate. The difference of the work function is as follows:

$$V_{CPD} = \frac{W_{probe} - W_{plate}}{|q|} \quad \text{Eq. 5.1}$$

KP measurement is normally employed to measure the sample work function. It also characterizes the surface voltage, surface barrier height, flat band voltage, oxide thickness, oxide leakage current, interface trap density, mobile charge density, oxide integrity, generation and recombination lifetime, and doping density [64]. These characteristics are important tools as they determine a way to develop a simplified method to measure surface properties of samples. A contactless method of KP is best adopted to monitor the changes and control of interface properties of the surface.

5.2.1 Metal-Semiconductor System

A schematic band diagram of metal–semiconductor contact between a metal and *n-type* semiconductor of true work functions, namely, qW_m and qW_s , respectively, and assuming that $W_s < W_m$, is shown in Figure 5.1. The potential barrier exists by means of the electron affinity χ , which is defined as the energy required releasing an electron from the conduction band to the vacuum ($\chi = E_{vac} - E_c$). The various effects of surface dipole $\Delta\phi_s$ may create some potential changes on the surface that preserves the effective electron affinity χ^* . The work function on the semiconductor surface in equilibrium W_s can be defined as the energy separation between the Fermi level and the local vacuum level on the surface. The expression of W_s is as follows:

$$W_s = (E_c - E_F)_b - qV_s + \chi + \Delta\phi_s \equiv (E_c - E_F)_b - qV_s + \chi^* \quad \text{Eq. 5.2}$$

The band diagrams of metal–semiconductors of *n-type* (Figure 5.1) were drawn for a semiconductor in thermal equilibrium without an applied external electric field. In the bulk region, the Fermi level E_F is flat with many electrons on the conduction band E_c , which represents majority carriers. Few of the holes that

act as minority carriers still remain in the conduction band E_c . When the surface state is present, a small charge potential is assumed to exist ($V > 0$). The accumulation of excess minority carriers on the conduction band edge E_c also bends upward near the surface and far from the Fermi level. The Fermi level transforms from flat to split levels to create two levels of E_{Fn} and E_{Fp} in the depletion region, namely, quasi-Fermi levels. The quasi-Fermi levels describe non-equilibrium situations where the two Fermi levels separate because of the applied voltage or charge potential. However, the quasi-Fermi levels undergo a downward split by a small but non-negligible amount. Given that E_{Fn} and E_{Fp} remain relatively constant and split inside the depletion region, one Fermi level remains in the bulk region.

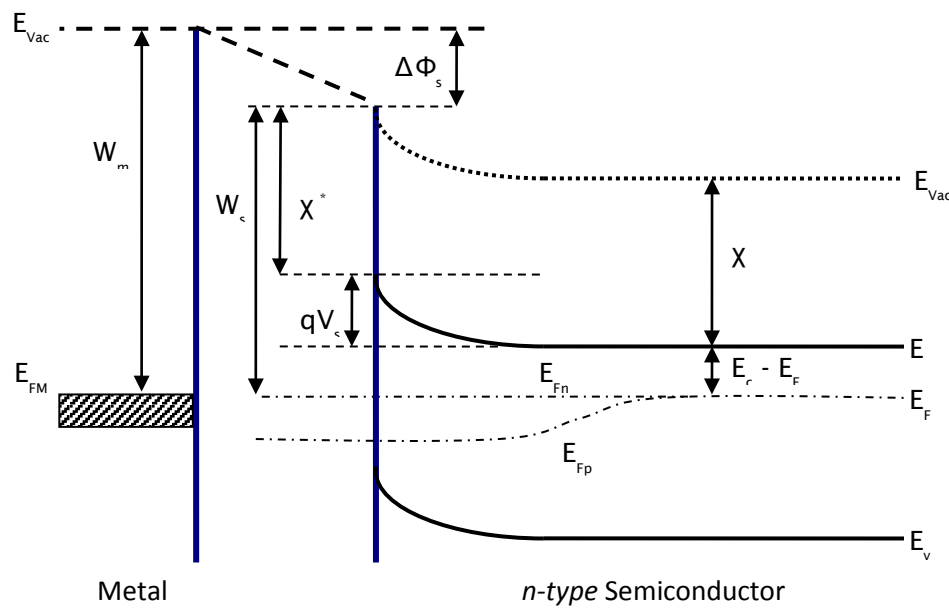


Figure 5.1 A schematic band diagram of metal-semiconductor (*n*-type) shows the barrier height, δV_s and splitting of quasi-Fermi levels E_{Fn} and E_{Fp} in the depletion region.

Near the surface, the existence of a potential barrier represents the depletion region where the fixed charges build up values until reaching an equilibrium

condition. When the semiconductor is in contact, the barrier height δV_s is created because of the difference between the potential barrier on the surface and in the bulk of the semiconductor. From the figure, the surface dipole $\Delta\phi_s$ is observed on the surface where the electric potential changes abruptly over several monolayers. Considering that the semiconductor is *n-type*, electrons are accumulated on the surface, giving rise to the negative charge. For consistency with the sign convention of the surface voltage, this study assumes that the surface dipole is positive if the local vacuum levels drop when passing through the semiconductor into a vacuum.

5.2.2 Work Function and Contact Potential Difference

The difference in the work function is determined by the value of external voltage at a null condition, where the null output result becomes $V_{CPD} = V_s$. If the work function of the vibrating plate is known, the work function of the sample can be determined. Given that KP measures the difference in the work function of the reference gold probe and the sample, the CPD can be derived as follows:

$$V_{CPD} = \frac{1}{q} [\chi - qV_s + (E_c - E_F)_b - W_M] \quad \text{Eq. 5.3}$$

where W_M is the work function of the reference gold probe. The work function W can also be defined as the least amount of energy required to remove an electron from the bulk of a conducting material through the surface by the following:

$$W = \chi - qV_s + (E_c - E_F)_b \quad \text{Eq. 5.4}$$

The barrier height of a semiconductor surface is given by the following:

$$\delta V_s = V_{bi} + V_n \quad \text{Eq. 5.5}$$

$$V_n = -(E_c - E_F) = -kT \ln(N_D/N_C) \quad \text{Eq. 5.6}$$

where N_c is the effective density of states in the Si conduction band and N_D is the donor impurity concentration.

5.3 Literature Review of Band Bending Measurements by the Kelvin Probe

The band bending of organic semiconductors in organic light-emitting diodes was examined by Ishii *et al.* [65]. They investigated the band bending behaviour of interfaces between organic semiconductors and various metals (e.g., Au, Cu, Al, Mg, and Ca) under ultrahigh vacuum. The characteristics of band bending on organic materials were measured by the KP method, and the concept of band bending leads to the Fermi level alignment using the Mott-Schottky model. The band bending of organic material (e.g., C₆₀) on metal interfaces was observed. However, the flat band condition was observed for N,N-bis(3-methylphenyl)-N, N-diphenyl-[1,1-biphenyl]-4,4 diamine (TPD)/metal interfaces because of the high purity of organic materials. A new type of band bending is observed for tris(8-hydroxyquinolato)aluminium (Alq₃)/metal interfaces where the energy level shifts proportionately to the distance of the interface. A large surface potential can be interpreted as characteristics of the molecular system and the orientation of a molecular dipole.

Okumura *et al.* [66] demonstrated a sandwich-type electrode configuration for the contactless characterization of silicon-on-insulator (SOI) wafers using KP methods. In their study, V_{CPD} was determined by applying the external voltage to the sandwiched circuit, to the primary charge, and to the air gap. The SPV was measured using infrared (IR) light at a wavelength of 808 nm and UV light at 304 nm. Upon illumination, a penetration of light absorption was observed at ultra-thin SOI (62 nm), thick SOI (1.5 μm), and bulk Si. At 304 nm, the penetration depth was several tens of nanometres, and all photons were absorbed by the 62 nm SOI sample. At IR illumination, no SPV was observed for the 62 nm SOI sample, in which most of the penetrating light was not absorbed in the SOI surface layer. However, it was absorbed in the substrate-thick SOI

(1.5 μm) and bulk Si. The authors proposed a technique of contactless I - V method with an approximation of the SPV V_{spv} , and increase with the logarithm of the number of photo-generated carriers J_L . However, this contactless I - V method is only applicable for UV light excitation because all photons are absorbed. The findings of this paper show that the light intensity dependence of SPV was applied in the contactless I - V method, but J_o was not determined.

The second study of the same authors [67] reported that the induced SPV was added to the original ΔV_{CPD} , where SPV is a function of light intensity. For both studies, the SOI sample was treated with pre-cleaning of RCA method and removal of the oxide layer by 0.1% HF + 1% H_2O_2 + H_2O . Using the same contactless I - V method, the authors calculated the effective saturation current density of $J_s = 3 \times 10^{-6} \text{ A.cm}^{-2}$ using an ideality factor of $n = 1.05$ – 1.2 . This saturation current density was determined using the theory of thermionic emission for the carrier transport over the surface depletion region, where the degree of band bending ($E_{FS} - E_v = 0.72 \text{ eV}$) is in the downward position. The determination of J_s can be interpreted as J_o [66].

The electronic properties of the HF-treated Si surfaces were characterized via SPV measurements by KP method [68]. Under the illumination of a 340 nm UV light source, this study reported a relatively large SPV of -0.45 V with a photocurrent density of 1 mA/cm^2 on the HF-treated p -Si (001) surface. A large surface band bending was observed toward the surface because of the residual fluorine on the treated surface. This study also estimated the value of the built-in potential of 0.60 eV from the result of the effective saturation current.

Nakamura *et al.* [69] investigated the electrical characterization on the interfaces of SOI and implanted oxygen (SIMOX) wafer by Kelvin-SPV measurements. In these measurements, a similar approach to Okumura *et al.* [67] employing complete contactless I - V method equations was derived with consideration of the effect of surface recombination current J_{SR} , and interface recombination current J_{IR} . The wafers of the p -Si sample were cleaned by RCA method and treated with HF solution before measurements were taken. For the sample SOI materials, the recombination current was determined using SRH theory for carrier recombination. Diffusion current through the saturation current density J_o was derived, where the equation used the Fermi level

position at the surface (V_p) and temperature dependence from $-40\text{ }^\circ\text{C}$ to $80\text{ }^\circ\text{C}$. From the contactless I - V equation, the authors estimated the surface state density N_{ss} and the SRV ($S_i = v_{th}\sigma N_{sr}$) at $6 \times 10^{11}\text{ cm}^{-2}$ and $6 \times 10^3\text{ cm/s}$, respectively. They also assumed the values of the thermal velocity ($v_{th} = 10^7\text{ cms}^{-1}$) and the capture cross-sections of carriers ($\sigma = 10^{-15}\text{ cm}^2$). For the top-Si/BOX interface for the SIMOX wafer, the values of the interface state density N_{si} and the interface recombination velocity S_i were estimated at approximately $3 \times 10^{12}\text{ cm}^{-2}$ and $3 \times 10^4\text{ cm/s}$, respectively. The estimation of SRV was based on SRH theory.

5.4 Methods of Kelvin Probe Measurements – Surface Photovoltage

SPV is the illumination-induced change in the surface potential [13]. Illuminating the semiconductor may change the population of the local electron states, provided that the photons have sufficient energy to induce electron transitions from and/or to the local state (**Section 3.2, Figure 3.3**). The changes in population may modify the width of the depletion region W and the magnitude of the surface potential δV_s [70]. δV_s can be expressed in terms of the differences of voltage between the dark V_s and under illumination V_s^* as follows:

$$\delta V_s = V_s - V_s^* \quad \text{Eq. 5.7}$$

The SPV signal is created by spatial separation of the photo-generated carriers. It is followed by net charge redistribution that is added to the electric field in the SCR Q_{sc} or near the surface states Q_{ss} (**Section 2.3.4**). The photo-generated minority carriers change the CPD between the probe and the sample by changing the surface band bending. V_{spv} measures the changes in the surface potential equal to V_{CPD} . However, an external applied voltage can also contribute to the SPV signal [13, 41]. The SPV mechanism mainly depends on the following: (i) the surface potential barrier associated with the surface space charge layer; (ii) generation and recombination processes of electrons and

holes; (iii) density and energy distribution of surface and bulk defect states; and (iv) the mobility of electrons and holes [41].

5.4.1 Intensity Dependence of Surface Photovoltage Saturation

Upon illumination, the SPV signal is generated on the front side of a Si surface with a monochromatic photon flux, whereas the rear side of the wafer is not illuminated. The following are the three characteristics of the dependence of illumination on SPV measurement: (i) linear increase in the SPV at low-level illumination, (ii) logarithmic dependence for higher intensities, and (iii) saturation at equilibrium band bending [71-73]. As proposed by Johnson [72], SPV is a logarithmic function of excess carrier of holes Δp as follows:

$$V_{spv} = \frac{kT}{q} \ln \left[1 + \left(\frac{\Delta p}{p_o} \right) \right] \quad \text{Eq. 5.8}$$

where p_o is the excess carrier of holes in the equilibrium.

At low light intensity, the absorbed photons create non-equilibrium carriers that decrease the surface potential barrier δV_s and increase the SPV signal V_{spv} (excess carrier density \ll equilibrium carrier density). An additional increase in the photon flux intensity decreases the surface barrier until it disappears (excess carrier density \gg equilibrium carrier density) [74]. The SPV signal then reaches a saturation stage, where the maximum V_{spv} is represented as the surface barrier height.

5.4.2 Intensity Dependence of Surface Photovoltage Constant

The dependence of intensity is required to maintain constant small-signal SPVs to determine the minority carrier diffusion length of semiconductors. The approximation of the continuity equation is required to obtain the distribution of the photo-generated electrons and holes in the semiconductor initiated by Moss [75]. The minority carrier diffusion length is one of the applications in

SPV measurement that provides information about the low defect densities of the surface. The SPV technique is non-destructive and a contactless measurement performed based on the measurement of the open circuit voltage V_{oc} in an illuminated surface barrier.

At *low injection* levels, SPV can also be seen as the difference between the quasi-Fermi levels of electrons and holes under illumination [76]. Upon illumination, the excess minority carrier Δp is generated to form the barrier height in accumulation, depletion, or inversion conditions. From the continuity equation, Δp can be determined at the edge of the SCR as follows [64, 75]:

$$\Delta p = \frac{\eta\Phi(1-R)}{(D_p/L_p) + S^*} \cdot \frac{\alpha L_p}{\alpha L_p + 1} \quad \text{Eq. 5.9}$$

where η is the collection efficiency; Φ is the photon flux density; R is the number of photons reflected from the surface; L_p is the minority carrier diffusion length of the holes; D_p is the minority carrier diffusion coefficient of holes; α is the optical absorption coefficient; and S^* is the SRV on the illuminated surface.

This equation is valid with the assumption of $W \ll L_p$; $W \ll 1/\alpha \ll H$; $\Delta p \ll n_0$; $L_p \ll H$; where H is the thickness of the sample and W is the width of space charge region. This equation also assumes that the SRV at the back contact is negligible.

Goodman [77] proposed a simplified method to determine the diffusion length by considering the SPV as a functional dependence of the excess minority carrier density injected on the surface upon illumination. Thus,

$$V_{spv} = f[\Delta p] \quad \text{Eq. 5.10}$$

This condition means the excess minority carrier density mainly depends on the number of photons of incident light intensity that generates carriers in the SCR Φ , optical absorption coefficient α , and minority diffusion length L_p . Considering the small variations in collection efficiency η and reflectance R ,

and assuming that the quasi-equilibrium through the SCR and the width of SCR W can be neglected [76, 78], the incident of photon flux is proportional to the optical absorption coefficient α and diffusion length L_p . Thus,

$$\Phi(\lambda) \propto \left(1 + \frac{1}{\alpha L_p}\right) \quad \text{Eq. 5.11}$$

If the wafer sample is thicker than L_p , W should be smaller than L_p and the absorption coefficient must be adequately low for $\alpha W \ll 1$ and satisfactorily high for $\alpha(H - W) \gg 1$, as suggested by Schroder [64].

The incident photon flux Φ at a different wavelength is selected with each wavelength having a different α . Upon illumination, the photon flux density is adjusted for each wavelength to maintain a constant SPV where a linear relationship between SPV and excess carrier density is found. From a plot of $1/\eta_L$ vs. α^{-1} (Figure 5.2), L_p can be obtained by extrapolating at the negative α^{-1} axis. The intensity of illumination must be adjusted for a small SPV signal (1 mV to 3 mV) to satisfy $\Delta p \ll n_o$, where n_o is a majority carrier concentration in the bulk [41]. Considering that the excess minority carrier Δp is linear with the exciting photon flux Φ , it can represent the dependence of SPV on Δp by using a collection efficiency minority carrier η_L in this study.

A past measurement of diffusion length on GaP samples via induced SPV was performed by KP force microscopy [79, 80]. This study is based on measuring the SPV between the probe tip of an atomic force microscope (AFM) and the surface of an illuminated semiconductor junction. The calculation of the minority carrier diffusion length was based on the edge of Δn_{SCR} , where the SPV was measured as a function of the exciting light intensity.

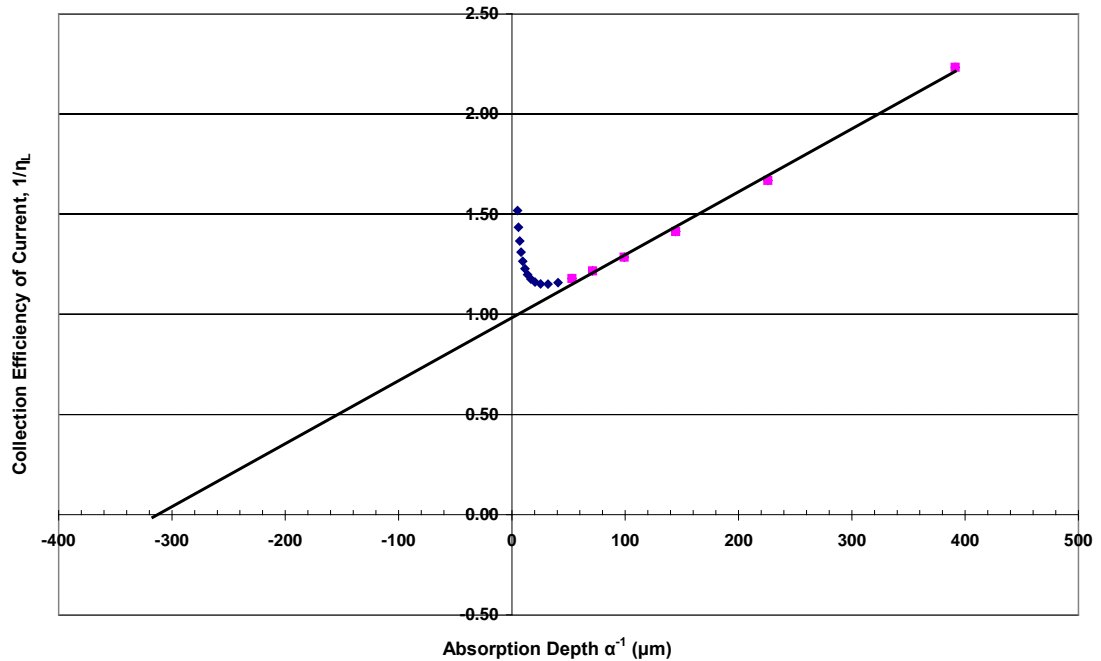


Figure 5.2 The dependence of SPV constant for diffusion length determination by plotting collection efficiency, ($1/\eta_L$) against absorption depth ($1/\alpha$) (points: data, lines: theory).

5.5 Measuring SPV and Surface Recombination by the Kelvin Probe

The surface potential effect has an important function on the semiconductor surface and can be measured by KP. The KP method consists of metallic probes that have a surface potential or work function. Semiconductor samples play the role of work electrodes of the capacitor, where the sample surface accumulates charges during KP measurements. Upon illumination, the semiconductor surface states (possibly including oxide) charge up and alter the threshold voltage as measured by the probe. The absorption of a photon generates the carrier's electrons and holes in the bulk that diffuse to the surface and alter the charge balance there.

Any changes in the localized charge in the surface state to maintain the charge neutrality affects the space charge Q_{sc} . In the *n-type* semiconductor, the space charge generally has a value of $Q_{sc} > 0$. The bands are bent upward by a large amount of positive charge trapped in the depletion region. This charge compensates the negative charge trapped in the semiconductor-oxide interface/surface layers. Considering that the light intensity dependence of SPV was applied in the KP measurements, V_{spv} can be determined based on a position of initial saturation SPV point at equilibrium band bending [72, 73].

The energy band diagram of the surface of a semi-infinite semiconductor and the various current components under illumination is shown in Figure 5.3. This study considers steady-state conditions of current balance for *n-type* silicon. The doping in the semiconductor is kept constant to be able to discuss the SPV due to illumination effects. Thus, no electric fields exist outside the depletion region. Detailed considerations and assumptions of the current balance are as follows: (i) no generation-recombination current exists in the depletion region, and (ii) the injected minority carrier densities are small compared with the majority carrier densities. The conditions imply that the electron and hole currents are constant throughout the depletion region, and that the quasi-Fermi levels remain constant in the depletion region. Similar to the bulk region of the solar cell, the net current outside the depletion region can be divided into two currents: from the surface toward the bulk semiconductor J_{dark} and reverse direction from the bulk semiconductor toward the surface J_L . This photocurrent that is dominated by the hole photocurrent in an *n-type* semiconductor is generated by the diffusion of minority carriers photo-generated in the neutral region into the depletion region. The resulting excess minority carriers on the surface give rise to quasi-Fermi level splitting.

The surface potential difference creates a current J_{dark} which acts in the opposite direction of the photo-generated current J_L . By analogy with an ideal diode, the dark current density $J_{dark}(V)$ is given by the following:

$$J_{dark}(V) = J_o \left(e^{qV_{spv}/kT} - 1 \right) \quad \text{Eq. 5.12}$$

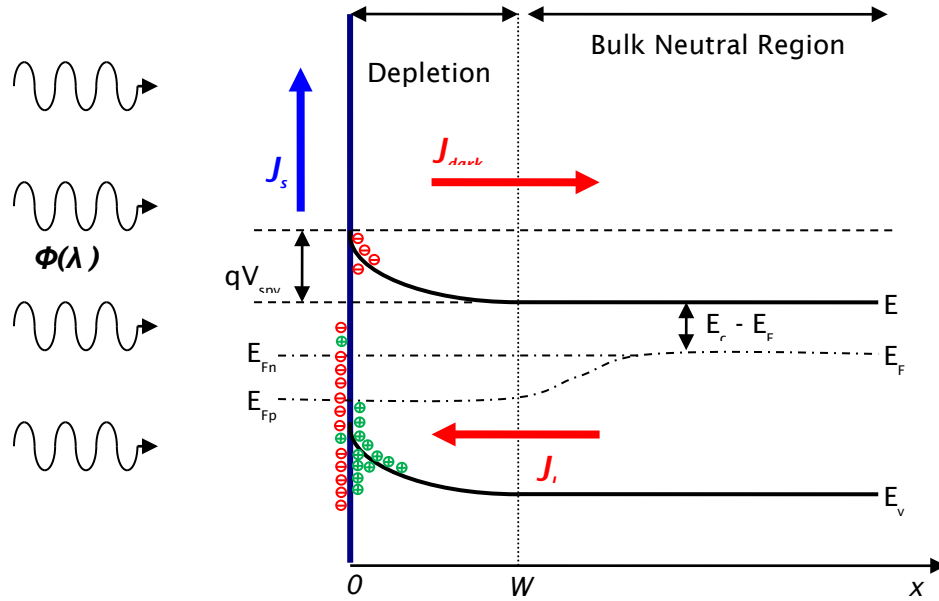


Figure 5.3 The band diagram of semiconductor (*n*-type) with surface states under illumination. Φ is the photon flux, V_{spv} is the surface photovoltage, W is the depletion width; E_{Fn} and E_{Fp} are the quasi-Fermi levels for electrons and holes, respectively.

The current J_o can be calculated by solving the diffusion equation for hole concentration in the quasi-neutral regions. For dark conditions, the homogeneous differential equations where $G(x) = 0$ are as follows:

$$D_p \frac{d^2 p_n(x)}{dx^2} + \frac{p_n(x) - p_{no}(x)}{\tau_p} = 0 \quad \text{Eq. 5.13}$$

With the boundary condition on the rear surface and $p_n = p_{no}$ at the junction, the following equation is derived:

$$S_p(p_n - p_{no}) = -D_p \left(\frac{d}{dx} \right) (p_n - p_{no}) \quad \text{Eq. 5.14}$$

where D_p is the diffusion coefficient for holes. The assumption was made by considering that the doping level on the *n*-sides is constant in the depletion

region. The electric fields outside the depletion region are also negligible. Thus, the equation can be derived using a homogeneous linear equation with constant coefficients as follows:

$$p_n - p_{no} = A \cosh\left(\frac{x}{L_p}\right) + B \sinh\left(\frac{x}{L_p}\right) \quad (x \geq H) \quad \text{Eq. 5.15}$$

where H is the thickness of the wafer. The solution is as follows:

$$J_o = q \frac{D_p}{L_p} \frac{n_i^2}{N_D} \left[\frac{\left(\frac{S_p L_p}{D_p}\right) \cosh\left(\frac{W}{L_p}\right) + \sinh\left(\frac{W}{L_p}\right)}{\left(\frac{S_p L_p}{D_p}\right) \sinh\left(\frac{W}{L_p}\right) + \cosh\left(\frac{W}{L_p}\right)} \right] \quad \text{Eq. 5.16}$$

The foregoing can be reduced to the following for a semi-infinite semiconductor:

$$J_o = \frac{q D_p p_{no}}{L_p} \equiv \frac{q D_p n_i^2}{L_p N_D} \quad \text{Eq. 5.17}$$

5.5.1 Photo-generated Current

The study derives the photo-generated current J_L under the assumptions that the thermal generation current can be neglected, and that the surface layer is much thinner than the absorption depth $1/\alpha$. The generation rate $G(x)$ is given as a function of the distance of x from the surface. Thus,

$$G(\lambda, x) = \alpha(\lambda) \cdot \Phi(\lambda) [1 - R(\lambda)] e^{-\alpha(\lambda)x} \quad \text{Eq. 5.18}$$

where $\Phi(\lambda)$ is the number of incident photons per cm^2 per second per unit bandwidth; $\alpha(\lambda)$ is the absorption coefficient of the semiconductor [81]; and $R(\lambda)$ is the fraction of the photons reflected from the illuminated surface. For $x > W$, the minority carrier density (holes) in the quasi-neutral region of the

semiconductor is determined by the following one-dimensional diffusion equation:

$$D_p \frac{d^2 p_n(x)}{dx^2} + \frac{p_n(x) - p_{no}(x)}{\tau_p} = G(x) \quad \text{Eq. 5.19}$$

where τ_p is the lifetime of minority carriers. The solution of Eq. 5.19 with boundary condition Eq. 5.14 results in the following:

$$J_L = \left[\frac{q\Phi(1-R)\alpha L_p}{\alpha^2 L_p^2 - 1} \right] e^{-\alpha w} \times \left[\alpha L_p - \frac{\left(\frac{S_p L_p}{D_p} \left[e^{-\alpha(H-w)} - \cosh\left(\frac{H-W}{L_p}\right) \right] + \alpha L_p e^{-\alpha(H-w)} - \sinh\left(\frac{H-W}{L_p}\right) \right)}{\left(\frac{S_p L_p}{D_p} \sinh\left(\frac{H-W}{L_p}\right) - \cosh\left(\frac{H-W}{L_p}\right) \right)} \right] \quad \text{Eq. 5.20}$$

with $L_p = \sqrt{D_p \tau_p}$. The collection efficiency is introduced by the following:

$$J_L = q\Phi(1-R)\eta_L \quad \text{Eq. 5.21}$$

The equation can be obtained from Eq. 5.20 as follows:

$$\eta_L = \frac{\alpha L_p}{(\alpha^2 L_p^2 - 1)} e^{-\alpha w} \times \left[\alpha L_p - \frac{\left(\frac{U_p L_p}{D_p} \left[\cosh\left(\frac{H-W}{L_p}\right) - e^{-\alpha(H-w)} \right] + \alpha L_p e^{-\alpha(H-w)} + \sinh\left(\frac{H-W}{L_p}\right) \right)}{\left(\frac{U_p L_p}{D_p} \sinh\left(\frac{H-W}{L_p}\right) + \cosh\left(\frac{H-W}{L_p}\right) \right)} \right] \quad \text{Eq. 5.22}$$

This equation introduces the correction factor for the collection efficiency as follows:

$$\eta_L = \frac{\alpha L_p}{\alpha L_p + 1} \times C.F.$$

where

$$C.F. = \frac{e^{-\alpha W}}{\alpha L_p - 1} \times \left[\alpha L_p - \frac{\left(\frac{U_p L_p}{D_p} \left[\cosh\left(\frac{H-W}{L_p}\right) - e^{-\alpha(H-W)} \right] + \alpha L_p e^{-\alpha(H-W)} + \sinh\left(\frac{H-W}{L_p}\right) \right)}{\left(\frac{U_p L_p}{D_p} \sinh\left(\frac{H-W}{L_p}\right) + \cosh\left(\frac{H-W}{L_p}\right) \right)} \right] \quad \text{Eq. 5.23}$$

If U_p is equal to zero, the correction factor can be simplified as follows:

$$C.F. = \frac{e^{-\alpha W}}{\alpha L_p - 1} \times \left[\alpha L_p - \frac{\tanh\left(\frac{H-W}{L_p}\right) - \frac{\alpha L_p e^{-\alpha(H-W)}}{\cosh\left(\frac{H-W}{L_p}\right)}}{\cosh\left(\frac{H-W}{L_p}\right)} \right] \quad \text{Eq. 5.24}$$

5.5.2 Surface Current Derivation

Upon illumination, the SRV may be measured as a function of surface potential. The changes in surface potential are directly proportional to the increase in excess carrier concentration on the surface. The relationship of effective SRV on the front surface S_{fs} of *n-type* and carrier concentration is given by the following [82, 83]:

$$S_{fs} = \frac{J_{os}}{q} \frac{N_D}{n_i^2} \quad \text{Eq. 5.25}$$

where J_{os} is the effective saturation current density; and N_D and n_i are the concentration of donor density ($1.12 \times 10^{12} \text{ cm}^{-3}$) and intrinsic carrier concentration in the semiconductor ($1.02 \times 10^{10} \text{ cm}^{-3}$), respectively.

Carrier loss on a surface because of surface recombination is described by S_{fs} , where the minority carrier current density is given by the following:

$$J_s = q S_{fs} (p_n - p_{no}) \quad \text{Eq. 5.26}$$

On the surface recombination current, J_s is equal to the interface surface current density because of the accumulation of charges trapped in the surface state/interface. Thus,

$$J_s = \text{const.}(p_s n_s - n_i^2) = J_{os} \left(\frac{p_s n_s}{n_i^2} - 1 \right) \quad \text{Eq. 5.27}$$

where p_s and n_s are the densities of holes and electrons near the surface, respectively. The electron and hole concentrations are related to the quasi-Fermi levels as follows:

$$n_s = N_C \left(e^{(E_{Fn} - E_C)/kT} \right) \quad \text{Eq. 5.28}$$

$$p_s = N_V \left(e^{(E_V - E_{Fp})/kT} \right) \quad \text{Eq. 5.29}$$

From the above equation, the $p_s n_s$ product is equal to n_i^2 at thermal equilibrium of the surface. When the sample is illuminated, the minority carrier densities on the surface and neutral regions are changed. The $p_s n_s$ product is no longer equal to n_i^2 , and is determined by the quasi-Fermi level splitting. Thus,

$$p_s n_s = N_V N_C \left(e^{(E_{Fn} - E_{Fp})/kT} \right) \quad \text{Eq. 5.30}$$

Given that the difference in quasi-Fermi levels is equal to V_{spv} , the surface current is proportionate to $(e^{qV_{spv}/kT} - 1)$. Using a similar approach of ideal current-voltage characteristics, the equation becomes the following:

$$p_s n_s - n_i^2 = n_i^2 \left(e^{qV_{spv}/kT} - 1 \right) \quad \text{Eq. 5.31}$$

Thus, J_s increases exponentially with the surface potential V_{spv} . Combining Eq. 5.27 and Eq. 5.31 results in the following:

$$J_s = J_{os} \left(e^{qV_{spv}/kT} - 1 \right) \quad \text{Eq. 5.32}$$

Utilizing the expression of balance between the three currents, the following equation is derived:

$$J_s = J_L - J_{dark} \quad \text{Eq. 5.33}$$

From **Eq. 5.12** and **Eq. 5.32**, the following equation is obtained:

$$J_{os}(e^{qV/kT} - 1) = J_L - J_o(e^{qV/kT} - 1) \quad \text{Eq. 5.34}$$

Rearrange the above equation yields the following:

$$J_L = (J_{os} + J_o)(e^{qV/kT} - 1) \quad \text{Eq. 5.35}$$

Substituting from **Eq. 5.21** results in following equations:

$$q\Phi = \frac{(J_{os} + J_o)}{(1-R)\eta_L} (e^{qV_{spv}/kT} - 1) \quad \text{Eq. 5.36}$$

$$C_L = \frac{(J_{os} + J_o)}{(1-R)\eta_L} \quad \text{Eq. 5.37}$$

where C_L is a gradient slope of the Fermi level between the exponent of V_{spv} and the photon flux intensity of the sample.

The C_L slope is very small but cannot be flat. **Eq. 5.37** represents the principal result of this chapter, and its general shape is shown in Figure 5.4. This equation will be applied in the analysis of the surface recombination of the fabricated samples described in **Section 8.3.4**.

Eq. 5.36 can be rearranged to determine V_{spv} ,

$$V_{spv} = \frac{kT}{q} \ln \left(\left(\frac{q\Phi(1-R)\eta_L}{J_{os} + J_o} \right) + 1 \right) \quad \text{Eq. 5.38}$$

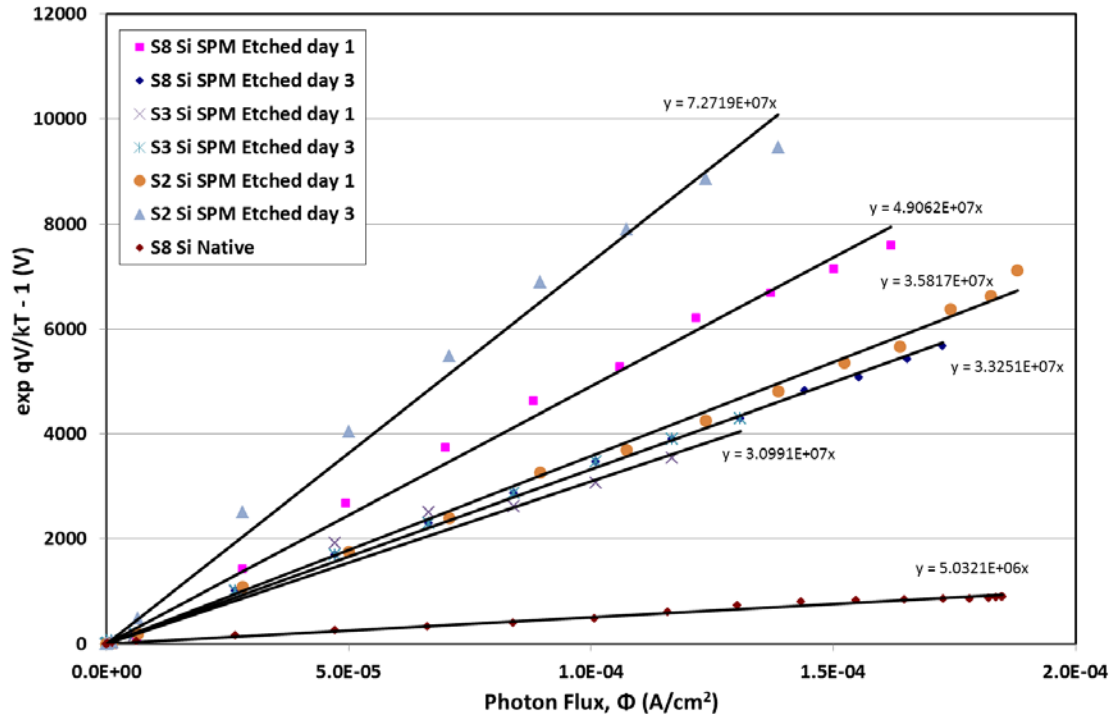


Figure 5.4 Typical graph of $(\exp qV/kT - 1)$ vs. photon flux, Φ – a linear slope represents C_L in Eq. 5.37 that used to estimate the SRV.

5.6 Chapter Summary

A current voltage characteristic applied to the KP method can be used to determine the electrical properties of the near-surface region of the semiconductor, as proven by Okumura *et al.* [66, 67], Watanabe *et al.* [68], and Nakamura *et al.* [69]. However, this equation was not used to estimate the SRV value of the samples.

In this study, surface current derivation via the KP method was presented based on the formulation of the reverse direction currents J_L and J_{dark} on the bulk of the semiconductors. The surface current was derived with the effect of the surface state by introducing the surface recombination current J_s into the equation. Charge accumulation in the depletion region can be interpreted as band bending that measures the SPV using the KP method. The determination of effective saturation current density J_{os} from the C_L slope made estimating the

accumulation of charge trapped in the surface state/interface of the sample possible. Indirectly, the J_{os} value is useful to evaluate the effective S_{fs} of a silicon surface. Surface current derivation through the KP method using SPV measurement is a novel approach in the way of quantitative analysis. It is also useful to determine SRV values for native and treated semiconductor samples. SPV determination also provides valuable information about surface characteristics and modifications, such as by depositing monolayers on the surface.

Chapter 6 Surface Passivation of Alkyl Monolayers on Silicon

6.1 Introduction

The surface has an important function in thin silicon solar cells, where the diffusion lengths of the minority charge carriers can substantially exceed the thickness of the device. The surface and interface electronic properties of silicon are important for the efficiency of the device. To a large extent, these properties are defined by the density and nature of the surface and interface states resulting from unsaturated dangling bonds [5]. These surface states created by the dangling bonds act as recombination centres for electrons and holes that may influence the surface properties.

Two passivation experiments were performed, namely, hydrogen termination and organic monolayer passivation on a silicon surface. At the initial stage, the surface is passivated to form a monolayer by removing the oxide layer. This treatment provides all surface atoms with a nearly ideal coordination and saturates all surface bonds. Hydrogen-terminated (H-terminated) surfaces of silicon are a common form of passivation at low temperatures and provide very low densities of mid-gap surface electronic states by treating the surface with NH_4F and HF solutions [84]. This study fabricated thin passivation layers that are a few monolayers thick using wet chemistry to prepare H-terminated silicon interfaces. The saturation of free bonds by hydrogen eliminates surface states, giving rise to excellent electronic properties. The interface properties of the passivated layers are characterized by the non-destructive and surface-sensitive method of spectroscopic ellipsometry to assess the effectiveness of the preparation methods.

The aim of this experiment is to investigate the effect of alkene monolayer formation as interface bonding for the platform environment of nanostructure molecular deposition. The formation of high alkene monolayers is important as they are bound to the substrate via covalent Si-C bonds and are capable of eliminating additional oxide components on the surface. The surrounding effects of air oxidation toward surface treatment are extremely challenging.

The 1-decene monolayer in the Lewis acid catalyst is used to preserve the interface layer for the long term in the air and to overcome this problem. This study considers the stability study on surface modification as significant alongside the formation of high-quality alkene monolayers on the silicon surface.

6.2 Preparation and Treatment for Surface Passivation

The surface has a major function in thin-film Si solar cells because the diffusion lengths of the minority charge carriers can substantially exceed the thickness of the device. In particular, surface states and interface defects are important to the efficiency of a device. The surface and interface electronic properties of silicon are mainly defined by the density and nature of the surface and interface states resulting from non-saturated (dangling) bonds [85]. The interface layer also has a major function in device operation, where the energy conversion efficiency can be severely decreased because of large interface recombination losses. This study monitors and controls interface properties after pre-cleaning treatments by minimizing the preparation of defect- and contamination-free solar cell structures.

Cleaning the silicon surface is required before any attachment of covalent monolayers to semiconductor surfaces. Cleaning processes have a major role in device performance, product yield, and reliability because the electronic properties of silicon interfaces are strongly influenced by the chemical integrity and morphological structure of the surface prior to heterostructure preparation. Cleaning steps are applied repeatedly within the semiconductor process flow and occupy 30% to 40% of all the process steps. In the manufacturing line of semiconductor devices, the surfaces of silicon wafers are influenced by contact with various chemical solutions, water, gases, and surrounding environment, such as clean room atmosphere and equipment.

Passivation is the process of making a surface layer chemically reactive in relation to another material to generate a passivated interface layer. Passivation can also be used to cover a surface layer, thus preventing the

dissolution of the underlying material. Passivation compounds must block the diffusion of charges, atoms, and ions into the material. As alternative methods are cheaper and require low-temperature passivation, wet chemical silicon passivation methods have been developed and optimized to provide silicon interfaces with excellent electronic properties [86]. Ultra-thin silicon oxide tunnel layers or covalently bound organic passivation layers employing long chain alkenes molecules can be prepared through wet chemical oxidation methods with different thicknesses and interface charges [87]. The advantage of these methods is that they can be performed under room temperature conditions.

The main significance of this study is the preparation of highly stable, organic monolayers by attaching covalent alkene molecules onto H-terminated silicon surfaces. The mechanism of an organic monolayer passivation on the silicon surface is shown in Figure 6.1. A clean silicon surface with native oxide is passivated in a diluted NH_4F and HF solution to obtain an H-terminated silicon surface. Next, an organic monolayer is created on the surface by a reaction with an organic solution at a temperature range of 100 °C to 120 °C.

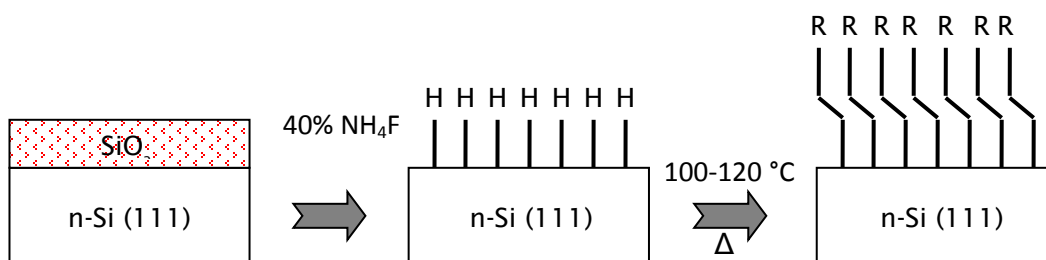


Figure 6.1 Schematic of alkene monolayer passivation process.

6.2.1 Silicon Oxide Terminated Surfaces

A thin layer of SiO_2 can be grown on silicon surface through a cleaning process formed by a combination of acidic and mixed basic solution. The famous

standard Radio Corporation of America (RCA) cleaning process was developed by Werner Kern in 1965 at RCA laboratories; this experiment resulted in a procedure for removing organic residue and films from silicon wafers [88]. The cleaning techniques consist of RCA-I, RCA-II, and sulphuric acid-hydrogen peroxide mixture (SPM).

RCA-I is a solution mixture of $\text{NH}_4\text{OH}:\text{H}_2\text{O}_2:\text{H}_2\text{O}$ with a ratio of 1:1:5 and heated at 75 °C to 80 °C for 10 min. In a 1:1:6 ratio, a solution of $\text{HCl}:\text{H}_2\text{O}_2:\text{H}_2\text{O}$ for RCA-II was also heated at 75 °C to 80 °C for 10 min [89]. The temperature control in this range is necessary to minimize excessive thermal decomposition of H_2O_2 . The solution compositions are based on ultra-filtered deionized (DI) water, electronic-grade NH_4OH (29 wt. %), electronic-grade HCl (37 wt. %), and high-purity unstabilized H_2O_2 (30%).

SPM etching consists of immersion in $\text{H}_2\text{SO}_4:\text{H}_2\text{O}_2$ (1:1) (noted as SPM1:1) for 10 min, as described by Chabal [90]. This cleaning process leaves about 0.6 nm to 1.5 nm of hydroxylated oxide on the silicon surface that prevents the recontamination of the surface. At this stage, the surface is hydrophilic and easily wetted by an aqueous solution. The selection of SPM solution is the best practice for the intermediate process in silicon wafer cleaning. The exposure of the silicon surface to inorganic bases or acids is able to modify the silicon surface potential that results principally in chemisorption of OH^- and H^+ ions [91, 92].

In principle, the SPM solution works to remove organic contamination that involves two distinct processes: i) removal of hydrogen and oxygen as units of water by the concentrated sulphuric acid, and ii) enhancement of sulphuric acid of the conversion of hydrogen peroxide from mild oxidizing agent into rigorous reaction. Mixing both solutions is an exothermic reaction that cleans organic compounds off the substrate and oxide on the silicon surface. The surface potential modification of the samples usually takes place within the first 10 seconds to 20 seconds of chemical exposure before reaching the steady states of the chemical solutions [93]. Later, the etched sample was washed with deionized water, resulting in the surface chemistry of the sample being etched with $-\text{OH}$ termination group to form silanol groups ($\equiv \text{Si} - \text{OH}$).

The formation of a hydrophilic surface through the RCA standard cleaning process is mainly based on H_2O_2 , which contains solutions that increase the micro-roughness of the silicon interface as a side effect of H_2O_2 decomposition [27]. Angermann *et al.* [27, 86, 94] combined both methods in a series of experiments to perform a cleaning treatment before the hydrogen termination process. In summary, the four different methods of cleaning process are as follows: (i) boiling of $H_2SO_4:H_2O_2$ (1:1) solution for 10 min; (ii) boiling of RCA-I solution at 80 °C for 10 min; (iii) boiling of RCA II solution at 80 °C for 10 min; and (iv) boiling of deionized water at 80 °C for 120 min.

6.2.2 Hydrogen Terminated Surfaces

In general, H-termination on silicon surface has four main characteristics [95]:

- i. It is complete after an immersion time of 1 min.
- ii. It is formed by chemical adsorption that yields a covalent bond.
- iii. Each surface silicon atom can be terminated by one hydrogen atom (Si-H) on Si (111) and two hydrogen atoms (SiH_2) on Si (100) (Figure 6.2).
- iv. It results in surface passivation.

In the case of Si (111), an atomically flat surface is formed with terraces on the scale of $\sim 10^2$ nm² by $\sim 10^4$ nm², but the H-terminated Si (100) surface is not atomically flat [96]. However, the degree of termination and type of hydrides depend on the surface condition, solution composition, and preparation procedure. The silicon surface is predominantly terminated by hydrogen in HF solutions. Si (111) surface tends to be terminated by Si-H or $Si-H_3$ because of the difference in the number of dangling bonds between the two surfaces. The H-terminated areas on silicon are hydrophobic surfaces that are not wetted by water or aqueous solution. SiO_2 dissolves by forming highly stable complex fluorosilicates according to the following:



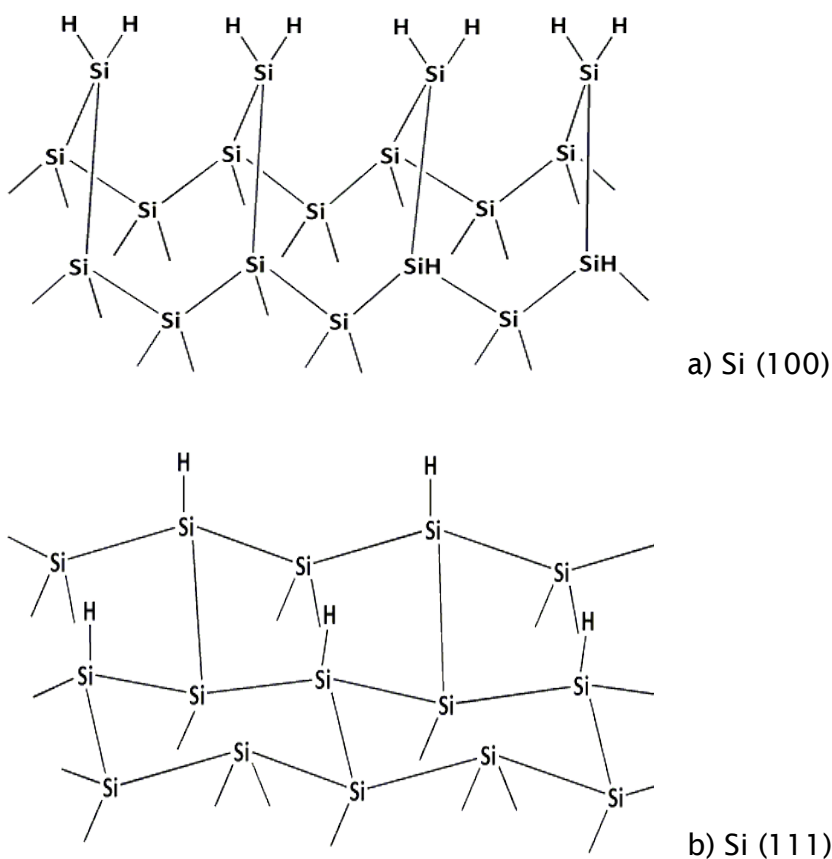
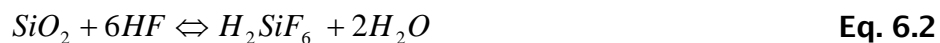


Figure 6.2 Schematic of the hydrogen terminated Si (100) and Si (111) surface [85].

Mixtures of HF and NH_4F solutions are also commonly used to prepare buffered solutions for the passivation of silicon and its oxides. Buffering results in a more stable etch rate and prevents loss of photo-resistant polymer films that cannot withstand strongly acidic un-buffered HF solutions [97]. According to Chabal *et al.* [90], Si-O bonds of the oxide layer are then removed preferentially in the existence of HF, which forms the hydrogen-terminated Si (111) on the surface. The effect of pH can be attributed to the dependence of the concentrations of HF, F^- , and HF_2^- species on pH. However, increasing the pH concentration results in more reactivity and a rapid attack of the atoms on the (111) plane, yielding a large scale of roughness. The most stable region for SiF_6^{2-} in HF is confined between pH 2 to pH 3.75 to control roughness, where two different boundaries occur. Thus,



Fluorine may exist in different forms depending on the composition of the solution. In aqueous solutions of concentrations up to that of fluorine, at least 1 M fluoride is required to have significant fluorine species of F^- , HF, and HF_2^- . In moderately high concentrations, HF has a tendency to polymerize. However, the addition of NH_4F increases the pH to 3 to 4, maintains the concentration F^- , stabilizes the etching rate, and produces the highly reactive HF_2^- . A combination of NH_4F (40 wt. %) and HF (49 wt. %) at a volume ratio of 7:1 results in pH of up to 4.5 and appears to contain only F^- and HF_2^- , with very little free HF acid [97].

6.2.3 Organic Monolayer Passivation

The formation of organic monolayers on the silicon surface can be considered as a new insulating material apart from the SiO_2 insulator in the semiconductor usage. Nevertheless, the research on the covalently bound organic monolayer has expanded significantly; these studies were conducted for many applications, i.e., alternative gate insulators [98]; biosensor applications on field-effect transistors (FETs) [99]; and attachment of bioactive materials such as DNA fragments [100, 101].

The formation of alkyl chains on the silicon surface may create a hydrophobic environment because of the strong covalent Si-C bond. This environment is not readily penetrated by water and oxygen molecules. Unfortunately, the stability of the monolayer could not last long term. One reason may be related to the passivation quality, where remaining Si-H sites (45% – 50%) [102-104] create small oxide patches after the completion of an alkyl monolayer. Generally, the organic monolayers of Si-C bonds can be prepared by various methods, including high temperatures, UV irradiation, electrochemical treatment, hydrosilylation catalysis and chemo-mechanical scribing [85]. The reactions of Si-H bonds on the surface with organic molecules that have terminal unsaturated bonds are called hydrosilylation or catalytic hydrosilylation. Many kinds of organic compounds (e.g., acids or esters,

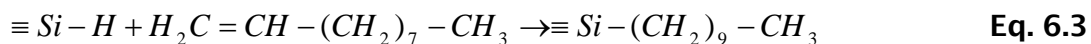
amines, alcohols, and aromatic rings groups [105]) with various functions and applications can be introduced onto the silicon surface by the hydrosilylation of an H-terminated surface.

Passivation technique with organic monolayers is stable in hot solvents, acids, and bases [106]. Organic monolayers on silicon can be thermally resistant and stable up to 615 K under vacuum. Specifically, the Si-C bond is thermodynamically and kinetically stable because of the high bond strength and low polarity of the bond [91]. The attachment of the organic monolayer of the Si-C bond on the silicon surface consists of the following:

- i. Preliminary cleaning of the surface and removal of the native oxide.
- ii. Passivation of the surface with hydrogen.
- iii. Substitution of hydrogen by the alkenes or alkynes molecule, either stimulated by illumination in the UV range or by heating at the temperatures of 100–180 °C [91]

In the alkene monolayer compounds of $(CH_2=CH-(CH_2)_{n-3}CH_3$ with $10 < n < 22$), the most promising organic monolayer formation on H-terminated Si (111) is 1-octadecene ($n = 18$), employing a UV illumination method and producing a monolayer thickness of 0.2 nm to 0.4 nm [19]. These organic monolayers deposited on the Si surface show electrical properties that mainly depend on the passivation method (either hydrogen or iodine passivation) and on the intensity of illumination [107]. They display lower electrical performance on high doping of the substrate [108].

In this study, the same approach of using alkene monolayers to form covalently bonded alkyl chains on the silicon surface is employed to create a surface environment for the development of new solar cell concepts, such as LH structures in the form of LB films [109]. Therefore, this study investigates the chemical properties and stability purposes by using 1-decene ($n = 10$). The experiment used mild thermal hydrosilylation of 1-alkenes in the presence of $C_2H_5AlCl_2$ as Lewis acid catalyst. The overall reaction can be written as follows:



AlCl_3 is an effective catalyst for the hydrosilylation of alkene monolayers. Given that $\text{C}_2\text{H}_5\text{AlCl}_2$ is soluble in non-polar solvents, the presence of a Lewis acid catalyst avoids multiphase reactions on the porous silicon surface [110]. Although the sample is impermeable, the stability for long-term passivation over oxidation as proved by Gorostiza *et al.* [111] is the main focus of this study.

i. Literature Review on Decene and Alkene Groups Monolayer

Organic monolayers are directly anchored onto silicon substrates via thermal reactions in a liquid phase that show strong covalent bonding and stability purposes. Kinser *et al.* [112] performed a stability study on alkyl monolayer with 1-decene and 10-bromodecene on Si (111). The samples were heated to induce free radical formation because of the high volatility of the solutions. The samples were monitored for 21 days by X-ray reflectivity measurements, during which the 1-decene sample showed no significant increases in surface roughness compared with others.

The doubly distilled methyl 10-undecenoate in vacuum was proposed by Sieval *et al.* [113]. Si (100) wafers with a guaranteed bulk lifetime of $\tau_b > 1000 \mu\text{s}$ were passivated with 1-alkene solutions, resulting in $\tau_{eff} = 132 \mu\text{s}$ maximum lifetime of the minority carrier. The effective lifetime was improved by more than 50% with double distillation, in which a small amount of impurities in the organic reagent could adsorb onto the silicon surface. Some defects still remain on the surface, and act as sites for charge carrier recombination, although the surface is a well-passivated, densely packed monolayer of 1-alkene.

The influence of silicon surface modification through $\text{Si}-\text{C}_n\text{H}_{2n+1}$ ($n = 10, 12, 16, 22$) monolayer on *p-type* (100) and *n-type* (100) was studied by Faber *et al.* [98]. The formation of covalently bound organic monolayers as an alternative insulator of SiO_2 is one of the main focuses of this study. It has a similar thickness as the current state of the art gate oxides, has good electrical properties, and can work as an MIS diode. The behaviour of different chain

alkyl monolayers serves as a better insulator compared with that of the SiO₂ sample. From the current–voltage measurement, the order of the current density J magnitude for the different monolayers on *n-type* silicon is $C_{10} > C_{22} > C_{16} > C_{12}$. Although Si-C₁₀ is the lowest order of J magnitude, the thickness of monolayer C₁₀ (1.21 nm) is better than that of the SiO₂ samples. Similar studies by Ishizaki *et al.* [114] on different alkyl molecular chain lengths ($n = 10, 12, 14, 16, 18$) directly attached to silicon were performed at 160 °C. The formation of alkyl monolayers on C10 (1-decene) was a less dense packing structure because the value was less than 110° by water contact angle measurement. A measurement by grazing incidence X-ray diffraction also revealed that the amorphous structure of the alkyl monolayers directly attached to the Si formed despite their alkyl chain length.

Gorostiza *et al.* [111] investigated the neat 1-alkenes on Si (111)-H surfaces for the conditions of long-term passivation of the interface silicon. The formation of an alkyl layer interface was examined through XPS data and capacitance–voltage plots that have lower density electronic traps ($< 10^{10}$ traps/cm²). These plots demonstrate and control the chemical state of the interface and the molecular density of the organic monolayer. Based on AFM imaging, 1-decene and the Lewis acid catalyst of ethylaluminumdichloride (C₂H₅AlCl₂) on a modified silicon surface (Si-C₁₀) have the same staircase structures as the Si-H surface (either passivated by NH₄F or HF solutions). Considering that the Si-H-terminated surface depends on aging time, the result shows a similar structure for several weeks in the air for the alkyl monolayer sample.

ii. Chemical Bonding of 1-Decene on the Silicon Surface

The configuration of bond length and angles in the van der Waals interaction is considered in the structural molecular of a silicon surface with decene chain as illustrated in Figure 6.3. The configuration of alkyl chain (C₁₀, $n = 10$) with tilt angle of $\theta = 35.5^\circ$ and the projection d_{chain} of its length on the normal surface is given by

$$d_{chain} (nm) = 0.189 + \left(\frac{n}{2} - 1 \right) 0.254 \cos \theta + 0.156 \sin 19^\circ + 0.11 \quad \text{Eq. 6.4}$$

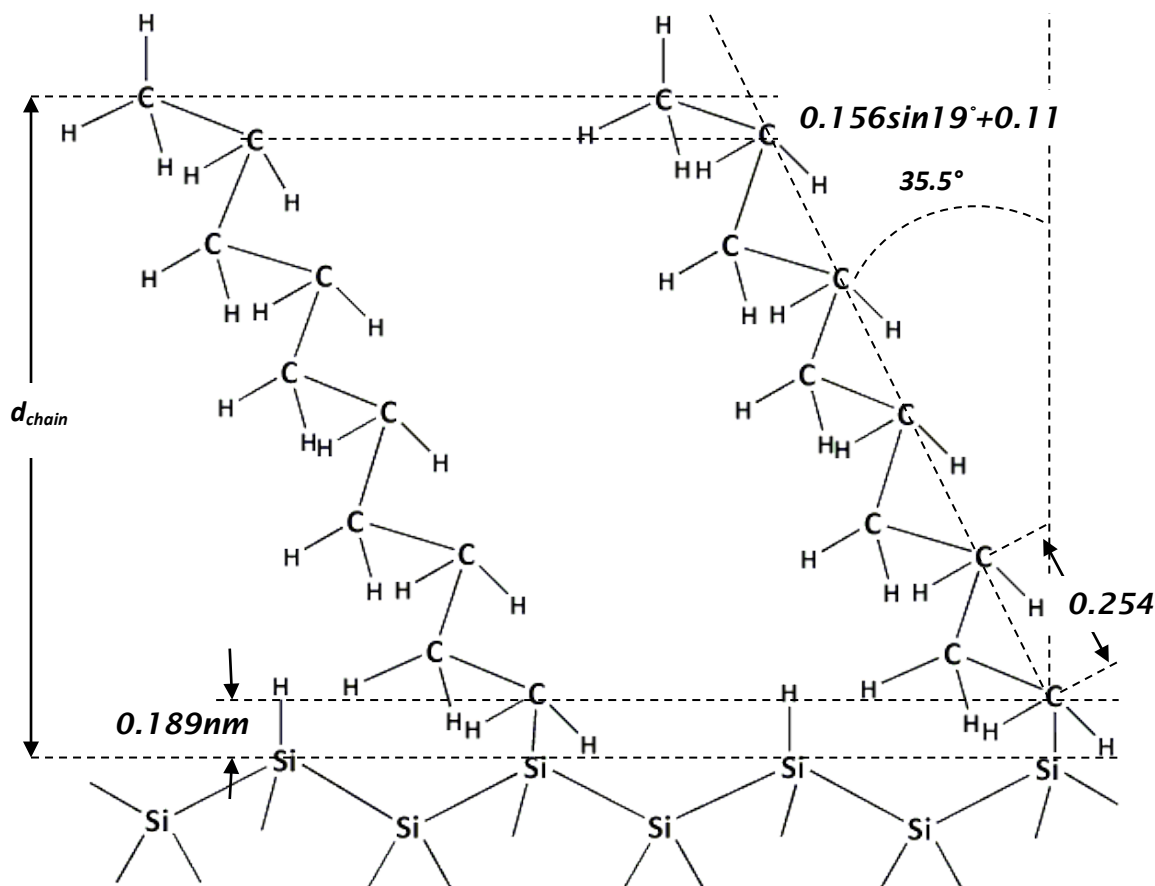


Figure 6.3 Structural molecular of a silicon cluster with decene chain. The tilt angle is 35.5° from the surface normal and d_{chain} is the chain length projected on the surface normal [111].

6.3 Methodology

Wet-chemical silicon passivation methods can be classified into two groups according to the underlying chemical mechanisms: (i) surface coverage by hydrogen (H) termination [94] and (ii) by thin chemical oxide layers prepared under carefully optimized conditions. The two different wet-chemical methods for the preparation of organic monolayer to form covalent Si-C bond are as follows: (i) alkylation of halogen-terminated silicon surfaces with organometallic substances (e.g., organo-magnesium, organo-lithium, and Grignard reagents) [91] and (ii) reaction between a hydrogen-terminated silicon surface and 1-alkene compounds [31]. Hydrogen is commonly introduced into Si solar

cells to decrease the deleterious effects of defects and increase the minority carrier lifetime. Nonetheless, the methods through which hydrogen is introduced during processing and its subsequent interactions with defects remain poorly understood. The goal of this experiment is to increase understanding of hydrogenation processes and passivation mechanisms for crystalline-Si PVs at a microscopic level.

6.3.1 Experimental Procedure of Hydrogen Terminated Surface

H-terminated silicon surfaces were prepared following a procedure reported by Angermann *et al.* [86]. The silicon sample strips were chemically re-oxidized. The oxide was stripped off with NH_4F solution (40%) and HF (1% in water) to prepare for H termination on the surface. The hydrogen termination experiment was performed as follows:

1. The sample was cleaned using RCA and SPM1:1 cleaning solutions.
2. Approximately 80 ml DI water was prepared and heated to 80 °C. The sample was placed in water for 10 min, and then rinsed in overflowing DI water for 10 min.
3. After rinsing in DI water, the Si (111) and Si (100) samples were immersed in NH_4F solution (40%) for 6.5 and 4 min, respectively. Nitrogen was bubbled through the solution to minimize any dissolved oxygen.
4. Finally, the sample was constantly immersed in HF solution (1%). Nitrogen was bubbled through the solution to minimize any dissolved oxygen. The samples were dried under dried nitrogen flow and used immediately for measurements.

6.3.2 Experimental Procedure of 1-Decene on the Silicon Surface

Samples of double-sided, *n-type* crystalline silicon wafers with (111) orientations and 525 μm thickness were used for all experiments. The resistivity of the wafers was in the range of 20 $\Omega\text{-cm}$ to 50 $\Omega\text{-cm}$, and each sample was cut into 1.0 cm^2 . In this study, the alkyl monolayer was experimented on utilizing a mild thermal hydrosilylation of 1-alkenes, in addition to the Lewis acid catalyst of ethylaluminum dichloride ($\text{C}_2\text{H}_5\text{AlCl}_2$). 1-decene solution was purchased from Sigma-Aldrich and later distilled twice under decreased pressure prior to use. The procedures of the experiment are as follows:

1. Approximately 10 ml acetone and isopropyl alcohol were prepared. The sample was degreased for about 15 min.
2. A reactive solution of 30 ml each for H_2SO_4 and H_2O_2 (ratio 3:1) (denoted as SPM3:1) were prepared and mixed. The solution reacted immediately, and the sample was placed in the solution for 20 min.
3. The NH_4F solution was purified by bubbling nitrogen through it at room temperature for 30 min. The sample was immersed in NH_4F solution (40%) for 15 min with continuous bubbling of nitrogen.
4. Given that the Lewis acid catalyst has high flammable risks with the existence of oxygen, the best solution for this experiment was to use a glove box. Alkyl monolayer passivation was performed in a glove box purchased from Saffron Scientific Equipment, Ltd. The doubly distilled 1-decene and Lewis acid catalyst mixed well in the round flask vessel at a ratio of 10:1.
5. The freshly prepared Si-H sample was dried under N_2 , and the flask was closed tightly. The reaction was performed at 110 $^\circ\text{C}$ and heated under pressure in the sealed flask. The reaction was left overnight and ran for about 20 h.

6. At the end of the passivation, the flask was cooled and the alkyl sample was removed from the glove box.
7. The sample was immediately rinsed with 1,1,1-trifluoroacetone (TFA) to neutralize the residual $C_2H_5AlCl_2$. The sample was then washed with methanol and cleaned ultrasonically with hexane.

6.3.3 Characterization Procedure

This section describes the relevant characteristics of any experiment executed that serves as a quantitative measure and indicator of the sample performance. The processes were ellipsometry, FTIR, contact angle measurement, and XPS.

i. Ellipsometry

Ellipsometry is the measurement of the polarization state of a polarized vector wave [115]. It is an optical instrument that can be used to study thin films by monitoring the reflection of polarized light. Ellipsometry measurements are used to measure the thickness and other properties of thin layers of dielectrics and semiconductors. It is also preferable for measuring very thin layers, especially for monolayer coverage of several tens of atoms deep.

Monochromatic light is supplied by a laser where the light beam passes through a polarizer to produce polarized light. In ellipsometry, *p*- and *s*-polarized light waves are irradiated onto a sample, and the changes in the polarization state are controlled by light reflection or transmission. The analyser can be used to determine the state of polarized light by locating the null point. The compensator is usually held at a fixed angle. A quarter-wave plate is used to convert linearly polarized light to elliptically polarized light. The component of the wave aligned to the fast axis passes through the faster plate than the wave aligned with the slow axis, resulting in the wave becoming out of phase with a phase shift between 0° and 360° .

Ellipsometry measures the two values of ψ and Δ that express the amplitude ratio and phase difference between p- and s-polarizations, respectively. When a sample structure is simple, the amplitude ratio ψ is characterized by the refractive index n , whereas Δ represents light absorption in the sample [116]. The silicon sample placed on the sample stage and values of Δ (change in phase difference that occurs upon reflection, 0° to 360°) and ρ_{ψ} (angle ψ of the tangent ratio of the total reflection coefficient magnitudes, $\psi = 0^\circ$ - 90°) were measured along the length of the sample, including a length of uncoated silicon. Thus, the instrument determines the state of the polarization. A detector measures the light intensity and passes this data to a computer for analysis. Finally, these values are inputted to a computer program to calculate the thickness of the sample layers over the length of the sample.

Ellipsometry is also a powerful technique to measure the optical constants of materials. However, it is very sensitive to surface roughness, naturally formed oxide layers, contamination, and surface damage [117]. The effects of surface roughness on ellipsometric parameters can be considered as a single layer or as multiple thin layers that characterize the anisotropic behaviour at different depths below the surfaces [118]. The effective thickness is determined by selecting an appropriate model where the roughness data fit with the theoretical framework.

The chemical stability of the samples was investigated when exposed to air (normal laboratory conditions), and ellipsometric spectroscopy was used to monitor oxide growth. A variable angle, spectroscopic phase-modulated ellipsometer (UVISEL, HORIBA Jobin Yvon) was used to record all ellipsometric measurements. The ellipsometric angles (Ψ , Δ) were collected over the spectral range of 260 nm to 800 nm at an angle of incidence of 70° . The measured angles (Ψ , Δ) were transformed into complex pseudo-dielectric functions (ϵ). Using appropriate models, the native oxide thickness and the surface condition were calculated. The model for the surface condition of the H-terminated surface was obtained with a two-layer model consisting of a bulk c-Si and a Bruggeman EMA layer with 50% c-Si and 50% air. The surface condition (micro-roughness) was given by the thickness values (d_m). Native oxide wafers were modelled after a bulk c-Si with a SiO_2 layer on top.

ii. Fourier Transform Infra-red Spectroscopy (FTIR)

IR spectroscopy is a measurement of IR radiation where the sample is subjected through the mechanisms of absorption, emission, or reflection. When IR electromagnetic radiation is absorbed, it increases the energy of the molecule and is only energetic enough to cause changes in the vibrational and rotational energy of molecules [119]. For a molecule to absorb IR, the vibrations or rotations within a molecule must cause a net change in the dipole moment of the molecule, where the energy of the radiation must be equal to the difference between allowed energy transitions of the molecules. The frequency at which a molecule absorbs IR radiation is determined by the types of atoms composing the molecule, the types of bonds forming the molecule, the location of the bonds and atoms in the molecule, and their interaction within the molecule. If the frequency of the radiation matches the vibrational frequency of the molecule, then radiation will be absorbed that causes a change in the amplitude of molecular vibration. The interaction of all the vibrations of the molecule can determine the energy of a vibration. Most of the interaction may be extremely weak, and definite vibrational modes can be strongly coupled. Vibrational coupling can cause the frequency of an absorption band from the same type of chemical bond and atoms in one molecule to be shifted to a higher or lower frequency. The exact position of an absorption band is determined by the combination of the different types of possible vibrational modes, overtones, difference bands, combination bands, and coupling.

FTIR spectroscopy is an extremely powerful technique to identify the molecular composition of many organic and inorganic materials. When a sample is analysed by IR spectroscopy, the equipment produces a spectrum range of 4000 cm^{-1} to 650 cm^{-1} . The sample of 1-decene monolayers was characterized by a variable angle reflection accessory of PIKE Technology VEEMAX II, which was fitted to a Tensor 27 spectrometer (Bruker Instruments). The sample was placed on a glass plate where the angle of incidence was set at 37° and S-polarization. This FTIR had a variety of crystal plates with a mercury-cadmium telluride (MCT) detector and selective control of the penetration depth of the IR beam in the samples. A total of 500 scans were taken, with the background scans of native oxide sample subtracted from each spectrum.

iii. Contact Angle Measurement

The contact angle measurement can be performed by employing droplet shape analysis to determine the surface energy of the solid materials. Contact angles are measured by fitting a mathematical expression to the shape of the drop. The slope of the tangent to the droplet shape is then calculated on the liquid–solid–vapour interface line. The contact angle Θ is a quantitative measurement of the wetting of a solid by a liquid (Figure 6.4). This figure shows that the low tangent value Θ is less than 90° , resulting in better wettability, adhesiveness, and cleanliness of a solid surface. When the solid surface consists of organic monolayer materials, water droplets form a larger contact angle where a high tangent value Θ is more than 90° . These solid surfaces with organic monolayers have low surface energy, worse wettability, and inferior adhesiveness. For a tangent value equal to 90° , the surface free energy is equivalent to the equilibrium contact angle where the solid–liquid and the solid–vapour interfacial tensions are equal.

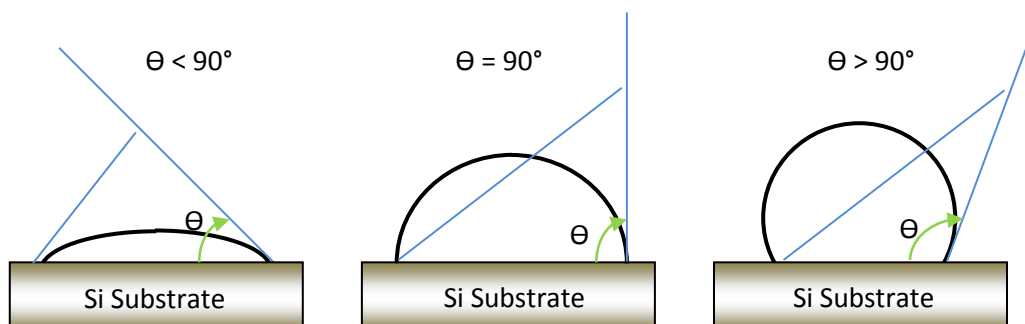


Figure 6.4 Measuring of water contact angle, Θ on the solid surface e.g. silicon substrate.

The static water contact angles were measured with a Kruss DSA 100 using a computer-controlled contact angle calculation program supplied by the manufacturer. The measurements were performed with water droplets of a fixed size of approximately $1.0 \mu\text{L}$ in volume. They represented an average of at least five points at room temperature under ambient humidity. The drop was produced before the measurement, and exhibited a constant volume during

the measurement. The contact angle data were taken on an average of three time measurements at different positions of the silicon surface.

iv. X-ray Photoelectron Spectroscopy (XPS)

The sample was characterized and analysed by Midlands Surface Analysis at Aston University, UK. The XPS spectra were recorded by Thermo Fisher ESCALAB 250 with a monochromatic Al X-ray source, which allowed an energy resolution of 0.45 eV FWHM. This setup made the identification of chemical states much more precise. The spatial resolution was 15 microns in spectroscopy mode and 3 microns in chemical imaging mode. It also had an Al/Mg dual anode X-ray source that allowed analysis areas of up to 8 mm in diameter. The base pressure in the instrument was $< 3 \times 10^{-10}$ mbar. Spectra were fitted with Gaussian profiles using standard procedures. The positions of all peaks were normalized to C1s at 285.0 eV.

6.4 Result and Discussion

6.4.1 Characterization of 1-Decene Monolayer Samples

Characterization of the alkene monolayer surface was performed by employing a variable angle reflection accessory of PIKE Technology VEEMAX II fitted to a Tensor 27 spectrometer (Bruker Instruments) (Figure 6.5). The figure displays the presence of alkyl groups taken after 24 h of exposure to air. The bottom slope of the graph indicates the C-H stretching region of the IR spectra that consist of symmetric and anti-symmetric CH_2 and anti-symmetric CH_3 stretch vibrations. The IR spectra of the measured peaks are in good agreement to those in the literature. The peaks observed are 2854 cm^{-1} to 2858 cm^{-1} [120] for symmetric CH_2 mode, 2917 cm^{-1} to 2923 cm^{-1} [121] for asymmetric CH_2 modes, and 2963 cm^{-1} to 2967 cm^{-1} [120] for asymmetric CH_3 modes of alkyl organic monolayers.

Three different IR spectra were placed in the glove box with different experimental temperature setups. The aim of this experiment is to form an

interface layer that consists of hydrophobic molecular bonding and longer surface stability in open air. The usage of a Lewis acid catalyst for the alkene monolayer has proven its surface stability against oxidation in open air [111, 122]. Similar to that approach, the same catalyst for alkene monolayer was heated at two different temperatures (90 and 110 °C) and left overnight. The Bruker FTIR recorded three broad peaks of the C-H stretching region, where the peak areas were approximately 0.136 unit² (90 °C) and 0.217 unit² (110 °C). Meanwhile, the experiment without catalyst for hydrosilylation of double-distilled 1-decene heated to 160 °C for the same period of time produced approximately 0.248 unit². Although the peak area of 1-decene without catalyst was higher than that of the catalysed sample, the grafted silicon samples still protected the surface properties from oxidation in open air [111, 122].

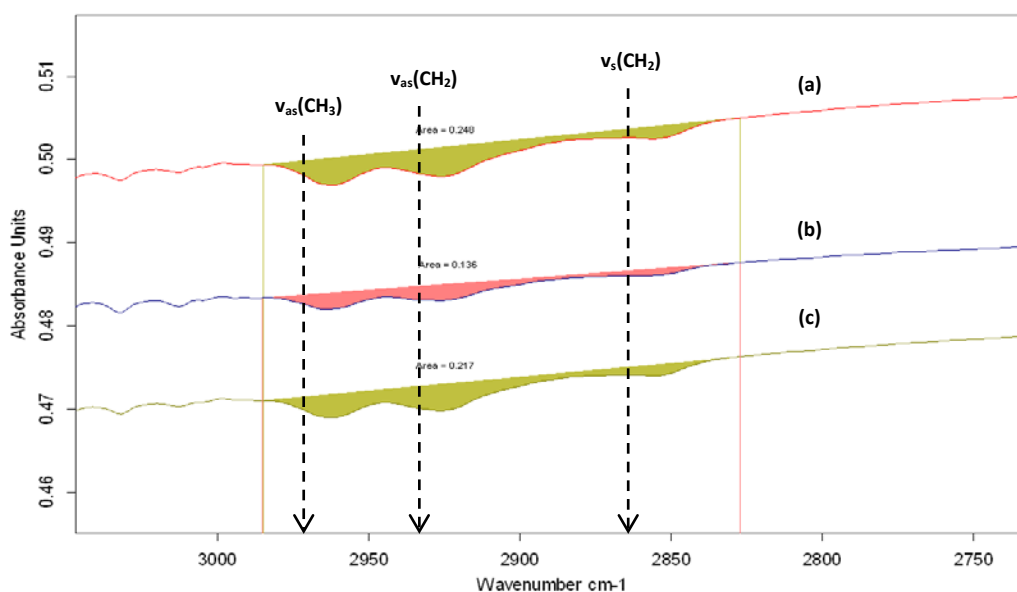


Figure 6.5 FTIR spectra of 1-decene (double distilled) monolayer directly attached to Si surface (a) hydrosilylation at 160 °C, $\tau = 12 \mu\text{s}$; (b) hydrosilylation with Lewis acid catalyst at 90 °C, $\tau = 10 \mu\text{s}$; and (c) hydrosilylation with Lewis acid catalyst at 110 °C, $\tau = 11 \mu\text{s}$.

The X-ray photoelectron survey spectrum of this surface (**Figure 6.6**) shows the binding energy of the 1-decene monolayer on the Si (111) sample. It has a significant peak in the Si, C, and O signals, which is in good agreement with

previous studies of Boukherroub *et al.* [34]. The alkyl chains of 1-decene yield a clear C 1s signal that is higher than the oxygen signal but smaller and closer to the Si signal. A small amount of fluorine was observed after exposure to NH_4F and HF. A small amount of chloride in the sample was also observed because of the residual $\text{C}_2\text{H}_5\text{AlCl}_2$ on the surface.

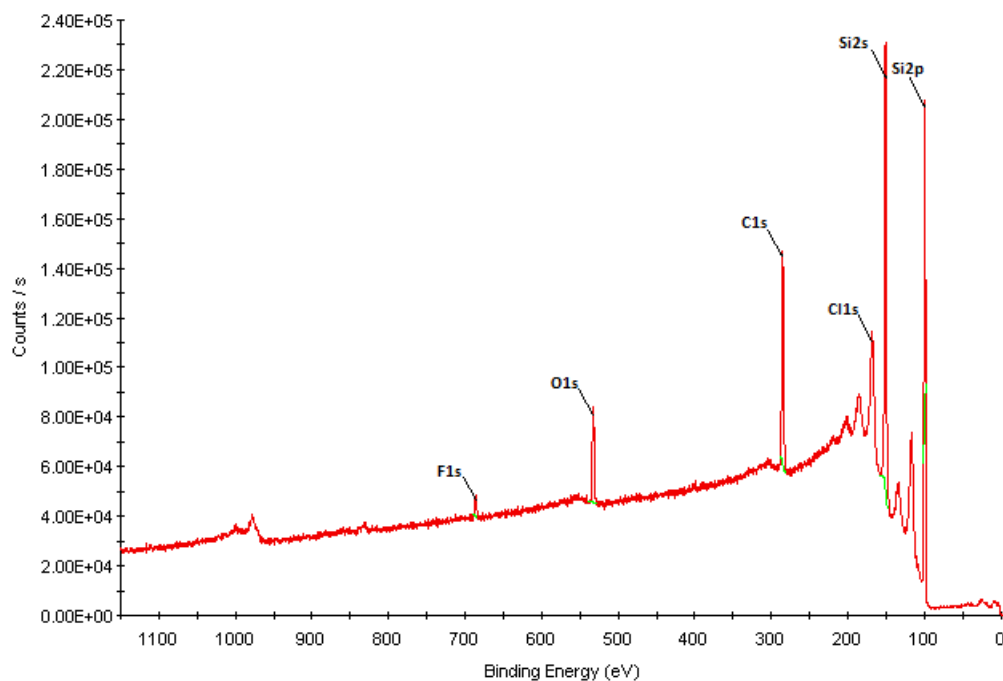


Figure 6.6 XP survey spectrum of Si (111)- $\text{C}_{10}\text{H}_{21}$ in the presence of $\text{C}_2\text{H}_5\text{AlCl}_2$ prepared by mild thermal hydrosilylation reaction of 1-decene.

Figure 6.7 and Table 6.1 show the high-resolution XPS spectra of the C 1s that consists of three components: C-C/C-H (85.6%), C-O (8.9%), and Si-C (5.5%). The XPS C 1s spectra showed a peak located at 285.0 eV, which is assigned to C-C/C-H bonding. An inflection point at 283.8 eV was observed in the spectra, indicating a peak at this binding energy. The inflection points at 286.5 and 283.8 eV in the spectra corresponded to a chemical bonding state originating from C-O and Si-C bonds, respectively.

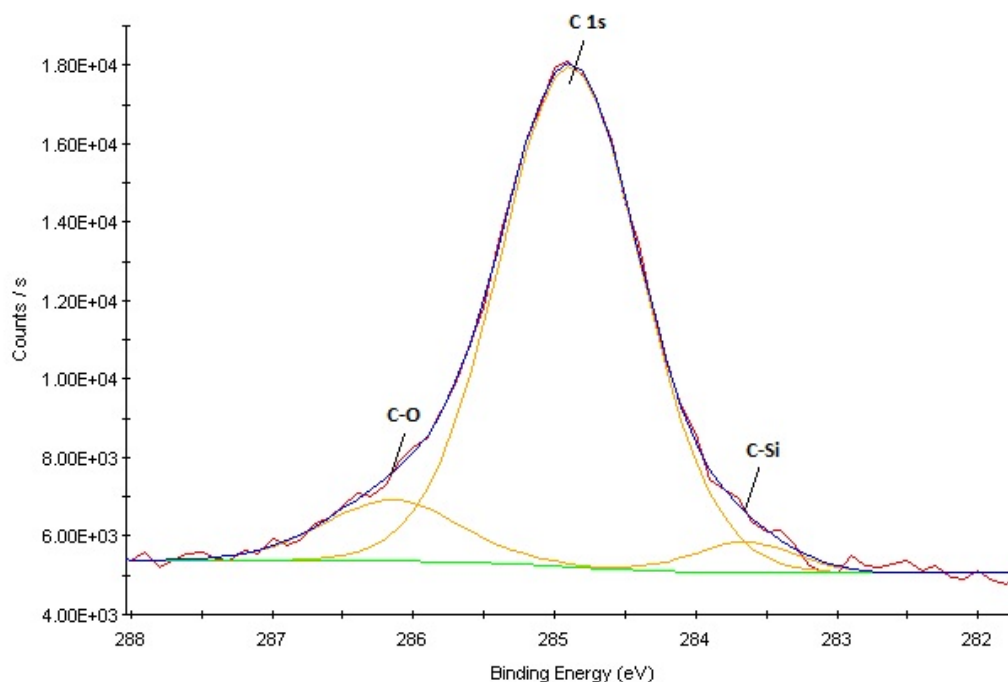


Figure 6.7 High-resolution XP spectra of surfaces (C 1s region) in the presence of $C_2H_5AlCl_2$ prepared by mild thermal hydrosilylation reaction of 1-decene.

Table 6.1 A summary of Percentage Component of XP spectra.

| Component | Peak BE | Wt. % |
|-----------|---------|-------|
| C-C\C-H | 285.0 | 85.6 |
| C-O | 286.5 | 8.9 |
| C-Si | 283.9 | 5.5 |

The Si 2p peak shown in Figure 6.8 has two components of Si 2p_{3/2} (Si1) and 2p_{1/2} (Si2), estimated at 100.1 and 99.6 eV, respectively. These results have three arguments by previous researchers. They used 1-decene as a precursor for the organic monolayer on a silicon surface. The existence of two component peaks of Si 2p is similar to the results obtained by Boukherroub *et al.* [34] and Rosso *et al.* [123]. Boukherroub *et al.* [34] saw peaks of Si 2p at

100.1 and 99.4 eV. This experiment was performed using the UV irradiation method. Rosso *et al.* [123] acquired their results from a demonstration of the peaks of Si 2p at exactly 101.1 and 100.4 eV employing H termination by HF and heated neat alkenes at 130 °C for 6 h. One component peak of Si 2p was achieved by Ishizaki *et al.* [114]. They utilized H-termination by NH_4F and thermal method (for 5 h at 160 °C). The energy of the primary Si 2p3 peak was at 99.4 eV, whereas the native Si 2p3 peak was at 99.0 eV. This result indicates that a portion of Si on the surface of this sample is H terminated. The peak shift is the only indication of H termination, indicating a possible method of completely removing the hydrogen bonding from the surface by minimizing pre-treatment of H-termination by employing either NH_4F or HF only. The Si 2p and C 1s spectra of the 1-decene monolayer were nearly identical to that of the H-terminated Si (111) surface. High-resolution XP spectra of the Si 2p and C 1s regions were consistent with the Si- CH_2 bond. The O 1s peak in the survey spectrum also did not appear to be associated with the formation of SiO_2 , which appears at about 102 eV [27] to 104 eV [34, 114]. These conditions indicate that the silicon dioxide layer on the Si substrate had been removed; it also proves that the alkylation of the H-terminated silicon substrate was accomplished.

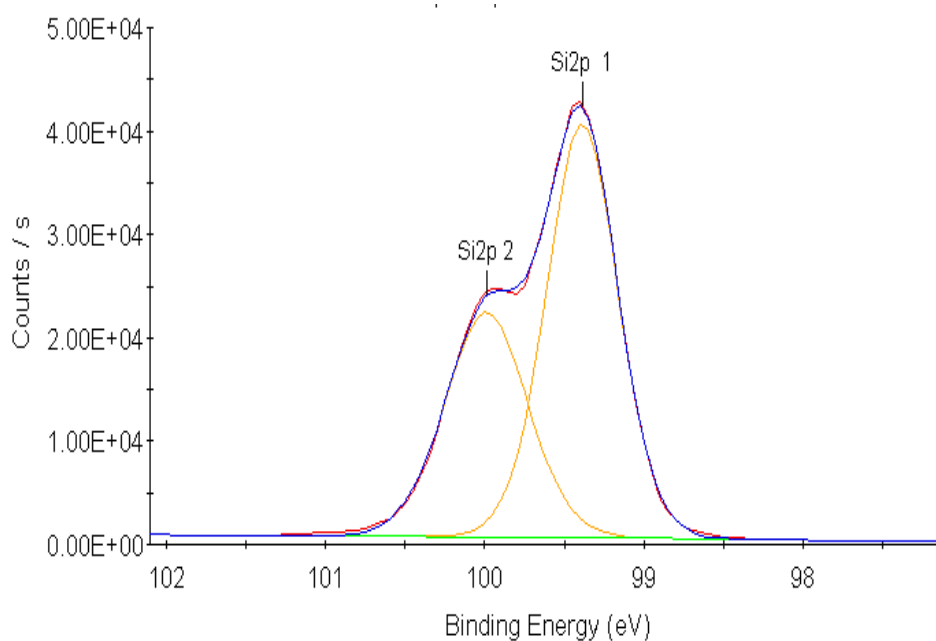


Figure 6.8 High-resolution XP spectra of surfaces (Si 2p region) prepared by the thermal reaction of 1-decene.

Hydrosilylation of alkenes using the Lewis acid catalyst [34] is well known in chemical literature and has been applied to modify porous silicon [110]. Although Lewis acid catalyst has been used in alkene monolayers, the presence of residual aluminium on the modified surface could be below the detection limit. Moreover, it could have resulted from the decomposition of the catalyst upon its neutralization. As evidence, the spectral of C 1s and Si 2p peak remain unchanged (same board and high binding energy) after 25 days in open air by applying the Lewis acid catalyst in the alkene monolayer [111]. The result of the quantitative XPS analysis of the sample is summarized in Table 6.2. The surface oxygen concentration sharply decreases from 28.9% to 5.7% because of the H termination and organic passivation processes. The surface oxide layer was removed earlier during the H-termination process. This oxygen concentration value of 5.7% was due to contamination, which is mostly due to adsorbed water molecules during exposure in air. The carbon amounts on the 1-decene monolayer samples increased to 27.7% compared with those on the native sample (9.4%), which was due to contamination during sample handling in open air.

This increase in surface carbon concentration supports our findings that 1-decene molecules have been passivated on the samples. Our results provide strong support for other characterization methods used for covalent-bound alkyl monolayers experiments on silicon surface.

Table 6.2 The relative atomic concentration (%) of the elements present in the samples by XPS

| Element | Relative atomic concentration (%) | |
|---------|-----------------------------------|----------|
| | Native | 1-decene |
| Si | 61.0 | 65.8 |
| C | 9.4 | 27.7 |
| O | 28.9 | 5.7 |
| F | 0.8 | 6.8 |

6.4.2 The Stability Study of 1-Decene Monolayer Passivation

Spectroscopic ellipsometry measurement is a sensitive tool to examine the relationship between surface morphology and chemical structure of treated substrates of Si (111) surface and Si/SiO₂ interfaces [27]. One of the objectives of this study is to investigate the degree of stability (oxidation resistance) of the alkene monolayer on silicon surfaces in air. The value of the imaginary portion of the pseudo-dielectric function ϵ_2 , is a measure of the degree of covalent termination with alkene bonding.

Figure 6.9 shows the typical spectra of the imaginary part of the effective dielectric function, ϵ_2 , for Si (111) after alkene monolayer passivation of n-type surfaces. The magnitude of ϵ_2 (367 nm) at the E2 silicon bulk critical point energy (~4.25 eV) is the highest in terms of sensitivity to surface modification and over layers [27, 86, 94]. Ellipsometry measurement can be used to monitor the smoothness of the surface based on the duration of time after the alkene-passivated sample is exposed to air. The ϵ_2 value for n-type Si (111) after the alkene monolayer-terminated surface is 32.3. The ϵ_2 value is consistent at ~31.9 and 32.6 after exposure in air for the next 24 and 144 h, respectively. A small change in ϵ_2 values occurs after exposure in air. The surface is stable, and the formation of alkenes is possibly terminated on the silicon surface.

A slight re-oxidation of the Si surface is observed after a few days of storage at room temperature in air. In this study, the term “micro-roughness” was used to describe changes of atomic scale irregularities on the silicon surface or in the Si/SiO₂ interfaces upon chemical treatment, reflecting a similar definition by Angermann *et al.* [27]. The ϵ_2 values slightly increased after exposure in air for 24 h. Figure 6.10 shows an indication of oxide and micro-roughness growth of the alkene monolayer on n-type Si surface. The growth is $\sim 2.824 \pm 0.080$ nm, which was measured immediately after the experiment. The micro-roughness growth increased to 2.883 ± 0.016 nm (24 h) and decreased to 2.663 ± 0.020 nm (144 h) after exposure in air. The change in ϵ_2 values is similar to the growth trend of micro-roughness of the surfaces. Any change in peak height in ϵ_2 reflects either an increase in surface roughness or an increasingly thick surface layer [27, 86, 94].

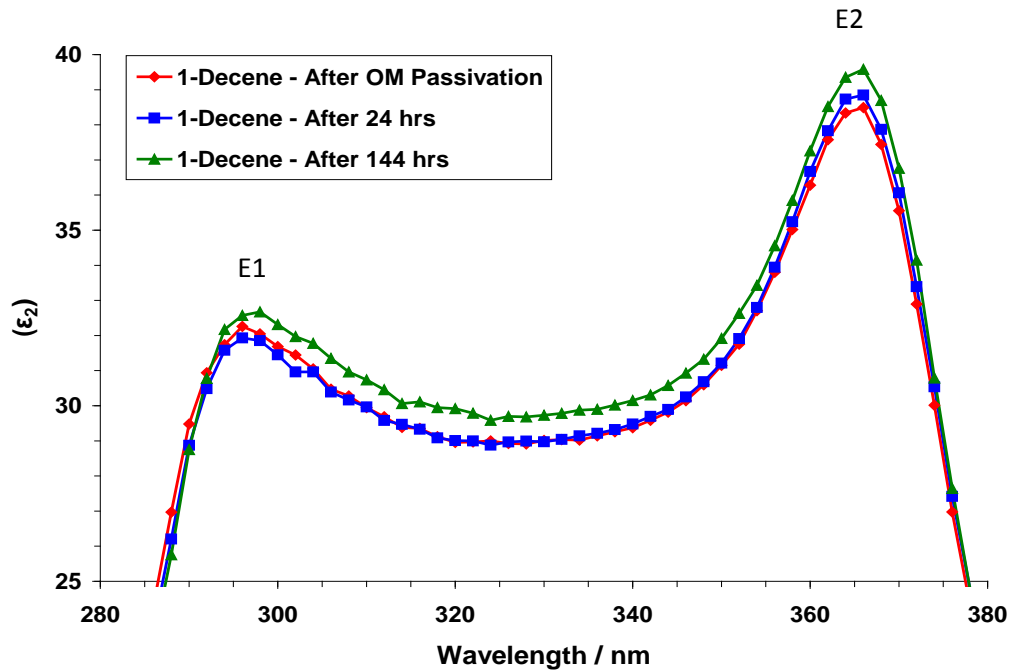


Figure 6.9 Spectra of the imaginary part of the pseudo dielectric function ϵ_2 measured by ellipsometry measurement on sample Si after organic passivation of *n-type* surfaces. The spectra of the same samples are shown after 24 hours and 144 hours exposure to air.

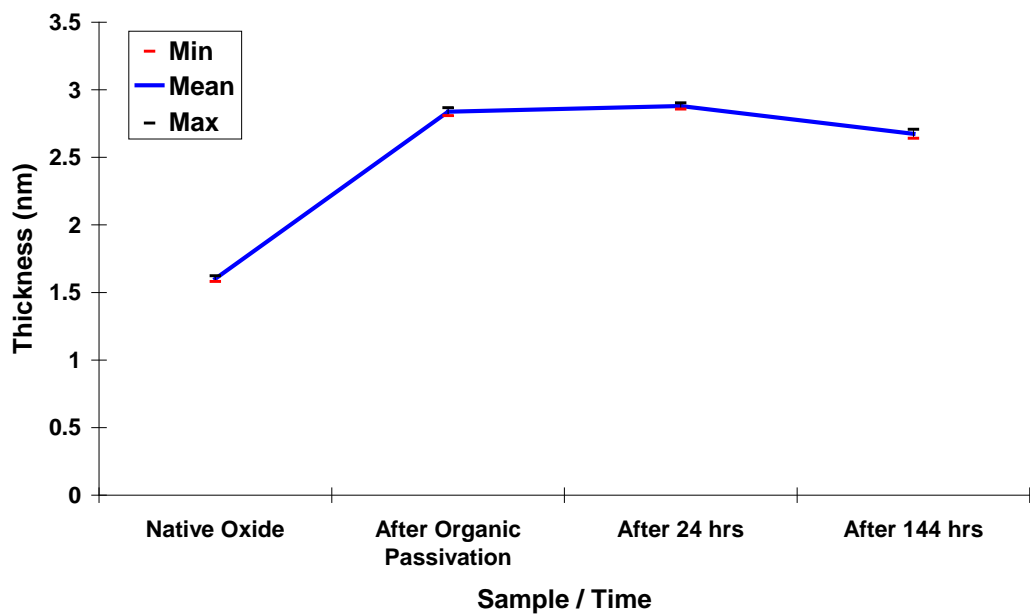


Figure 6.10 The estimation of surface micro roughness growth as a function of time, before and after alkene monolayer passivation from ellipsometry measurement. The apparent roughness over time for Si (111) *n-type* is shown after 24 hours and 144 hours exposure to air.

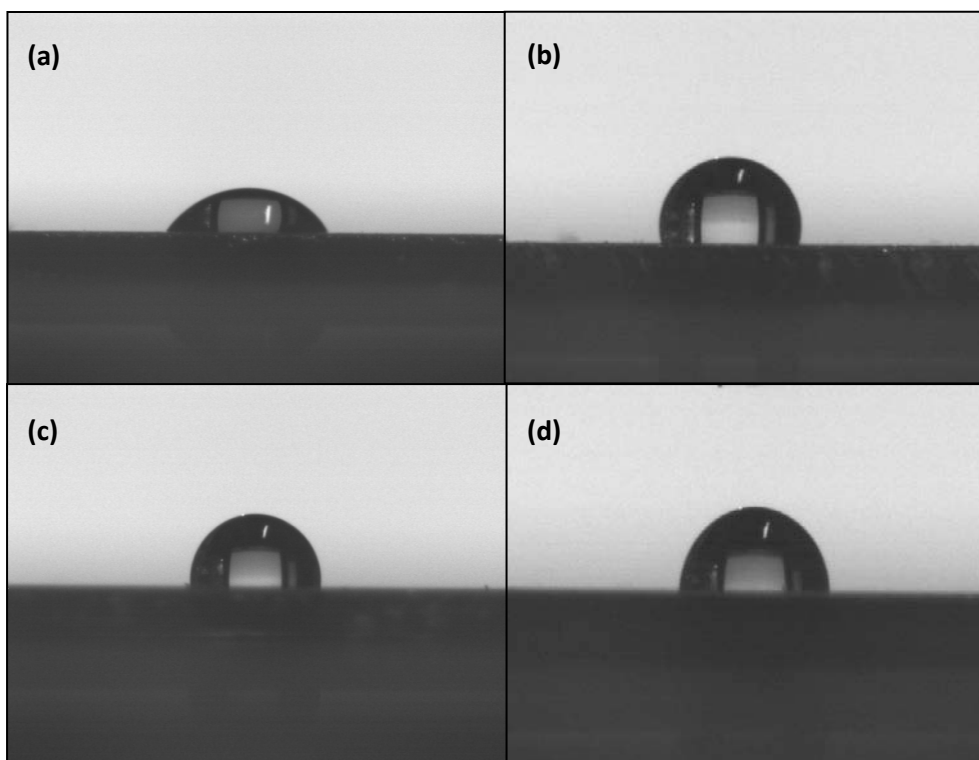


Figure 6.11 Images of water contact angles of the samples a) Native oxide; and 1-decene monolayers b) 24 hours; c) 192 hours and d) 624 hours.

The formation of water droplets on the flat surface mainly depends on the cleanliness of the surface or contamination by the organic layer on the surface. The hydrophilic molecules attract water molecules and disperse on the surface because of polar and ionic molecules that have positive and negative charges; thus, these hydrophilic molecules attract water molecules. By contrast, hydrophobic molecules are nonpolar molecules that are repelled by water because of the latter's neutral charge (no charge). The native oxide surface has a tendency to interact with water and has better wettability and adhesiveness [Figure 6.11(a)], indicating a hydrophilic surface where the contact angle is normally $<90^\circ$. The water droplet is more firm and undispersed on the surface; thus, a hydrophobic layer was formed on the silicon surface [Figures 6.11(b), (c), and (d)]. The changes of the contact angle in Figures 6.11(c) and (d)

indicate that the Si-C layer was oxidized after exposure to air for a certain period of time.

The H-Si (111) surface shows a water contact angle of $\sim 84^\circ$ (Table 6.3), which is consistent with reported values [124]. The surface wetting properties of H-terminated surface that reacted with 1-decene achieved maximum value (104°) within 24 h of exposure to air. These values correspond to the 1-decene monolayer, which consists of closely packed alkyl-terminated surfaces and correlate well with reported literature values of 102° [125], 107° [98], and 108° [114]. Ishizaki *et al.* [114] reported that the water contact angle strongly depends on the molecular structure of the monolayer, with C_{10} (1-decene) value of $<110^\circ$. Furthermore, the sample maintained hydrophobic surfaces ($>101^\circ$) within 192 h before the contact angle decreased to 93° . The minimal difference ($\sim 11^\circ$) after the sample was exposed to air for ~ 624 h suggests very low inherent reactivity of the oxide surface toward 1-decene.

Table 6.3 Water contact angles of the samples.

| Samples | ($^\circ$) |
|----------------------|--------------|
| Native oxide | 58 |
| Si-H | 84 |
| 1-decene (24 hours) | 104 |
| 1-decene (192 hours) | 101 |
| 1-decene (624 hours) | 93 |

6.5 Chapter Summary

This study describes the preparation and characterization of alkene monolayers on Si surface through a hydrosilylation reaction. The results of XPS, ellipsometry, and water contact angle showed the stability of the whole

monolayer surface and the very low inherent reactivity of the oxide surface toward 1-decene. Alkene formation was also very stable because of the Si-C bonds that created dense monolayers, as proven by FTIR spectroscopy and wetting experiments. The IR spectra recorded three broad peaks of the C-H stretching region, with peak areas at ~ 0.217 unit² and low temperature reaction at 110 °C. The significant results of IR spectra show that the covalently bound alkyl monolayers were well passivated by the presence of carbonyl groups on the monolayer surface. High-resolution XPS spectra of the Si 2p and C 1s regions were consistent with Si-CH₂ bond and increased carbon amounts of up to 27.7%. These results support our findings that 1-decene molecules have been passivated on the samples. Finally, the presence of the Lewis acid catalyst in the 1-decene monolayer rendered the grafted silicon samples resistant to oxidation in air. Moreover, the surface passivation for long-term stability conditions increased.

Chapter 7 Deposition of Langmuir-Blodgett Films on Silicon

7.1 Introduction

LB technique is one of the most promising for preparing thin-film layers on semiconductor surfaces. LH materials via LB films can transfer photon energy through photo-excitation from excited dye layers to the semiconductor to improve the low absorption coefficient of silicon. This study shows that a similar energy transfer process may occur to sensitize silicon via a dipole-induced dipole mechanism, which is similar to Förster energy transfer between two molecules or a molecule and a metal [126]. This approach to enhance the photo-generation carrier rates in solar cells was proposed by Dexter [127], wherein silicon sensitization is possible via non-radiative electronic energy from dye molecules on the surface. A significant technique to deposit an LB film monolayer requires control of the molecular organization and intermolecular distances for high efficiency of excitation energy transfer within dye molecules [126, 128]. In this chapter, the experimental steps of dye monolayers deposited on n-type silicon surface using LB technique are studied. Two different types of hydrophobic layers on the Si substrate are used, which later become the interface layers of LB films and Si substrate. This study reports and discusses electrical properties via contactless KP measurements in Chapter 8.

7.2 Background Study of LB Films

Traditionally, the term “LB films” refers to monolayer structures that are deposited from monolayers floating on the water surface onto a solid substrate. Normally, the substrate can be glass, mica, silicon, or quartz. Two common methods have been developed to deposit LB films. One technique is vertical deposition, which is the most common method of LB transfer [128]. The other strategy is horizontal deposition involving horizontal lifting of Langmuir monolayers onto a solid substrate; it is also called Langmuir-

Schaeffer deposition [129]. LB films can be formed as single layers or multilayers of various thicknesses, which contain one or more monolayers of an organic material. A monolayer is adsorbed homogeneously with each immersion or emersion step, where films with precise thickness can be formed. Multilayer structures can be created and added to determine the total thickness of an LB film because the thickness of each monolayer is identified. The advantages of the LB technique for the preparation of highly organized thin films are the following [129]:

- (i) Precise control of monolayer thickness and phase state.
- (ii) Homogeneous deposition of a monolayer over large areas.
- (iii) Possibility to prepare multilayer films.
- (iv) Structure with varying layer composition, e.g., two different surfactants or different orientation.
- (v) Deposition of a large variety of surfactants on different kinds of solid substrates.

7.2.1 Mechanisms of LB Films Formation

LB films are assembled vertically and are usually composed of amphiphilic molecules with a hydrophilic head and a hydrophobic tail. The orientation of surfactants may form when they interact with air at the air-water interface. This orientation allows surfactants to spread in the air-water interface to form insoluble monomolecular layers. The amphiphilic nature of surfactants on an air-water interface results in an orientation wherein the hydrophilic head group is immersed in water and the hydrophobic tail points toward the air. The surfactant molecules arrange themselves as shown in Figure 7.1. This tendency can be explained by surface-energy considerations. In addition, the thermodynamic variables of surfactants, such as surface pressure, surface area and number of surfactant molecules, are also significant for LB film formation.

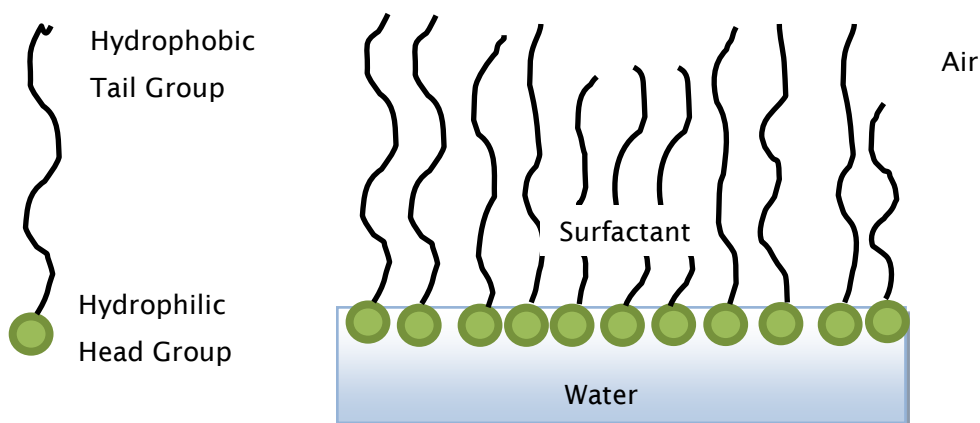


Figure 7.1 The surfactant orientation at an air-water interface.

The floating monolayers can be transferred from the air-water interface onto solid substrates by vertical deposition through an established method by Blodgett and Langmuir [127]. Initially, the solid substrate is immersed vertically through the sub-phase monolayers in the trough area. The barrier presses the floating monolayers to move toward the solid substrate and simultaneously move the substrate upward. The function of a moving barrier is to control the surface pressure constantly at a range of 1 mm/min to 5 mm/min. Subsequently, the floating monolayer is transferred onto the solid substrates, which depend on the wettability of the substrate and the hydrophilicity of the monolayer materials. The mechanism of monolayer deposition on a solid substrate is shown in Figure 7.2.

Deposition of LB films can involve highly organized multilayers of an amphiphilic compound. The continuous dipping and pulling process is required until the desired number of layers is achieved for a second layer or multilayer deposition. LB films can be deposited in a symmetrical mode in a multilayer deposition where the molecule layers form a head-to-head and tail-to-tail orientation. This arrangement is called Y-type films, wherein the monolayer is not deposited during the first dipping of the substrate (down strokes) but in subsequent upstrokes. Two other deposition types are X-type (deposition in down strokes) and Z-type (deposition in upstrokes) [130]. The different types of LB deposition are shown in Figure 7.3.

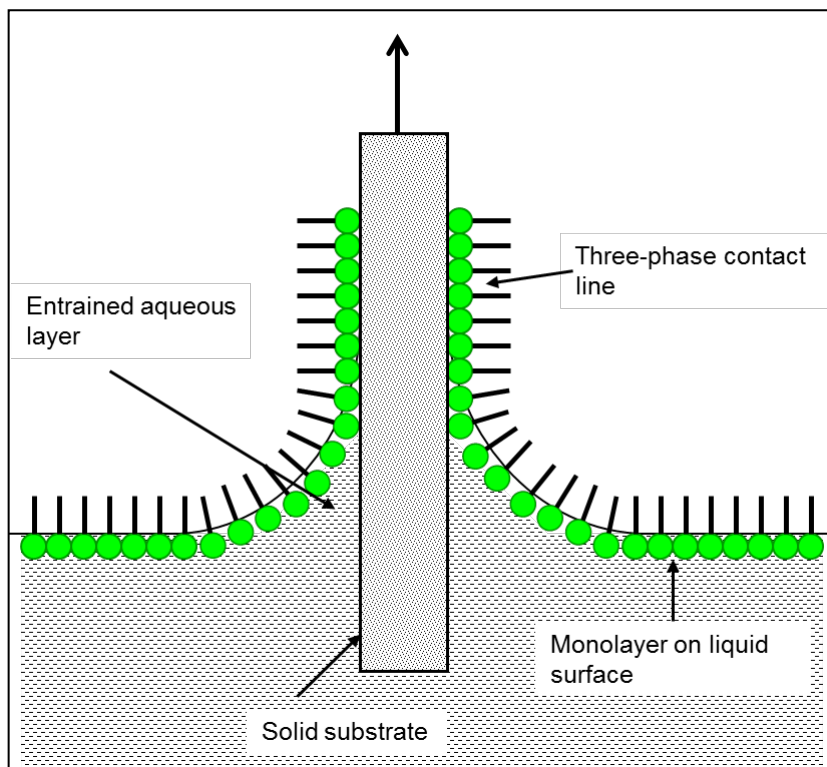


Figure 7.2 Deposition of a floating monolayer onto a solid substrate.

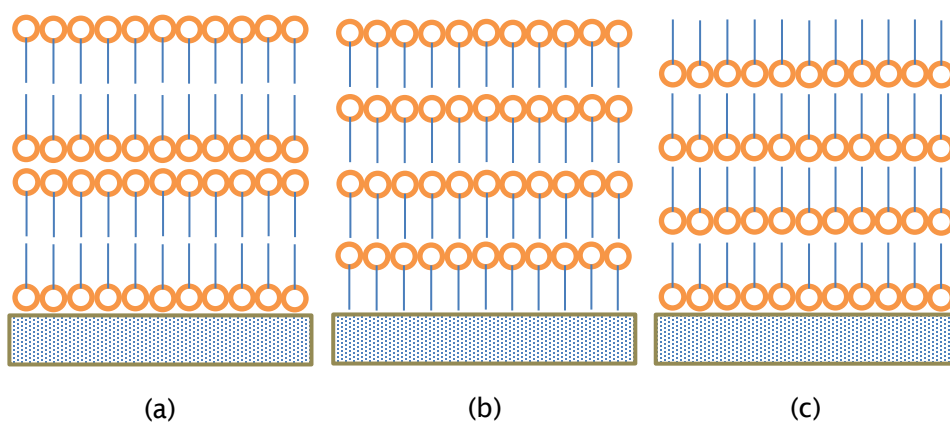


Figure 7.3 Different type of LB deposition a) Y-type; b) X-type and Z-type [130].

The surface pressure should be controlled to ensure sufficient cohesion in the monolayer, where the attraction between the molecules in the monolayer is sufficiently high and does not weaken during transfer to the solid substrate. The surface pressure is controlled by the Wilhelmy plate method (usually with filter paper), as shown in Figure 7.4. The Wilhelmy plate is a small piece of extremely thin hydrophilic material that is controlled by the air-water interfaces and intercepts support from the arm of an electronic electro-balance. The force acting on the plate is proportional to the surface tension. The container of the trough that consists of the sub-phase is typically made of Teflon to prevent any outflow of the sub-phase over the edges. The circulating water in channels that are placed underneath the Teflon trough is controlled by the thermostat trough. The movable barriers are used to compress the sub-phase toward the Langmuir balance, and the surface pressure is maintained constant during compression.

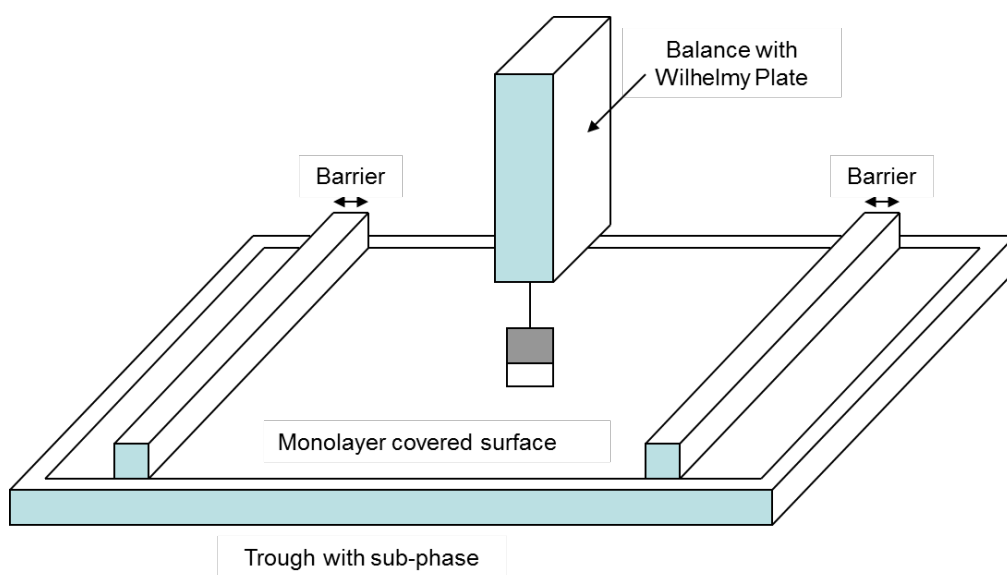


Figure 7.4 Schematic diagram of a Langmuir film balance with a Wilhelmy plate electro-balance and barrier function for measuring the surface pressure.

7.2.2 Methods and Parameter Control of LB Films Formation

A certain degree of equilibrium between hydrophilic and hydrophobic molecules is required to spread monolayers on the water surface. The properties of LB films mainly depend on the different electrical, optical, thermodynamic, and rheological characteristics of monolayers. The most significant aspects to be considered are related to the effect of sub-phase conditions on the monolayer properties and uniformity of the water surface. The formation of a monolayer structure via LB technique onto a substrate can be controlled with appropriate conditions.

i. Surface Tension

The degree of molecule attraction in a liquid is called cohesion, which is dependent on the substance properties. The interaction of a molecule in the bulk of a liquid is balanced by an equally attractive force in all directions. However, molecules on the surface of a liquid under imbalanced forces because of a molecule at the air-water interface exhibit greater attraction toward the liquid phase rather than the gaseous phase. The net effect of attractive force toward the bulk and the air-water interface is due to the presence of free energy at the surface. The existence of excess free energy at the surface is mainly attributed to the difference in environments between surface and bulk molecules. The resultant of the surface tension γ is given by partial derivative as follows [131]:

$$\gamma = (\partial G / \partial s)_{T, P, y_i} \quad \text{Eq. 7.1}$$

where G is the Gibbs free energy of the system, s is the surface area, T is the temperature, P is the pressure, and y_i is the composition. T , P , and y_i are constant.

Polar liquids normally have strong intermolecular interaction and high surface tension. Thus, a lower surface tension exists because of the weakness of the interaction strength or by increasing the temperature of the system. Any contamination or additional surfactants will lower the surface tension.

ii. Surface Pressure

Surface pressure is defined as the decrease in the surface tension of the liquid because of the presence of the monolayer [130]. This interfacial free energy in monolayer experiments is normally measured by the surface pressure Π . The excess free energy exists on the air-water interface; thus, water ($\Pi = 72.8$ mN/m at 20 °C) is a very good sub-phase for monolayer experiments. The surface pressure Π is equal to the reduction of the pure liquid surface tension by the monolayer films, which is expressed as follows:

$$\Pi = \gamma - \gamma_0 \quad \text{Eq. 7.2}$$

where γ is the surface tension with the presence of monolayer on the interface or the monolayer film-covered surface and γ_0 is the surface tension of the sub-phase in the absence of a monolayer (i.e., pure liquid).

iii. Surfactants

Surfactants are a larger class of molecules that consist of hydrophilic and hydrophobic groups. The surfactants accumulate at the interface and must be water insoluble but soluble in a volatile solvent, such as chloroform or benzene, to form a Langmuir monolayer. The hydrophobic group is typically a tail group that consists of long chains like a hydrocarbon. By contrast, the hydrophilic group is typically a polar group that consists of strong dipole moment and hydrogen bonding, such as -OH, -COOH, -NH₂, -NH₃⁺ and -PO₄⁻ (CH₂)₂NH₃⁺ [132]. The amphiphilic molecules are LB-compatible compounds that consist of both hydrophilic and hydrophobic groups, such as long-chain fatty acids (stearic acid, arachidonic acid, and so on). The most significant properties and behaviour of surfactants in the solution are the size and shape of the hydrocarbon chain, as well as the size, charge, and hydration of the hydrophilic head group.

iv. The Influence of Surfactants Concentration

Stable monolayers and organization of LB films on the substrate can be controlled by pH. The surfactant concentration of LB monolayer is usually prepared at pH 6.5 [133] and 7 [134]. In some situations, the surfactant concentration can be prepared to be more acidic because of the chemical properties of the mixing solutions. Danos *et al.* [135, 136] prepared dye monolayers in chloroform with the addition of water sub-phase and 10^{-4} M CdCl_2 concentration at pH 5.6. A stable LB film organization must not exceed pH 8.5, as suggested by Takamoto *et al.* [134]. Generally, the behaviour of surfactants in the solution and their associated interface layers are determined by the physical and chemical properties of the hydrophobic and hydrophilic groups, respectively.

7.2.3 Literature Review on the LB Films

Pioneering studies related to the energy transfer in molecular engineering were conducted by Kuhn [126]. Robert [137] initiated important studies on molecular energy transfer via LB film applications in semiconductors. Kuhn proposed that the direct excitation energy transfer (DET) is a very efficient method related to the average structure of monolayer assemblies on scales ≤ 10 nm. However, the molecular diffusion in LB films is much slower compared with DET; thus, the Förster mechanism is dominant for excited singlet states [138]. A mixed LB film on different conducting polymers create molecular electronics in both optical and electrical reversible switching, where ET can occur upon excitation by visible laser light [130].

The transition from homogeneous to striped bilayers of LB films on the oxidized silicon substrate was studied by Howland *et al.* [139]. Octadecylsiloxane Langmuir monolayers were prepared on the Si surface of an acidic sub-phase (pH 2) at room temperature. The morphological structures of striped bilayers are linear, periodic, micrometre-scale in width, and nano-scale in height, which can be controlled in an air-water interface by withdrawing and re-immersing the Si substrate. The proper control and stable order of LB films were studied by Takamoto *et al.* [134]. LB films were deposited from the

hexagonal phase of cadmium arachidate (CdA_2) at pH 7 and the monolayer viscosity was 0.98 ± 0.04 dyne-s/cm. Multilayer deposition of LB films can be performed by controlling the organization of LB structure at $\text{pH} < 8.5$. The monolayer phase with high pH has a lower energy lattice structure and is more condensed than the monolayer at pH 7.

Danos *et al.* [136] observed the excitation energy transfer of monomers and dimers in mixed LB oxacarboxyanine monolayers with stearic acid (1:100) on glass and silicon. Their study also confirmed that quenching occurs in a short distance at <10.0 nm and that the Förster radius is $\sim 5.5 \pm 0.5$ nm. The monomer and dimer energy transfer rates to the silicon surface are measured at a close distance of ~ 5.0 nm. Specifically, two significant factors are present for efficient energy transfer in the molecular system, which consists of the following: (i) sufficient energy to be transferred from one molecule to another by excitation energy and (ii) a closer distance between the molecules that is related to the uniform distribution of molecules.

7.3 Methodology

The nanostructure-molecule is a dye compound fabricated on silicon substrate via LB technique. The LB method produces highly uniform monolayers and precise control of the space thickness at 2.5 nm. The molecular-semiconductor separation is controlled by means of stepped structure deposited on the treated silicon surface.

7.3.1 Experimental Procedure

A sample of double-sided, 525 μm -thick, n-type crystalline Si (111) was used for all experiments. The resistivity of all the wafers was in the range of 20 $\Omega\cdot\text{cm}$ to 25 $\Omega\cdot\text{cm}$, and each sample was cut to 1.0 cm^2 . The following types of silicon substrate were prepared: (i) silicon native oxide and (ii) silicon passivated by 1-decene. Stearic acid (SA), hexamethyldisilazane (HMDS) (99%), cadmium chloride (CdCl_2) (99.999%), and chloroform (99.9%, A.C.S. HPLC

grades) were purchased from Sigma Aldrich. 3,3'-Dioctadecyloxacarbocyanine perchlorate (DiO) was purchased from Molecular Probes (Invitrogen, Ltd). LB deposition was prepared using mixed layers of SA (99%, grade I) and fluorescent cyanine dye molecule (DiO). Chloroform was used to prepare all spreading solutions, and all chemicals were used directly upon acquisition. The deposition of LB films followed a similar technique by Danos *et al.* [128, 129]. For the preparation of the sample, the silicon native oxide was rendered hydrophobic by overnight exposure to the HMDS vapour. For silicon passivated by 1-decene, a detailed experiment is presented in **Section 6.3.2**. The LB monolayers and multilayers were fabricated using a Langmuir Blodgett trough (Nima Technology, UK) equipped with three dipping wells and barriers. The experimental procedure is as follows:

1. The mixed DiO:SA solution was prepared at 1:5 ratio in chloroform.
2. The mixed DiO:SA solution was added into a water sub-phase with 10^{-4} M CdCl_2 on the trough at pH 5.6.
3. A silicon sample was placed on the trough holder at the vertical position toward the solutions.
4. The monolayers were deposited as a cadmium salt at a constant pressure of 28 mN/m and at a rate of 15 mm/min.
5. The water used for the sub-phase was ultra-pure from Sartorius Reverse Osmosis System (ARIUM-UV) with a resistivity of 18.2 M Ω .cm and a total organic content (TOC) of < 2 ppb.
6. The automatic barrier with the sample slowed down to sub-phase solutions using the computer software by Nima Technology.
7. A number of layers formed a stepped monolayer structure on the silicon substrate. For example, four steps represent eight monolayers on the silicon substrate. A similar procedure was applied for the sample silicon passivated by 1-decene with a new sub-phase solution.

7.3.2 Substrate and LB Films Preparation

The structure of dye monolayers deposited on the silicon surface, along with experimental steps, is shown in Figure 7.5. The first step for creating LB films is the formation of a hydrophobic layer by exposing the deposition overnight to HMDS vapour on the native silicon oxide. Another sample was prepared by organic passivation of 1-decene on the hydrogen-terminated Si surface. This experiment was explained in detail in **Section 6.3.2**. The second step is the formation of a stepped LB film structure consisting of four steps from eight monolayers of SA on the treated silicon surface. The stepped structure was created by depositing SA monolayers at cadmium stearate monolayers, wherein each step consisted of two SA layers. Then, a mixed DiO:SA (1.5 %) monolayer was deposited on top to cover the whole stepped LB film structure.

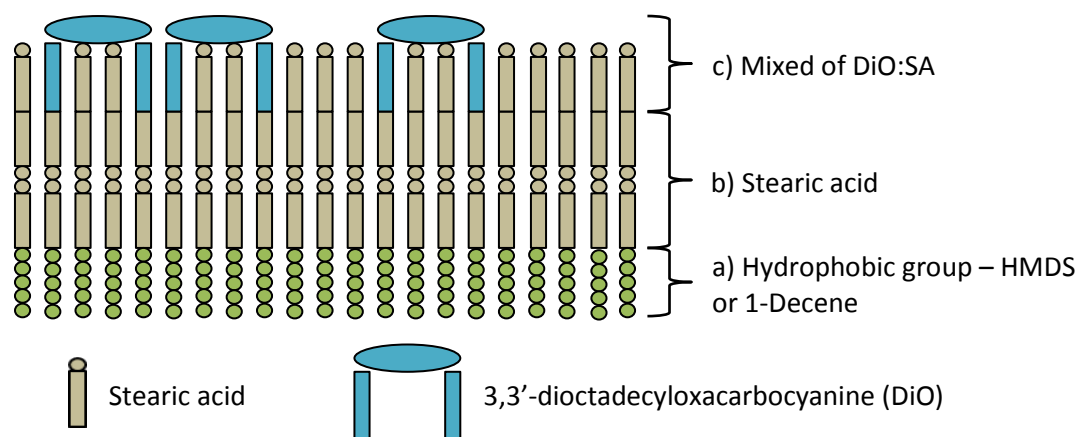


Figure 7.5 Schematic cross section of the structure of a dye monolayer deposited on silicon surface – a) formation of hydrophobic group by HMDS or 1-decene; b) two layers of cadmium stearate were initially deposited followed by; c) a monolayer of DiO with stearic acid.

The stepped LB film structure on the silicon surface is illustrated in Figure 7.6. Step 0 corresponds to the hydrophobic native oxide covered with HMDS with thickness of ~ 2.5 nm [136]. The thickness of the 1-decene monolayer is estimated at the range of 1.2 nm {projection structural modelling by Gorostiza *et al.* [111]} and 1.3 ± 0.2 nm based on a fit model for the decane SAM at 160 °C [140]. For steps 1 to 4, LB films consist of two SA layer depositions for each step, with a top layer of mixed DiO:SA. The whole stepped structure consists of a variation for two SA layers equal to a distance of ~ 7.5 nm and eight SA layers corresponding to ~ 30 nm. A similar thickness was previously reported by Danos *et al.* [109, 135, 136]. The distance of the monolayer to the silicon was accurately checked with spectroscopic ellipsometry on each SA step.

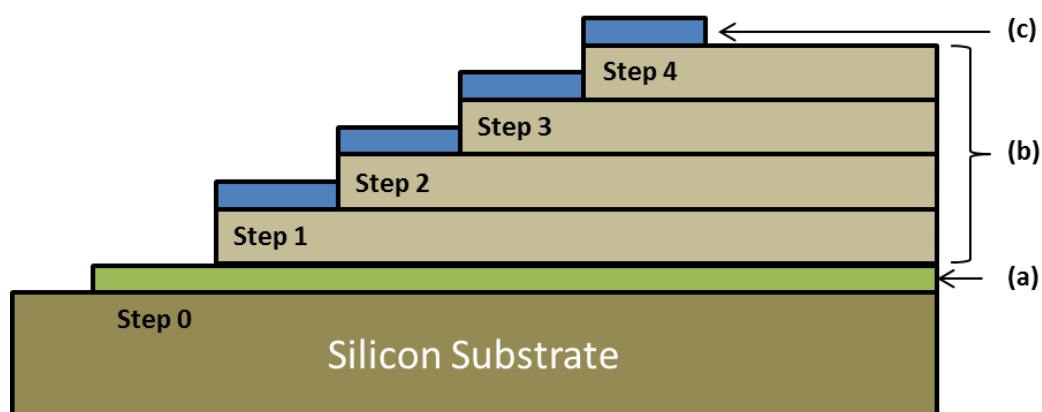
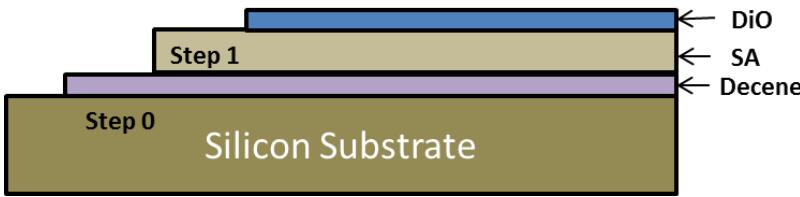
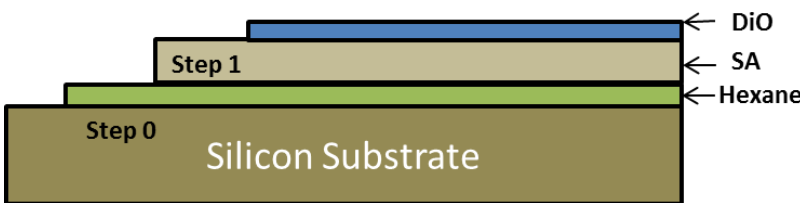
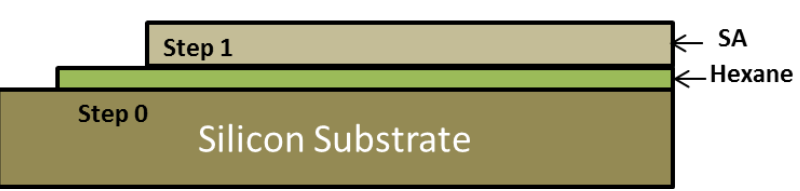
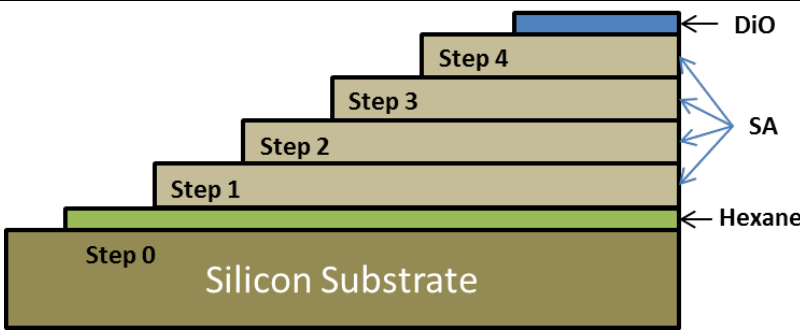


Figure 7.6 Schematic illustration of the stepped LB film structure on the sample: a) Hydrophobic group; b) Stearic acid; and c) DiO.

7.3.3 Samples Identification

The formation of the LB films on the silicon surface is described by detailed identification, as shown in Table 7.1. For example, Si-dec-LB is noted as Si-dec-2L 1.5 DiO:SA and Si-hex-LB is noted as Si-hex-2L 1.5 DiO:SA. Two other samples indicate Si-hex-2L SA and Si-hex-8L 1.5 DiO:SA, which are used for comparison and evaluation of the distance from the silicon surface.

Table 7.1 Samples structure, description and identification with LB films

| Sample Structure and Description | Identification Name |
|--|--|
|  <p>This sample consists of mixed monolayer of DiO:SA (1.5 %) on the top of 2 SA layers as LB films with an interface layer of decene monolayers on the silicon substrate.</p> | <p>Si-dec-2L 1.5 DiO:SA or Si-dec-LB</p> |
|  <p>This sample consists of mixed monolayer of DiO:SA (1.5 %) on the top of 2 SA layers as LB films with an interface layer of hexane monolayers on the silicon substrate.</p> | <p>Si-hex-2L 1.5 DiO:SA or Si-hex-LB</p> |
|  <p>This sample consists of 2 SA layers with an interface layer of hexane monolayers on the silicon substrate.</p> | <p>Si-hex-2L SA</p> |
|  <p>This sample consists of mixed monolayer of DiO:SA (1.5 %) on the top of 8 SA layers as LB films with an interface layer of hexane monolayers on the silicon substrate.</p> | <p>Si-hex-8L 1.5 DiO:SA</p> |

7.4 Chapter Summary

This chapter highlighted the importance of controlled experimental parameters to perform the deposition of LB films on Si substrate. The preparation and experimental procedures for LB films were also demonstrated. The hydrophobic 1-decene monolayer and HDMS on the silicon surface were used as interface layers for deposition of dye (DiO) monolayers via the LB technique. The formation of LB films on the Si substrate is a novel approach for functional groups of LH materials for solar photovoltaic systems. Further functionalization and patterning of Si-C surface provide 90% full coverage [37] and effectively inhibit the oxidation of Si (111) surfaces in air [141]. These results prove the diffusion of oxygen atoms into the monolayer/Si interface, and prolong stability against oxidation in air [111, 122]. The characteristics of LH materials (LB films) on the Si surface can be identified and linked to the measurement of barrier height and estimation of SRV by KP (**Section 8.3.4**). This experimental procedure is also linked to **Section 9.3.2**, which is related to the study on charge trapping of the dye monolayer in LB films that function as LH materials. Furthermore, a fundamental study is necessary to achieve proper understanding of the mechanism of trapped charges on the silicon surface.

Chapter 8 Electrical Characterisation of Silicon Surfaces

8.1 Introduction

This chapter describes the electrical characterization of silicon surfaces via KP and quasi-steady-state photo-conductance technique (QSSPC). This chapter focuses on the measurement of surface recombination in samples passivated by alkyl monolayers on the surface, as described in **Section 5.5.2**. The measurement of diffusion length is described, which is needed for an in-depth characterization of the surface by the KP method. This study demonstrates KP surface characterization for surface recombination, which is consistent with the results of the QSSPC technique. QSSPC is the industry standard in this field. We also demonstrate that alkyl deposition on silicon produces a reasonably well-passivated surface and may be considered as a low-temperature surface passivation technique for industrial applications.

8.2 Methodology

Samples of double-sided polished n-type silicon with (111) crystal orientations were purchased from Siltronic. Wafer thickness of 525 μm , sheet resistivity of 20 to 25 $\Omega\cdot\text{cm}$, and size of 1 cm^2 were used in this study. A solution comprising isopropyl alcohol (99.5%), H_2SO_4 (30%), and H_2O_2 (30%) was used without treatment and purchased from Fisher Scientific. The substrates were degreased in acetone and isopropyl alcohol solution and placed in an ultrasonicator for 15 min. Then, the substrate was treated in an SPM solution at a ratio of 3:1 for 15 min. This cleaning process leaves ~ 0.6 nm to 1.5 nm of hydroxylated oxide on the silicon surface, which prevents surface recontamination.

The samples were uniformly illuminated by a low-response monochromic light source (Bentham CL2 universal spectral irradiance standard lamp; Bentham, Inc.) with a wavelength of 250 nm to 3000 nm. The optical fiber source was

placed ~5 cm away and at 45° from the sample base of KP, which was covered by a black, square box. The light emitted by the IL1 lamp was filtered by TMc300 in 5 nm steps. Light escaping from the monochromator was guided to the solar cell by a 1 mm UV/visible optical fibre. The cell response was measured in Amperes at each rotation of the monochromator where the spectral response of the cell (in $\text{AW}^{-1} \text{nm}^{-1}$) was determined. The illumination system was composed of an IL1 lamp, TMc300 monochromator, and optical fibre calibrated against a reference (1 cm^2 calibrated DH-Si silicon low-noise photodiode) prior to any measurement.

8.2.1 Kelvin Probe Method

SPV measurement via KP method is a suitable technique to continuously monitor passivated layers of silicon surfaces under light and dark conditions. Furthermore, the KP method is very sensitive to small changes in surface passivation which are measured in a small area (under probe tip). Thus, a simultaneous monitoring of SRV and observing the charge injected into the passivated layers appears to provide a promising technique. SPV and barrier height were measured using the Ambient KP System (KPSP) with SKP 4.5 software (KP Technology, Ltd.).

The SPV measurements were obtained at a wavelength of 900 nm by setting a maximum slit opening of monochromator at 8.00 mm (**Appendix 1**). The work function of the semiconductor can be measured at high resolution ($< 50 \mu\text{eV}$) with a characteristic voice-coil actuator [142]. KP consists of a flat circular electrode (reference tip, W_m) placed on the top and parallel to a stationary electrode (sample, W_s). The KP reference tip ($\phi = 2.5\text{mm}$) is created from gold that functions accurately, vibrates, and does not go in contact with the sample. The difference of the work functions is determined by the value of the external voltage at a null condition, which produces a CPD between the metals ($V_{CPD} = W_m - W_s$). The electric field created charges of opposite sign by V_{CPD} on the capacitor electrodes. These induced charges were detected by the gold tip as transient current flows in an external circuit by changing the spacing between electrodes [41]. The current generated by the vibrating capacitor can

be converted into a measurable voltage using high resistance, which is connected across the vibrating capacitor.

8.2.2 Photo-conductance Decay Method

Lifetime measurement procedures with transient photo-conductance decay and quasi-steady-state photo-conductance techniques are commonly applied to characterise the passivation of silicon wafers. Inductively coupled photo-conductance decay (PCD) and quasi-steady-state photo-conductance techniques are inexpensive and can easily determine the effective lifetime. Both techniques are the only extensively used methods to determine lifetimes under low-, mid-, and high-injection conditions [143]. However, the surface recombination effect that limits the actual lifetime is sometimes neglected and used to determine the bulk recombination properties of the wafer [144].

Photo-conductance measurements are based on the voltage output of an impedance bridge, which contains an inductively coupled Si wafer in one branch. The bridge is first balanced and the wafer is subsequently illuminated by a flash of light. The change in wafer conductivity causes the bridge to be unbalanced. The generated voltage is then recorded. In the PCD technique, a short flash of light or a stroboscopic lamp is used and the generated voltage is monitored after switching off the light. In the QSSPC technique, a slow flash is used and the voltage is recorded while the light is still on [145].

WCT-120 Photo-conductance (PC) Lifetime Tester instrument was used to characterize the surface recombination lifetime. The effective carrier lifetime (τ_{eff}) of the samples was measured using a contactless photo conductance decay system supplied from Sinton Consulting, Inc. (USA). In this system, the sample is inductively coupled to a calibrated RF circuit whose output voltage is directly correlated to the sample's conductance. The sample is exposed to a short light pulse generated by means of a flash lamp during each measurement. The time-dependent output signal of the RF circuit is recorded with an oscilloscope after termination of the light pulse and converted into photo-conductance. The minority carrier recombination lifetime and SRV of the

samples were compared between KP and PC to determine the correlation and bias in the results.

8.3 Result and Discussion

8.3.1 Estimation of Diffusion Length

The work function is defined as the minimum energy needed to remove an electron from the Fermi level E_f to a point immediately outside the solid surface [1]. SPV can be defined as a change in the surface potential ($\delta V_s = |V_s - V_{s0}|$), where V_{s0} is the equilibrium surface band bending and V_s is band bending under illumination [41]. The relationship of δV_s can be used to estimate the total space charge and excess carrier density (Δp) at the surface using Poisson's equation via collection efficiency (η_L) of the minority carrier (Eq. 5.22).

Diffusion length was measured within the wavelength interval of $800 \text{ nm} \leq \lambda \leq 1100 \text{ nm}$ to minimize the uncertainty in diffusion length values obtained by the SPV method. SPV measurement was conducted using KP method to determine the minority diffusion length of the silicon surface. The surface of the sample is illuminated by monochromatic light at long wavelengths with a large absorption coefficient. A photovoltage is generated between the surface and bulk because of the diffusion of electron-hole pairs to the depletion region and the subsequent charge separation in this region. Diffusion of minority carriers will determine the actual distance the carrier moves between generation and recombination.

SPV measurement was performed at low incident illumination and constant SPV to monitor photon flux density (Φ), whereas light absorption coefficient (α^{-1}) varied. Diffusion length (L_p) was determined based on a linear relationship between SPV and Δp with low SPV signal. The Φ vs. α^{-1} plot in Figure 8.1 shows that diffusion length is equal to the negative intercept along the α^{-1} axis. These graphs also show the η_L^{-1} vs. α^{-1} plot of the collection efficiency, which were determined in Eq. 5.22 (Section 5.5.1; pg. 77).

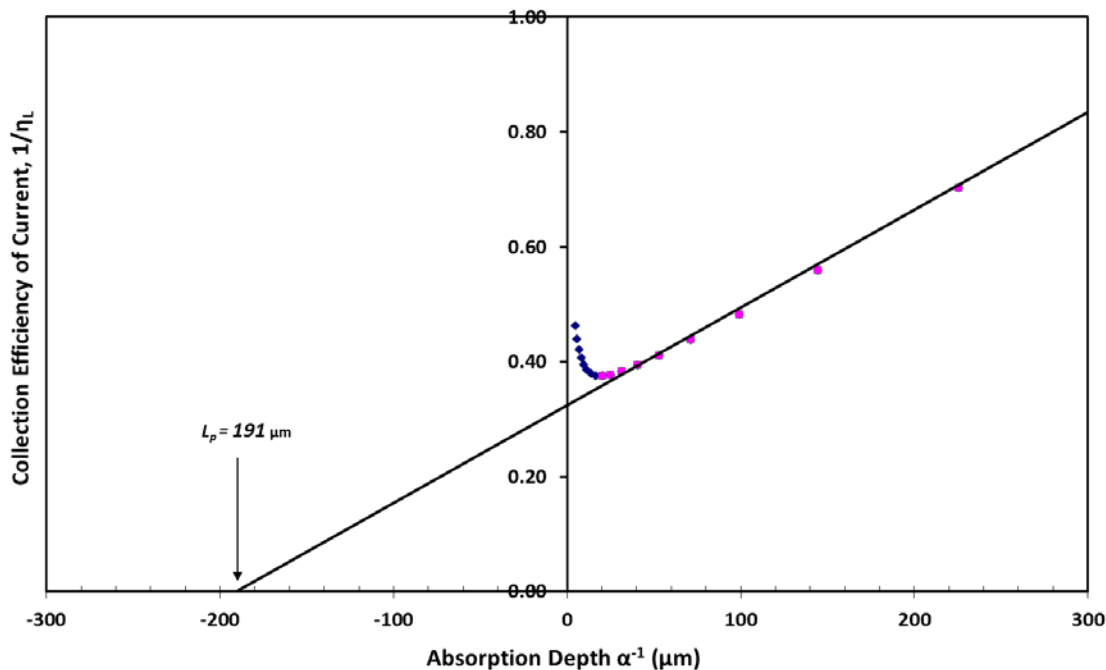


Figure 8.1 The theoretical value according to Eq. 5.22 for diffusion length determination by plotting the collection efficiency, $(1/\eta_L)$ against absorption depth $(1/\alpha)$.

The diffusion length was determined through a straight line at the wavelength interval of $860 \text{ nm} \leq \lambda \leq 1020 \text{ nm}$. The optical absorption coefficient of Si measured the diffusion length in the narrow wavelength interval compared with the studies of Saritas and McKell [146, 147]. The validation of diffusion length measurement satisfies the following conditions: thickness of the sample (H), depletion region width (W), and excess minority carrier (Δp) with $H < \alpha^{-1} < L_p$; $L_p \ll H$ and $n_0 \gg \Delta p$. The sample is assumed to be illuminated homogeneously with homogenous photo-generation $G(x)$ to fulfil $L_p \ll H$ [148]. The parameters of this study were as follows: $H = 525 \text{ } \mu\text{m}$, $W = 2.034 \text{ } \mu\text{m}$, and α^{-1} range = $5 \text{ } \mu\text{m}$ to $391 \text{ } \mu\text{m}$. Figure 8.2 shows five graphs to determine the diffusion length by plotting photon flux vs. absorption depth. The average value of L_p was $191 \text{ } \mu\text{m}$ and the average lifetime of the minority carriers (τ_p) of each sample can be estimated as $27 \text{ } \mu\text{s}$ using the following equation:

$$L_p = \sqrt{D_p \tau_p} .$$

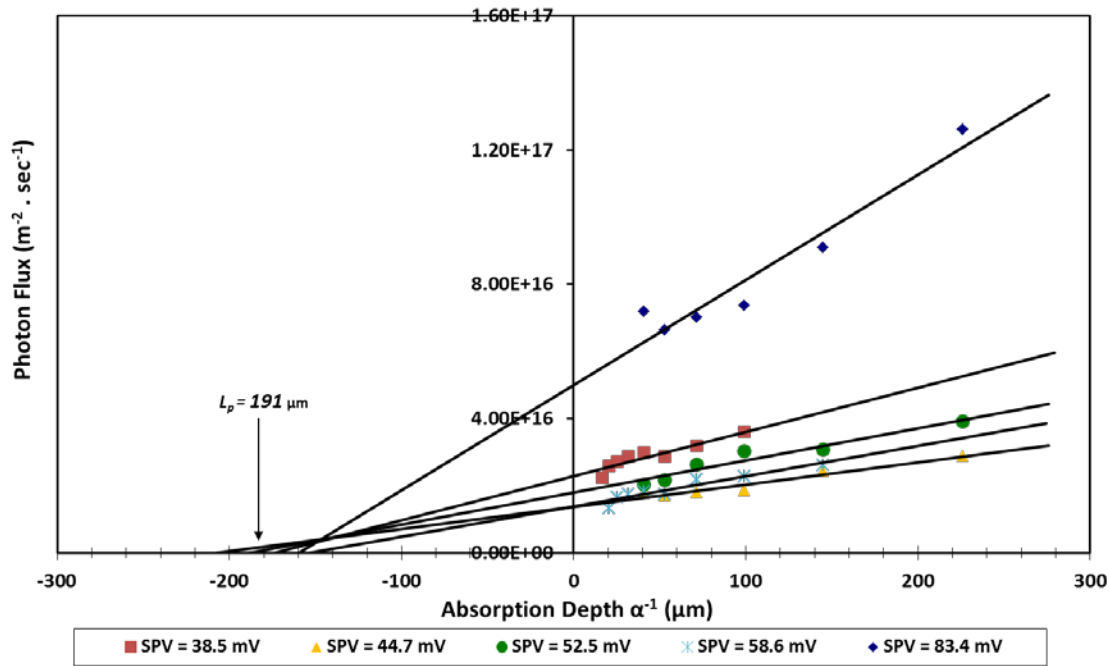


Figure 8.2 The experimental data for sample silicon native oxide by plotting photon flux, Φ against α^{-1} . The average diffusion length is estimated based several values of SPV – a) 38.5 mV; b) 44.7 mV; c) 52.5 mV; d) 58.6 mV and e) 83.4 mV.

L_p inconsistency is mainly ascribed to the surface effect that contributes to the slow states and the surface recombination on the sample [41]. The sample was possibly exposed to surface recombination throughout the experiment because of a native oxide on the surface. Another possible error may result from CPD fluctuation between the work function of the tip (W_m) and the sample (W_s). The charges accumulate on the sample surface because the sample is under illumination. The slow trap and fast trap of charges may have also contributed to this error. Some of these problems can be avoided using chopped light. However, the equipment was not available in our setup, which was conducted under constant illumination (direct current SPV). Tousek *et al.* [148] suggested using thicker samples to obtain more accurate diffusion length. However, L_p does not depend on thickness. Shikler *et al.* [80] also proposed that the KP method is useful in measuring very short diffusion lengths ($\leq 2 \mu\text{m}$) but is less sensitive to narrow or medium band gap

semiconductors (≤ 1 eV) because the SPV is exponential to the band gap energy.

8.3.2 Measurement of Barrier Height

i. Sample Silicon with $\text{H}_2\text{SO}_4/\text{H}_2\text{O}_2$ solution

The SPV technique monitors semiconductor surface potential changes introduced by illumination; thus, this technique can be used to investigate the surface states on the silicon surface [73]. The surface potential can be measured via the SPV signal, which corresponds to the electrical charges residing on the silicon or in its vicinity. A modification of the surface potential by electrical charge transfer can be treated using many chemical treatments and biological species. Chemisorption allows the chemisorbed species a binding energy of >0.1 eV to form chemical bonds with the silicon surface. Moreover, the physisorption requires a binding energy <0.1 eV via electrostatic interaction with the silicon surface states [12]. In this study, the samples were dipped in aqueous solutions of mixed inorganic bases and acids to investigate the effect of chemical species on the silicon surface potential.

An initial stage of the cut Si (111) sample was cleaned by sequential rinsing in acetone, IPA, and deionized water. Then, the sample was placed in a hot SPM solution by mixing concentrated H_2SO_4 and H_2O_2 at a ratio of 3:1 for 20 min. This treatment removes organic contaminants from the Si surface while forming a thin layer of chemical oxide [102]. Figure 8.3 shows the intensity dependence of the SPV for sample Si etched by SPM solution and fresh Si native oxide at a wavelength of 900 nm. When light intensity was increased, SPV growth was exponential until saturation was reached. SPV saturation indicates the barrier height of the sample. The highest SPV of sample S8 etched at Day 1 with SPM solution was recorded at ~ 233 mV. The SPV value of this sample is much higher than that before treatment (174 mV); thus, the surface potential is greater than that of Si native oxide. The sample still maintains high SPV (> 224 mV) even after 14 d of sample exposure to air. As mentioned in **Section 6.2.1**, the etched sample was washed with deionized water after SPM treatment. The resulting surface chemistry of the sample etched with $-\text{OH}$

termination group formed silanol groups ($\equiv Si-OH$). Subsequently, accumulation of electrons occurred on the n-type silicon interface, as reported by Angerman *et al.* [86]. This mechanism created higher SPV signal and surface potential on the etched samples.

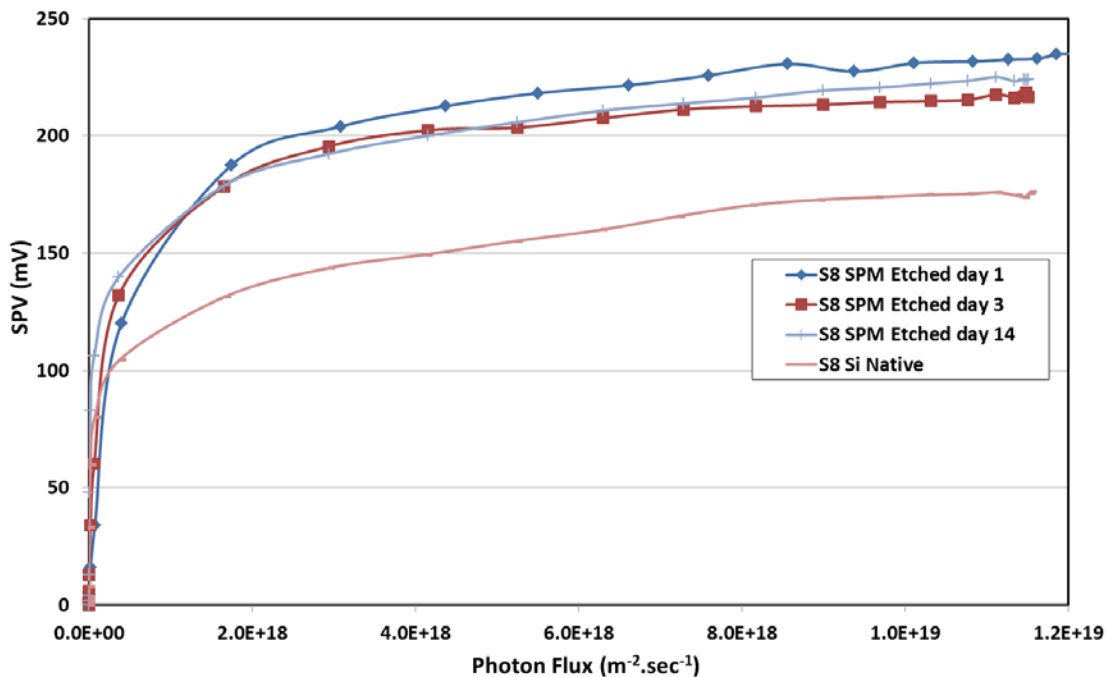


Figure 8.3 The barrier height measurement on silicon samples by plotting Photon Flux vs. SPV. A different SPV values for (i) Si etched with SPM solution at various days after exposed to air; (ii) Si native oxide (Measured at wavelength of 900 nm).

ii. Sample Silicon with Decene as Interface Layer

The 1-decene monolayer of sample S2 was passivated on the silicon surface and compared with the silicon etched with SPM solution (Figure 8.4). The SPV of Si decene sample recorded lower values of 21 mV (1st day) and 28 mV (3rd day) compared with Si etched with SPM solution. By contrast, Si treated with SPM demonstrated higher SPV value [~ 229 mV (1st day) and 241 mV (3rd day)].

Difference in SPV value indicates a variance of surface potential because of the surface modification on the samples.

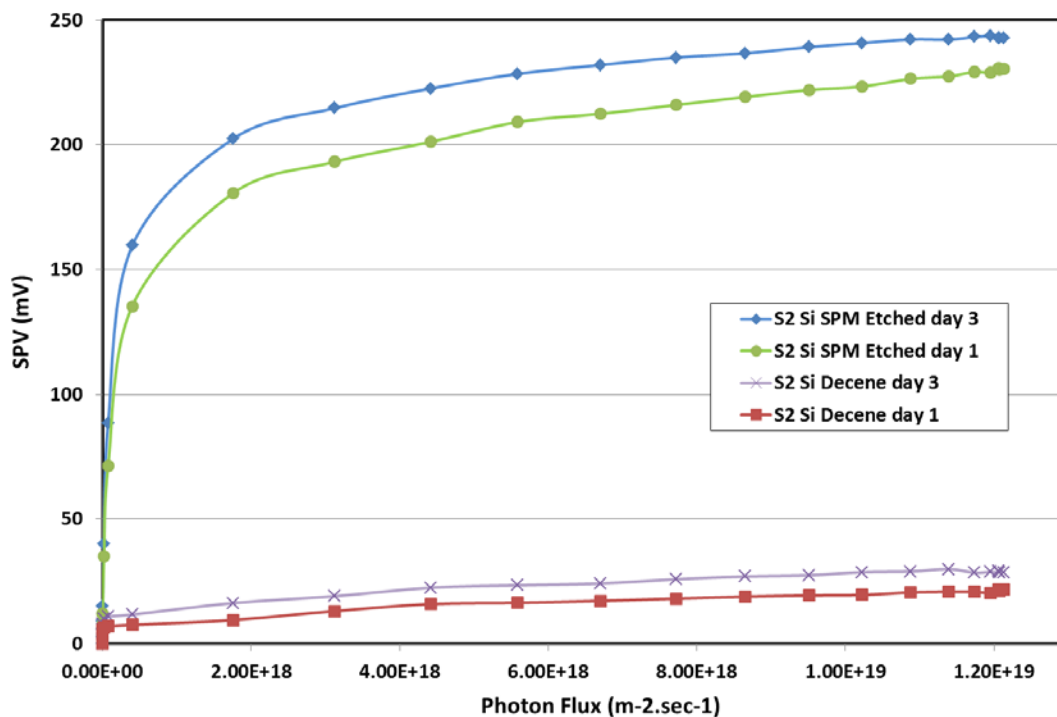


Figure 8.4 The barrier height measurement on samples Si-decene and Si etched with SPM solution by plotting Photon Flux vs. SPV. Different SPV values are observed on 1st and 3rd days for both samples (Measured at wavelength of 900 nm).

High SPV of silicon with treated SPM reflects electron accumulation on the silicon interface and distribution of carrier density in the surface states, which are caused by surface recombination of excess holes and electrons. Surface passivation of 1-decene monolayers allows the sample to minimize the surface recombination by replacing the silicon–oxygen bonding with Si-C bonding on the dangling bonds. The surface potential of Si decene is small because the centre of recombination of surface states is removed. The results show that the sample completely covered the silicon surface, which was consistent with the XPS data (**Section 6.4.1**).

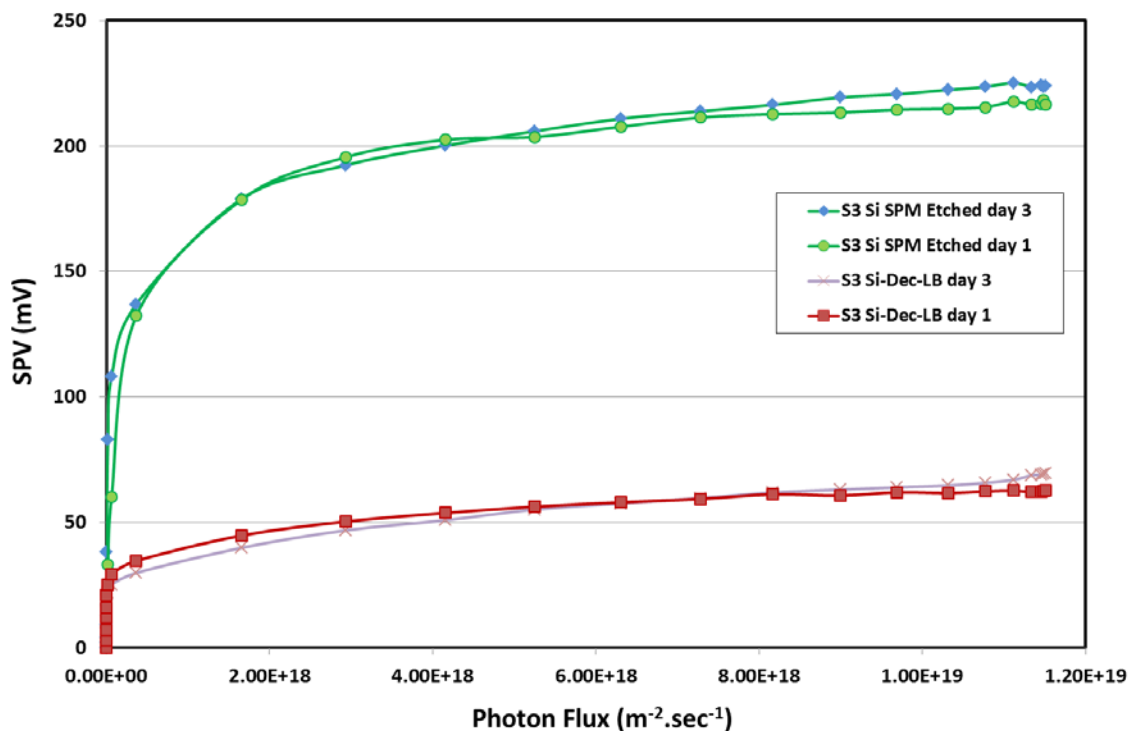


Figure 8.5 The barrier height measurement on samples Si-dec-LB and Si etched with SPM solution by plotting Photon Flux vs. SPV. Different SPV values are observed on 1st and 3rd days for both samples (Measured at wavelength of 900 nm).

Figure 8.5 demonstrates the SPV of silicon sample deposited with LB films on the interface layer of 1-decene. For sample S3 Si-decene-LB, the SPV was recorded lower at ~63 mV (Day 1) and 64 mV (Day 3), indicating that the sample is stable and resists oxidation in air. The SPV of Si treated with SPM was recorded to be higher at ~221 mV (Day 1) and 222 mV (Day 3). The surface was resistant against oxidation and was depleted after surface modification by the interface decene/LB films. Surface potential that is slightly higher than Si decene (Figure 8.4) can be ascribed to the blockage of the residual oxidation current, which trapped the electron in the LB/decene interface. Thus, the holes diffuse toward the surface and accumulate in the surface charge region.

iii. Sample Silicon with Hexane as Interface Layer

For sample S5 Si-hexane-LB, the SPV value was recorded lower at 32 mV on the 1st day but increased to 83 mV after Day 3 (Figure 8.6). The observed slow surface oxidation indicates that the interface layers are not stable against oxidation in air after 3 days. This change indicates that water or oxygen molecules are capable of penetrating through non-branched monolayers or defects.

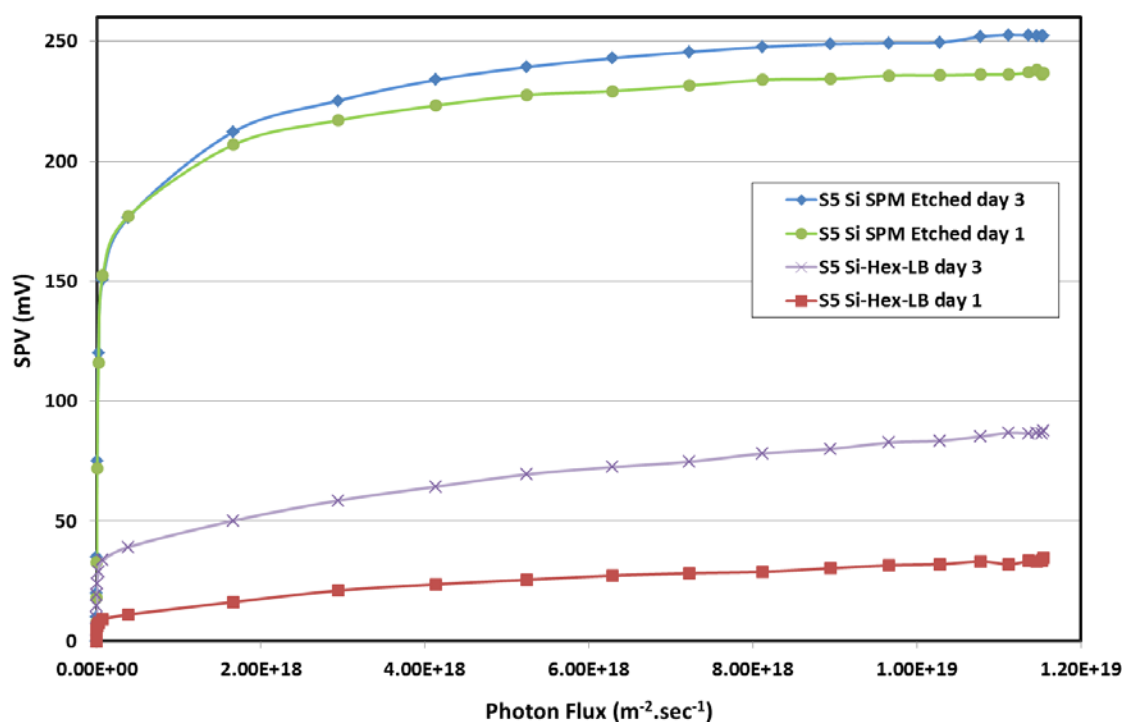


Figure 8.6 The barrier height measurement on samples Si-hex-LB and Si etched with SPM solution by plotting Photon Flux vs. SPV. Different SPV values are observed on 1st and 3rd days for both samples (Measured at wavelength of 900 nm).

Thus, the Si surface was oxidized and allowed an accumulation of electron traps on the interface. Therefore, the barrier height measurement is generally sensitive to pre-deposition during surface preparation [1], wherein the surface potentials of samples Si-decene (21 mV), Si-decene-LB (63 mV), and Si-hex-LB

(32 mV) are much smaller than the native Si samples (222 mV to 241 mV). The barrier height measurements show good representative values for contactless KP on passivation treatments of chemically cleaned semiconductor surfaces.

8.3.3 Estimation of Surface Current

The measurement of surface potential also allows making a parallel with the current through a diode as a function of SPV. The expression for the surface current from Eq. 5.32 (Section 5.5.2; pg. 79) as $J_s = J_{os} \left(e^{qV_{spv}/kT} - 1 \right)$ indicates that J_s increases exponentially with the surface potential (V_{spv}). Experimental data shown in Figure 8.3 were used to confirm this dependence by plotting the photon flux Φ against SPV V_{spv} (Figure 8.7). The samples were monitored continuously at different days upon treatment with SPM solutions. This result shows the electrical characteristics for sample S8 Si treated by SPM solution compared with fresh Si native oxide at a wavelength of 900 nm. The highest V_{spv} of the sample S8 after SPM treatment was recorded at ~233 mV. The average voltage after the sample S8 was treated with SPM solution (235 mV) remained higher than that of fresh Si native oxide (174 mV).

Derivation of Eq. 5.36 allows the experimental data to be fitted through calculation, as determined in Eq. 5.38. Eq. 5.38 shows that the contribution of surface current is mainly through the collection efficiency of minority carriers (η_L), number of incident photons per cm² per second per unit bandwidth (Φ), and the fraction of these photons reflected 30° from the illuminated surface ($1 - R$). This study identifies the effective saturation current (J_{os}) as a variable parameter that can influence the surface recombination current (J_s) and SRV. J_{os} is obtained as 9.2 nA/cm² (Si treated SPM Day 1), 11.5 nA/cm² (Day 3), 15.3 nA/cm² (Day 14), and 92.1 nA/cm² (Si native) using the values of $\eta_L = 0.8$, $kT/q = 25.9$ mV, and fixed J_o value = 63 pA/cm². Different sample voltages reflect J_{os} values. This study also showed that the theoretical values of Eq. 5.38 are consistent with the experimental values. A higher voltage of the samples will contribute a higher J_{os} value.

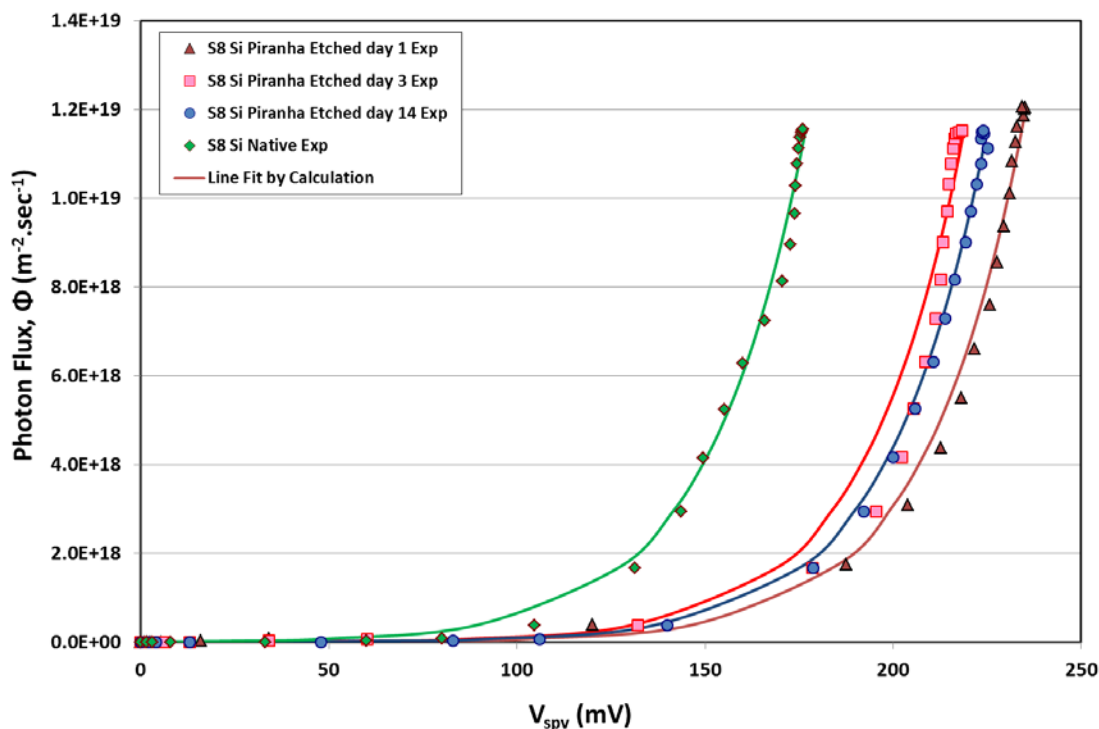


Figure 8.7 The graph of photon flux, Φ vs. V_{spv} for sample S8 Si etched SPM at different days. Points are experimental data and line is obtained from calculation.

The comparison between the photon flux–voltage curves quantitatively shows that the existence of alkyl monolayers at the interfaces dramatically changes sample performance. Experimental data shown in Figures 8.4 to 8.6 were used to demonstrate the expression of surface current of passivated samples by plotting the photon flux (Φ) against SPV V_{spv} (Figure 8.8). The decrease in the voltage of passivated samples is due to the limitation of SPV to penetrate the monolayers and limit the barrier height of the samples. A lower SPV voltage indicates a variance of surface potential because of the surface modification on the samples. Furthermore, the J_{os} values of passivated samples for Si–decene and Si–hex–LB were both 0.1 nA/cm^2 , whereas the J_{os} value for Si–dec–LB was $\sim 0.2 \text{ nA/cm}^2$. This study shows that a small voltage is proportional to low J_{os} value. Moreover, the theoretical data of Eq. 5.38 were not consistent with the experimental values for passivated samples. This theory may not apply to samples with low barrier height of the order of kT .

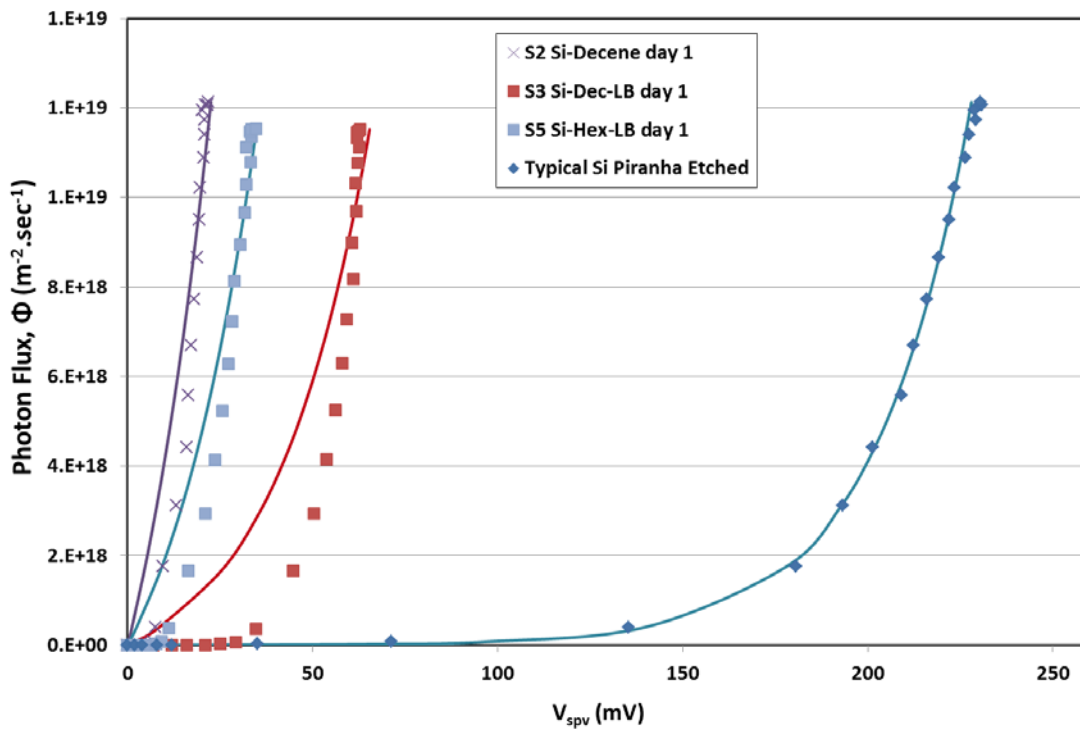


Figure 8.8 The graph of photon flux, Φ vs. V_{spv} for several of passivated samples on Si and typical of etched SPM at day 1. Points are experimental data and line is obtained from calculation.

8.3.4 Estimation of Surface Recombination Velocity

Generally, the silicon/native oxide interface shows a high SRV rate that reflects a significant density of electrically active trap sites [149]. Understanding the Si-SiO₂ interface is important, and the surface electronic properties should be controlled through chemical methods by protecting the surface from unwanted activity. The formation of Si-C bonds is a promising solution to control Si surface from oxidation. By contrast, the treatment of hydrogen-terminated silicon (Si-H) exhibits a very low surface recombination but these surfaces degrade rapidly and are unstable upon exposure to ambient air, as reported by various researchers [29, 37, 150]. Therefore, the Si-H bond surface was not used to evaluate passivation with organic monolayers.

SRV determination is directly related to the number of electronic defects that are present on the surface. The treatment on the crystalline silicon surface with

the organic passivation through the use of alkenes [33, 113, 149] and alkynes [110] exhibit low surface recombination velocities. Yablonovitch *et al.* [150] proposed the following reasons for an extremely low SRV: 1) the presence of a net surface charge, which bends the bands from the surface and reduces the recombination velocity or 2) very few recombination centres on the surface.

This study considers a similar approach for surface states on the n-type semiconductor, wherein the quality of the surface is characterized by the effective saturation current density (J_{os}), as shown in **Eq. 5.36 (Section 5.5.2)**. The voltage dependence of the minority carrier concentration at the edges (located at $x = W$) of the depletion region is as follows:

$$\Delta p(W) = p_{no}(W) \left[\exp\left(\frac{qV}{kT}\right) - 1 \right] \quad \text{Eq. 8.1}$$

If $p_{no} \approx n_i^2/N_D$ and with the combination of **Eq. 5.32** and **Eq. 5.36**, the recombination current into the surface (at low injection) is as follows:

$$J_s(\Delta p)|_{x=W} = \frac{J_{os} N_D}{n_i^2} \Delta p \quad \text{Eq. 8.2}$$

The effective SRV on the front surface of n-type silicon compared with the boundary condition for a non-diffused surface [$J_s = qS_p = qS_p \Delta p$] is as follows [82, 83]:

$$S_{fs} = \frac{J_{os} N_D}{q n_i^2} \quad \text{Eq. 8.3}$$

The inverse C_L value can be determined from Figure 8.9 by measuring J_{os} and interpreting the effective SRV S_{fs} value.

The surface recombination current (J_s) is used to estimate SRV at the surface by measuring the intensity dependence of the SPV. The determination of diode current is directly proportional to SRV at the Si-SiO₂ interface. The contactless diode equation consists of the combination of interface dark current at the

surface and bulk plus collection efficiency that is used to predict the SRV at the front surface using KP method. The comparison of SRV characteristic of sample S8 before and after SPM treatment is shown in Figure 8.9. The slope of the C_L linear curve (Eq. 5.37) is shown in the figure of the photon flux (Φ) over the exponential qV/kT . The inverse value of C_L is used to estimate the J_{os} and SRV values (Table 8.1). The determined range of SRV value consists of 97,866 cm/s (for Day 1), 122,635 cm/s (for Day 3), and 163,672 cm/s (for Day 14). Moreover, 982,799 cm/s was obtained for S8 Si native oxide. The increase in SRV values is proportional to the days of air exposure after the samples are treated with SPM solution. A sample with higher recombination will reduce V_{spv} from the sample, which is considered as recombination losses (Table 8.1). The J_{os} values also showed a similar increasing trend, which is proportional to the SRV values. Determination of these SRV values via quantitative analysis indicates the changes of the surface properties after surface treatment.

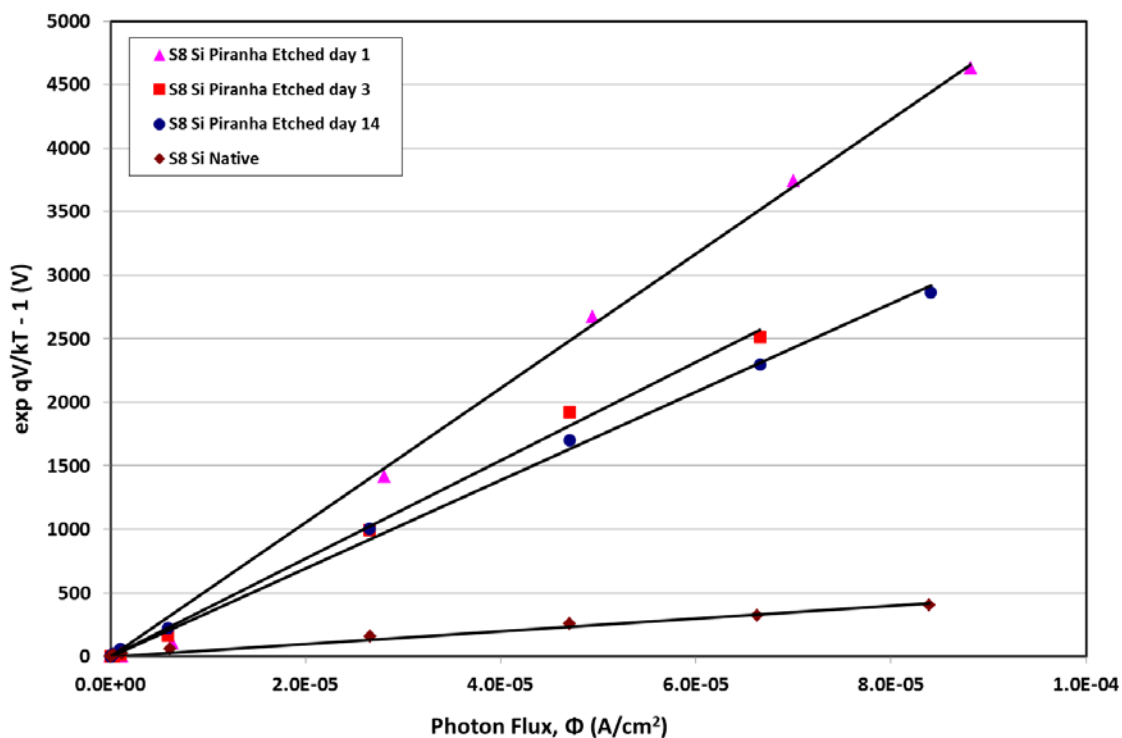


Figure 8.9 Estimation of SRV at the front surface for samples (i) Si etched with SPM solution at day 1, 3 and 14; (ii) Si native oxide at 900 nm ($U_p = 1000$ cm/s).

Table 8.1 Summary results of V_{spv} , Q_{sc} , J_{os} and SRV values for Si samples with SPM treatment

| Samples S8 | Q_{sc} (10^{+10} C/cm ²) | V_{spv} (mV) | J_{os} (nA/cm ²) | S_{fs} (cm/s) |
|----------------------|--|-------------------|-----------------------------------|--------------------|
| Si SPM Etched day 1 | 3.4 | 233 | 9.2 | 97,866 |
| Si SPM Etched day 3 | 3.4 | 220 | 11.5 | 122,635 |
| Si SPM Etched day 14 | 3.4 | 224 | 15.3 | 163,672 |
| Si Native Oxide | 3.2 | 174 | 92.1 | 982,799 |

i. Surface Recombination Velocity on Different Passivated Layers

Long bulk lifetime ($> 1000 \mu\text{s}$) *Si-Fz* wafers were used to evaluate the effects of various surface treatments on the electrical properties of the Si surface. Table 8.2 shows several results of surface passivation of Si (111) oriented in contact with different hydrophobic layers. Each sample exhibits different surface properties as explained in **Section 8.3.2**. The SRV on Si surfaces (S2) terminated with C_{10} were measured and determined as the lowest SRV value after the sample was exposed for 24 h to air. The surface was depleted with a small band bending for samples S2 Si-decene. Some charges filled the interface trap and recorded a low Q_{sc} (determined from **Eq. 2.42; pg. 20**) of $\sim 2.6 \times 10^{+10}$ C/cm² with an effective saturation current density (J_{os}) of 0.1 nA/cm². However, a more complex behaviour was observed on sample S3 (Si surface terminated with decene and LB films). This S3 Si-dec-LB behaved similarly, with a slightly higher SRV of $\sim 1,903$ cm/s.

Table 8.2 Summary results of V_{spv} , Q_{sc} , J_{os} and SRV values for Si samples with several passivated surfaces

| Samples (day 1) | Q_{sc} (10^{+10} C/cm ²) | V_{spv} (mV) | J_{os} (nA/cm ²) | S_{fs} (cm/s) |
|--------------------|--|-------------------|-----------------------------------|--------------------|
| S2 Si-decene | 2.6 | 21 | 0.1 | 1,020 |
| S2 Si SPM Etched | 3.4 | 229 | 13.2 | 140,963 |
| S3 Si-dec-LB | 2.8 | 63 | 0.2 | 1,903 |
| S3 Si SPM Etched | 3.4 | 221 | 13.2 | 140,425 |
| S5 Si-hex-LB | 2.7 | 32 | 0.1 | 1,056 |
| S5 Si SPM Etched | 3.4 | 222 | 8.1 | 85,912 |

By contrast, sample S5 (Si-hex-LB) also recorded low Q_{sc} , indicating a low SRV (1,056 cm/s) on the 1st day. Although this sample recorded low SRV on Day 1, the passivation layer of hexane with LB films is not stable (rapidly changes in band bending) as previously reported in **Section 8.3.2(c)**. A high J_{os} value indicates high SRV as previously reported for the Si sample treated with SPM solution and Si native oxide. SRV estimation via contactless KP method has generated important information about the surface properties after treatments. Table 8.2 also shows that the SRV value determined from the surface recombination current (J_s) indicates a significant relationship between the surface properties and SRV, wherein SRV is principally dependent on the elementary properties of the surface defects.

ii. Comparison Measurements of Surface Recombination Velocity

The steady-state photo-conductance decay creates an excess electron-hole pair concentration by an optical flash lamp illumination. The PC signal is proportional to the number of excess electron-hole pairs integrated to the

entire surface of the sample. QSSPC that was used in this study functions accurately and is suitable for short lifetimes ($< 200 \mu\text{s}$) [151]. In the QSSPC technique, the effective lifetime is determined by exposing a multiple light intensity until a saturation value of a lifetime is achieved. Table 8.3 shows a summary of the different passivated samples on the Si surface, which is measured as the recombination lifetime by the PCD method. The calculation of the lifetime is based on the SRV, with the assumption that both sides of the surface are equally the same ($S_{rs} = S_{fs} = S_s$). This table shows that the highest effective lifetime was recorded by sample S2 (Si-decene) with $11.24 \mu\text{s}$, followed by sample S3 (Si-dec-LB) with $8.61 \mu\text{s}$, and sample S5 (Si-hex-LB) with $10.51 \mu\text{s}$. Good agreement was observed between the SRV calculated from the PCD lifetime tester and KP data for all passivated samples. Higher SRV was measured by the PCD, which resulted in a lower calculated value by the KP method. The change in recombination with different surface terminations is due to the surface coverage, as suggested by Nemanick *et al.* [152].

Table 8.3 A summary of the different passivated sample on the Si surface with the effective recombination lifetime and implied SRV as measured by the PCD and KP method

| Samples | PCD Method | | | KP Method |
|--------------|--|--|--------------------------------------|---------------------------------------|
| | <i>Measured</i> τ_{eff} (μs) | <i>Implied</i> τ_{os} (μs) | <i>Implied</i> S_{fs} (cm/s) | S_{fs} <i>Measured</i> (cm/s) |
| S2 Si-decene | 11.24 | 19.44 | 1,350 | 1,020 |
| S3 Si-dec-LB | 8.61 | 12.72 | 2,064 | 1,903 |
| S5 Si-hex-LB | 10.51 | 17.35 | 1,513 | 1,056 |

The recombination lifetime results of passivated samples were slightly higher (Table 8.3) compared with those of several samples of etched Si SPM (Table 8.4), which are expected to have a low SRV on the passivated surfaces. A slightly higher recombination lifetime indicated better surface coverage because of the formation of a straight chain of alkyl monolayer groups as interface layers on the Si surface. Thus, a lower recombination lifetime resulted in higher SRV values for several Si samples treated with SPM solution and native oxide (Table 8.4). Although the treatments of the SPM etched on the Si surfaces are the same for all samples, the SRV value samples S2 and S3 are > 140,000 cm/s compared with samples S5 and S8 (etched Si SPM). Both S2 and S3 samples recorded higher SRV values via the KP method, which was further validated by the PCD method. Both samples also showed higher calculated SRV values in the PCD method (S_{fs} column, Table 8.4). By contrast, both S5 and S8 samples generated lower SRV values in both measurements. Thus, consistent results were obtained for all the samples tested using both methods.

Table 8.4 A summary of several sample of Si treated with SPM etched and native oxide with the effective recombination lifetime and implied SRV as measured by the PCD and KP method

| Samples | PCD Method | | | KP Method |
|------------------|---|---|--------------------------------------|---------------------------------------|
| | <i>Measured</i> τ_{eff} (μ s) | <i>Implied</i> τ_{os} (μ s) | <i>Implied</i> S_{fs} (cm/s) | S_{fs} <i>Measured</i> (cm/s) |
| S2 Si SPM Etched | 3.52 | 4.06 | 6,472 | 140,963 |
| S3 Si SPM Etched | 3.47 | 3.99 | 6,580 | 140,425 |
| S5 Si SPM Etched | 3.62 | 4.19 | 6,266 | 85,912 |
| S8 Si SPM Etched | 3.55 | 4.10 | 6,409 | 105,257 |
| S8 Si Native | 3.32 | 3.79 | 6,922 | 982,799 |

iii. Relationship of Kelvin Probe Measurement and Sinton Photo-Conductance Lifetime Measurement

The experiments were conducted using the same samples for both measurements. An experimental procedure was performed for each Si surface treatment, wherein the first characterization step was examined using Sinton measurement before proceeding with KP measurement. The difference between the two measurements is most probably due to the effective lifetime and measured full area of the sample that is attributed to the Sinton measurements. The KP method was measured at a smaller area (under the probe tip) and was more sensitive to minor changes in the passivation layer, which can affect the recombination lifetime [153].

Figure 8.10 shows a graph of $1000/S$ (KP) vs. $1000/S$ (Sinton) of the inverse SRV data determined from KP and Sinton measurements. A linear line corresponds to equal values obtained by the two measurement techniques and is marked with a dashed line. Although KP measures SPV and Sinton measures the photo-conductance lifetime, the inverse SRV data between the two measurements are correlated. The SRV values for Si-decene and Si-hex-LB samples, determined via the KP method, are more accurate (above a dashed line). By contrast, the SRV values below the dashed line show better accuracy with the Sinton method for samples Si native oxide, etched Si with SPM, and Si-dec-LB). The surface lifetime was estimated and compared with the measured SRV data by considering the $S_{fs} = S_{rs} = S_s$ inline as the “double-sided” wafer used in this experiment. This study showed linear correlations in the presence of surface recombination effects for all samples, i.e., Si native oxide and etched SPM. The illumination method is different (i.e., continuous illumination on the samples), namely, trapped charges in the surface states release slow detrapping upon deactivation of light. Thus, the surface recombination effect in the surface states of the silicon is a main contributing factor for the differences in SPV and PCD measurements. Earlier studies by Buczkowski *et al.* [154] show that both techniques can result in an agreement within 15% if the influence of surface recombination effects is neglected.

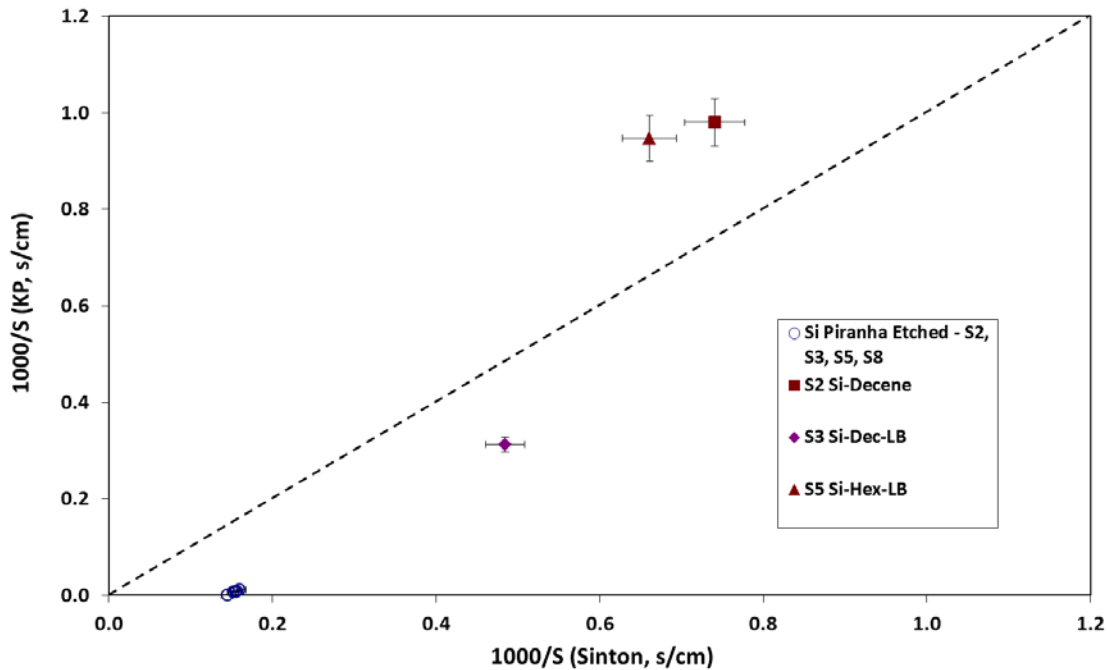


Figure 8.10 A measurement comparison of SRV - summary of inverse SRV data of graph of 1000/S (KP) vs. 1000/S (Sinton).

The photo-generated minority carrier in the KP method is generated by SPV upon illumination. The absorbed photons generate electron-hole pairs that diffuse toward the illuminated surface and are separated by the electric field in the depletion region. The carrier changes the V_{CPD} between the tip and the sample by changing the surface band bending. The induced SPV is a function of the excess minority carrier concentration. In this study, the collection efficiency of minority carrier (η_L) was used to represent the dependence of excess minority carrier concentration.

The SPV diffusion length was estimated by obtaining the experimental effective diffusion length and assuming that SRV was ~ 1000 cm/s. The intensity dependence on the SPV constant mode of operation was applied. The diffusion length was obtained from the intercept point of $1/\alpha$ of the straight line. The minority diffusion length (L_p) for the experiments in the KP method was determined in the wavelength interval between $920 \text{ nm} < \lambda < 1020 \text{ nm}$ at $159 \text{ }\mu\text{m}$ (SPV = 83.4 mV), $152 \text{ }\mu\text{m}$ (SPV = 58.6 mV), $188 \text{ }\mu\text{m}$ (SPV = 52.5 mV),

207 μm (SPV = 44.7 mV), and 174 μm (SPV = 38.5 mV). These results were compared with the inverse collection efficiency (η_{lc}^{-1}), wherein the average minority diffusion length was $\sim 191 \mu\text{m}$. The estimation of the average lifetime minority carrier (τ_p) of each sample was 27 μs using the following equation:

$$L_p = \sqrt{D_p \tau_p} .$$

SRV determinations were performed using a contactless KP method through SPV measurements. SRV was estimated from the slope of a linear curve of the photon flux (Φ) over the exponential qV/kT . A range of the SRV value determined for several Si samples treated with SPM solutions was 85,912 cm/s to 140,963 cm/s. The SRV value was estimated to be much lower than that of Si native oxide (982,799 cm/s) because of the chemical treatment of the surfaces. The SRV for samples with the Si passivated layer was much lower for S2 (Si-decene; 1,020 cm/s), S3 (Si-dec-LB; 1,903 cm/s), and S5 (Si-hex-LB; 1,056 cm/s).

An excess electron-hole pair concentration is created in the PCD technique using a short light pulse from a flash lamp, and the effective lifetime (τ_{eff}) is obtained from the slope of decay curve. The breakdown of effective lifetime (τ_{eff}) is the sum of two recombination lifetime components, i.e., bulk and surface lifetime. The PC signal is proportional to the excess carrier concentration. τ_{eff} mainly depends on the bulk defects and impurities in the bulk lifetime (τ_b) and the surface quality, i.e., sample thickness and carrier mobility through the surface lifetime (τ_s) component. This τ_{eff} value is applicable for any optical absorption depth, if the excess carrier density has sufficient time to distribute uniformly.

The τ_s value can be determined using the lifetime value from KP measurement as a bulk lifetime. τ_s consists of two sub-components of a lifetime based on the standard kinetic argument, i.e., the effective lifetime of the surface recombination (τ_{os}) and hole-diffusion lifetime (τ_{diff}). The generation rate $G(\lambda, x)$ (Eq. 3.13 in Section 3.3) is a function of distance of x from the surface where the carrier generation occurs within a distance 5 μm to 10 μm of the surface. If the recombination lifetime (τ_{os}) is very short, the time is insufficient to establish

uniform distribution and the surface traps will react rapidly while being filled with minority carriers during a period that is much shorter than τ_{diff} .

Furthermore, a non-uniform distribution of carriers can be assumed on the passivated surface layer because excess carriers may reach the surface and diffuse at lengths shorter than the thickness of the samples. Thus, τ_{diff} is neglected. The Si wafer is double-sided and the surface recombination is assumed to occur in both surfaces because $S_{fs} = S_{rs} = S_s$. Furthermore, the sample was completely immersed in the solution during chemical passivation stages. Thus, the SRV can be estimated by the following equation: $S_s = H/2\tau_{os}$.

8.4 Chapter Summary

This study derived the surface current in **Eq. 5.36** and was fitted to the KP method. The SPV measurement demonstrated a novel approach in quantitative analysis and a new technique to determine the SRV value for passivated semiconductor samples. The collection efficiency of minority carriers (η_L), a component of the surface current, is an important tool to estimate the diffusion length and SRV for *n-type* silicon. The barrier height and SPV measurement using KP were able to predict the effective saturation current (J_{os}), an important parameter to measure the surface recombination of the sample.

In summary, alkyl passivated with Si-decene as an interface layer showed promising results and displayed strong stability against oxidation in air. This material possesses smaller surface potential (21 mV to 28 mV), lower surface charge ($2.6 \times 10^{+10}$ eV/cm²), and lower SRV (1,020 cm/s) compared with Si SPM etched on naturally oxidized silicon. The deposition of LB with a stable foundation of Si-C bond, i.e. sample Si-dec-LB, shows better reproducibility, moderate SRV (1,903 cm/s), and effective saturation current density (J_{os}) of 0.2 nA/cm². The calculated surface state density (Q_{sc}) of all passivated monolayer interface is lower than the SiO₂/Si interface. KP was shown to be an alternative instrument that can be used to monitor changes or modifications on the semiconductor surface. SRV determination via the KP method was

validated by comparing the lifetime measurement using Sinton. The inverse of SRV data is correlated between the two measurements, where KP measures SPV and Sinton measures photo-conductance lifetime.

Chapter 9 Charge Trapping Passivated Silicon Surface via Illumination of Dye Monolayers

9.1 Introduction

A passivation treatment on the silicon surface will improve the surface properties and directly reduce the number of unsaturated dangling bonds. These passivation treatments, such as RCA cleaning, SPM solutions, and terminated hydrogen application, create a new surface environment for the deposition of the organic monolayer and the LH structures on the semiconductor surfaces. LH materials consist of a large number of pigment molecules that absorb the energy of the incident light and transfer it to the RC where chemical reactions occur. The principle of LH that enhances the optical absorption cross-section can be found in many organisms with photochemical apparatus. The deposition of LH materials is an alternative way to minimize the amount of silicon required in the manufacture of solar cells [4]. LH materials are organic thin films that can be deposited on a solid substrate by several techniques, such as thermal evaporation, sputtering, electrodeposition, molecular beam epitaxy, adsorption from solution, LB technique and self-assembly molecules (SAM).

This chapter describes the charge-trapping mechanism and the detrapping in several passivated samples by alkyl monolayers and dye monolayers of the LB films deposited on the silicon surface. The focus of this chapter is on the amount of charge injected into the passivated layers that result in LH properties, which are measured via contactless KP.

9.2 Understanding of Fast and Slow Charge Trapping

9.2.1 Literature Review on the Charge Trapping

To our knowledge, only a few studies have been published on the charge trapping processes that are discussed in this chapter. The closest publications may be on the charge trapping processes that were discussed in early modern semiconductor literature.

For example, Garrett and Brattain [155] assumed that the surface states are associated through trapping with the recombination of minority carriers at the surface. They also proposed that the charge trapping centres were either donor type lying high in the band or acceptor type lying low or both. The current flow between the conduction band and the traps in low-lying acceptors as trapping centres will be proportional to the number of electrons in the conduction band on the surface. The current flow for the number of empty traps will be much less than that between the traps and the valence band, which is proportional to the number of holes and occupied traps. Surface potential variations affects the electron densities near the surface; but surface recombination should be unaffected by changes in surface potential that do not affect the number of traps.

Bardeen and Brattain [156] demonstrated that the surface region of the etched germanium surface contains a density of states and capture cross-sections of $\sim 10^{11}$ per cm^2 and 10^{-14} cm^2 , respectively [38]. The formation of states can be divided into fast states and slow states. The fast states were rapidly formed at equilibrium with the region space charge, wherein the decay time is in microseconds or less at room temperature. By contrast, the slow states occur much longer in terms of the relaxation time from seconds to hours and have a larger density of states compared with fast states. Similar states are found on an etched silicon surface [157].

Horng-Sen and Chih-Tang [158] also divided the charge trapping mechanism on the MOS transistor structure into fast and slow surface states. They described the surface states on the surface ($x = 0$) as fast surface states or

interface states, which can readily exchange charges with the conduction and valence bands. States that are located at a certain distance away from the interface states ($x = -x$) are known as slow surface states or oxide traps because they cannot readily exchange charges directly with the conduction or valence bands. A fast surface state with an energy level on the surface will act as an SRH recombination centre. This state will thermally capture electrons from the conduction band and trap them. Similarly, holes generate transitions between the surface states and the valence band states. A trapped electron in the fast interface surface state can also tunnel into an empty oxide trap located in the oxide at some distance away from the interface and vice versa.

9.2.2 Calculating Lifetime Decay for Charge Trapping

The interpretation of charge trapping and detrapping mechanism on the semiconductor surface can be related to the lifetime in an exponential decay functions as follows:

$$\frac{dV}{dt} = -\frac{V}{\tau} \tag{Eq. 9.1}$$

$$V(t) = V_0 \exp\left(-\frac{t}{\tau}\right) \tag{Eq. 9.2}$$

where $V(t)$ is time dependence of the work function; V_0 is the initial value of work function and τ is the lifetime constant.

Several values of the work function, i.e., V_0 , V_1 , and V_2 , were introduced to fit the actual experimental data. Thus, the specific equation with two lifetimes is identified as follows:

$$V(t) = V_0 \mp [(V_1 - V_0) - V_2] \exp\left(-\frac{t-t_0}{\tau_1}\right) \mp V_2 \exp\left(-\frac{t-t_0}{\tau_2}\right) \tag{Eq. 9.3}$$

where V_0 , V_1 , and V_2 are different values of the work function, t_0 is the decay time in seconds, τ_1 and τ_2 are the two lifetime constants applied for both charge trapping and detrapping processes, and "⌘" represents the light and dark switching mode.

9.3 Results and Discussion

9.3.1 Absorption Spectrum Measurements

Carbocyanine dyes were deposited on hydrophobic glass slides using the LB monolayer deposition technique to represent the fluorescent layer and the silicon layer of the light trapping scheme, respectively. The absorption spectra of the dye were obtained using Avantes spectrometer AvaSpec-2048, wherein the solution was diluted to a point where absorption intensity was < 0.1 . The spectra were measured in the solution because of the difficulty in measuring dye monolayer absorbance on the silicon. The absorption spectra of 1-decene in hexane solution were measured using a UV-Vis spectrometer (UV-1601, Shimadzu). The absorption spectra of single materials, i.e., decene and DiO, were used as references to identify the absorption region. Several dyes were shown on the absorption spectra, including mixed DiO:SA, DiO, SA, and decene (Figure 9.1).

Figure 9.1 shows that the absorption region of mixed DiO:SA is ~ 400 nm to 550 nm, wherein the peak absorbance is at the wavelength of 440 nm to 450 nm. A shift in peak absorbance for sample DiO mixed with SA occurs compared with the single DiO peak absorbance at 482 nm. Two distinct peaks are present in the absorption spectrum at 440 nm to 450 nm and 480 nm to 500 nm. Similar evidence of two distinct peaks was also reported by Danos *et al.* [135], which was attributed to the presence of monomers and dimers in the layers. The strong maximum peak of the dimer shifted relative to the maximum of the monomer from 500 nm to the region of 440 nm to 450 nm. No absorption peak was observed in the SA sample; thus, the SA compound does not absorb in this region.

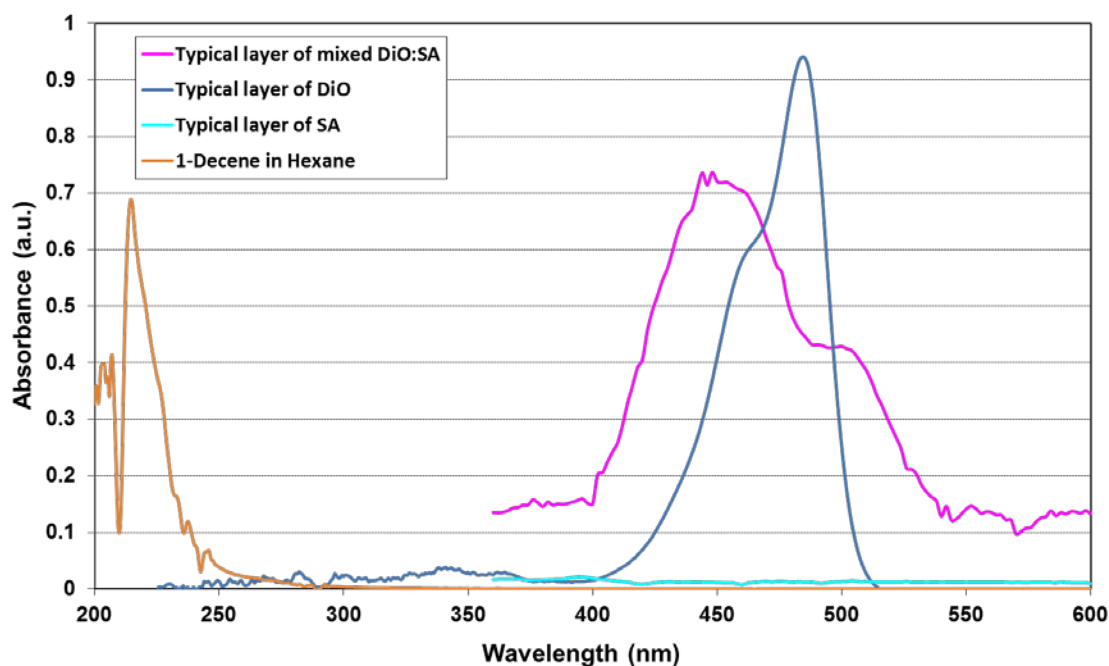


Figure 9.1 Absorption spectrum of several dyes including mixed of DiO:SA, SA, DiO and 1-decene in hexane using Avantes and UV-Vis Spectrometer.

9.3.2 Charge Trapping by Illumination of Dye Monolayers

The interface layer of alkene monolayers has an important function in the formation of LB films on a silicon surface. The following silicon n-type substrates are prepared to form a hydrophobic surface: (i) silicon with organic passivation of the 1-decene monolayer and (ii) silicon native oxide with HMDS vapours. The Si-C bond structure possesses a functional group (LB films) that has strong affinity to the substrate and anchors the molecules to it. Thus, the investigation of stability of the interface layers is crucial because the LB films were physically formed with physisorbed bond.

The method has two advantages in monitoring surface modification. Surface charging can be measured by continuously monitoring the position of the Fermi level of the illuminated semiconductor. The samples can also be

measured in the dark, which provides information about the decay process upon deactivation of light. Thus, the samples of passivated organic monolayer and Si native oxide on the silicon surface were subjected to treatment, and their resulting surface properties were monitored by KP method. The minus sign indicates that the work function of the the tip is larger than for the silicon surface, which is due to the *n-type* silicon material used in this study.

i. Silicon Native Oxide as Control

An investigation on charge trapping and detrapping mechanism was conducted on the sample silicon native oxide. This measurement is important for comparison and reference purposes.

Figure 9.2 shows the initial time for the work function of this sample in the dark. A rapid decrease in the signal was observed upon illumination because of the excess electrons and holes produced by the light in the conduction and valence band, which flatten the semiconductor band. The flattening of the bands upon irradiation is considered as a fast process of trapping the electron in the surface states of the silicon native oxide. The band flattening disappears when the light is extinguished, and the signal rapidly increases to a level similar to the case before illumination. This mechanism reflects the decrease in carrier density, which was caused by recombination of excess holes and electrons in the valence and conduction bands. Upon repetition of the switching on and off of the light, the mechanism of band flattening occurs again even during the relaxation time between measurements for 200 s. A similar phenomenon in the SPV plot was observed, which indicates that charge trapping and detrapping are fast processes. The signal returns almost to the previously recorded baseline after 500 s. A similar charge-trapping mechanism was described by Haynes and Hornbeck [159].

This sample was measured at 900 nm where the absorbed photon induces the formation of free carriers by creating electron-hole pairs in the bulk. The minority hole carrier diffused and was swept toward the surface from the bulk and/or redistributed within the surface. The potential decreased across the

surface SCR and the surface potential changed [13] because the electric potential and charge distribution are interrelated through Poisson and continuity equations. The illumination-induced SPV value was ~ 182 mV, which indicates that the surface potential of the sample was changed. A similar surface potential response has been reported in **Section 8.3.2(a)**.

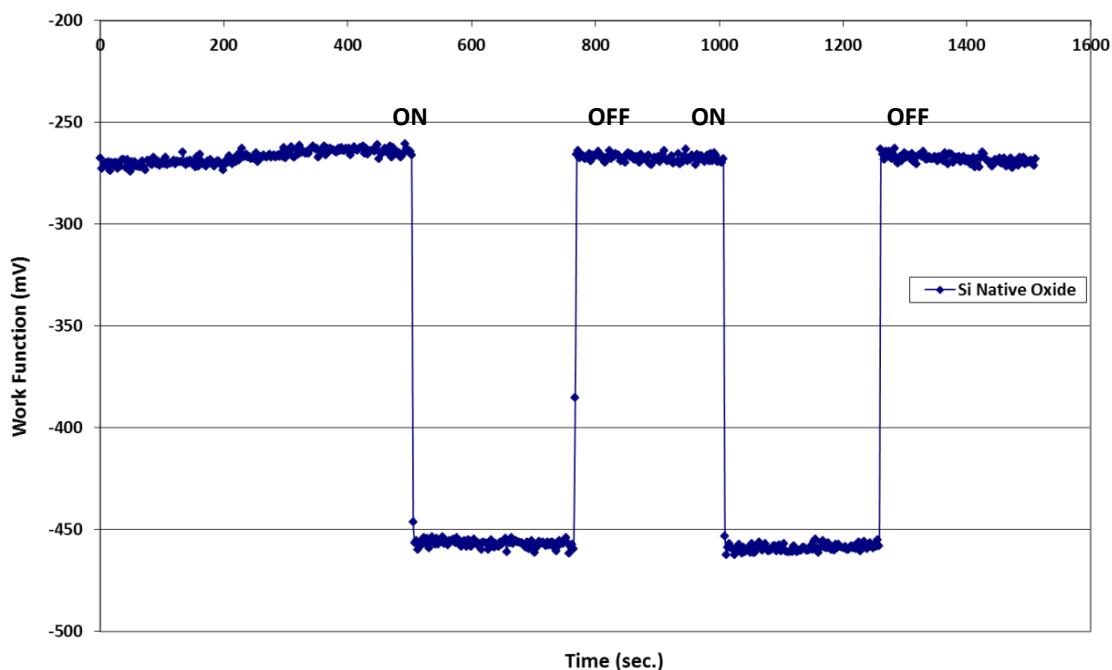


Figure 9.2 SPV measurements on silicon *n-type* Si native oxide at 900 nm wavelength.

ii. Silicon with Decene as Interface Layer

A sample of 1-decene monolayer on the silicon surface was characterized after 48 and 504 h of exposure to air (Figure 9.3). The SPV measurements were conducted at a wavelength of 900 nm with the same intensity as Si native oxide. A change from the baseline work function for both samples indicates a different distribution of carrier concentration before it reaches equilibrium in KP measurements.

Charge Trapping on Passivated Silicon Surface via Illumination of Dye Monolayers

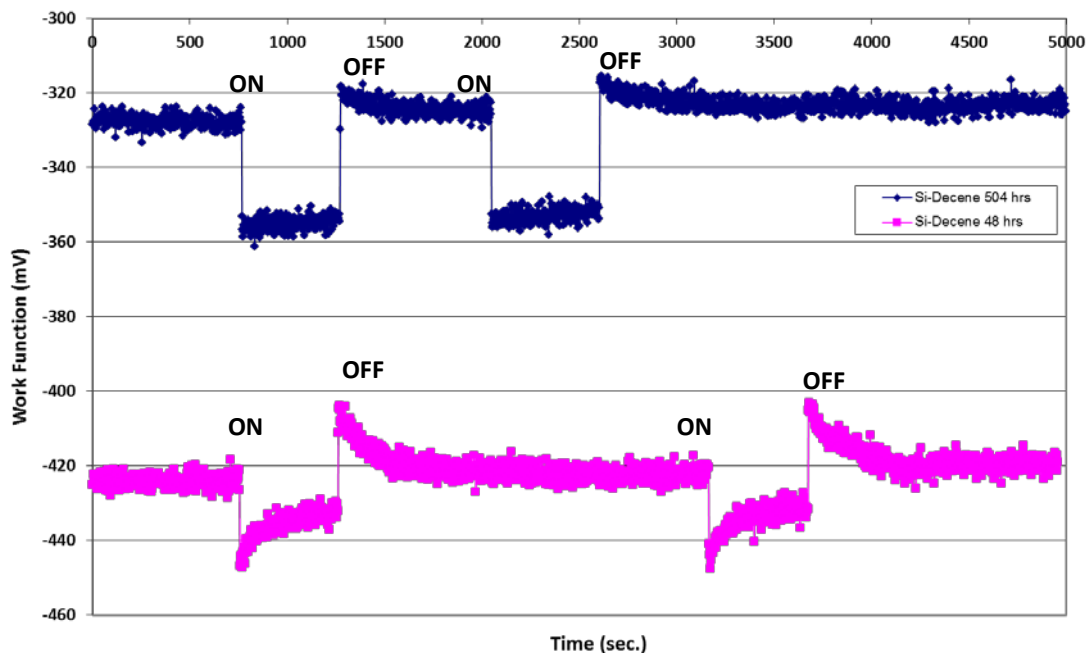


Figure 9.3 SPV measurements on 1-decene monolayers of silicon surface (after 48 and 504 hours exposed in air) at wavelength 900 nm.

The initial time for the signal was designated in dark conditions. Upon illumination, a rapid decrease in signal is due to the light-induced flattening of the bands of the samples. The subsequent slow exponential increase in work function is due to slow extra charging of the carriers. The resulting Q_{sc} and Q_{ss} changes are due to both carrier injection and change in surface potential. The illumination-induced SPV value is much smaller, i.e., 25 and 31 mV for samples on 48 and 504 h, respectively. The induced SPV depleted the surface. The minority photo-carriers were swept toward the surface where the majority carrier density was lower and the chances for recombination were minimal. Some excess electrons but no excess holes were captured in the alkene/silicon interface layer. Q_{ss} became more negative and Q_{sc} become more positive. Trapping of charges at the illuminated sample surface shifts the Fermi level of the 1-decene monolayer sample. The signal increases in the first few seconds and increases exponentially with slow charging until saturation.

When the shutter was closed, the signal suddenly increased and reached the optimum point of the work function before decay over time. The mechanism of the extinguished light is reflected to a normal recombination process because of the recombination of the excess holes and electrons in the valence and conduction bands. This study identified two lifetimes which were fitted to the actual experimental data shown in Figure 9.4. The lifetime decay occurs much slower with lifetime constant at 107 and 301 s for 48 h. These lifetimes were applied for both generation of charge trapping and lifetime decay of the charge detrapping. The changes of the occurrences of the charge detrapping depend on the Q_{sc} on the edge of the SCR. The low Q_{sc} is recorded in the range of $2.6 \times 10^{+10} \text{ C/cm}^2$ to $2.7 \times 10^{+10} \text{ C/cm}^2$ for two different sampling times. Although the alkene monolayer samples were measured at two dissimilar times, the mechanism of the charge trapping and detrapping still occurred with minor changes in the surface potential. The lifetime decay was a slow process with lifetime constant of 61 and 105 s for 504 h (Figure 9.5). Approximately 45% to 65% reduction of the lifetime decay was observed, which shows the least amount of oxidation that occurred after a longer exposure of 21 d. A similar finding by Honeyman *et al.* [160] for the decene monolayer showed that the least amount of oxidation occurred after 19 d. The relative increase in carbon amounts on the surface partially blocked the penetration of oxygen molecules into the alkene monolayer/Si interface. The changes in the relative amount of carbon in the samples were monitored by XPS measurements.

This result showed that the SPV of the 1-decene monolayer is much lower compared with that of the silicon native oxide. A low SPV obtained for 1-decene monolayers is due to the reduced number of states by surface passivation and replaces the silicon–oxygen bonding with Si-C bonding on the dangling bonds. A low SPV indicated a small band bending for alkyl monolayers. A similar surface potential was obtained as previously reported in **Section 8.3.2(b)**. A difference in SPV value indicates a variation of the surface potential because of the surface modification on the samples. Indirectly, this phenomenon may reduce surface recombination and surface potential of the samples. A high surface potential of the silicon native oxide reflects the distribution of carrier density in the surface states, which is caused by surface recombination of excess holes and electrons. Thus, the alkene monolayer is

stable, has strong affinity to silicon, and anchors the molecules to it. A similar slow degree of electron trapping on 1-alkenes on H-terminated Si surfaces was observed but the lifetime values were not clearly indicated, as observed by Sieval *et al.* [113].

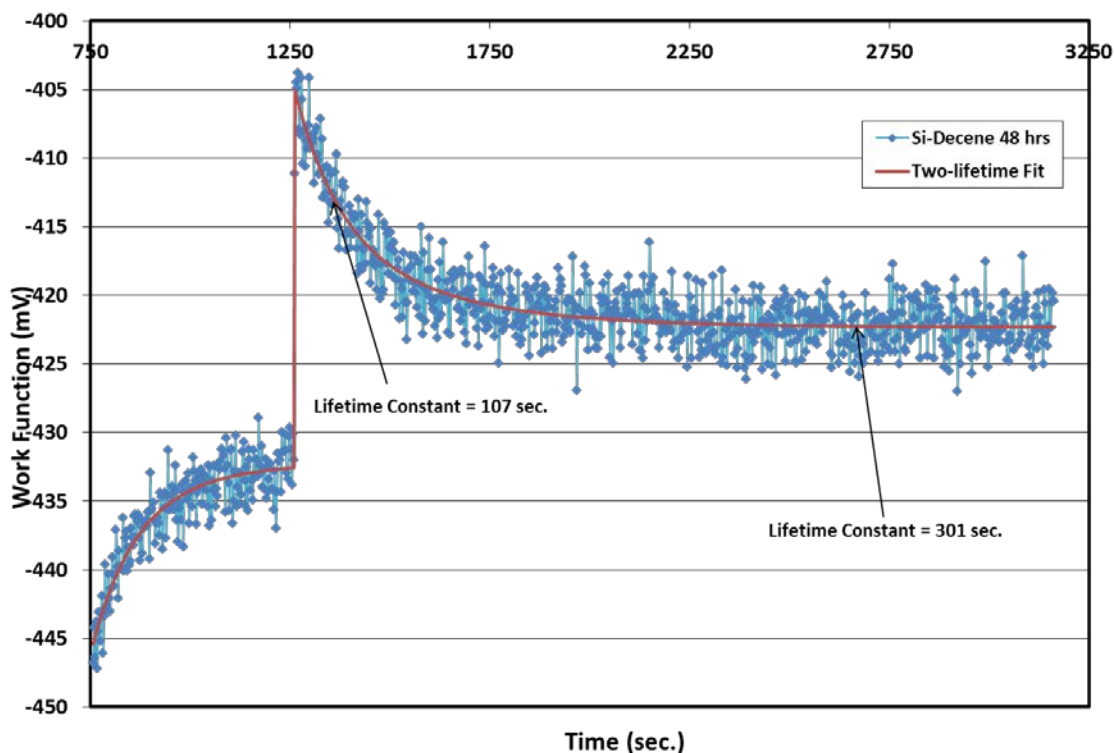


Figure 9.4 Two lifetimes fitted to the experimental data for generation charge trapping and lifetime charge detrapping for sample Si-decene (48 hours) at wavelength 900 nm.

The SPV of the 1-decene monolayer sample that was exposed to air for 504 h was slightly higher but still below the SPV value obtained by Bin *et al.* [105]. This study reported that Si-decene (C_{10}) was prepared without catalyst and SPV rapidly changed from 80 mV to 160 mV, as characterized by KP. Thus, the surface potential increases because the water or oxygen molecules are capable of penetrating through the shorter non-branched monolayers and oxidizing the Si surface. A low barrier height with Lewis catalyst is present in the formed

alkene monolayer on the silicon surface, which prolongs the stability against oxidation in air [111, 122]. These results were consistent with the IR spectra and contact angle results reported earlier in **Sections 6.4.1** and **6.4.2**. Furthermore, these monolayers maintain low inherent reactivity of the oxide surface toward the Si-C bond.

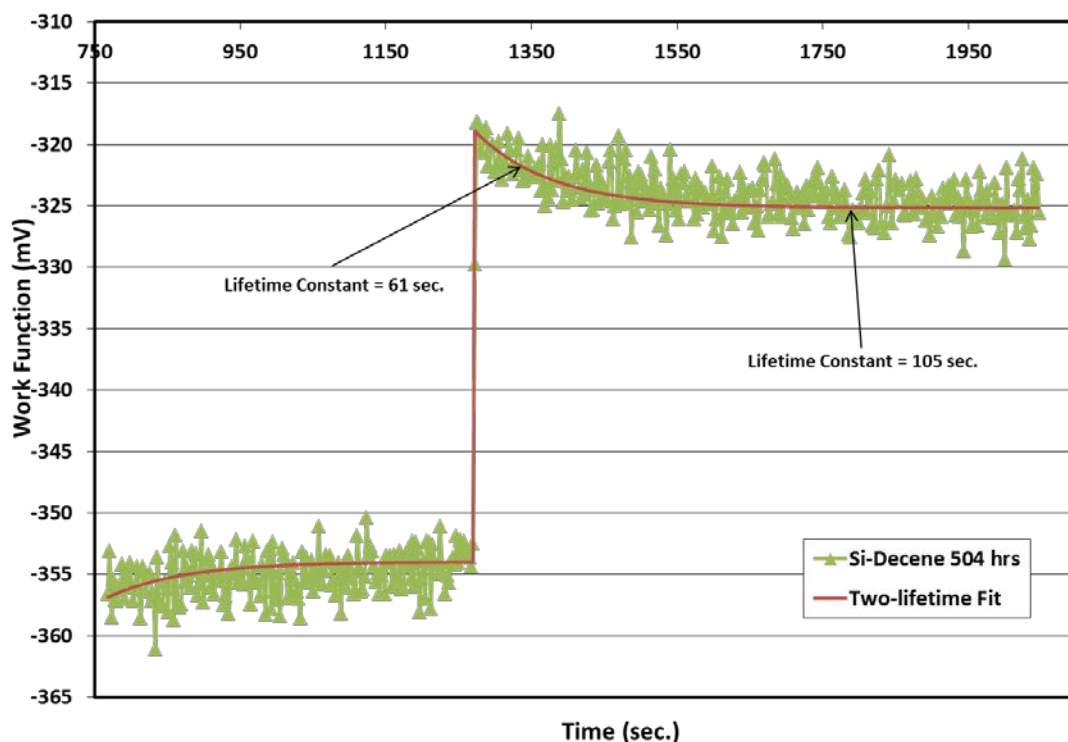


Figure 9.5 Two lifetimes fitted to the experimental data for generation charge trapping and lifetime charge detrapping for sample Si-decene (504 hours) at wavelength 900 nm.

iii. Silicon-Decene with Deposited LB Films of Dye

The charge trapping mechanism of the Si-dec-2L 1.5 DiO:SA sample was measured at 450, 500, and 600 nm (Figure 9.6). The SPV signal upon illumination shows upward growth where it increases rapidly in the first few seconds and grows exponentially over time. A slow exponential increase in SPV

signal resulted in higher band bending than the baseline. The surface potential in the LB films/silicon interfaces indicated a positive sign for the CPD V_{CPD} , which is equal to V_{spv} .

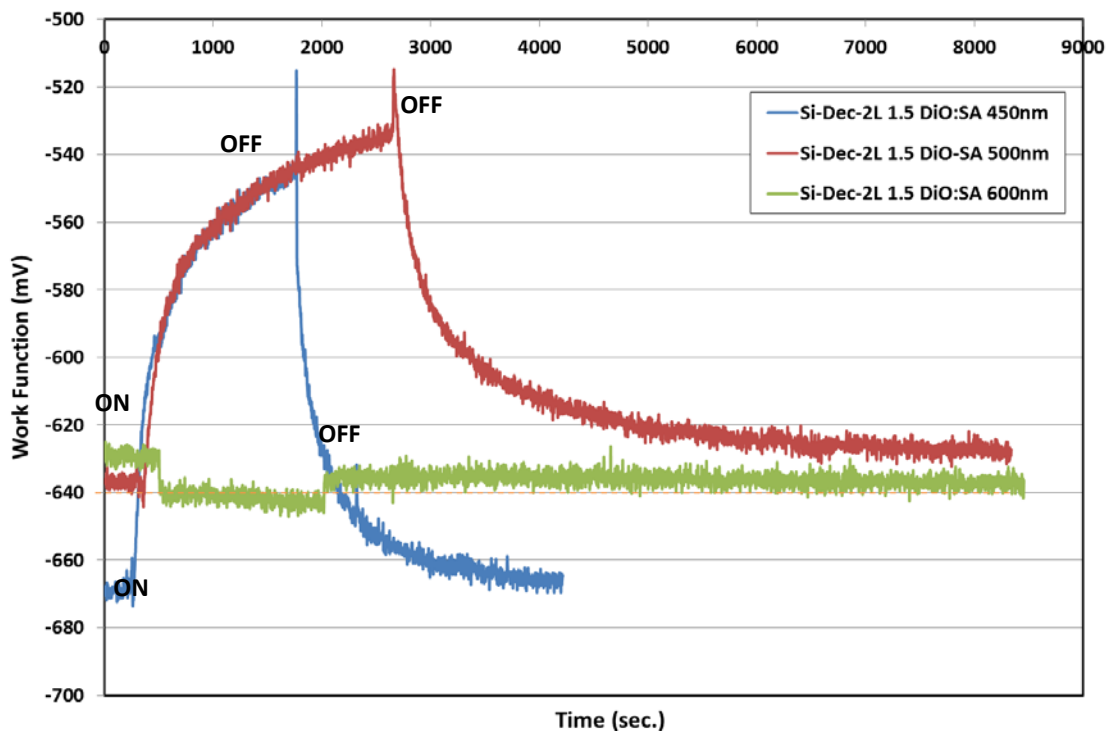


Figure 9.6 Changes of work function upon illumination of sample Si-dec-2L 1.5 DiO:SA for wavelength 450, 500 and 600 nm. Sign of ‘on’ and ‘off’ light indicated mechanism of charge trapping and detrapping, respectively.

This study suggests that some of the excess holes were captured in the dye monolayers of LB films/decene layers and accumulated electrons on the surface. The changes of the surface charge under illumination are due to the alteration in the surface free carrier densities, wherein the calculated Q_{sc} is quite high at $\sim 3.6 \times 10^{10} \text{ C/cm}^2$ (for 450 nm) and $3.4 \times 10^{10} \text{ C/cm}^2$ (for 500 nm). The positive sign on the *n-type* silicon indicated that Q_{ss} should be more positive; thus, Q_{sc} became more negative on the SCR edge. Both wavelengths

also show a similar trend of SPV signal during illumination and deactivation of light, wherein the SPVs obtained are ~121 and 101 mV, respectively. A long period of the illumination mode with much slower charge trapping was filled in the LB films/silicon interface layer, which was also observed for 500 nm wavelength in a similar study.

After the bias light was switched off, the signal was stimulated to the optimum point before it decayed with initial lifetime constant of 60 s for both wavelengths. This result can be considered the optimum point of work function (SPV_{max}) if the illumination period is much longer. Thus, the estimated SPV_{max} for wavelengths of 450 and 500 nm are 153 and 122 mV, respectively. Figures 9.7 and 9.8 show two lifetimes that fit with the actual experimental data. The lifetime decay occurs as a slow process with lifetime constants of 550 (for 450 nm) and 750 s (for 500 nm), respectively. The same lifetimes were applied for both generation charge trapping and lifetime decay of charge detrapping. These values were similar to the slow states of the lifetime constants of 300 s to 500 s in the oxide film of germanium [161]. A reason for this result is the light trapping inside the LB films/silicon interface with a slow process of ~ 550 s to 750 s to establish equilibrium between the surface states and the space charge region. A small band bending was lifted upon irradiation with a fast process of charge trapping and detrapping for the 600 nm wavelength.

Unusual charge trapping and time dependence of the lifetime decay is observed for the sample dye of LB films on the alkyl monolayers of the Si surface. The photon energy charge increased and generated excess carriers that were trapped in the dye monolayers of LB films/decene layers. This result demonstrates the effect of light passing through/transmitted through a charge layer because the illumination was visible in the absorption region of the DiO compound.

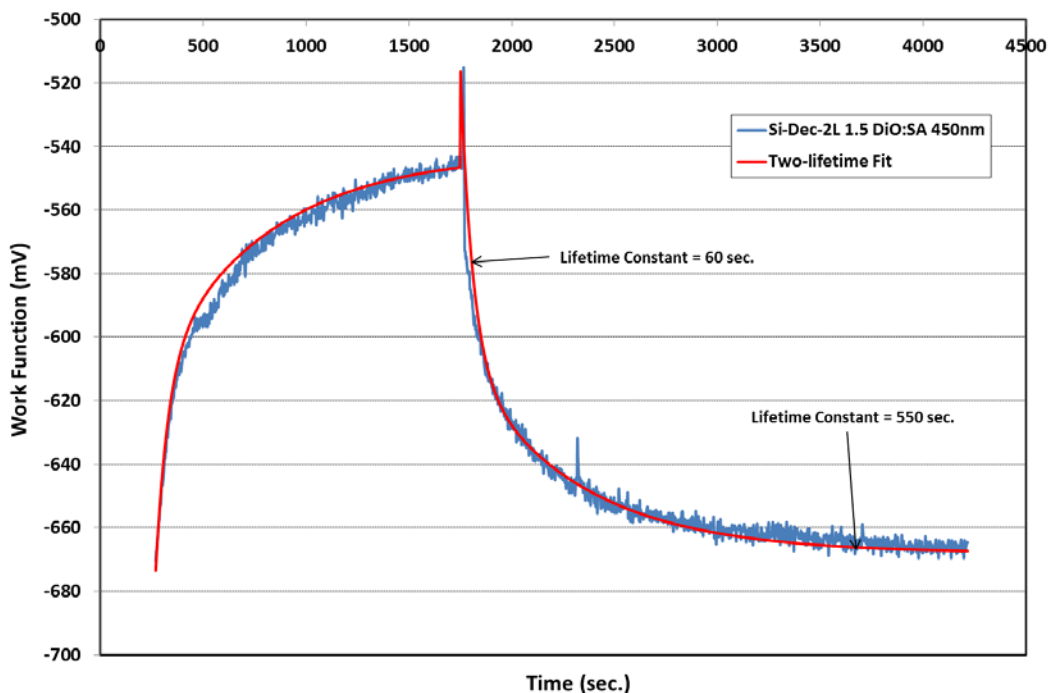


Figure 9.7 Two lifetime fitted to the experimental data for generation charge trapping and lifetime charge detrapping for sample Si-dec-2L 1.5 DiO:SA at wavelength 450 nm.

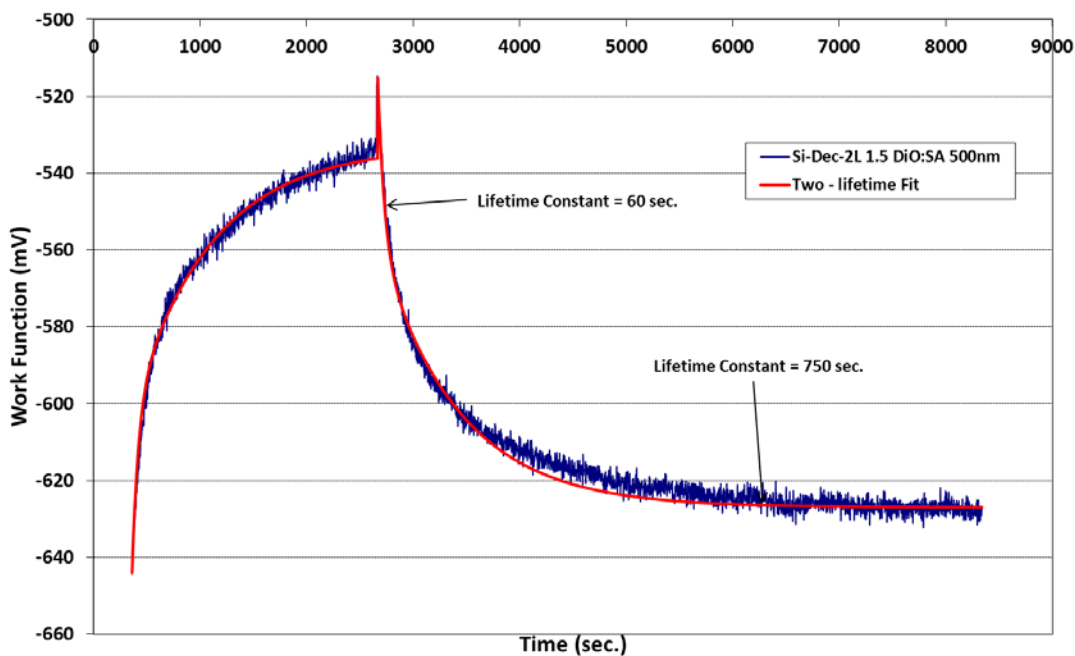


Figure 9.8 Two lifetime fitted to the experimental data for generation charge trapping and lifetime charge detrapping for sample Si-dec-2L 1.5 DiO:SA at wavelength 500 nm.

iv. Silicon-Hexane with Deposited LB Films of Dye

Figure 9.9 shows a different SPV of the Si-hex-2L 1.5 DiO:SA sample, which was measured at 450, 500, and 600 nm wavelengths. The work function was initially measured in the dark. A rapid decrease in SPV signal was observed upon illumination, which increased gradually. This pattern is due to the slow extra charging on the surface. The sign of the slow increase of the work function indicates that a negative charge can be formed on the Si/LB film interface, and the positive charges are present on the surface depletion region. This mechanism suggested that some excess electrons were trapped in the Si/LB film interface layer.

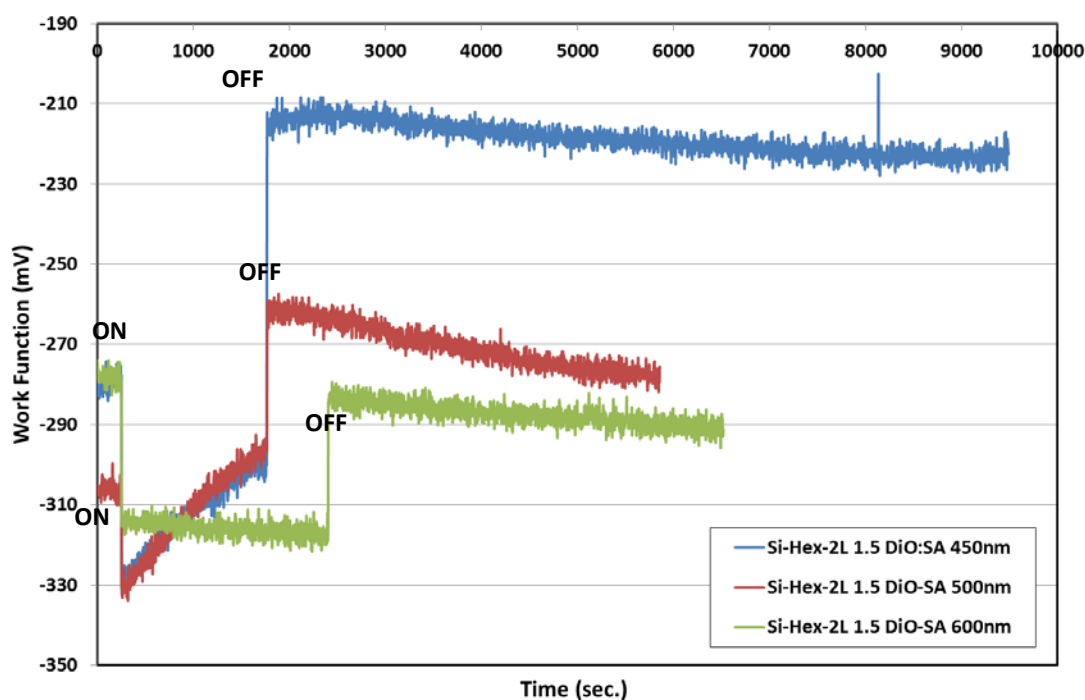


Figure 9.9 Changes of work function upon illumination of sample Si-hex-2L 1.5 DiO:SA for wavelength 450, 500 and 600 nm. Sign of ‘on’ and ‘off’ light indicated mechanism of charge trapping and detrapping, respectively.

The signal suddenly increased while the shutter was closed, wherein SPV gained an optimum point of the work function before it decayed. Therefore, charge detrapping gradually decreased and required longer time to reach the initial value. Figures 9.10 and 9.11 show that lifetime decay occurred much slower than that in sample Si-dec-2L 1.5 DiO:SA with lifetime constants of 1450 (1200 s) and 1900 s (1330 s) for 450 nm (500 nm) wavelength, respectively. Low band bending was observed for this sample, which obtained the SPV at ~66 mV (450 nm) and 44 mV (500 nm) with calculated Q_{sc} of $3.4 \times 10^{10} \text{ C/cm}^2$ and $3.2 \times 10^{10} \text{ C/cm}^2$, respectively. The injected Q_c is much smaller in this sample compared with sample Si-dec-2L 1.5 DiO:SA, indicating that the decene monolayer interface layer has significantly greater LH mechanism. The band is flattened upon irradiation for the 600 nm wavelength, which is considered as a rapid process of electron trapping in the interface layers of the silicon/LB film.

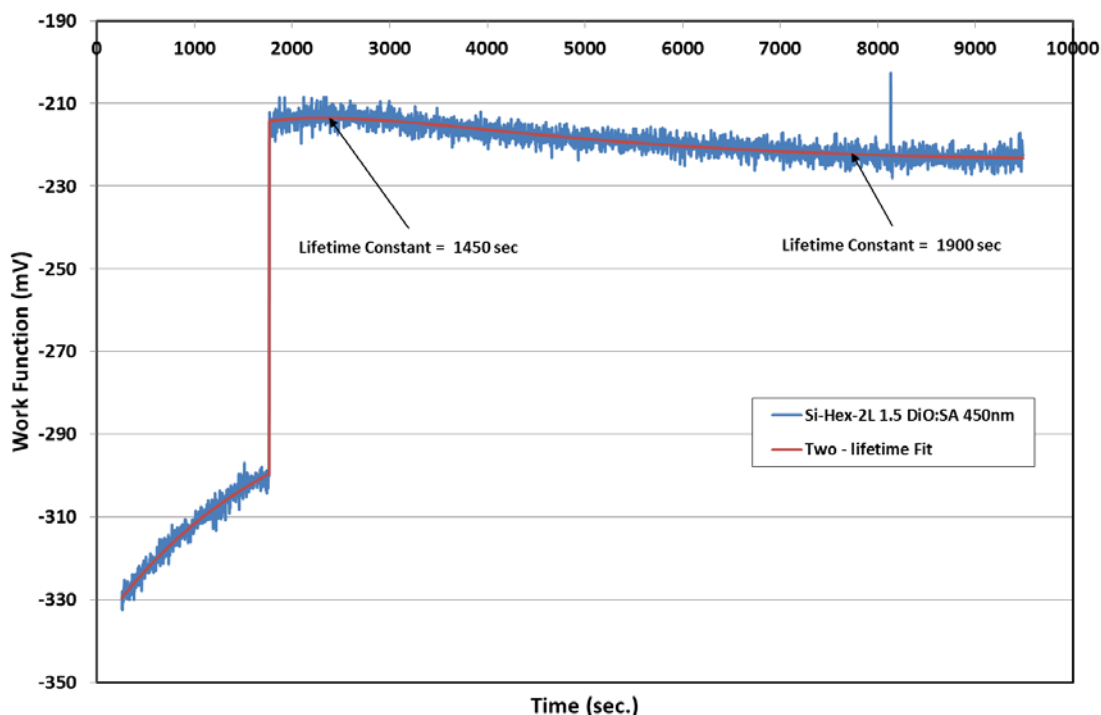


Figure 9.10 Two lifetimes fitted to the experimental data for generation charge trapping and lifetime charge detrapping for sample Si-hex-2L 1.5 DiO:SA at wavelength 450 nm.

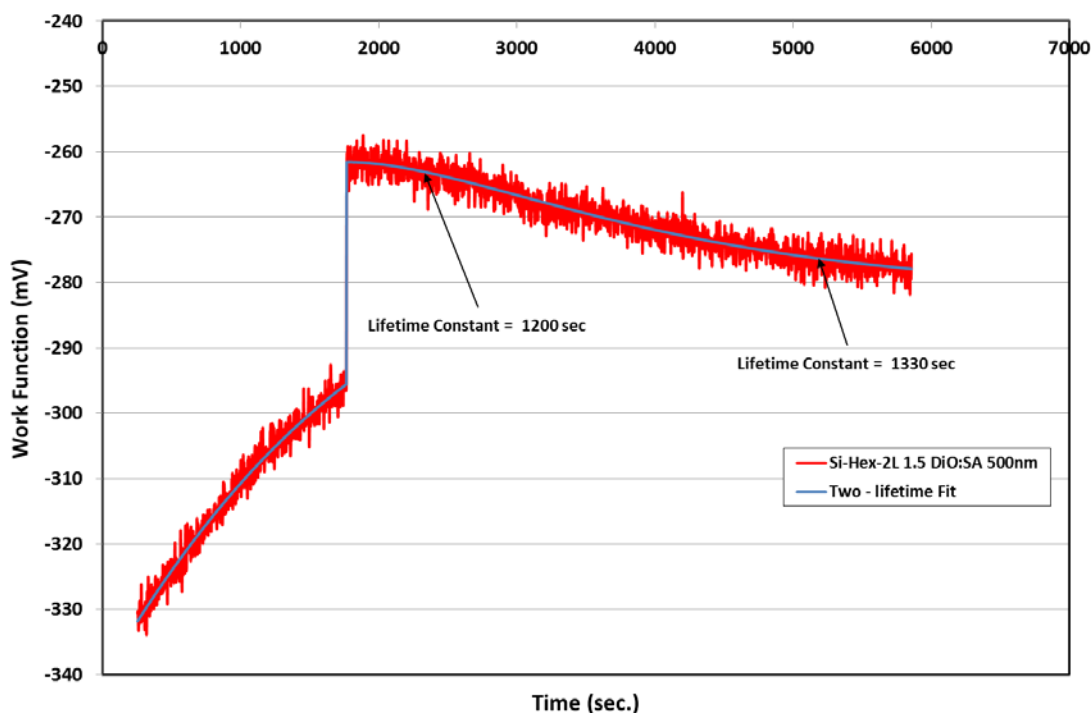


Figure 9.11 Two lifetimes fitted to the experimental data for generation charge trapping and lifetime charge detrapping for sample Si-hex-2L 1.5 DiO:SA at wavelength 500 nm.

Figure 9.12 shows the change in work function for a sample 8L with a wider spacer layer compared to sample 2L (Figure 9.9). The measurement of the SPV of sample Si-hex-8L 1.5 DiO:SA was recorded at different wavelength about 42 mV (450 nm); 68 mV (500 nm) and 77 mV (600 nm), respectively. This indicates the band bending is slightly higher than sample 2L. The measurement of SPV on wavelength dependence was done in-sequence with one measurement per day started from experimental day. The change of SPV indicates a modification occurs on the surface and interface layer because of oxidation process takes place after sample exposure to air.

The sample Si-hex-8L 1.5 DiO:SA shows a stable V_{CPD} in the dark and under illumination. A fast drop of SPV signal is observed which shows a similar trend as Si native oxide. A fast drop of signal is observed due to the excess electrons

and holes produced by the light in the conduction and valence band. This mechanism flattens the bands of the semiconductor. This situation represents a fast trapping process where the band bending under illumination is shifted. When the shutter is closed, the SPV signal gains an optimum point of work function before it decay over time for wavelength 450 nm. It is possibly due to the charge trapping and detrapping because of a strong energy photon and the sample decay takes much longer time compared to the 500 nm wavelengths.

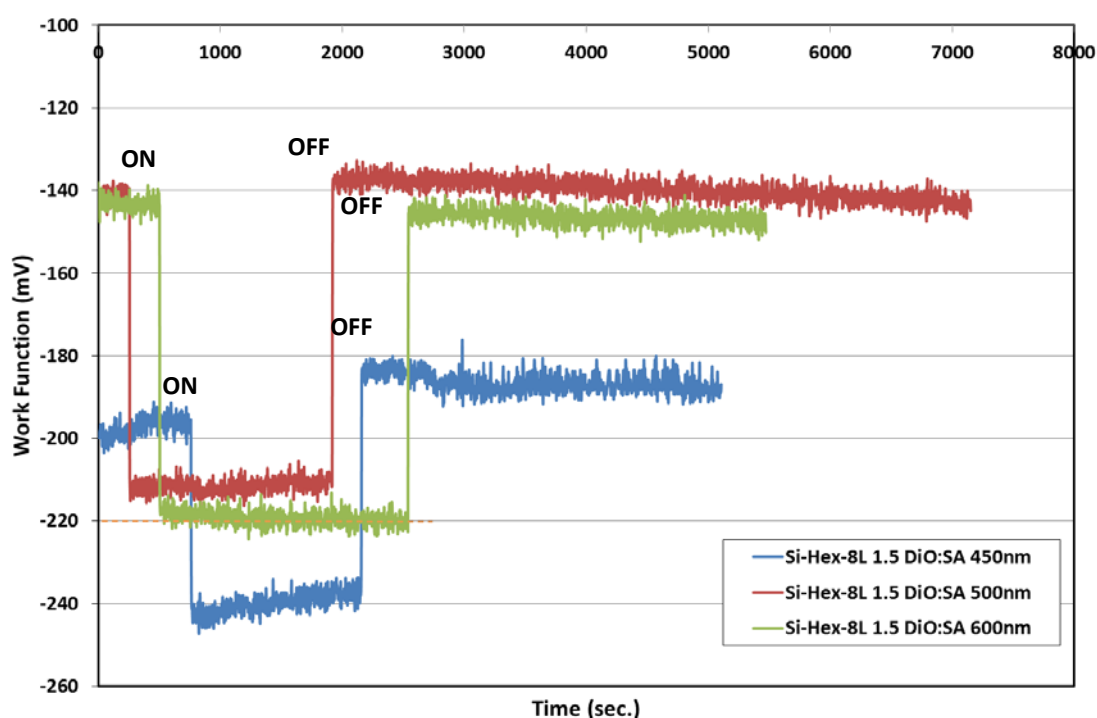


Figure 9.12 Changes of work function upon illumination of sample Si-hex-8L 1.5 DiO:SA for wavelength 450, 500 and 600 nm. Sign of 'on' and 'off' light indicated mechanism of charge trapping and detrapping, respectively.

A close observation reveals the irradiance effect for sample Si-hex-2L SA (Figure 9.13). The SPV signal rapidly decreases under illumination and the bands flatten, indicating that charge trapping is a fast process. When the light is removed, the SPV signal increases immediately by an amount equal in

magnitude as under illumination. This mechanism reflects the normal recombination process because of the recombination of excess holes and electrons in the valence and conduction bands. The decay even after removal of light remains almost the same as that during illumination. Similar trends can be observed for Si native oxide and Si-hex-8L 1.5 DiO:SA, as explained in previous sections.

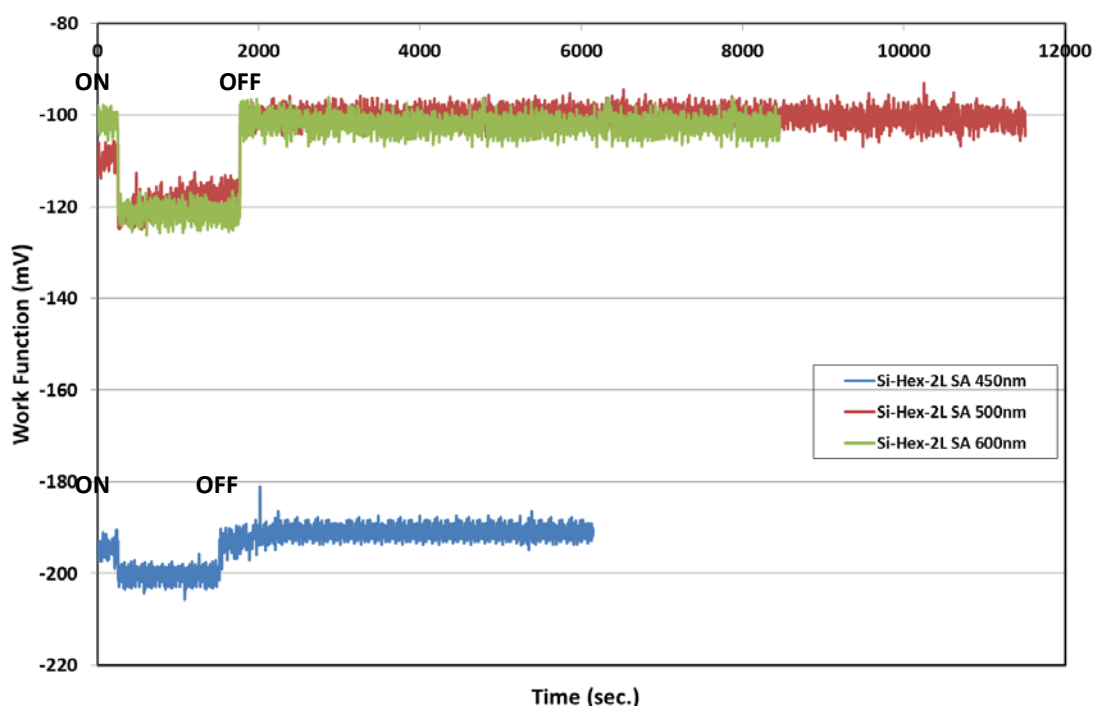


Figure 9.13 Changes of work function upon illumination of sample Si-hex-2L SA for wavelength 450, 500 and 600 nm. Sign of ‘on’ and ‘off’ light indicated mechanism of charge trapping and detrapping, respectively.

9.3.3 Effect of Light Absorption through Dye Monolayers

As mentioned in **Section 2.2**, high-energy photons have a high absorption coefficient and are strongly absorbed near the surface at short wavelengths. The longer wavelength (500 nm) is absorbed slightly deeper compared with

450 nm in the silicon because the absorption depth is the inverse of absorption coefficient. Penetration of light through the dye monolayers resulted in trapped charges in the interface layers, as observed on samples Si-dec-2L 1.5 DiO:SA and Si-hex-2L 1.5 DiO:SA. Although the charge trapping experiment was performed on different wavelengths 450, 500, and 600 nm, penetration of light can be concluded because of the absorption region of the dye monolayer (Figure 9.1). Slow charge trapping and detrapping processes were observed at 450 and 500 nm wavelengths for both samples. Furthermore, a slow charge carrier trapping process in the LB films/silicon interface reduces electron hole recombination before it reaches equilibrium state. The 2-lifetime fit of charge trapping and detrapping is summarized in Table 9.1. The charge carrier trapping and detrapping can be categorized as a fast process for 600 nm wavelength. A similar result was obtained for Si native oxide (**Figure 9.2, pg. 159**).

Table 9.1 A summary of 2-lifetimes fit of charge trapping and detrapping on the different samples

| Samples | Measured at wavelength | 2 - Lifetimes Fit (s) | |
|------------------------|------------------------|-----------------------|----------|
| | | τ_1 | τ_2 |
| Si-decene at 48 hours | 900 nm | 107 | 301 |
| Si-decene at 504 hours | 900 nm | 61 | 105 |
| Si-dec-2L 1.5 DiO:SA | 450 nm | 60 | 550 |
| Si-dec-2L 1.5 DiO:SA | 550 nm | 60 | 750 |
| Si-hex-2L 1.5 DiO:SA | 450 nm | 1450 | 1900 |
| Si-hex-2L 1.5 DiO:SA | 550 nm | 1200 | 1330 |

A different trend of lifetimes at 450 and 500 nm indicates that the effect of the interface layers has a significant function in LH mechanism. The calculated lifetimes on sample Si-hex-2L 1.5 DiO:SA were much slower compared with those on sample Si-dec-1.5 DiO:SA. The formation of LB films on the samples creates a certain thickness of interface layers. As explained in **Section 7.3.2**, the estimated thickness of sample Si-Hex-2L 1.5 DiO:SA and Si-Dec-1.5 DiO:SA were 10.0 and 8.8 nm. Thicker layers will create excitation further from the surface. However, a thicker layer results in the loss of excitation energy transfer, as observed in sample Si-hex-8L 1.5 DiO:SA. Therefore, this study proposed that charge trapping via excitation of a molecular layer occurs only when the molecules are close to the surface. Previous studies also confirm that energy transfer occurs in much closer distances (< 5.0 nm) to the silicon surface [136].

9.4 Chapter Summary

This study evaluated the trapping and detrapping of surface charge induced by the illumination of LB films containing an organic DiO dye using KP. The samples include surfaces passivated with 1-decene and hexane, which were compared with samples covered with native oxide. Although the mechanisms have yet to be explained in detail, this study demonstrated different mechanisms of charge trapping in samples passivated with decene compared with samples treated with hexane. Thus, charge trapping in the surface states probably occurs through a similar mechanism as photosynthetic LH. The calculated Q_{sc} is quite high at $\sim 3.4 \times 10^{+10} \text{ C/cm}^2$ to $3.6 \times 10^{+10} \text{ C/cm}^2$ for 450 or 500 nm illumination wavelengths. The charge trapping and detrapping could be fitted with two lifetimes, which are identically slow processes. This charge trapping via excitation of a molecular layer occurs only when the molecules are close to the surface (2L layers). By contrast, surface charging occurs during large separation (8L layers) by bulk carrier generation in the bulk, which is similar to the samples without any dye.

*Charge Trapping on Passivated Silicon Surface via Illumination of Dye
Monolayers*

Chapter 10 Conclusion and Future Work

10.1 Introduction

The overall aim of this thesis was to develop a technique for charge injection into silicon by light energy absorbed in organic dyes attached to the surface to overcome the poor optical absorption of silicon. Molecular 1-decene and hexane monolayers were deposited on the surface and formed a covalent bond with silicon. Light-harvesting structures were deposited on the surface to form LB films. Furthermore, experimental and theoretical studies were conducted to apply photosynthetic light harvesting to generate electron-hole pairs in silicon, aiming to improve the performance of crystalline silicon solar cells. This research also focused on the development of a novel technique to evaluate surface recombination and monitor any modification of a passivated silicon surface using the contactless KP method.

This chapter presents a summary of this study and recommendations for future studies. This chapter consists of the following sections: (1) conclusions and key contributions and (2) recommendations for future work.

10.2 Conclusions and Key Contributions

The research objective of this thesis was clearly stated in Chapter 1 as follows:

“The methodologies are created to develop a technique for attachment of organic dyes to silicon and to enhance energy transfers between the dyes and the silicon surface. Furthermore, a new mathematical model is developed to estimate surface recombination velocity for surface passivation and to investigate charge generation in the semiconductor based on the KP method. Alongside the main contributions, supporting analysis on the development of a new simplified energy model of photosynthesis, which works parallel to solar cell operation, is also carried out.”

A comprehensive discussion on solar cell operation was initially introduced, including the formation of the p-n junction and the electrical performance of the solar cell. The associated depletion approximation for space charge region width and potential curve determination were also discussed. The author examined the important principle of charge generation in the semiconductor surface to achieve the thesis objective. The effects of charge neutrality on the surface states (Q_{ss}) and surface charge in the space charge region (Q_{sc}) were highlighted in the further investigation of surface passivation in Chapters 8 and 9. Moreover, an explanation on carrier recombination and the mechanisms of bulk recombination processes was presented.

Chapter 3 gave a detailed account of the characteristics of the semiconductor surface. The concept of surface state was defined, and its properties were explained. The SRV at the conditions of flat band and band bending mainly depended on the properties of the surface state, charge carrier concentration, capture cross-sections for electrons and holes, injection level at the surface, and doping level of semiconductors. At the end of the chapter, the effect of charge on the surface, especially fast trap and slow trap mechanisms, was shown to be an important factor in the formation of surface potential and barrier height of the semiconductor surface.

A review on energy conversion mechanisms was presented in Chapter 4, and it was shown that the photovoltaic energy conversion had many similarities to the photosynthetic system at the fundamental level [4]. A novel simplified model for the primary energy conversion step in photosynthesis was successfully developed by identifying the most significant chemical potentials involved in the photosynthetic system. This mathematical model was derived from the elementary redox reaction of electron transfer across the photosynthetic membrane in purple bacteria. The electrochemical potential ($\Delta\mu$) can be detailed into three components: concentration gradients across the semi-Quinone membrane (QH), proton gradient H^+ movement across the membrane cells, and gradient $\delta\mu_Q$ of the oxidized quinone (Q). The internal free energy in bacterial photosynthesis had many similarities to the voltage of qV , which followed the Shockley solar cell equation and described the operation of a solar cell. From this model, the electrochemical potential $\Delta\mu$ and the photo-generation rate K_L were calculated based on the wavelength of

bacteria at 800 nm using an analogue of the Shockley equations as 0.93 eV and 1.55 eV/s, respectively.

The new theoretical model of surface current via a mathematical model using KP method was established in Chapter 5. The surface current through surface states was derived by introducing the surface recombination current (J_s) in the equation. The accumulation of charge in the depletion region can be interpreted as band bending, which measures the surface photovoltage using the KP method. The determination of interface saturation current density (J_{os}) from the C_L slope was used to estimate the accumulation of charge trapped in the surface state/interface of the sample. Indirectly, the J_{os} value was shown to be useful in evaluating the surface recombination velocity (S_{fs}) of a silicon surface. The determination of surface recombination velocity and barrier height measurement via KP method can be considered a novel technique, and used to further examine the passivated samples in Chapter 8.

The objective of this thesis was discussed further in the succeeding chapters (Chapters 6, 7, 8, and 9), particularly the development of a new method for chemical passivation of silicon using organic dyes.

The author examined the properties of interface layers before any deposition of LB films on the silicon surface in Chapter 6. A series of passivation treatments, including RCA Clean, sulphuric acid-hydrogen peroxide mixture solution, and hydrogen termination, was conducted. Initial treatment/cleaning was important in preparing high-purity materials without residue before further surface modification. The author prepared the 1-decene monolayers on Si surface using hydrosilylation reaction at low temperature (110 °C) with a Lewis acid catalyst. The results of XPS, ellipsometry, and water contact angle and lifetime measurements demonstrated the stability of the monolayer structure and the very low inherent reactivity of the oxide surface toward 1-decene. The results also showed that alkene formation had very stable Si-C bonds that yielded dense monolayers, as proven from the FTIR and wetting experiments. The IR spectra recorded three broad peaks of the C-H stretching region, with peak areas at $\sim 0.217 \text{ unit}^2$ and low temperature reaction at 110 °C. The significant IR spectral results showed that the covalently bound alkyl monolayers were well passivated by the presence of carbonyl groups on the

monolayer surface. High-resolution XPS spectra of the Si 2p and C 1s regions were consistent with the Si-CH₂ bond and increased carbon amounts up to 27.7%. Thus, the 1-decene molecules were passivated on the samples. Finally, the presence of a Lewis acid catalyst in 1-decene monolayer rendered the grafted silicon samples resistant to oxidation in air and maintained the surface passivation for long-term stability conditions.

Chapter 7 discussed a novel approach to deposit LB films on the silicon substrate as functional groups of light-harvesting materials for a solar photovoltaic system. The preparation and experimental procedures for LB films were also discussed. The hydrophobic layers of 1-decene and the hexane monolayers on the silicon surface were used as interface layers for deposition of dye (DiO) monolayers through the LB technique. A review of recent literature of LB film on silicon was also described, which emphasized the stability control and surfactant concentration effect for LB deposition.

The results of the characterization on different passivated samples using KP were demonstrated in Chapter 8. The formulation of the surface current equation from Chapter 5 was used to determine the surface recombination velocity for passivated semiconductor samples. The recombination velocity obtained from surface photovoltage measurement is a novel approach for quantitative analysis in KP methods and an alternative measurement to Sinton PCD lifetime technique. As the surface current equation was derived, the collection efficiency of minority carriers (η_L) was used to estimate the average diffusion length (191 mV) and to determine the bulk lifetime (27 μ s) for native silicon. Moreover, the measurement of barrier height is important to estimate the effective saturation current (J_{os}) and predict the surface recombination of the sample. J_{os} was determined using the same equation as the surface current because J_{os} variation depends on different voltages applied on the samples. These results indicated the effect of surface treatment (Chapter 6) on silicon. As results of Figures 8.7 and 8.8, the theoretical data J_s (Eq. 5.38) were consistent with the experimental value for treated SPM Si and native Si. However, the findings do not fit the passivated samples because this theory is not applicable to samples with low barrier heights (order of kT).

The second part of the chapter discussed the estimation of surface recombination velocity on the passivated samples. The alkyl passivated Si-decene as an interface layer shows promising results and display strong stability against oxidation in air. The deposition of LB with a stable foundation of Si-C bond, i.e. sample Si-dec-LB, shows better reproducibility, consistently moderate SRV (1,903 cm/s), and effective saturation current density (J_{os} , 0.2 nA/cm²). The calculated surface state density (Q_{sc}) of all passivated monolayer interfaces is lower than the silicon oxide/silicon interface. The determination of surface recombination velocity by KP method was validated by comparing the lifetime measurement with the Sinton PCD method. The results of the surface recombination velocity are correlated and comparable with the different method of measurement (**Section 8.3.4 (iii)**). The KPs were shown to be new alternative instruments for monitoring any changes or modification of the semiconductor surface. The determination of surface recombination velocity using the derived surface current (Chapter 5) generated valuable information on surface modification, which will facilitate further deposition of nanostructure monolayers on silicon surface.

This study also discussed the effect of organic dyes and demonstrated related optical absorption and charge carrier trapping. Chapter 9 demonstrated the trapping and detrapping of surface charge induced by the illumination of LB films containing organic DiO dye using KP method. The samples under study included surfaces passivated with 1-decene and hexane, which were compared with the results obtained from samples covered with native oxide. Charge excitation in silicon via light-harvesting materials was demonstrated on the Si-dec-2L 1.5 DiO:SA sample, which contained DiO compound in the dye monolayer of LB films. A different charge trapping mechanism was observed by Si-dec-2L 1.5 DiO:SA sample, wherein some of the excess holes were captured in the dye monolayers of LB films/decene layers. The charge trapping and detrapping mechanisms are described as slow processes with two identical lifetimes, where the slower component is different between the decene and hexane samples. Charge trapping was also studied as a function of distance between the dye molecules and silicon surface using different 2L and 8L layers with LB spacers made from SA. This charge trapping process via excitation of a molecular layer occurs only when the molecules are close to the surface (2L

layer). For large distance from the surface (8L layer), the carrier generation possibly occurs in the bulk, which is similar to the samples without any dye.

In summary, this thesis described a novel method for passivation of silicon using organic dyes through LB techniques (Chapters 6, 7, 8, 9), development of a theory of passivated semiconductor surface through mathematical modelling (Chapter 5), and determining chemical potential in the energy conversion of photosynthesis (Chapter 4). A new method was developed using the KP technique to demonstrate and characterize the passivation and enhancement of properties. Surface photovoltage measurement via a contactless KP method demonstrated a novel approach in quantitative analysis and a useful technique to determine surface recombination velocity data for passivated semiconductor samples.

The key contributions of this study can be summarized as follows:

- A novel method is developed in depositing organic dyes as light-harvesting materials on silicon with different interface layers of alkene and hexane monolayers. Moreover, the formation of alkene monolayer as an interface layer shows the significance of the light-harvesting mechanism.
- A novel approach is adopted to estimate the surface recombination velocity via KP method for the passivated monolayers and native silicon. A close correlation is found between KP and PCD methods for passivated monolayers compared with native silicon.
- The variation in charge generation on different passivated monolayers through charge trapping and detrapping is characterized by the KP method. Charge excitation in silicon is proposed to only occur in samples containing organic dyes (DiO compound) when the dye molecules are close to the surface.
- A novel energy model is used to calculate the electrochemical potential in the energy conversion of bacterial photosynthesis that is comparable to the performance of a solar cell. This model provides deeper understanding on how the structure and function of the molecular machinery can work almost perfectly to convert light energy into useful chemical energy in the primary reactions of the photosynthetic system.

10.3 Future Work

The results of novel methods for charge trapping and detrapping for the Si-dec-LB sample should be investigated further. The addition of an 8L spacer on the interface layer of the decene monolayer should be considered and compared with hexane interface layer. The distance to the surface is significant; thus, the effect of the spacer should be investigated and the characteristics and surface properties compared with the Si-hex-LB sample.

The formation of alkene monolayer as interface layer is becoming popular as an alternative replacement for the SiO_2 insulator layer. A similar approach to form a diode (a mercury-molecule-silicon junction) has been conducted using $\text{Hg-C}_{10}\text{H}_{21}\text{-Si}$ [162]. Another approach is to fabricate an electrolyte-molecule-semiconductor structure, wherein ET is distance dependent through an organic chain with n-alkyl monolayers ($\text{C}_n\text{H}_{2n+1}$) on Si (111) [163]. However, the most crucial issue is the stability of alkyl monolayers against oxidation in air. The alkene monolayers are proven as suitable interface layers; thus, the deposition of a top layer of the functionalization of LB films is a novel approach that requires further investigation.

Low temperatures of wet chemical routes for formation of SAMs have exhibited possible application in solar cells. A different approach of texturing the silicon surface can be extended to porous silicon [164] by applying hydrosilylation of olefins and alkynes [110] on the porous silicon surface. A different organic bonding of alkynes with Lewis acid catalyst also shows strong stability against oxidation in air.

The ultimate aim of this research is to fabricate a novel photovoltaic structure that consists of the deposition of compact dye molecules that integrate with solar cells structure as complete devices. A molecular layer near the semiconductor with emission energy that exceeds the band gap can transfer non-radiative excitation energy to excite an electron from the valence band to the conduction band of the semiconductor. The possibility of silicon sensitization via non-radiative electronic energy transfer from dye molecules on the surface has been suggested by Dexter [127]. In this study, energy

transfer from contact formation and electrical properties is investigated between the dye molecules and a potential photovoltaic device.

Appendices

Appendix 1 Characterization Procedure of Kelvin Probe Measurements

Appendix 2 Publications

Appendix 1 Characterization Procedure of Kelvin Probe Measurements

A. Introduction

The KP from KP Technology Ltd was used to determine work function of the silicon sample using vibrating gold probe which is perpendicular to a stationary sample surface. Since the KP is a contactless and non-destructive technique, this characterization is most suitable to monitor any changes of the charge on the treated surface. Once the samples are in contact and assume $W_{probe} > W_{sample}$, the charge transfer takes place where charges flows from the smaller work function sample to larger work function probe. This process will continue until the work function of the samples and probe are equal. The work function of probe becomes more negative than sample by an amount equal to the difference in the work function between the sample and probe which is known as CPD.

B. Light Source of Bentham Spectrometer

The optical fibre source was placed at a distance of 10 cm at an angle of 30° angles from the sample base of KP which is covered by square black box. A Xenon light source (75W, 5.4A) was used in this experiment which is supplied with associated of 605 constant current system. The light emitted by the IL1 lamp is filtered by the TMc300V Bentham-300mm focal length single monochromator in 5 nm steps and light escaping have two fibre optical outlet from the monochromator. The small optical fibre is terminated by a silicon detector that used as a reference measurement of the light, which is transmitted through the medium fibre optical into the KP equipment. The cell response is measured in *Amperes* at each rotation of the monochromator where the spectral response of the cell (in $AW^{-1}nm^{-1}$) is determined. Prior to any measurements, the illumination system composed of the IL1 lamp, TMc300

monochromator and optical fibre was calibrated against a reference (1 cm² calibrated DH-Si silicon low-noise photodiode).

C. Solar Cells Calibration

The photon flux was estimated using a 6.637 mm x 6.317 mm c-Si solar cell. Prior to the KP measurements, the solar cell was placed at the same position as the silicon sample on the KP base. The light source of spectrometer was positioning to the sample base of KP at the angle of 30° with distance of 10 cm. Upon illumination, photon absorption was detected by solar cell and then the output signal was connected to the Spectrometer Current Pre-amplifier as signal current in unit *nA*. The photon flux is determined on the spectral response of the calibrated solar cell which is carried out at the end of each measurement.

D. Light Intensity Distribution Test

The distribution of light intensity is measured in order to determine the uniformity of the light on the illumination area of the sample. The distribution test of light is carried out using halogen lamp at direction of *y* and *z* as shown in Figure A1.1. Since direction *x* is fixed, the direction *y* is changes from front to backside of KP base. Meanwhile, the direction *z* is changes from upper to lower down the KP base.

The movement of the sample base is about $\pm 1.4\text{mm}$ for the *y* direction measurements as shown in Figure A1.2 (a). The percentage variation of the photon flux is about 1.13%. It shows that the light distribution is uniform to a sufficient degree throughout the distance. For the *z* direction measurements, the movement of sample base was varies from upper to lower the KP base is about $\pm 1.0\text{mm}$ as shown in Figure A1.2 (b).

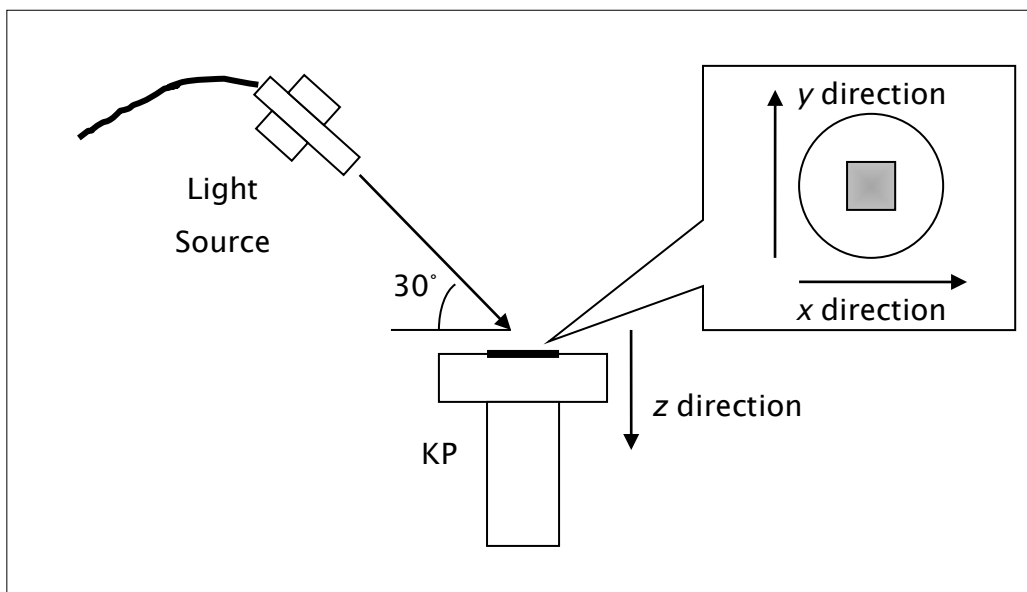
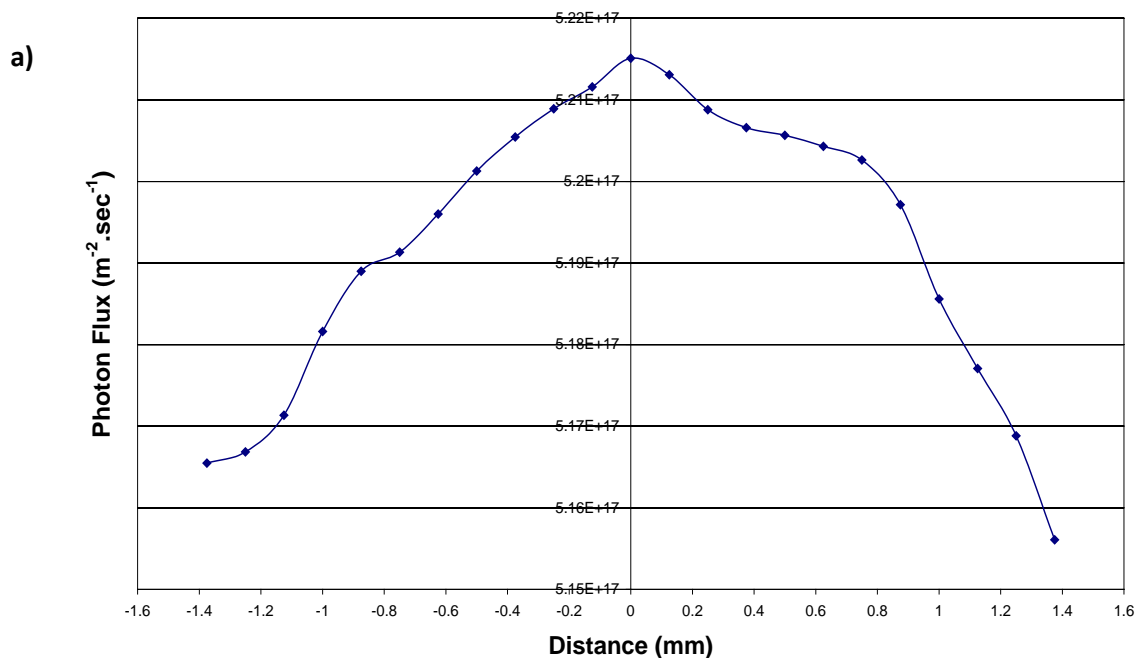


Figure A1.1 Schematic of characterization setup of KP measurement and light source angle for light intensity distribution test.



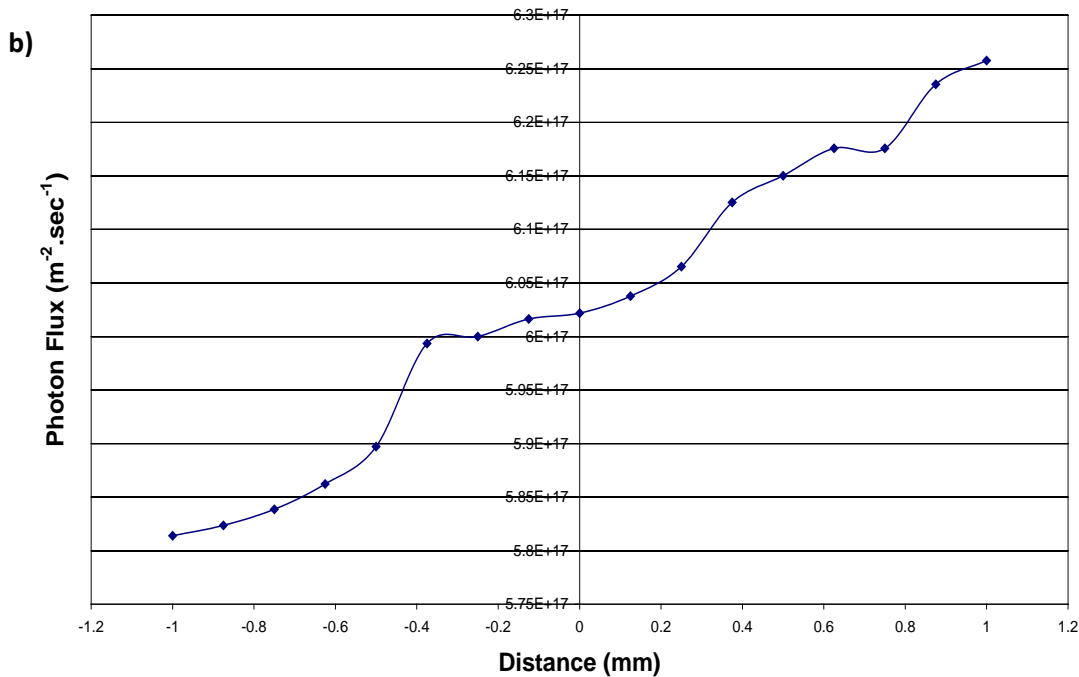


Figure A1.2 Distribution of light intensity through calculated photon flux on a) y direction; and b) z direction.

E. Photon Flux Determination

The measurement method and calculation of photon flux is determined after fixing the optimum position of light distribution. The light escaping from the monochromator is guided to the solar cell by a 1 mm UV/visible optical fibre which are used in as a source for SPV in KP Measurements. Since the monochromator is not chopping type, the light intensity can be varies of opening slits width from 0 to 15 mm. By changing the slit opening much wider, it will give much higher the intensity of light. In this study, the slit was measured from 0 to 10 mm in order to investigate the how much varies of the light intensity. The step of measurements as follows:

- (i) In order to determine the right photon flux, the calibrated silicon detector of 1 cm x 1 cm size was used in this study.
- (ii) The optical fibre was placing directly 90° to the calibrated silicon detector at 1 mm distance.

- (iii) Measuring the signal current of light intensity by changing the slit width within 1 mm interval from 0 to 10 mm.
- (iv) Upon completed, replace the calibrated silicon detector with calibrated solar cell at the same position and measure the signal current by following a same slit opening as before.
- (v) The ratio of gap intensity between calibrated silicon detector (SD) and solar cell (SC) for each slit width is defined as

$$G(\lambda) = \frac{\text{SiliconDetector}(\lambda)}{\text{SolarCell}(\lambda)} \quad \text{Eq. A.1}$$

- (vi) The spectral response, $SR(\lambda)$ was determined using the same optical fibre which is measuring the calibrated solar cell as a reference.

Since the photon flux, $\Phi(\lambda)$ is known as number of photons per second per unit meter square, the formulation of photon flux can be simplified as

$$\Phi(\lambda) = \left(\frac{I(\lambda)}{A \cdot SR(\lambda)} \right) \left(\frac{\lambda}{hc} \right) \quad \text{Eq. A.2}$$

From Figure A1.3, it can be seen the gap ratio of slit 1mm is much lower compare to the others slits. Meanwhile the gap ratio of slit 2mm to 10mm is almost similar which is representing the accurate of the measurements. Based on photon flux calculation, the percentage difference of gap ratio between slit width of 1mm and 10mm is about 23-24 %. This percentage value is varies due to the opening slit width which is characterize of the intensity of light. It means when the intensity is high, the probability to obtain photon flux is also higher.

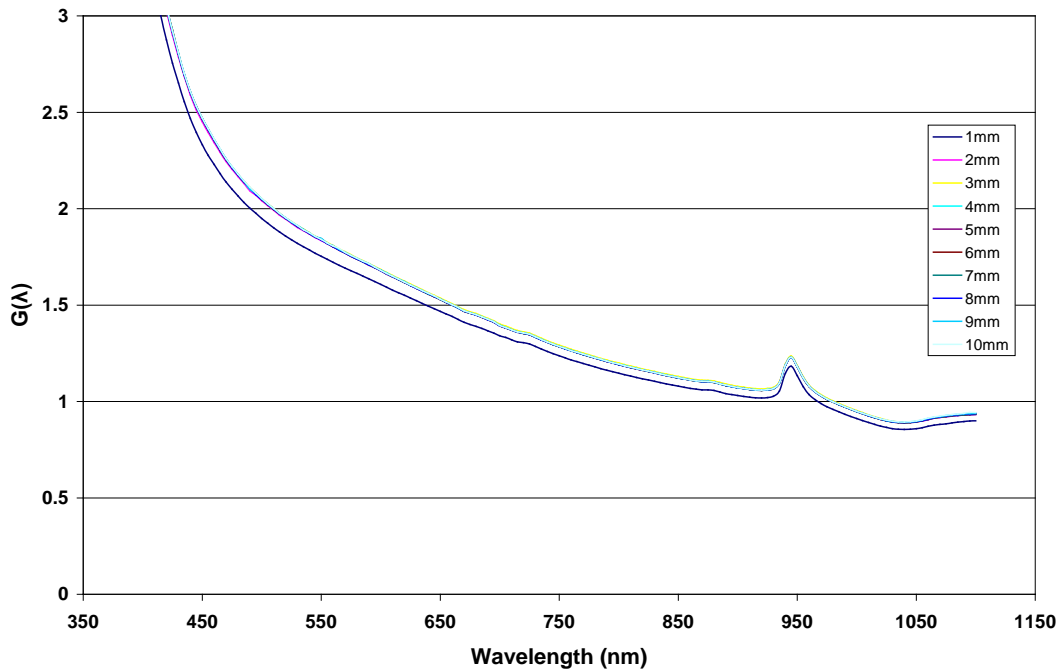


Figure A1.3 The gap ratio of intensity of light, $G(\lambda)$ is measured at different slit width from 1 mm to 10 mm.

F. Measurement Procedure

The work function was measured using KP Measurement System version DELTA 5+ software which is purchased from Technology Ltd as follows:

A. For Measuring Work Function using Kelvin Probe Measurement

- 1) Click and open 'SKP ver. 5.05 icon' application on the computer desktop.
- 2) Choose File command and select 'Open parameter file'.
- 3) Choose directory 'Backup (D:)', select subdirectory under 'Results/Sep 07' and choose 'Southampton 130807' file.
- 4) Choose sub-menu 'Setup Probe & Data Acquisition' and click 'Enable' to permit the KP system is running and that command change to 'Enabled'.

- 5) Click 'Start' and choose show 'Gradient' under Oscilloscope sub-menu. After placing the sample on the KP base, adjust the KP base by changing the height of '▲' and '▼' until it reach the 'GD (au)' about 280 and click 'Stop' as shown in Figure A1.4.
- 6) For measuring work function, choose sub-menu 'Work Function Measurement' and set Measurement Parameters to 5000 points and then click 'Start' to activate the measurement is running as shown in Figure A1.5.
- 7) When the measuring the work function is completed or click 'Stop', automatic menu to save a file is appear.

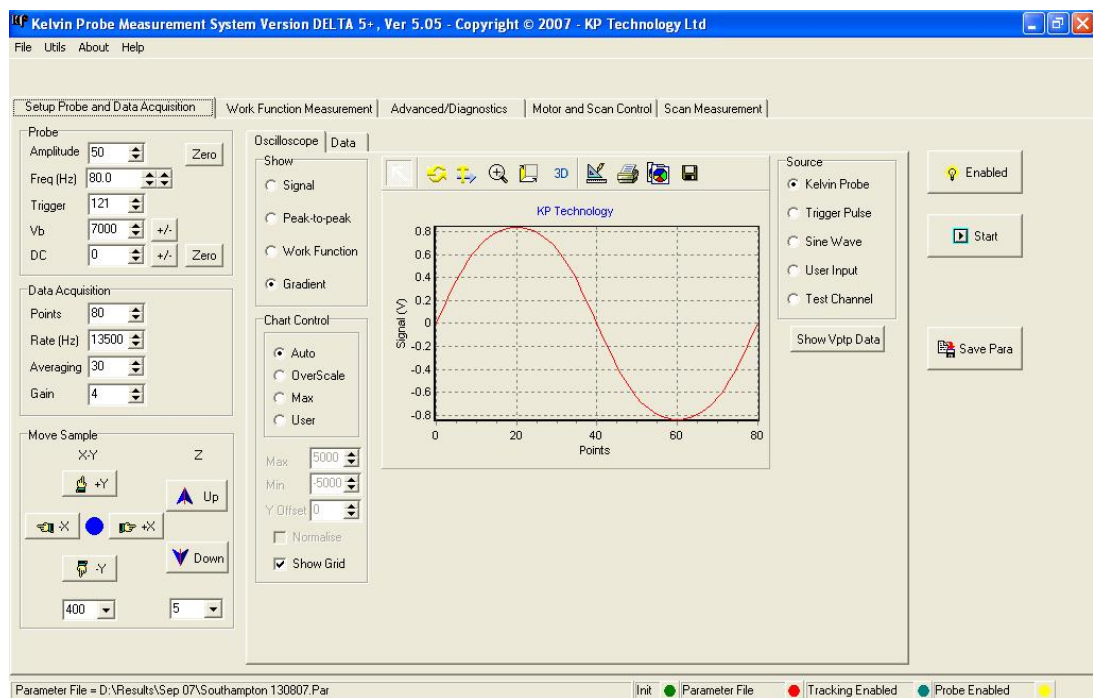


Figure A1.4 Sub-menu of 'Setup Probe and Data Acquisition' for KP Measurements.

Characterization Procedure of Kelvin Probe Measurements

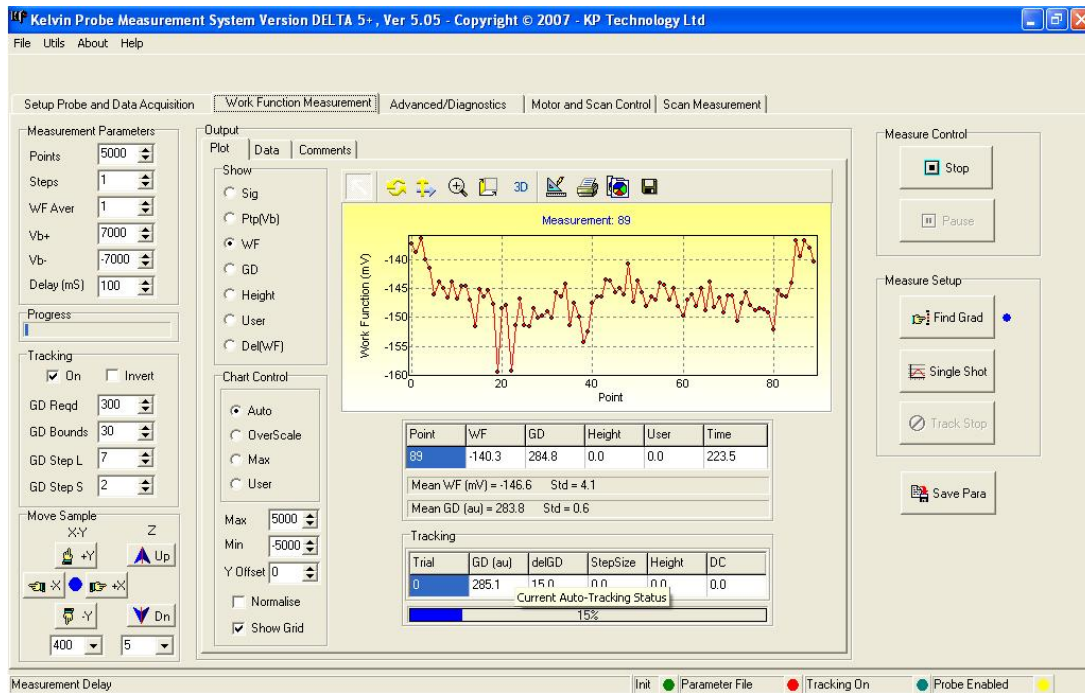


Figure A1.5 Sub-menu of 'Work Function Measurement' for KP Measurements.

B. Measuring Surface Photovoltage, Barrier Height and Diffusion Length using Bentham Spectrometer

- 1) Click and open 'BenWin+ icon' application on the computer desktop.
- 2) Switch on the TMc300 monochromator, 605 power supply for halogen beam or xenon beam, current amplifier/detectors power supply and PMC-Mac power supply.
- 3) Choose 'Tools' command and select 'configuration' directory. Choose 'spectra_response_low.xml file' specifically for low signal use 487 for signal recovery. Click 'use' for system initialising.
- 4) Choose 'Scan' command, select 'Scan Setup' for measuring full scan of wavelength from range 350-1100nm. Set 'step size' to 5nm and click 'new scan'.
- 5) Under 'Scan' command, select 'Stationary Scan Setup' for specific wavelength to test. Set 'scan length' to 40 s, 'scan interval' to 1 s, choose specific wavelength to test e.g. 450, 475, or 900 nm and then click 'new scan' to start the measurements.

- 6) Upon completing the measurement, the results can be interpreted by converting data into excel spread sheet.

C. For Measuring Surface Photovoltage, Barrier Height and Diffusion Length using Kelvin Probe Measurement

- 1) Follows similar setup as work function measurement from step 1-5.
- 2) In sub-menu 'Setup Probe and Data Acquisition', choose show 'Work Function' under Oscilloscope sub-menu and click 'Start'.
- 3) The work function of the sample need to be stabilising before any measurement of SPV is done.
- 4) In order to measure SPV, the difference of work function in the dark and illumination was recorded based on average of 20 point in excel spread sheet.
- 5) The relaxation time is needed about 90-100 point between two wavelength tests for barrier height and diffusion length measurements.
- 6) For diffusion length measurement, the constant of SPV will be considered in the range of ± 5.0 mV.
- 7) By remote desktop connection of KP computer, interface two software's is required for easy access and fast measurement as shown in Figure A1.6.

Characterization Procedure of Kelvin Probe Measurements

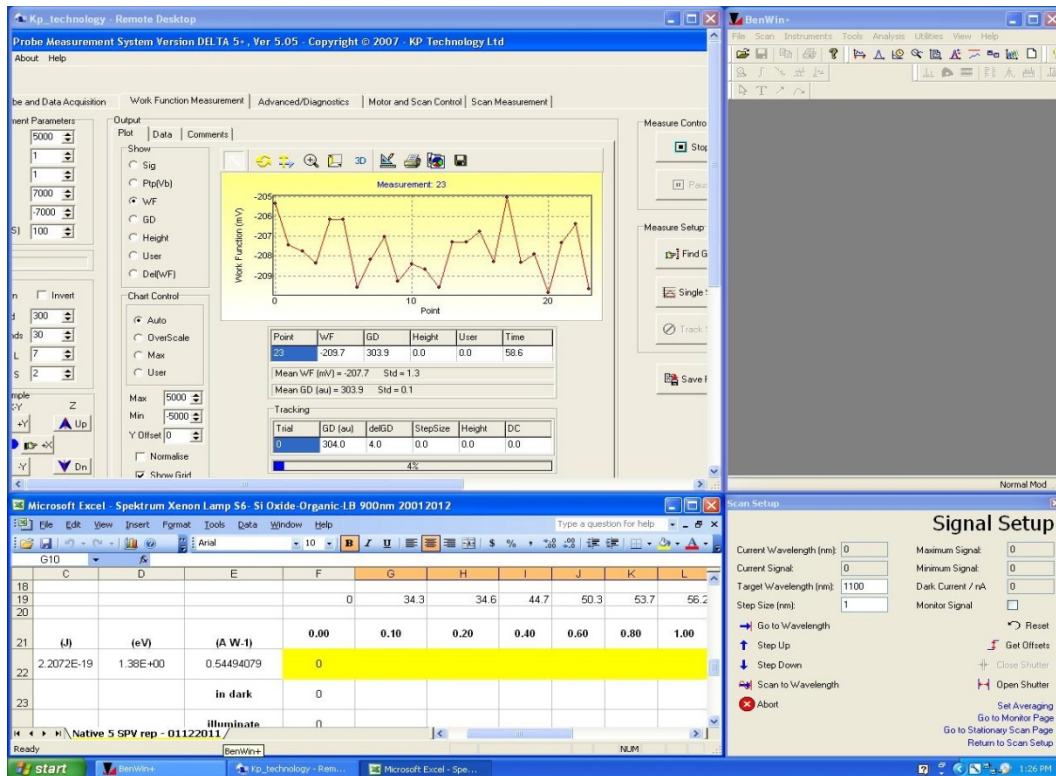


Figure A1.6 Interface of BenWin+ software of Bentham Spectrometer and KP software of KP Measurements.

Appendix 2 Publications

The following are in-progress, under review and published papers during the course of this thesis work.

1. **Mohd Adib Ibrahim**, Mohd Asri Mat Teridi, Norasikin Ahmad Ludin, Suhaila Sepeai, Kamaruzzaman Sopian, Nicholas Alderman, Lefteris Danos, Tom Markvart, 2014, *Surface Passivation of Alkyl Monolayers on Silicon for Solar Photovoltaic*. **In-progress Manuscript for International Journal of Photoenergy**.
2. **Mohd Adib Ibrahim**, Nicholas Alderman, Lefteris Danos and Tom Markvart, 2014. *Determination and Validation of the Surface Recombination Velocity on the Silicon Surface using Kelvin Probe Method and PC1D Simulation*. **In-progress Manuscript for Applied Physics Letters**.
3. **Mohd Adib Ibrahim**, Dmitry Bavykin and Tom Markvart, 2014. *A System Model of Photosynthesis Inspired by Photovoltaics*. **In-progress Manuscript for Biophysical Journal**.
4. **Mohd Adib Ibrahim**, Masita Mohammad, Mohd Asri Mat Teridi, Norasikin AhmadLudin, Kamaruzzaman Sopian, Dmitry Bavykin, Tom Markvart, 2014. *Interpretation of Chemical Potentials in Photosynthetic Electron Transport*. Renewable and Sustainable Energy Review, January, **Submitting for 2nd Review**.
5. Nicholas Alderman, **Mohd Adib Ibrahim**, Lefteris Danos, Martin C. Grossel and Tom Markvart, 2013. *Determination of Surface Recombination Velocities of Organic Monolayers on Silicon through Kelvin Probe*. Applied Physics Letters, 103(8): 081603.
6. Nicholas Alderman, **Mohd Adib Ibrahim**, Lefteris Danos, Martin C. Grossel and Tom Markvart, 2013. *A Novel Method for the Determination*

of Surface Recombination Velocity through Surface Photovoltage Measurements, Proceedings of 9th Photovoltaic Science Applications and Technology (PVSAT-9), April 10th - 12th, Swansea University, Swansea, Wales.

7. **Mohd Adib Ibrahim**, Mohd Asri Mat Teridi, Norasikin Ahmad Ludin, Suhaila Sepeai, Kamaruzzaman Sopian, Nicholas Alderman, Lefteris Danos, Tom Markvart, 2013. *Stability Study of Alkyl Monolayers Directly Attached to Si (111) Surface for Solar Cells Application*, 7th International Conference on Renewable Energy Sources (RES '13), April 2nd - 4th, Kuala Lumpur, Malaysia.
8. **Mohd Adib Ibrahim**, Kamaruzzaman Sopian, Lefteris Danos and Tom Markvart, 2012. *Characterization of Langmuir-Blodgett Films on Silicon Surface by Kelvin Probe Method*. The 3rd ISESCO International Workshop and Conference on Nanotechnology (IWCN 2012), December 5th - 7th, Kuala Lumpur, Malaysia.
9. **Mohd Adib Ibrahim**, Lefteris Danos and Tom Markvart, 2010. *Characterization of 1-Decene Monolayers directly attached to Si (111) surface*. Proceedings of 6th Photovoltaic Science Applications and Technology (PVSAT-6), Page 123-126, 24-26th March, Chilworth Manor, University of Southampton, Southampton, United Kingdom.
10. **Mohd Adib Ibrahim**, Dmitry Bavykin and Tom Markvart, 2009. *Determination of Chemical Potential in Simplified Model of Photosynthesis for Solar Cell Application*. Proceeding of the 15th Postgraduate Conference in Engineering Materials, Page 43-44, 2nd October, Lyndhurst Park Hotel, New Forest, United Kingdom.
11. **Mohd Adib Ibrahim**, Lefteris Danos and Tomas Markvart, 2009. *Formation of Organic Monolayer on the Silicon Surface*. Proceedings of 5th Photovoltaic Science Applications and Technology (PVSAT-5), Page 93-96, 1-3rd April, Glyndwr University, Wrexham, Wales.

12. **Mohd Adib Ibrahim**, Dmitry Bavykin and Tom Markvart, 2008, *Energy Conversion in Bacterial Photosynthesis: Simplified Model for Solar Cell Application*. Proceeding of the 14th Postgraduate Conference in Engineering Materials, Page 23-24, 1st October, Hilton Hotel, Southampton, United Kingdom.
13. Bo Feng, **Mohd Adib Ibrahim**, Lefteris Danos and Tom Markvart, 2008, *Characterization of Silicon Surface State by Quasi-Steady-State Photo-conductance Method*. Proceeding of the 14th Postgraduate Conference in Engineering Materials, Page 21-22, 1st October, Hilton Hotel, Southampton, United Kingdom.
14. **Mohd Adib Ibrahim**, Tom Markvart and Dmitry Bavykin, 2008. *Photosynthesis and Photovoltaics: A Comparative Study of Conversion Processes*. Proceedings 4th of Photovoltaic Science Applications and Technology (PVSAT-4), Page 153-156, 2-4th April, Bath University, Bath, United Kingdom.
15. Lefteris Danos, **Mohd Adib Ibrahim** and Tom Markvart, 2008. Wet chemical passivation methods for application in silicon solar cells. Proceedings of Photovoltaic Science Applications and Technology (PVSAT-4), Page 75-78, 2 - 4th April, Bath University, Bath, United Kingdom.

Glossary

- Light Harvesting* A complex compound of sub-unit protein which is part of a larger super complex of a photosystem in a photosynthesis system. It is found and used by plants, alga and bacteria.
- Surface passivation* A thin films of materials as passivating surface such as silicon nitride, silicon dioxide or an organic monolayers that can reduce a surface recombination
- Alkyl monolayer* A self-assembled monolayer of organic molecules that are molecular assemblies formed spontaneously on the surface by the chemisorption process
- Langmuir Blodgett* A technique of deposition of an organic material that creates monolayers (films) on the surface. A film was deposited from the surface of a liquid onto a substrate surface by immersing the substrate into the liquid (vertical deposition).
- Energy conversion* The process of changing one form of energy into another e.g. solar energy into electrical energy.
- Kelvin probe* A contactless and non-destructive method to measure a work function of the surfaces.
- Charge trapping* A process of charge carrier trapped at irregularities in the crystal lattice of the semiconductor (defects) which have different energy level.
- Charge detrapping* A process of charge carrier relaxation (detrapping) or decay time to initial states.
- Contact Potential Difference* The difference of the work functions of two conductors which are connected electrically through a circuit.

Glossary

Photo-conductance decay A measurement to determine the bulk lifetime of semiconductors.

Surface recombination Any defects or impurities on the semiconductor surface contribute to recombination.

Surface recombination velocity A parameter that used to identify the recombination on a surface and measured in unit of cm/s.

Surface photovoltage A measurement to determine the minority carrier diffusion length of semiconductors.

List of References

- [1] S.M. Sze, K.K. Ng, Physics of Semiconductor Devices, 3rd ed., John Wiley & Sons, Inc., New York, US, 2007.
- [2] D.A. Neamen, Semiconductor Physics and Devices - Basic Principles, 3rd ed., Mc Graw Hill, New York, 2003.
- [3] T. Markvart, L. Danos, R. Greef, High-Efficiency Low Cost Silicon Solar Cells, Report 2003-8-5154-1 to Carbon Trust 2006.
- [4] T. Markvart, Light harvesting for quantum solar energy conversion, Progress in Quantum Electronics, 24 (2000) 107-186.
- [5] W. Ruppel, P. Würfel, Upper Limit for the Conversion of Solar Energy, IEEE Transactions on Electronic Devices, 27 (1980) 877-882.
- [6] D. Trivich, P.A. Flinn, Maximum Efficiency of Solar Energy by Quantum Processes, in: F. Daniels, J. Duffie (Eds.) Solar Energy Research, Thames and Hudson, London, 1955, pp. 143.
- [7] A. Goetzberger, J. Knobloch, B. Voss, Crystalline Silicon Solar Cells, John Wiley & Sons Ltd, Chichester, England, 1998.
- [8] M.A. Green, M.J. Keevers, Optical properties of intrinsic silicon at 300 K, Progress in Photovoltaics: Research and Applications, 3 (1995) 189-192.
- [9] G. Parker, Introductory semiconductor device physics, Prentice Hall Europe (UK) Limited, Hertfordshire, 1994.
- [10] R.H. Bube, Photovoltaic Materials, Imperial College Press, London, 1998.
- [11] J. Nelson, The Physics of Solar Cells, Imperial College Press, London, 2003.
- [12] W. Monch, Semiconductor Surfaces and Interfaces, 3rd ed., Springer-Verlag Berlin Heidelberg, New York, 2001.
- [13] L. Kronik, Y. Shapira, Surface photovoltage phenomena: theory, experiment, and applications, Surface Science Reports, 37 (1999) 1-206.
- [14] A.M. Cowley, S.M. Sze, Surface states and barrier height of metal-semiconductor systems, Journal of Applied Physics, 36 (1965) 3212-3220.
- [15] D.A. Tryk, A. Fujishima, K. Honda, Recent topics in photoelectrochemistry: achievements and future prospects, Electrochimica Acta, 45 (2000) 2363 - 2376.
- [16] T. Markvart, Solar Electricity, 2nd edition ed., John Wiley & Sons, Chichester, West Sussex, England, 2000.
- [17] P.T. Landsberg, Recombination in semiconductors, University Press, Cambridge, U.K., 1991.
- [18] A.G. Aberle, Crystalline Silicon Solar Cells - Advanced Surface Passivation and Analysis, 1st ed., Centre for Photovoltaic Engineering, UNSW, Sydney, Australia, 1999.
- [19] R.A. Sinton, R.M. Swanson, Recombination in Highly Injected Silicon, IEEE Transactions on Electron Devices ED-34 (1987).
- [20] W. Shockley, W.T. Read, Statistics of the Recombinations of Holes and Electrons, Physical Review, 87 (1952) 835-842.
- [21] R.N. Hall, Electron-Hole Recombination in Germanium, Phys. Rev., 87 (1952) 387.

- [22] M.A. Green, Intrinsic Carrier Concentration, Effective Densities of States and Effective Mass in Silicon, *Journal of Applied Physics*, 67 (1990) 2944-2954.
- [23] P.B. Weisz, Effects of Electronic Charge Transfer between Adsorbate and Solid on Chemisorption and Catalysis, *The Journal of Chemical Physics*, 21 (1953) 1531-1538.
- [24] G.P. Srivastava, Theory of semiconductor surface reconstruction, *Rep. Prog. Phys.*, 60 (1997) 561-613.
- [25] Y.R. Wang, C.B. Duke, A. Paton, K. Stiles, A. Kahn, Relaxation and surface states on cleavage faces: CdSe (1010), *Phys. Rev.*, 36 (1987) 9406-9409.
- [26] H. Ibach, *Physics of Surfaces and Interfaces*, Springer, Verlag Berlin Heidelberg, 2006.
- [27] H. Angermann, W. Henrion, A.R. seler, M. Rebien, Wet-chemical passivation of Si(111)- and Si(100)-substrates, *Materials Science and Engineering B*, 73 (2000) 178-183.
- [28] L.H. Terman, An investigation of surface states at a silicon/silicon oxide interface employing metal-oxide-silicon diodes, *Solid-State Electronics*, 5 (1962) 285-299.
- [29] H. Angermann, Characterization of wet-chemically treated silicon interfaces by surface photovoltage measurements, *Anal Bioanal Chem*, 374 (2002) 676-680.
- [30] Y. Dan, K. Seo, K. Takei, J.H. Meza, A. Javey, K.B. Crozier, Dramatic reduction of surface recombination by in situ surface passivation of silicon nanowires., *Nano Letters*, 11 (2011) 2527-2532.
- [31] A.B. Sieval, A.L. Demirel, J.W.M. Nissink, M.R. Linford, J.H.v.d. Maas, W.H.d. Jeu, H. Zuilhof, E.J.R. Sudhölter, Highly Stable Si-C Linked Functionalized Monolayers on the Silicon (100) Surface, *Langmuir*, 14 (1998) 1759-1768.
- [32] A.B. Sieval, V. Vleeming, H. Zuilhof, E.J.R. Sudhölter, An Improved Method for the Preparation of Organic Monolayers of 1-Alkenes on Hydrogen-Terminated Silicon Surfaces, *Langmuir*, 15 (1999) 8288-8291.
- [33] M.R. Linford, C.E.D. Chidsey, Alkyl Monolayers Covalently Bonded to Silicon Surfaces, *Journal of the American Chemical Society*, 115 (1993) 12631-12632.
- [34] R. Boukherroub, S. Morin, F. Bensebaa, D.D.M. Wayner, New Synthetic Routes to Alkyl Monolayers on the Si(111) Surface, *Langmuir*, 15 (1999) 3831-3835.
- [35] J. Terry, M.R. Linford, C. Wigren, R. Cao, P. Pianetta, C.E.D. Chidsey, Determination of the bonding of alkyl monolayers to the Si(111) surface using chemical-shift, scanned-energy photoelectron diffraction, *Applied Physics Letters*, 71 (1997) 1056-1058.
- [36] R. Boukherroub, D.D.M. Wayner, Controlled Functionalization and Multistep Chemical Manipulation of Covalently Modified Si(111) Surfaces, *Journal of the American Chemical Society*, 121 (1999) 11513-11515.
- [37] E.J. Nemanick, P.T. Hurley, B.S. Brunschwig, N.S. Lewis, Chemical and electrical passivation of silicon (111) surfaces through functionalization with sterically hindered alkyl groups, *Journal of Physical Chemistry B*, 110 (2006) 14800-14808.
- [38] P. Handler, Electrical Properties of the Surfaces of Semiconductors, in: H. C.Gatos, J.W. Faust, W.J. Lafleur (Eds.) *The Surface Chemistry of Metals and Semiconductors*, John Wiley & Sons, Inc., New York, 1960.

- [39] T. Markvart, Principles of Solar Cell Operation, in: T. Markvart, L. Castaner (Eds.) Practical Handbook of Photovoltaics: Fundamentals and Applications, Elsevier Science Ltd, Oxford, UK, 2003.
- [40] A.B. Sproul, Dimensionless solution of the equation describing the effect of surface recombination on carrier decay in semiconductors, *Journal of Applied Physics* 76 (1994) 2851-2854.
- [41] A. Subrahmanyam, C.S. Kumar, Kelvin Probe for Surface Engineering: Fundamentals and Design, Ane Books Pvt. Ltd., New Delhi, India, 2009.
- [42] L.L. Rosier, Surface state and surface recombination velocity characteristics of Si-SiO₂ interfaces, *IEEE Transactions on Electron Devices*, 13 (1966) 260-268.
- [43] A.S. Grove, E.H. Snow, B.E. Deal, C.T. Sah, Simple physical model for the space-charge capacitance of metal-oxide-semiconductor structures, *Journal of Applied Physics*, 35 (1964) 2458-2460.
- [44] P.K. Kashkarov, E.A. Konstantinova, A.B. Matveeva, V.Y. Timoshenko, Photovoltage and photo-induced charge trapping in *Applied Physics A*, 62 (1996) 547-551.
- [45] I. McConnell, G. Li, G.W. Brudvig, Energy Conversion in Natural and Artificial Photosynthesis, *Chemical Biology*, 17 (2010) 434-447.
- [46] R.K. Clayton, Photosynthesis: Physical mechanisms and chemical patterns, 1st published ed., Cambridge University Press, Cambridge, London U.K., 1980.
- [47] R.E. Blankenship, Molecular Mechanisms of Photosynthesis, 2nd ed., Blackwell Science, Victoria, Australia, 2008.
- [48] J.R. Bolton, D.O. Hall, Photochemical conversion and storage of solar energy, *Ann. Rev. Energy* 4(1979) 353-401.
- [49] M.D. Archer, J.R. Bolton, Requirements for Ideal Performance of Photochemical and Photovoltaic Solar Energy Converters, *The Journal of Physical Chemistry* 94 (1990) 8028-8036.
- [50] V. Sundstrom, Light in elementary biological reactions, *Progress in Quantum Electronics*, 24 (2000) 187-238.
- [51] T. Markvart, P.T. Landsberg, Solar cell model for electron transport in photosynthesis, Proc. 29th IEEE Photovoltaic Specialists Conference, New Orleans, 2002, pp. 1348-1351.
- [52] M.Y. Okamura, M.L. Paddock, M.S. Graige, G. Feher, Proton and electron transfer in bacterial reaction centers, *Biochimica et Biophysica Acta*, 1458 (2000) 148-163.
- [53] R.S. Knox, Thermodynamics and the primary processes of photosynthesis, *Biophysical Journal*, 9 (1969) 1351-1362.
- [54] W.A. Cramer, G.M. Soriano, Chapter 1 Thermodynamics of Energy Transduction in Biological Membranes, *BTOL-Bioenergetics*, (2002) 1-58.
- [55] P. Mitchell, Coupling of phosphorylation to electron and hydrogen transfer by a chemiosmotic type of mechanism., *Nature*, 191 (1961) 144-148.
- [56] A. Crofts, Model proton pump, *Biophysics* 354 - Biological Energy Conversion 1996.
- [57] D.L. Nelson, M.M. Cox, Lehninger Principles of Biochemistry, Fifth Edition ed., W.H. Freeman and Company, New York, US, 2008.
- [58] R.T. Ross, M. Calvin, Thermodynamics of light emission and free-energy storage in photosynthesis, *Biophysical Journal*, 7 (1967).
- [59] T. Markvart, Photovoltaic Solar Energy Conversion, European Summer University: Energy for Europe, Strasbourg, 2002.

- [60] T. Markvart, P.T. Landsberg, Thermodynamics and reciprocity of solar energy conversion, *Physica E*, 14 (2002) 71 - 77.
- [61] J. Lavergne, P. Joliot, Dissipation in bioenergetic electron transfer chains, *Photosynthesis Research*, 48 (1996) 127-138.
- [62] L. Kelvin, Contact Electricity of Metals, *Philosophical Magazine*, 46 (1898) 82.
- [63] W.A. Zisman, A new method of measuring contact potential differences in metals, *Rev. Sci. Instrum.*, 3 (1932) 367-370.
- [64] D.K. Schroder, Surface voltage and surface photovoltage: history, theory and applications, *Measurement Science and Technology*, 12 (2001) R16-R31.
- [65] H. Ishii, N. Hayashi, E. Ito, Y. Washizu, K. Sugi, Y. Kimura, M. Niwano, Y. Ouchi, K. Seki, Kelvin probe study of band bending at organic semiconductor/metal interfaces: examination of Fermi level alignment, *Phys. Stat. Sol. (a)*, 201 (2004) 1075 - 1094.
- [66] T. Okumura, K. Eguchi, A. En, M. Suhara, Contactless Method for Electrical Characterization of Silicon-on-Insulator Materials, *Japanese Journal of Applied Physics*, 40 (2001) 5217-5220.
- [67] T. Okumura, A. En, K. Eguchi, M. Suhara, Contactless characterization of surface and interface band-bending in Silicon-On-Insulator (SOI) structures, *Materials Science and Engineering*, B91 - 92 (2002) 182 - 185.
- [68] D. Watanabe, A. En, S. Nakamura, M. Suhara, T. Okumura, Anomalously large band-bending for HF-treated p-Si surfaces, *Applied Surface Science*, 216 (2003) 24-29.
- [69] S. Nakamura, D. Watanabe, A. En, M. Suhara, T. Okumura, Contactless electrical characterization of surface and interface of SOI materials, *Applied Surface Science*, 216 (2003) 113-118.
- [70] M. Leibovitch, L. Kronik, E. Fefer, Y. Shapira, Distinction between surface and bulk states in surface-photovoltage spectroscopy, *Physical Review B*, 50 (1994) 1739-1745.
- [71] D.L. Lile, Surface photovoltage and internal photoemission at the anodized InSb surface, *Surface Science*, 34 (1973) 337-367.
- [72] E.O. Johnson, Large signal surface photovoltage studies with Germanium, *Physical Review*, 111 (1958).
- [73] L. Szaro, J. Rebisz, J. Misiewicz, Surface photovoltage in semiconductors under sub-band-gap illumination: continuous distribution of surface state, *Applied Physics A*, 69 (1999) 409-413.
- [74] K. Nauka, J. Lagowski, Advances in surface photovoltage technique for monitoring of the IC processes, in: D.G. Seiler, A.C. Diebold, W.M. Bullis, T.J. Shaffner, R. McDonald, E.J. Waiters (Eds.) *The 1998 international conference on characterization and metrology for ULSI technology*, American Institute of Physics, Gaithersburg, Maryland (USA), 1998, pp. 245-249.
- [75] T.S. Moss, Photovoltaic and photoconductive theory applied to InSb, *J. Electron Control*, 1 (1955) 126-138.
- [76] M. Saritas, H.D. McKell, Diffusion length studies in silicon by the surface photovoltage method, *Solid-State Electronics*, 31 (1988) 835-842.
- [77] A.M. Goodman, A method for the measurement of short minority carrier diffusion lengths in semiconductors, *Journal of Applied Physics*, 32 (1961) 2550-2552.

- [78] M.K. Alam, Y.T. Yeow, Evaluation of the Surface Photovoltage method of Minority-carrier diffusion-length measurement, *Solid-State Electronics*, 24 (1981) 1117-1119.
- [79] T. Meoded, R. Shikler, N. Fried, Y. Rosenwaks, Direct measurement of minority carriers diffusion length using Kelvin probe force microscopy, *Applied Physics Letters*, 75 (1999) 2435-2437.
- [80] R. Shikler, N. Fried, T. Meoded, Y. Rosenwaks, Measuring minority-carrier diffusion length using a Kelvin probe force microscope, *Physical Review B*, 61 (2000) 11041-11046.
- [81] A. International, Standard Test Methods for Minority Carrier Diffusion Length in Extrinsic Semiconductors by Measurement of Steady-State Surface Photovoltage, in: A. International (Ed.), United States., 2003, pp. 1-10.
- [82] S.C. Jain, R. Muralidharan, Effect of emitter recombinations on the open circuit voltage decay of a junction diode, *Solid State Electronics* 24 (1981) 1147-1154.
- [83] T. Markvart, Relationship between dark carrier distribution and photogenerated carrier collection in solar cells, *IEEE Transactions on Electron Devices*, 43 (1996) 1034-1036.
- [84] R.J. Hamers, Formation and Characterization of Organic Monolayers on Semiconductor Surfaces, *Annu. Rev. Anal. Chem.*, 1 (2008) 707-736.
- [85] L.C.P.M.d. Smet, Covalently Bound Organic Monolayers on Silicon Surfaces. Visible Light Attachment, Characterization, and Electrical Properties, Wageningen University 2006, pp. 182.
- [86] H. Angermann, W. Henrion, M. Rebien, A. Roseler, Wet-chemical preparation and spectroscopic characterization of Si interfaces, *Applied Surface Science* 235 (2004) 322-339.
- [87] A.B. Sieval, B.v.d. Hout, H. Zuilhof, E.J.R. Sudhölter, Molecular Modeling of Alkyl Monolayers on the Si(111) Surface, *Langmuir*, 16 (2000).
- [88] W. Kern, *Handbook of Semiconductor Cleaning Technology*, Noyes Publishing, Park Ridge, New Jersey, 1993.
- [89] W. Kern, The Evolution of Silicon Wafer Cleaning Technology, *J. Electrochem. Soc.*, 137 (1990) 1887-1892.
- [90] Y.J. Chabal, G.S. Higashi, K. Raghavachari, V.A. Burrows, Infrared spectroscopy of Si(111) and Si(100) surfaces after HF treatment: Hydrogen termination and surface morphology, *Journal of Vacuum Science & Technology A: Vacuum, Surfaces, and Films* 7(1989) 2104-2109.
- [91] J.M. Buriak, Organometallic Chemistry on Silicon and Germanium Surfaces, *Chemical Reviews*, 102 (2002) 1271-1319.
- [92] T.I. Kamins, K. Nauka, R.S. Williams, Effect of self-assembled Ge nanostructures on Si surface electronic properties, *Applied Physics A Materials Science & Processing*, 73 (2001) 1-9.
- [93] K. Nauka, Z. Li, T.I. Kamins, Surface photovoltage in silicon. Novel applications for chemical and biological sensing, *Materials Science-Poland*, 23 (2005) 653-661.
- [94] H. Angermann, W. Henrion, M. Rebien, A. Roseler, Wet-chemical passivation and characterization of silicon interfaces for solar cell applications, *Solar Energy Materials & Solar Cells*, 83 (2004) 331-346.
- [95] X.G. Zhang, *Electrochemistry of Silicon and Its Oxide*, Kluwer Academic: Plenum Publishers, New York, 2001.
- [96] L.C.P.M.d. Smet, G.A. Stork, G.H.F. Hurenkamp, Q.-Y. Sun, H.s. Topal, P.J.E. Vronen, A.B. Sieval, A. Wright, G.M. Visser, H. Zuilhof, E.J.R.

- Sudhölter, Covalently Attached Saccharides on Silicon Surfaces, *Journal of the American Chemical Society*, 125 (2003) 13916-13917.
- [97] Y.J. Chabal, G.S. Higashi, R.J. Small, Surface Chemical Composition and Morphology, in: K.A. Reinhardt, W. Kern (Eds.) *Handbook of Silicon Wafer Cleaning Technology*, William Andrew Inc.2008, pp. 523.
- [98] E.J. Faber, L.C.P.M.d. Smet, W. Olthuis, H. Zuilhof, E.J.R. Sudhölter, P. Bergveld, A.v.d. Berg, Si-C Linked Organic Monolayers on Crystalline Silicon Surfaces as Alternative Gate Insulators, *ChemPhysChem*, 6 (2005) 2153 - 2166.
- [99] P.K. Hurley, K. Cherkaoui, S. McDonnell, G. Hughes, A.W. Groenland, Characterisation and passivation of interface defects in (100)-Si/SiO₂/HfO₂/TiN gate stacks, *Microelectronics Reliability*, 47 (2007) 1195-1201.
- [100] B.J. Eves, Q.-Y. Sun, G.P. Lopinski, H. Zuilhof, Photochemical Attachment of Organic Monolayers onto H-Terminated Si(111): Radical Chain Propagation Observed via STM Studies, *Journal of the American Chemical Society*, 126 (2004) 14318-14319.
- [101] B. Sun, P.E. Colavita, H. Kim, M. Lockett, M.S. Marcus, L.M. Smith, R.J. Hamers, Covalent Photochemical Functionalization of Amorphous Carbon Thin Films for Integrated Real-Time Biosensing, *Langmuir*, 22 (2006) 9598-9605.
- [102] M.R. Linford, P. Fenter, P.M. Eisenberger, C.E.D. Chidsey, Alkyl Monolayers on Silicon Prepared from 1-Alkenes and Hydrogen-Terminated Silicon, *Journal of the American Chemical Society*, 117 (1995) 3145-3155.
- [103] A.B. Sieval, B.v.d. Hout, H. Zuilhof, E.J.R. Sudhölter, Molecular Modeling of Covalently Attached Alkyl Monolayers on the Hydrogen-Terminated Si(111) Surface, *Langmuir*, 17 (2001) 2172-2181.
- [104] A.B. Sieval, R. Linke, H. Zuilhof, E.J.R. Sudhölter, High-Quality Alkyl Monolayers on Silicon Surfaces, *Advanced Materials*, 12, (2000).
- [105] X. Bin, T.K. Mischki, C. Fan, G.P. Lopinski, D.D.M. Wayner, Electrochemical Characterization of Si(111) Modified with Linear and Branched Alkyl Chains, *Journal of Physical Chemistry C*, 111 (2007) 13547-13553.
- [106] P.W. Atkins, J.d. Paula, *Elements of Physical Chemistry*, 4th ed., Oxford University Press, Oxford, UK, 2005.
- [107] I.V. Antonova, R.A. Soots, V.A. Seleznev, V.Y. Prints, Electrical Passivation of the Silicon Surface by Organic Monolayers of 1-Octadecene, *Semiconductors*, 41 (2007) 991-997.
- [108] C. Miramond, D. Vuillaume, 1-octadecene monolayers on Si(111) hydrogen-terminated surfaces: Effect of substrate doping, *Journal of Applied Physics* 96 (2004) 1529.
- [109] L. Danos, T. Markvart, Efficient light harvesting with LB films for application in crystalline silicon solar cells, *Mater. Res. Soc. Symp. Proc.*, Materials Research Society2009, pp. M01-04.
- [110] J.M. Buriak, M.J. Allen, Lewis Acid Mediated Functionalization of Porous Silicon with Substituted Alkenes and Alkynes, *Journal of the American Chemical Society*, 120 (1998) 1339-1340.
- [111] P. Gorostiza, C.H.d. Villeneuve, Q.Y. Sun, F. Sanz, X. Wallart, R. Boukherroub, P. Allongue, Water Exclusion at the Nanometer Scale Provides Long-Term Passivation of Silicon (111) Grafted with Alkyl Monolayers, *J. Phys. Chem. B*, 110 (2006) 5576-5585.

- [112] C.R. Kinser, H. Jin, M. Bedzyk, M. Hersam, B. Honeyman, Stability Study of Self-Assembled Monolayers on Silicon(111), *Nanoscope*, 2 (2005) 89-95.
- [113] A.B. Sieval, C.L. Huisman, A. Schonecker, F.M. Schuurmans, A.S.H.v.d. Heide, A. Goossens, W.C. Sinke, H. Zuilhof, E.J.R. Sudhölter, Silicon surface passivation by organic monolayers: Minority charge carrier lifetime measurements and Kelvin probe investigations, *Journal of Physical Chemistry B*, 107 (2003) 6846-6852.
- [114] T. Ishizaki, N. Saito, L. SunHyung, K. Ishida, O. Takai, Study of Alkyl Organic Monolayers with Different Molecular Chain Lengths Directly Attached to Silicon, *Langmuir*, 22 (2006) 9962-9966.
- [115] R.M.A. Azzam, N.M. Bashara, *Ellipsometry and Polarized Light*, North-Holland, Amsterdam, 1977.
- [116] H. Fujiwara, *Spectroscopic Ellipsometry: Principles and Applications*, Maruzen Co. Ltd., Tokyo, Japan, 2003.
- [117] S.-M.F. Nee, Ellipsometric analysis for surface roughness and texture, *Applied Optics*, 27 (1988) 2819-2831.
- [118] D.E. Aspnes, Optical properties of thin films, *Thin Solid Films*, 89 (1982) 249-262.
- [119] J. Workman, L. Weyer, *Practical guide to interpretive near-infrared spectroscopy*, CRC Press, New York, U.S., 2007.
- [120] M. Rosso, M. Giesbers, A. Arafat, K. Schroën, H. Zuilhof, Covalently Attached Organic Monolayers on SiC and SiN Surfaces: Formation Using UV Light at Room Temperature, *Langmuir*, 25 (2009) 2172-2180.
- [121] T. Ishizaki, N. Saito, S. Lee, O. Takai, Comparative study of the molecular aggregation state of alkyl organic monolayers prepared on Si and hydrogen-terminated Si substrates, *Nanotechnology*, 19 (2008) 1-6.
- [122] X. Wallart, C.H.d. Villeneuve, P. Allongue, Truly Quantitative XPS Characterization of Organic olayers on Silicon: Study of Alkyl and Alkoxy Monolayers on H-Si(111), *Journal of the American Chemical Society*, 127 (2005) 7871-7878.
- [123] M. Rosso, A. Arafat, K. Schroen, M. Giesbers, C.S. Roper, R. Maboudian, H. Zuilhof, Covalent Attachment of Organic Monolayers to Silicon Carbide Surfaces, *Langmuir*, 24 (2008) 4007-4012.
- [124] Y. Sato, M. Maeda, Study of HF-treated heavily doped Si surface using contact angle measurements, *Jpn. J. Appl. Phys.*, 33 (1994) 6508-6513.
- [125] T.K. Mischki, R.L. Donkers, B.J. Eves, G.P. Lopinski, D.D.M. Wayner, Reaction of Alkenes with Hydrogen-Terminated and Photooxidized Silicon Surfaces. A Comparison of Thermal and Photochemical Processes, *Langmuir*, 22 (2006) 8359-8365.
- [126] H. Kuhn, Classical Aspects of Energy Transfer in Molecular Systems, *The Journal of Chemical Physics* 53 (1970).
- [127] D.L. Dexter, Two ideas on energy transfer phenomena: Ion-pair effects involving the OH stretching mode and sensitization of photovoltaic cells, *Journal of Luminescence*, 18-19 (1979) 779-784.
- [128] K.B. Blodgett, I. Langmuir, Built-Up Films of Barium Stearate and Their Optical properties, *Physical Review*, 51 (1937) 964-982.
- [129] M.C. Petty, *Langmuir-Blodgett Films: An Introduction* Cambridge University Press University of Durham, 1996.
- [130] O.N.O. Jr., *Langmuir-Blodgett Films - Properties and Possible Applications*, *Brazilian Journal of Physics* 22 (1992).
- [131] R.A. Hann, Molecules for Langmuir-Blodgett film formation, *Philosophical Transactions of the Royal Society of London. Series A*,

- Mathematical and Physical Sciences, The Royal Society 1990, pp. 141-152.
- [132] R.G. Laughlin, *The Aqueous Phase Behavior of Surfactants*, Academic Press Ltd, London, UK, 1994.
- [133] J.K. Basu, S. Hazra, M.K. Sanyal, Growth Mechanism of Langmuir-Blodgett Films, *Physical Review Letters* 82 (1999) 4675-4578.
- [134] D.Y. Takamoto, E. Aydil, J.A. Zasadzinski, A.T. Ivanova, D.K. Schwartz, T. Yang, P.S. Cremer, Stable Ordering in Langmuir-Blodgett Films, *Science*, 293 (2001).
- [135] L. Danos, R. Greef, T. Markvart, Efficient fluorescence quenching near crystalline silicon from Langmuir-Blodgett dye films, *Thin Solid Films*, 516 (2008) 7251-7255.
- [136] L. Danos, T. Markvart, Excitation energy transfer rate from Langmuir Blodgett (LB) dye monolayers to silicon: Effect of aggregate formation, *Chemical Physics Letters*, 490 (2010) 194-199.
- [137] G.G. Roberts, K.P. Pande, W.A. Barlow, Inp/langmuir-film m.i.s.f.e.t., *IEEE J. Solid State Electron. Devices UK*, 2 (1978) 169-175
- [138] P.W. Bohn, Aspects of Structure and energy Transport in Artificial Molecular Assemblies, *Annu. Rev. Phys. Chem.*, 44 (1993) 37-60.
- [139] M.C. Howland, M.S. Johal, A.N. Parikh, Transition from Homogeneous Langmuir-Blodgett Monolayers to Striped Bilayers Driven by a Wetting Instability in Octadecylsiloxane Monolayers, *Langmuir*, 21 (2005) 10468-10474.
- [140] M.R. Kosuri, H. Gerung, Q. Li, S.M. Han, P.E. Herrera-Morales, J.F. Weaver, Vapor-phase adsorption kinetics of 1-decene on hydrogenated Si(111), *Surface Science*, (2005).
- [141] S.R. Puniredd, O. Assad, H. Haick, Highly Stable Organic Monolayers for Reacting Silicon with Further Functionalities: The Effect of the C-C Bond nearest the Silicon Surface, *Journal of the American Chemical Society*, 130 (2008) 13727-13734.
- [142] I.D. Baikie, K.O.v. derWerf, H. Oerbekke, J. Breeze, A.v. Silfhout, Automatic kelvin probe compatible with ultrahigh vacuum, *Review of Scientific Instruments*, 60 (1989) 930-934.
- [143] D. Macdonald, R.A. Sinton, A.s. Cuevas, On the use of a bias-light correction for trapping effects in photoconductance-based lifetime measurements of silicon, *Journal of Applied Physics*, 89 (2001) 2772-2778.
- [144] A. Cuevas, D. Macdonald, Measuring and interpreting the lifetime of silicon wafers, *Solar Energy*, 76 (2004) 255-262.
- [145] R. Lago-Aurrekoetxea, I. Tobías, C.d. Cañizo, A. Luque, Lifetime Measurements by Photoconductance Techniques in Wafers Immersed in a Passivating Liquid, *Journal of The Electrochemical Society*, 148 (2001) G200-G206.
- [146] M. Saritas, H.D. McKell, Absorption coefficient of Si in the wavelength region between 0.80-1.16 μm , *Journal of Applied Physics* 61 (1987) 4923-4925.
- [147] M. Saritas, H.D. McKell, Comparison of minority-carrier diffusion length measurements in silicon by the photoconductive decay and surface photovoltage methods, *Journal of Applied Physics*, 63 (1988) 4562-4567.
- [148] J. Tousek, S. Dolhov, J. Tuskova, Interpretation of minority carrier diffusion length measurements in thin silicon wafers, *Solar Energy Materials & Solar Cells*, 76 (2003) 205-210.

- [149] W.J. Royea, A. Juang, N.S. Lewi, Preparation of air-stable, low recombination velocity Si(111) surfaces through alkyl termination, *Applied Physics Letters*, 77 (2000) 1988-1990.
- [150] E. Yablonovitch, D.L. Allara, C.C. Chang, T. Gmitter, T.B. Bright, Unusually Low Surface-Recombination Velocity on Silicon and Germanium Surfaces, *Physical Review Letters*, 57 (1986) 249-252.
- [151] R.A. Sinton, A. Cuevas, M. Stucking, Quasi-steady-state photoconductance, A new method for solar cell material and device characterization 25th PVSC, Washington D.C., 1996, pp. PP457-460.
- [152] E.J. Nemanick, P.T. Hurley, L.J. Webb, D.W. Knapp, D.J. Michalak, B.S. Brunschwig, N.S. Lewis, Chemical and electrical passivation of single-crystal silicon(100) surfaces through a two-step chlorination/alkylation process, *Journal of Physical Chemistry B*, 110 (2006) 14770-14778.
- [153] N. Alderman, M.A. Ibrahim, L. Danos, M.C. Grossel, T. Markvart, Determination of surface recombination velocities of organic monolayers on silicon through Kelvin probe, *Applied Physics Letters* 103 (2013) 1-5.
- [154] A. Buczkowski, G. Rozgonyi, F. Shimura, Photoconductance minority carrier lifetime vs. surface photovoltage diffusion length in silicon, *J. Electrochem. Soc.*, 140 (1993) 3240-3245.
- [155] C.G.B. Garrett, W.H. Brattain, Physical Theory of Semiconductor Surfaces, *Physical Review*, 99 (1955) 376-387.
- [156] W.H. Brattain, J. Bardeen, Surface Properties of Germanium, *The Bell System Technical Journal*, 32 (1953).
- [157] H. Statz, G.A. deMars, J. L. Davis, J. A. Adam, Surface States on Silicon and Germanium Surfaces, *Physical Review*, 106 (1957).
- [158] H.-S. Fu, C.-T. Sah, Theory and experiments on surface 1/f noise, *Electron Devices*, *IEEE Transactions* 19 (1972) 273-284.
- [159] J.R. Haynes, J.A. Hornbeck, Trapping of minority carriers in silicon. II. n-type silicon, *Physical Review*, 100 (1955) 606-615.
- [160] B. Honeyman, M. Bedzyk, M. Hersam, H. Jin, C.R. Kinser, Stability Study of Self-Assembled Monolayers on Silicon (111), *Nanoscape*, 2 (2005).
- [161] G. Elliott, Direct observation of charge storage in the surface states of germanium and silicon, *Brit. J. Appl. Phys.* , 17 (1966) 167-174.
- [162] Y.-J. Liu, H.-Z. Yu, Alkyl Monolayer Passivated Metal-Semiconductor Diodes: Comparison with Native Silicon Oxide, *ChemPhysChem*, 4 (2003) 335-342.
- [163] B. Fabre, F. Hauquier, P. Allongue, Electrochemical transfer at p-type silicon(111)-alkyl monolayer hybrid electrodes in acetonitrile medium, *Journal of Electroanalytical Chemistry*, 629 (2009) 63-68.
- [164] H. Foll, M. Christophersen, J. Carstensen, G. Hasse, Formation and application of porous silicon, *Materials Science and Engineering*, 39 (2002) 93-141.